

Metal-Organic Frameworks for Platinum Group Metal Extraction

William Trenholme

Thesis submitted to the University of Nottingham for the degree of Doctor of Philosophy

April 2016

Declaration

Except where specific reference is made to other sources, the work presented in this report is the original work of the author. It has not been submitted in whole or in part for any other degree.

Signed: William Trenholme

Date:

Abstract

This Thesis describes the synthesis and characterisation of a variety of functionalised metal-organic frameworks (MOFs). These MOFs have been used for the extraction of platinum group metal (PGM) compounds from aqueous and organic solvents and for the storage of gases such as CO_2, CH_4 and the C_2 hydrocarbons.

Chapter 1 contains an introduction to PGM properties and uses with specific focus on the chemical properties which allow for separation of PGMs from base metal compounds and for separation between different PGM compounds. The synthesis and structure prediction of MOFs is then introduced, leading into an overview of the use of functionalised MOFs, especially those used for the encapsulation and extraction of metal ions from solution. General experimental techniques and details are described, as is the theory behind inductively coupled plasma optical emission spectrometry (ICP-OES), the most widely used analytical technique reported in this work.

Chapter 2 describes the synthesis of chemically stable amine-functionalised Zr(IV) MOFs; UiO-68-NH_2 and UiO-66-NH_2, for extraction of PGM anions from aqueous and acidic solutions. ICP-OES was used to show that both materials exhibit close to 100% uptake of $PtCl_6^{2-}$ when present in just 3.5 equivalents per anion, comparable to the best materials reported for $PtCl_6^{2-}$ extraction. Furthermore, UiO-66-NH_2 exhibited consistently higher $PtCl_6^{2-}$ uptake from aqueous solutions than four industrially used materials supplied by Johnson Matthey. Back-extraction of $PtCl_6^{2-}$ was demonstrated simply by heating the doped MOF in 4 M HCl, removing 99% of the PGM while maintaining the phase and crystallinity of UiO-66-NH_2. Separation of $PdCl_6^{2-}$ from $PtCl_6^{2-}$ from acidic HCl solutions was exhibited by UiO-66-NH_2,

showing an exceptional selectivity of 20:1 for Pd:Pt from 2 M HCl. Likewise, 100% selectivity for $PtCl_6^{2-}$ and $PdCl_6^{2-}$ over $CuCl_2$ and $CuSO_4$ from acidic solutions was demonstrated, even in cases in which Cu was in 100-fold excess. Solid state NMR was employed to confirm the interaction between the framework and the PGM anions, with XPS results suggesting that the encapsulated Pt species within UiO-66-NH_2 may be $PtCl_3(NH_2)_3$ or $PtCl_4(NH_2)_2$.

Chapter 3 describes the synthesis and characterisation of a series of functionalised Cu(II) MOFs, NOTT-151, -155, -125 and -150, for the removal of neutral PGM complexes, $Pd(OAc)_2$, $PtCl_4$ and $Rh_2(OAc)_4$, from THF. The design of the MOFs allowed for an investigation into the effect of different topologies (**ssa** and **fof**), cage sizes and functional groups (amine, oxamide and methyl) on the uptake of each PGM complex. ICP-OES analysis showed that the MOFs were capable of extracting each PGM complex. The oxamide-functionalised NOTT-125 exhibited the most consistent uptake of $Pd(OAc)_2$ with a maximum capacity of 35 mg g^{-1} (7 $NH(CO)_2NH$ groups per $PtCl_4$). The amine-functionalised NOTT-155 showed the highest uptake of $PtCl_4$, with a maximum capacity of 73 mg g^{-1} (4 NH_2 groups per $PtCl_4$). Uptake of $Rh_2(OAc)_4$ was generally low, however NOTT-125 showed a maximum extraction of 87 mg g^{-1} (3 $NH(CO)_2NH$ groups per PGM). The larger pore **fof** MOFs, NOTT-155 and NOTT-125, were more effective for each extraction than the MOFs of **ssa** topology, NOTT-151 and NOTT-150. However, of the **ssa** MOFs, amine-functionalised NOTT-151 was shown to give higher uptake of each PGM than the isostructural methyl-functionalised NOTT-150. This demonstrated the importance of incorporating a functional group capable of coordinating to the metal complex.

Chapter 4 introduces the use of a nitrogen-rich triazine core in the synthesis of a variety of organic linkers to prepare MOFs for gas storage applications. The

preparation of a novel 3,24-connected Cu(II) MOF of **rht** topology, denoted NOTT-160, is described and the structure characterised using X-ray crystallography. The material is shown to exhibit good uptake of C_2 hydrocarbons with uptake of 128 cc g^{-1}, 115 cc g^{-1}, 110 cc g^{-1} for C_2H_2, C_2H_4, C_2H_6 respectively at 298 K and 1 bar (this becomes 212 cc g^{-1}, 175 cc g^{-1} and 201 cc g^{-1} at 273 K and 1 bar). The selectivities of 79:1 and 70:1 calculated using Henry's law for the separations of C_2H_2:CH_4 and C_2H_4:CH_4 respectively at 298 K are the third and second highest reported values for a MOF under these conditions. Ideal adsorbed solution theory (IAST) was also employed to calculate and predict these selectivities and shows agreement with the results obtained using Henry's law. In addition, NOTT-160 shows an exceptional volumetric working capacity for CH_4 of 221 cm^3 cm^{-3} at 80 bar and 298 K. This is the second highest working capacity reported for a MOF under these conditions, with the excellent performance attributed to the high porosity and comparatively high crystal density of the material.

Chapter 5 contains a summary of the work presented in this thesis.

Acknowledgements

I would like to thank Prof. Martin Schröder for the opportunity to work on this project and for his support and guidance over the last 4 years. I would also like to thank Dr Tim Easun, Dr Yong Yan and Dr Florian Moreau for their help and advice in the lab and Prof. Sandy Blake and Dr William Lewis for help with crystallography. I am very grateful to my collaborators at Johnson Matthey, particularly Dr Hugh Hamilton, Dr Ian Casely, Dr Pasi Kauppinen and Dr Sheena Hindocha, for their advice with regards to planning experiments and for data collection at Johnson Matthey Technology Centre. Finally I would like to thank my friends at Nottingham, especially Martyn, Chris, Maggie, Simona, Ruth, Sav, Laura, Nevo and Jenny for helping to make my PhD so enjoyable.

Table of Contents

List of Abbreviations 5

1.1 Platinum Group Metals 10

1.2 Metal-Organic Frameworks 13

1.2.1 Introduction 13

1.2.2 MOF Synthesis 15

1.2.3 Predicting MOF Structures 15

1.3 Gas Storage Applications of Functionalised MOFs 20

1.4 Functionalised MOFs for Metal Encapsulation 23

1.4.1 Transition Metals 23

1.4.2 Lanthanides and Actinides 26

1.4.3 Heavy Metal Ions 29

1.4.4 Precious Metals 31

1.5 Scope of this Work 36

1.6 ICP-OES 37

1.7 General Experimental Methods 39

1.7.1 Reagents and Analytical Techniques 39

1.7.2 Single Crystal X-ray Diffraction 40

1.7.3 Gas Adsorption Isotherms 40

1.8 References 41

2.1 Introduction 50

2.2 Aims of this Work 58

2.3 Results and Discussion 60

2.3.1 UiO-68-NH_2 60

2.3.1.1 Synthesis 60

2.3.1.2 Structural Analysis 62

2.3.1.3 Thermal Stability and N_2 Sorption 63

2.3.1.4 Aqueous Extraction of K_2PtCl_6 64

2.3.2 UiO-66 and UiO-66-NH_2 71

2.3.2.1 Synthesis 71

2.3.2.2 Structural Analyses 72

2.3.2.3 Phase Purity, Thermal Stability and N_2 Sorption 73

2.3.2.4 Comparison of K_2PtCl_6 Uptake in UiO-66-NH_2 and UiO-68-NH_2 75
2.3.2.5 Aqueous $PtCl_6^{2-}$ Extraction in UiO-66 and UiO-66-NH_2 *Versus* Industrial Materials 76
2.3.2.6 Back-Extraction of $PtCl_6^{2-}$ from UiO-66-NH_2 82
2.3.2.7 Extraction of $PtCl_6^{2-}$ from Acidic Solutions 84
2.3.2.8 BET Surface Area Comparison of Doped UiO-66-NH_2 Samples 85
2.3.2.9 Investigating the Effect of HCl Concentration on $PtCl_6^{2-}$ Uptake 87
2.3.2.10 Extraction of $PdCl_6^{2-}$ from Acidic Solutions 90
2.3.2.11 ^{13}C Solid State NMR of PGM-Doped Samples of UiO-66-NH_2 92
2.3.2.12 Separation of $PdCl_6^{2-}$ from $PtCl_6^{2-}$ 95
2.3.2.13 Separation of PGM Anions from Base Metals 98
2.4 Current and Future Work 105
2.4.1 NOTT-300(Al) vs UiO-66 105
2.4.2 Synthesis of New Amine-Containing Ligands 107
2.4.2.1 Synthesis of H_2L^2 108
2.4.2.2 Synthesis of H_2L^3 and H_2L^4 109
2.4.2.3 Synthesis of H_2L^5 110
2.5 Conclusions 111
2.6 Experimental 112
2.7 References 120
3.1 Introduction 124
3.2 Aims of this Work 126
3.3 Results and Discussion 127
3.3.1 NOTT-151 127
3.3.1.1 Synthesis of $[Cu_2(L^6)(H_2O)_2]\cdot 4DMF\cdot H_2O$ (NOTT-151) 127
3.3.1.2 Structural Analysis 128
3.3.1.3 Phase Purity, Thermal Stability and N_2 Sorption 130
3.3.2 NOTT-155 132
3.3.2.1 Synthesis of $[Cu_2(L^7)(H_2O)_2]\cdot 7DMF\cdot H_2O$ (NOTT-155) 132
3.3.2.2 Structural Analysis 133
3.3.2.3 Phase Purity, Thermal Stability and N_2 Sorption 134
3.3.3 NOTT-125 137
3.3.3.1 Synthesis of $[Cu_2(L^8)(H_2O)_2]\cdot 3DMA\cdot 3H_2O$ (NOTT-125) 137
3.3.3.2 Structural Analysis 138

3.3.3.3 Phase Purity, Thermal Stability and N_2 Sorption 139
3.3.4 NOTT-150 142
3.3.4.1 Synthesis and Structural Analysis of $[Cu_2(L^9)(H_2O)_2]\cdot 5DMF\cdot 4H_2O$ (NOTT-150) 142
3.3.4.2 Phase Purity, Thermal Stability and N_2 Sorption 143
3.3.5 Structure Summary 145
3.3.6 Extraction of $Pd(OAc)_2$, $PtCl_4$ and $Rh_2(OAc)_4$ from THF 147
3.3.7 X-ray Photoelectron Spectroscopy of PGM-Doped MOFs 154
3.3.8 Structure and Properties of MOFs Synthesised from a Novel Amine-Functionalised Ligand 157
3.3.8.1 Synthesis of H_4L^{10} 157
3.3.8.2 Synthesis and Structural Analysis of $[Co_2(L^{10})(H_2O)_2(DMF)]_n$ 158
3.3.8.3 Synthesis and Structural Analysis of $[In_4(L^{10})_3]_n[cation_4]_n$ 159
3.3.8.4 Thermal Stability and Phase Purity of $[Co_2(L^{10})(H_2O)_2(DMF)]_n$ and $[In_4(L^{10})_3]_n[cation_4]_n$ 160
3.4 Current and Future Work 163
3.5 Conclusions 166
3.6 Experimental 167
3.7 References 175
4.1 Introduction 180
4.2 Aims of this Work 185
4.3 Results and Discussion 186
4.3.1 $[Cu_3(L^{11})(H_2O)_3]\cdot 11DMF\cdot 3H_2O$ 186
4.3.1.1 Synthesis of $[Cu_3(L^{11})(H_2O)_3]\cdot 11DMF\cdot 3H_2O$ 186
4.3.1.2 Structural Analysis and Characterisation 187
4.3.1.3 Phase Purity, Thermal Stability and N_2 Sorption 188
4.3.2 Extraction of $Pd(OAc)_2$, $PtCl_4$ and $Rh_2(OAc)_4$ from THF 190
4.3.3 NOTT-160 193
4.3.3.1 Synthesis of $[Cu_3(L^{12})(H_2O)_3]\cdot 13DMF\cdot 7H_2O$ (NOTT-160) 193
4.3.3.2 Structural Analysis 194
4.3.3.3 Phase Purity, Thermal Stability and N_2 Sorption 195
4.3.3.4 CO_2, CH_4 and H_2 Sorption from 0-20 Bar 199
4.3.3.5 Low Pressure Sorption of C_2 Hydrocarbons and CH_4 201
4.3.3.6 Virial Fitting and Henry's Law Selectivity of 0-1 Bar Isotherms 202

4.3.3.7 Langmuir-Freundlich Fitting of Isotherm Data and Predicted IAST Selectivities 205
4.3.3.8 High Pressure CH_4 Adsorption 208
4.3.4 NOTT-161 211
4.3.4.1 Synthesis of $[Cu_3L^{13}(H_2O)_3]\cdot 6DMF\cdot 5H_2O$ (NOTT-161) 211
4.3.4.2 Structural Analysis of NOTT-161 213
4.4 Current and Future Work 214
4.4.1 $[Zn_3(L^{14})(H_2O)_2]_n$ 215
4.4.1.1 Synthesis of H_8L^{14} and $[Zn_3(L^{14})(H_2O)_2]_n$ 215
4.4.1.2 Structural Analysis 216
4.4.2 $[Cu_3(L^{15})(OH)_2]$ 218
4.4.2.1 Synthesis of H_4L^{15} and $[Cu_3(L^{15})(OH)_2]$ 218
4.4.2.2 Structural Analysis 219
4.4.3 Synthesis of H_3L^{16}, H_3L^{17} and H_3L^{18} 220
4.5 Conclusions 224
4.6 Experimental 225
4.7 References 234
5.1 Conclusions 239
Appendices 245

List of Abbreviations

Å	Ångström
BET	Braun-Emmett-Teller
C	Celsius
CP-MAS	Cross-polarisation magic angle spinning
d	Doublet (NMR)
DCM	Dichloromethane
DEF	N,N-Diethylformamide
DFT	Density functional theory
DIPEA	*N*,*N*-Diisopropylethylamine
DMA	N,N-Dimethylacetamide
DMF	N,N-Dimethylformamide
DMSO	Dimethylsulfoxide
DNP	Dynamic nuclear polarisation
dppf	1,1'-Bis(diphenylphosphino)ferrocene
ESI	Electrospray ionisation
Et_2O	Diethyl ether
EtOAc	Ethyl acetate
EtOH	Ethanol
IAST	Ideal adsorbed solution theory
ICP-OES	Inductively coupled plasma-optical emission spectrometry
INS	Inelastic neutron scattering

IR	Infrared
K	Kelvin
MALDI	Matrix-assisted laser desorption/ionisation
m	Multiplet (NMR)
MeCN	Acetonitrile
MeOH	Methanol
MOF	Metal-organic framework
MS	Mass spectrometry
m/z	Mass:charge ratio
NMP	*N*-Methyl-2-pyrrolidone
NMR	Nuclear magnetic resonance
PGM	Platinum group metal
ppm	Parts per million
PXRD	Powder X-ray diffraction
q	Quartet (NMR)
Q_{st}	Heat of adsorption
RT	Room temperature
s	Singlet (NMR)
SCXRD	Single crystal X-ray diffraction
SS-NMR	Solid state nuclear magnetic resonance
t	Triplet (NMR)
TGA	Thermogravimetric analysis
THF	Tetrahydrofuran

UV-vis	Ultraviolet-visible
vdW	van der Waals
XPS	X-ray photoelectron spectroscopy

Chapter 1

Introduction to Platinum Group Metals and

Metal-Organic Frameworks

1.1 Platinum Group Metals

The platinum group metals (PGMs), which consist of Ru, Rh, Pd, Os, Ir and Pt, are an exceptionally rare and valuable set of elements with a wide range of highly desirable properties. These properties, such as catalytic activity, corrosion resistance, thermal durability, biocompatibility and electrical conductivity lead to the use of PGMs for many applications including autocatalysis, jewellery, medicine, fuel cells and electronics.[1] The low natural abundance of these elements, coupled with the increasing need for their use means that efficient methods of PGM extraction and recycling are essential to meet demand.

Natural PGM deposits are found mainly in ores located in South Africa, Russia and Canada and require separation from base metals such as Cu, Ni and Fe.[2] A variety of processes such as crushing, smelting and magnetic separation are used to give a PGM-Cu-Ni-Fe phase and dissolution under acidic conditions removes the majority of the base metals to give a 60% PGM concentrate.[1,2] To selectively remove the desired PGM from this mixture, a number of aspects of PGM chemistry must be considered. Of particular importance is the nobility of each metal, which refers to their high insolubility in media which dissolve nearly all base metals. It may also be described as the high potential of the reaction shown below.[3]

$$M^0 \rightleftharpoons M^{n+} + n\,e^-$$

The nobility of PGMs can be used to separate the more insoluble elements (Ir, Ru, Rh and Os) from Pd and Pt, which dissolve more quickly under appropriate acidic conditions. The second factor to consider is the coordination environment and oxidation state of the metal ion. By far the best known and most well studied group of precious metals are the PGM chloro complexes as aqueous chloride solutions are

the only cost effective medium in which to bring all PGMs into solution. The major species present in such chloride solutions are shown below in Table 1.1.[4]

Table 1.1. PGM chloro species observed in acidic chloride solutions. Reproduced from reference 4.

Ru(III)	**Ru(IV)**	**Rh(III)**	**Rh(IV)**	**Pd(II)**	**Pd(IV)**
$[RuCl_6]^{3-}$ $[RuCl_5(H_2O)_2]^{2-}$ $[RuCl_4(H_2O)_2]^{-}$ $[RuCl_3(H_2O)_3]$	$[RuCl_6]^{2-}$ $[Ru_2OCl_{10}]^{4-}$ $[Ru_2OCl_8(H_2O)_2]^{2-}$	$[RhCl_6]^{3-}$ $[RhCl_4(H_2O)_2]^{-}$ $[RhCl_5(H_2O)]^{2-}$	$[RhCl_6]^{2-}$	$[PdCl_4]^{2-}$	$[PdCl_6]^{2-}$
	Os(IV)	**Ir(III)**	**Ir(IV)**	**Pt(II)**	**Pt(IV)**
	$[OsCl_6]^{2-}$	$[IrCl_6]^{3-}$ $[IrCl_5(H_2O)]^{2-}$ $[IrCl_4(H_2O)_2]^{-}$	$[IrCl_6]^{2-}$	$[PtCl_4]^{2-}$	$[PtCl_6]^{2-}$

As the majority of these species are anionic, they are able to undergo anion-exchange reactions with a variety of organic bases (B) to form an ion-pair, as shown below.[1]

$$n\,B^+Cl^- \;+\; A^{n+}[MCl_x]^{n-} \rightleftharpoons [B]_n[MCl_x] \;+\; n\,A^+Cl^-$$

The tendency of a PGM anion to undergo this kind of ion-pair formation is dictated by the charge to size ratio and charge density of the species. Species with a lower charge density are paired more easily, attributable to larger hydration spheres leading to a weaker coulombic interaction with the counter cations.[5] Thus, the ease of ion-pair formation follows the order $[MCl_6]^{2-} > [MCl_4]^{2-} >> [MCl_6]^{3-} >$ aquo species.[1] A number of different methods have been used over the past 50 years to make use of this ion-pair formation to separate PGM anions from one another. The most common method to achieve this is solvent extraction, which involves the use of a receptor molecule dissolved in solution to interact with the desired PGM. This proceeds either *via* the formation of an inner-sphere complex, usually with a dialkylsulfide or hydroxyoxime receptor or *via* the formation of an outer-sphere salt with hydrophobic

alkylamine reagents.[6-8] The solvent extraction process consists of three main steps – (1) an extraction step to bind the metal, (2) transport of the metal from the aqueous phase to the organic phase, (3) back-extraction from the organic phase using NaOH to recover the metal (Figure 1.1).[9] The pure PGM is then obtained using an electrorefining technique such as electrowinning.[10]

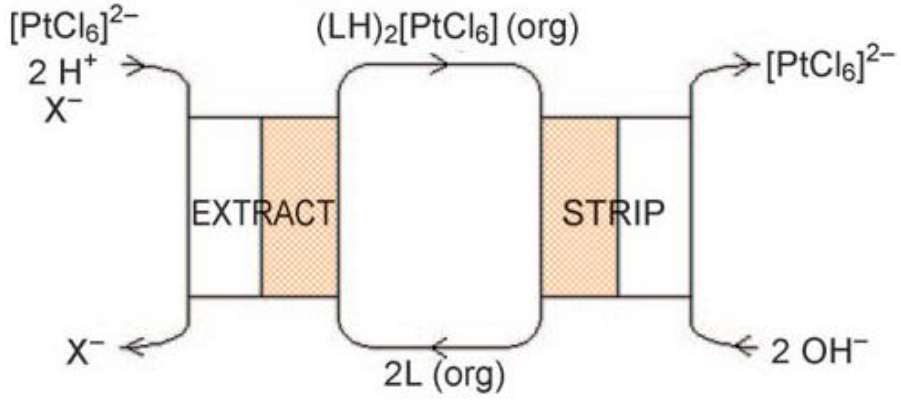


Figure 1.1. A scheme showing pH-swing-controlled transport and extraction of the $PtCl_6^{2-}$ anion, where L denotes a receptor molecule. The organic and aqueous phases are represented by the shaded and non-shaded boxes respectively. Reproduced from reference 9.

Solvent extraction has previously been demonstrated to great effect in the Schröder group using amine and amide and urea-functionalised receptor molecules for the extraction of $PtCl_6^{2-}$ (Figure 1.2).[9,11] However, solvent extraction is a time and energy-consuming process and in more recent years, other methods have been investigated to perform these extractions more efficiently.

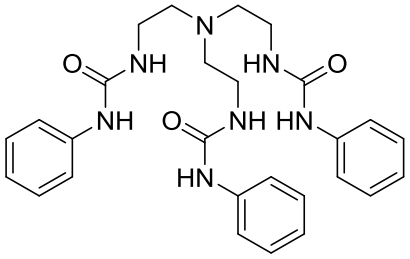


Figure 1.2. The strucutre of a highly functionalised solvent extraction receptor used previously in the Schröder group for the removal of $PtCl_6^{2-}$ from acidic solutions.[11]

Solid phase extractants are one such example and consist of a broad range of different sorbent materials including silica gels, vinyl chlorides, activated carbons, polyamine-polyurea materials and chitosans.[12] Whilst these sorbents do show promise for specific extractions, many suffer from poor chemical stability, low sorption capacities and slow uptake.[12] Therefore there is a real need for the synthesis of new materials able to address these problems and to avoid the time-consuming phase transfer step needed for solvent extraction processes.

1.2 Metal-Organic Frameworks

1.2.1 Introduction

Metal-organic frameworks (MOFs) are a class of hybrid materials that consist of metal ions or clusters bound to organic linkers to form an infinite crystalline lattice (Figure 1.3).[13] These lattices can exhibit permanent porosity, allowing the possibility of guest molecule encapsulation within the structure. This has led to a multitude of potential applications for MOFs such as gas storage[14-25] and separation,[26-35] catalysis,[36-40] drug delivery,[41-46] chemical sensing[47-52] and proton conduction.[53-58]

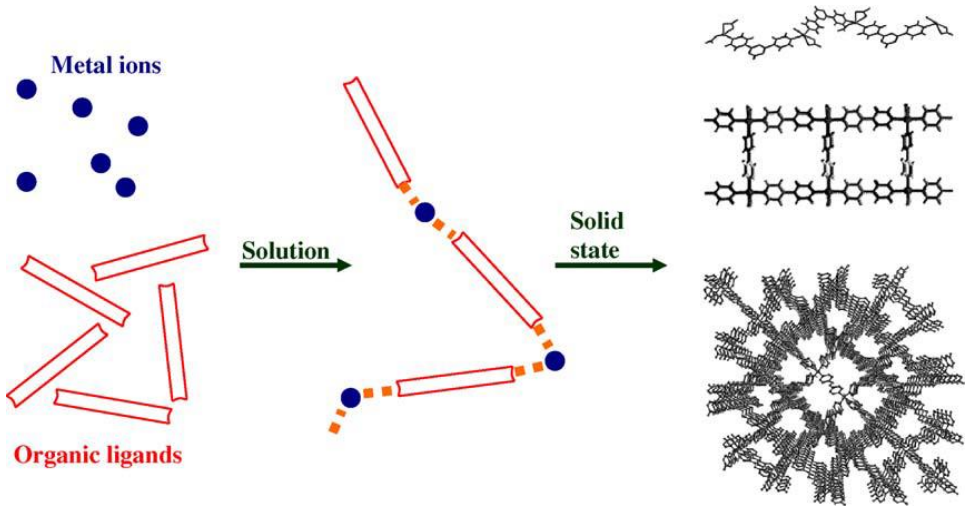


Figure 1.3. Generic scheme showing metal-organic framework formation.

Reproduced from reference 13.

Some advantages of MOFs over similar porous materials such as activated carbons and zeolites include the relative ease of structure determination, the ability to predict structures and very high internal surface areas (up to ~7000 m^2 g^{-1}).[59] However, the key feature that makes MOFs so intriguing is the chemical tunability of the organic linkers, which are not present in other inorganic materials. The linkers are usually bound to the metal node *via* O- or N-donating groups. O-donors are more commonly employed and generally take the form of mono- or polycarboxylates which provide a huge range of potential binding modes with different metal nodes. In addition to these binding groups, the carbon backbone of the linker may be decorated with a variety of different functional groups such as $–NH_2$, $-CH_3$, -OH, -Br etc.[60] Thus, when considering the number of organic linkers that could be synthesised and the different inorganic metal nodes available, the number of potential MOF products is almost infinite.[60] As a result of their tunability, high surface areas and stability, we propose MOFs to be the ideal materials for the selective adsorption of PGMs from

solution. As a type of solid phase extractant, they would also negate the need for the phase transfer step required in solvent extraction techniques.

1.2.2 MOF Synthesis

MOFs are generally prepared by solvothermal synthesis using a conventional heating method. This is carried out by reacting the linker and metal precursor in solution at high temperature and pressure in a sealed vessel – usually a stainless steel autoclave or a pressure-rated glass tube or vial. Polar, high boiling point solvents such as DMF, DEF, DMA, NMP, H_2O and 1,4-dioxane are most commonly used and acids or amines are frequently added to promote crystal growth.[60] Important factors to consider in addition to the choice of solvent system are temperature, pH and concentration of the reagents, which are usually optimised by trialling a wide range of conditions.[60] The metal ions are added in the form of a soluble precursor such as a nitrate, chloride or acetate salt and the organic linkers usually dissolve upon sonication or heating in the solvent.[60] Alternative methods of MOF synthesis such as microwave heating,[61] ball-milling[62] and continuous flow synthesis[63] are known.

The mechanism of MOF formation is *via* a reversible self-assembly process. The organic linkers are able to bind reversibly to the metal nodes until the most thermodynamically stable product (the MOF) is formed.[64] The addition of protons to the synthesis aids this self-assembly by re-protonating the COO^- groups and facilitating the breaking of the M-O bonds.

1.2.3 Predicting MOF Structures

Clearly the two main components of the framework, the metal ions and the linkers, are the most important factors that determine the resulting structure. The metal ions can take the form of a mononuclear node or, more commonly, will form metal-

carboxylate clusters which are referred to as secondary building units (SBUs).[65] These SBUs are usually rigid as the metal ions are held in place by the carboxylate groups, allowing them to serve as vertices between the organic linkers and play an important role in preventing framework collapse upon solvent removal.[66] A huge variety of SBUs are known and their formation depends largely upon the chemical properties of their constituent metal ions. Some common examples of SBUs are shown below (Figure 1.4).[67]

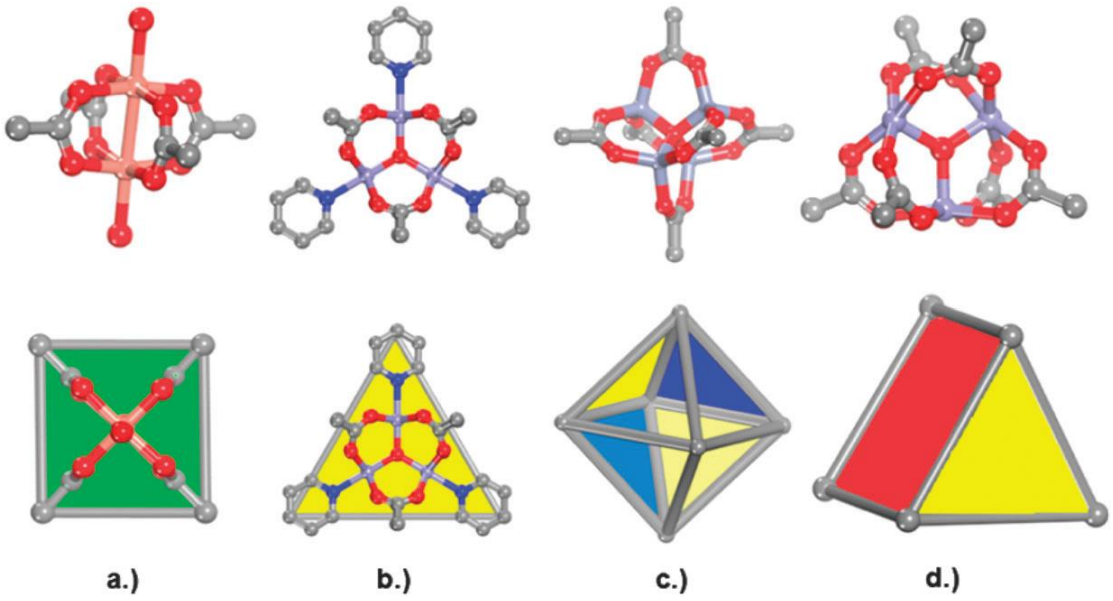


Figure 1.4. Examples of SBUs commonly used in the preparation of MOFs. (a) The square Cu paddlewheel motif, $[Cu_2(O_2CR)_4(H_2O)_2]$ present in the majority of Cu(II) MOFs. (b) the μ_3-oxo trimetallic basic M(III) acetate structure depicted as a triangle and a triangular prism (d). (c) The octahedral basic Zn(II) acetate node, a μ_4-oxo tetrametallic cluster. Reproduced from reference 67.

From these SBUs, one can identify points of framework extension which describe a simple geometric shape, allowing a simplification of the chemical structure. Likewise, the organic linkers may be deconstructed into simple shapes and the combination of these simplified representations gives a clear picture of the

underlying connectivity (topology) of the framework (Figure 1.5).[68] This deconstruction is known as reticular chemistry.[69]

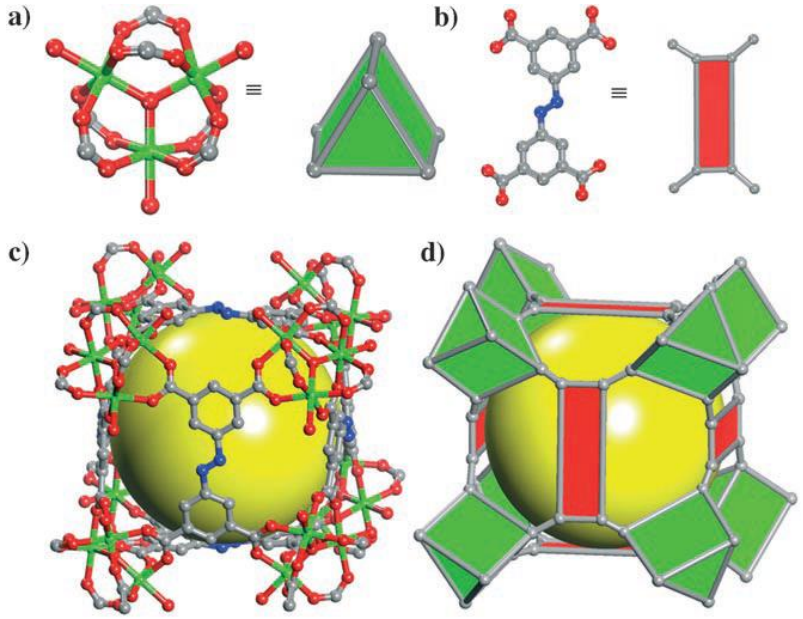


Figure 1.5. Deconstruction of the metal node (a) and organic linker (b) of an In(III) tetracarboxylate MOF to show the underlying **soc** topology (d). Reproduced from reference 68.

Using this approach to create an isoreticular series of MOFs with the same topology is well known.[16, 70-74] The first example of an isoreticular series was reported by Yaghi and co-workers in 2002 with the aim of investigating the CH_4 uptake capacity of each framework.[70] This involved the systematic variation of a range of parameters such as carbon chain length and altering pendant functional groups along the carbon backbone of linear dicarboxylate linkers. For example, phenyl, naphthyl, pyrenyl, biphenyl and triphenyl spacers were used to vary the chain length and bromo, amino, cyclobutyl and ether groups were used to introduce functionality. These linkers, combined with a basic zinc acetate node, created a series of isoreticular MOFs of **pcu** topology, denoted as IRMOF-1 to IRMOF-16 (Figure 1.6).[70]

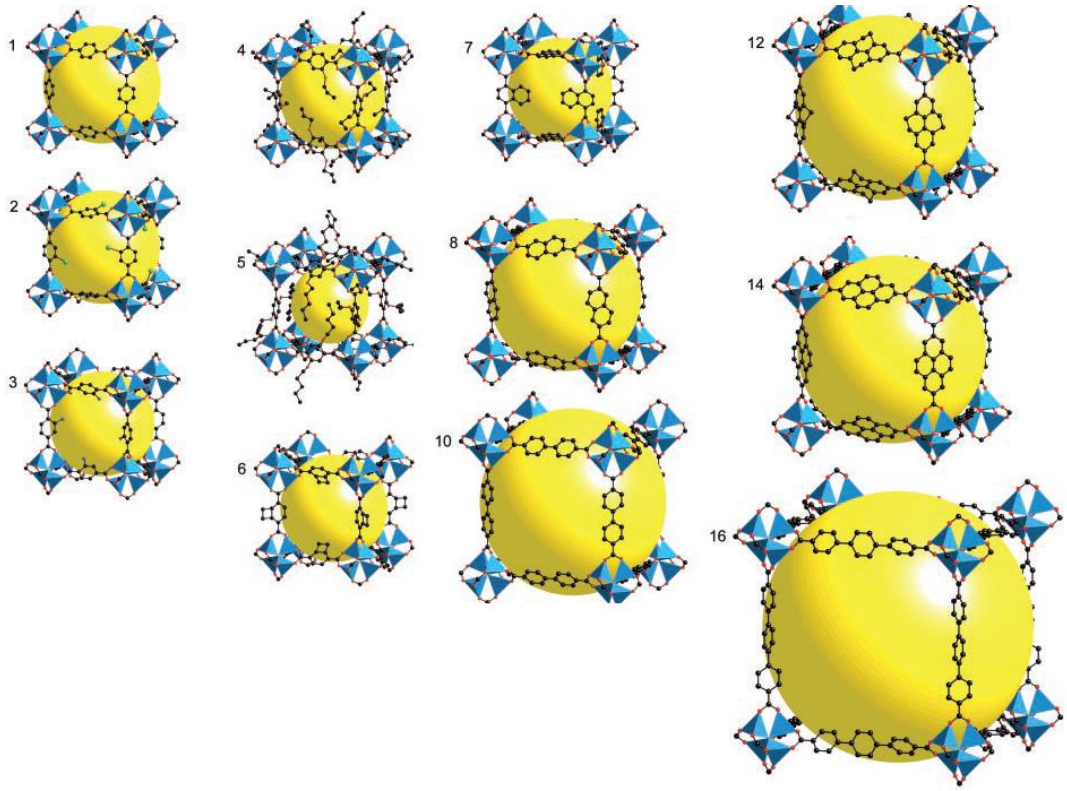


Figure 1.6. View of the single crystal structures of IRMOFs 1-16 in which the tetrahedral Zn_4O node is represented as a blue polyhedron, the C atoms are shown in black and the O atoms in red. The yellow sphere represents the accessible pore diameter, taking into account van der Waals radii. Reproduced from reference 70.

As shown clearly in Figure 1.6, the size of the pore varies greatly depending on the linker used (3.8 Å in diameter for IRMOF-5 to 28.8 Å for IRMOF-16). Similarly, the accessible pore volumes ranged from 55.8% (IRMOF-5) to 91.1% (IRMOF-16). Of this series, IRMOF-6 was found to be the most effective for CH_4 storage with an uptake of 240 cm^3 g^{-1} at 36 bar and 298 K. As the very similar IRMOF-1 and IRMOF-3 structures show a much lower capacity for CH_4 despite their larger pore sizes, the authors attributed the performance of IRMOF-6 to the favourable interactions of the pendant cyclobutyl functional groups with the guest CH_4 molecules.[70]

A similar example of an isoreticular series was reported by the Schröder group in 2009.[16] This involved the synthesis of a range of tetracarboxylate linkers which were combined with a Cu(II) paddlewheel node to give frameworks of **nbo** topology. These linkers ranged from a simple biphenyl to extended tri-, tetra- and pentaphenyl carboxylates in addition to a series of fluoro and methyl substituted analogues designed for high H_2 uptake (Figure 1.7).

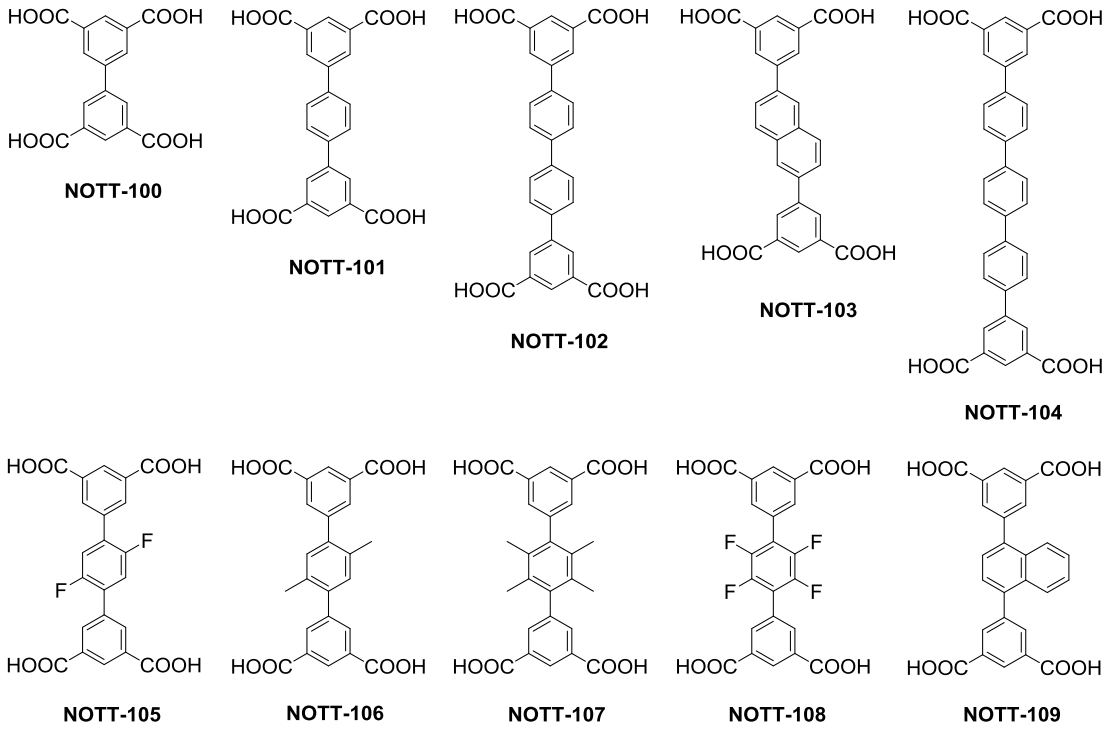


Figure 1.7. The linkers and corresponding MOF nomenclature for the NOTT-10X series.[16]

This combination of **nbo** topology and open Cu(II) metal sites resulted in each MOF exhibiting good uptake of H_2 at 78 K (between 2.26 and 2.63 wt% at 1 bar). Interestingly, the gas uptake did not follow the trend of the BET surface area and pore volumes. Each of NOTT-101, -102 and -103 showed a significantly higher uptake than NOTT-100 at 20 bar, however the larger pore NOTT-102 performed less

well than NOTT-101 and NOTT-103, with NOTT-103 exhibiting an exceptional capacity for H_2 of 6.51 wt% at 20 bar. This was attributed to the weaker overlap potential between H_2 molecules and the walls of the larger pore NOTT-102 and the favourable interactions between the naphthyl groups of NOTT-103 and H_2.[16]

1.3 Gas Storage Applications of Functionalised MOFs

As discussed earlier, the inclusion of a functional group such as $–NH_2$, -OH, -SH, -Br etc. on the organic linker is often employed in MOF chemistry. This is carried out to tailor the framework for a specific application, most commonly to enhance interactions between the MOF and gas molecules such as CO_2, H_2 and CH_4.[75-81] In 2012, Long *et al.* reported the synthesis of a Mg(II) MOF, Mg_2(dobpdc) (dobpdc = 4,4'-dioxido-3,3'-biphenyl dicarboxylate), incorporating 18.4 Å channels through the structure.[75] The Mg^{2+} ions lining these channels were then functionalised with N,N-dimethylethylenediamine (mmen) to give $Mg_2(dobpdc)(mmen)_{1.6}(H_2O)_{0.4}$ (Figure 1.8). This amine-doped framework showed excellent uptake of carbon dioxide at very low pressures, taking up 2.0 mmol g^{-1} at 0.39 mbar and 25 °C and 3.14 mmol g^{-1} at 0.15 bar and 40 °C – conditions relevant for the removal of CO_2 from flue gas.[75] For comparative purposes, it is worth noting that the CO_2 uptake in the unfunctionalised framework is 15 times lower under the same conditions.[75]

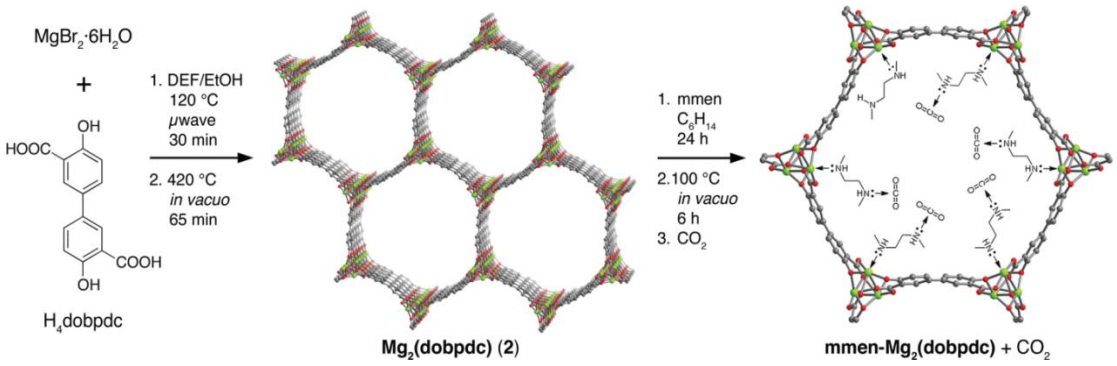


Figure 1.8. A scheme showing the synthesis, activation and mmen-functionalisation of Mg_2(dobpdc). Reproduced from reference 75.

The isosteric heat of adsorption (Q_{st}) calculated from the isotherms suggested that, at low loadings, the CO_2 molecules were physisorbed in the MOF. However, the Q_{st} increased rapidly to -71 kJ mol^{-1} with increased loading, which is indicative of chemisorption of the CO_2 molecules onto the free amine groups, explaining the high uptake. Gas adsorption/desorption cycling experiments in flue gas demonstrated that $Mg_2(dobpdc)(mmen)_{1.6}(H_2O)_{0.4}$ is stable to repeated use and re-activation.

Computational methods have also been used to compare the effect of different functional groups on the sorption of a variety of gases. In 2010, Mellot-Draznieks *et al.* published a report on the CO_2 and CH_4 sorption capacity of MIL-53(Al) frameworks with $–(OH)_2$, -COOH, $-NH_2$ and $-(CH_3)_2$ functional groups and calculated the heats of adsorption in each case.[76] This was carried out using a combination of Grand Canonical Monte Carlo (GCMC) and density functional theory (DFT) methods.[76] As shown below in Figure 1.9, each material exhibited higher a higher Q_{st} for both CO_2 and CH_4 in comparison to the non-functionalised MIL-53(Al)-NF. At zero loading, the order of Q_{st} for CO_2 is –COOH > $-(OH)_2$ > $-(CH_3)_2$ > $-NH_2$, with MIL-53(Al)-COOH showing the highest Q_{st} by 14 kJ mol^{-1}. Whilst the functionalised MOFs display higher heats of adsorption for CH_4 than the

parent material, it is only moderately increased (~3 kJ mol^{-1} for MIL-53(Al)-$(CH_3)_2$).[76]

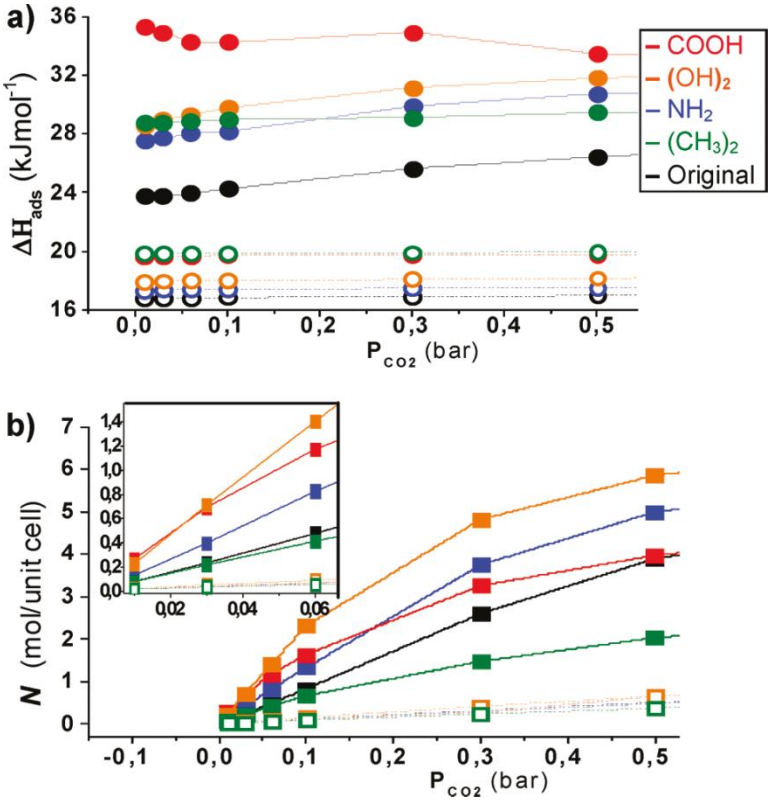


Figure 1.9. (a). GCMC calculated heats of adsorption for CO_2 (full circles) and CH_4 (open circles) for each MOF. (b). Predicted isotherms for CO_2 (full squares) and CH_4 (open squares) at 303 K from 0 – 0.5 bar. Reproduced from reference 76.

The predicted isotherms for CO_2 do not follow the Q_{st} trend, in this case MIL-53(Al)-$(OH)_2$ > -NH_2 > -COOH > -$(CH_3)_2$. This is unsurprising as the bulk of the various functional groups also affects the gas uptake, hence the poor performance of MIL-53(Al)-COOH at 0.5 bar. However, the quick CO_2 uptake in this MOF between 0 - 0.1 bar in comparison to MIL-53(Al)-NF suggests that the functional group does enhance gas storage. Likewise, the very low uptake predicted for MIL-53(Al)-$(CH_3)_2$ compared to the other materials strongly suggests that the interactions of polar functional groups with CO_2 are far more favourable than with non-polar groups. The

predicted CH_4 isotherms exhibited a negligible change across the series. The selectivity of CO_2:CH_4 of 15-17 for MIL-53(Al)-$(OH)_2$, -NH_2 and -COOH is far higher than that of MIL-53(Al)-NF (~ 7) and shows clearly that functional groups can greatly improve the uptake of one gas over another.

1.4 Functionalised MOFs for Metal Encapsulation

With regards to our focus on the extraction of PGMs, the most significant literature reports concern the encapsulation of metal ions from solution using MOFs. To date there has been very little research into PGM scavenging using MOFs, however there are a significant number of reports of functionalised frameworks used for sensing and encapsulation of a variety of metals.

1.4.1 Transition Metals

The most common use of MOFs in this context is for sensing of transition metal ions such as Fe(III),[82-85] Co(II)[86,87] and Cu(II)[88,89] in solution. One of the first examples of such work was reported by Qian *et al.* in 2009 using a luminescent Eu(III) MOF containing a pyridyl isophthalate linker.[87] Importantly, the structure contains 1D channels surrounded by six pyridyl groups (Figure 1.10), an ideal arrangement for interaction with guest metal ions. Activated samples of the MOF were added to DMF solutions containing a variety of different metal nitrates (Na^+, K^+, Mg^{2+}, Ca^{2+}, Mn^{2+}, Co^{2+}, Cu^{2+}, Zn^{2+} or Cd^{2+}) to give metal-incorporated $[Eu(pdc)_{1.5}]\cdot xDMF\cdot yM^{n+}$ crystals for luminescence studies.[87] Photoluminescence spectra of these crystals exhibited characteristic transitions corresponding to Eu^{3+} ions at 590, 616 and 698 nm.

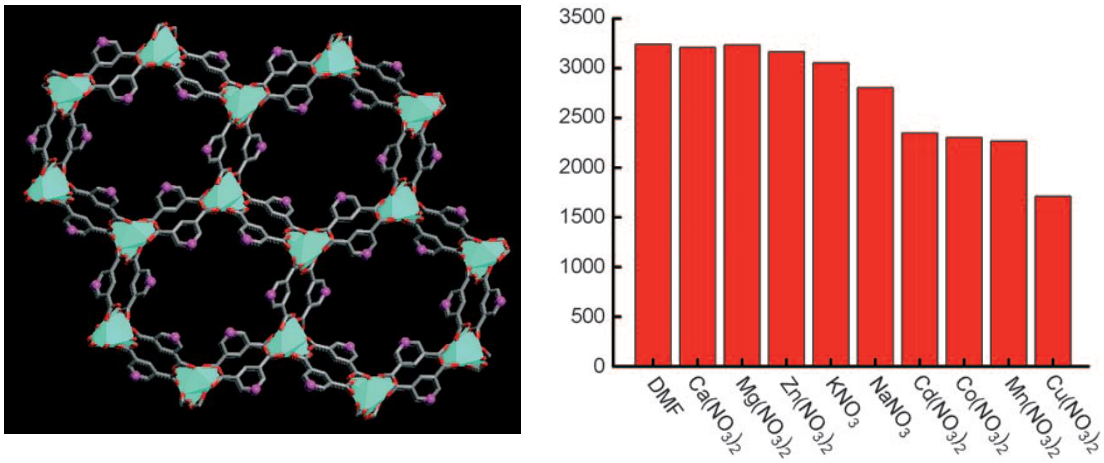


Figure 1.10. The 1D channels in $[Eu(pdc)_{1.5}]$ surrounded by pyridyl groups (left) and a comparison of the luminescence intensity of $[Eu(pdc)_{1.5}]\cdot xDMF\cdot yM^{n+}$ incorporating various metal ions. Reproduced from reference 87.

The intensity of these transitions was shown to be heavily dependent on the identity of the metal encapsulated within the $[Eu(pdc)_{1.5}]\cdot xDMF\cdot yM^{n+}$ framework. For example, the incorporation of alkali and alkaline-earth metal ions resulted in negligible quenching of the luminescence intensity, whereas the transition metal ions reduce the intensity by varying degrees (Figure 1.10). The Cu(II)-doped material showed the greatest reduction in luminescence intensity at approximately half that of the metal-free framework. Cd(II), Co(II) and Mn(II) also decreased the intensity significantly. XPS studies of these transition metal-doped crystals showed a shift corresponding to the N 1s orbital of the free pyridyl groups (398.5 to 399.2 eV), indicating a weak interaction between the Lewis basic sites and the M^{2+} ions.[87]

The sensing of Fe^{3+} ions is of particular interest as they play a crucial role in many cellular processes and a deficiency or overload of Fe^{3+} can lead to medical conditions such as hemochromatosis, diabetes and Parkinson's disease.[83] In 2013, Yan *et al.* reported the use of MIL-53(Al) as a highly sensitive and selective detector of Fe(III) from solution *via* a cation exchange mechanism (Figure 1.11).[82]

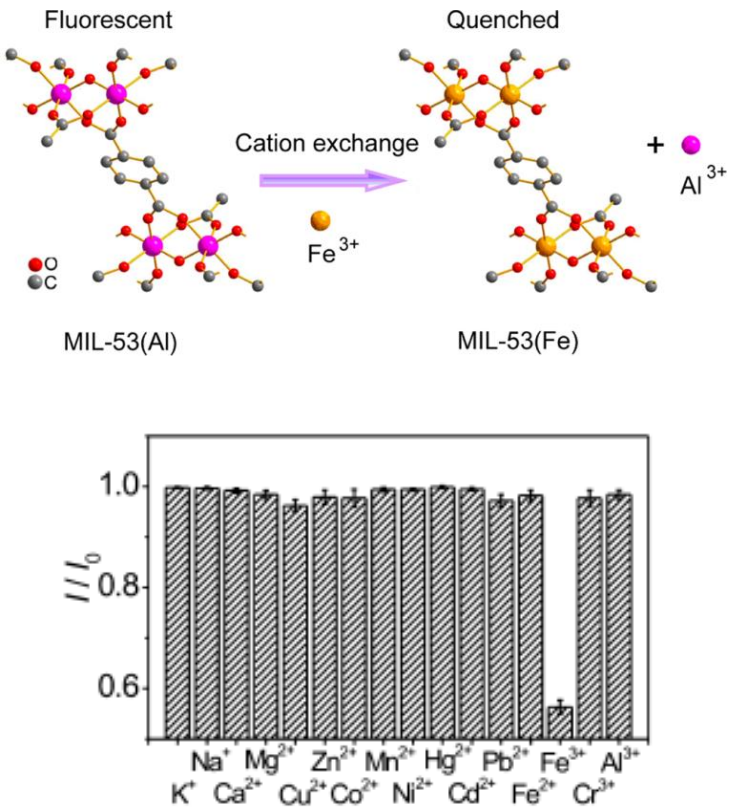


Figure 1.11. The cation exchange mechanism (top) and the fluorescence responses of MIL-53(Al) to a variety of metal ions (bottom). Reproduced from reference 82.

Metal sensing was carried out *via* the addition of MIL-53(Al) to a series of solutions containing a variety of metal ions and measuring the fluorescence of the resulting material. As MIL-53(Al) is strongly fluorescent, the cation exchange leading to weakly fluorescent MIL-53(Fe) was easily observable. This allowed for detection of Fe^{3+} from an aqueous solution with a linear range of 3-200 µM and a detection limit of 0.9 µM.[82] Furthermore, to determine its potential for application in biological samples, MIL-53(Al) was used as a probe to detect levels of Fe^{3+} in samples of human urine. Recovery of Fe was shown by fluorescence to be between 98 and 106%, which was in very good agreement with ICP-MS analysis of the same samples. This cation exchange strategy offered promise for MOF use in detection

applications, although the authors suggested that the synthesis and purification of MIL-53(Al) needed improvement before it could be used on a larger scale.[82]

1.4.2 Lanthanides and Actinides

Another area of great interest is the encapsulation of lanthanide ions for biomedical and drug delivery applications and to enable tunable luminescence.[90-95] The first known example of lanthanide extraction in a MOF was reported by Rosi and co-workers using an anionic Zn(II) adenate framework, denoted as bio-MOF-1, with dimethylammonium cations residing in the 1D channels.[93] Samples of bio-MOF-1 were soaked in solutions of DMF containing nitrate salts of Tb^{3+}, Sm^{3+}, Eu^{3+} or Yb^{3+} to give a series of Ln^{3+}@bio-MOF-1 materials *via* replacement of the dimethylammonium cations (Figure 1.12).

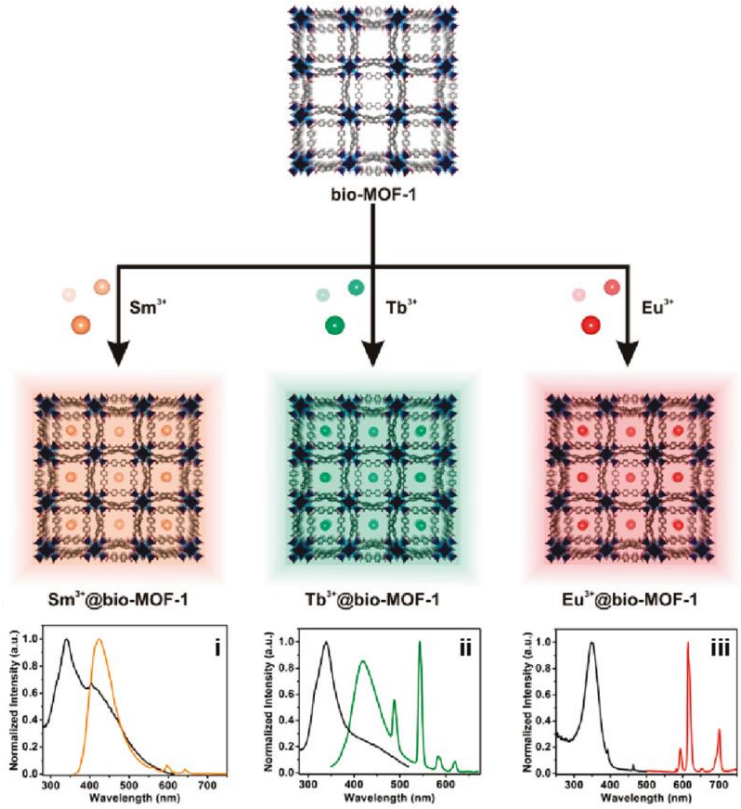


Figure 1.12. A depiction of Ln^{3+} ion encapsulation in bio-MOF-1 and the excitation/emission spectra of the resulting materials. Reproduced from reference 93.

Luminescence studies in the presence of water (a solvent with the ability to quench NIR emitting lanthanides) showed that the Ln^{3+} ions could be easily detected, suggesting that bio-MOF-1 protects the encapsulated ions from the solution. As bio-MOF-1 was acting as a scaffold for the Ln^{3+} ions, the authors hypothesised that the doped materials could act as small molecule sensors. To test this, Yb^{3+}@bio-MOF-1 was evaluated as an oxygen sensor. The MOF was activated and placed into a gas chamber and the luminescence in response to the addition of O_2 gas was monitored. A signal decrease of ~40% was observed after 5 minutes of exposure to O_2 which, importantly, returned to its original intensity upon removal of the gas, showing that reversible sensing was possible.[93]

In more recent years, the extraction of actinides and radionuclides from solution has been explored using MOFs, with particular focus on the removal of uranium from seawater.[96-100] As nuclear power is helping to overcome the shortage of fossil fuels it is vital to find new sources of uranium to improve the sustainable development of nuclear power. The available supply of terrestrial uranium is predicted to last just 80 years, however, the quantity of uranium in seawater is estimated to be ~1000 times greater than this.[101] Hence the development of technology able to selectively remove uranium ions from seawater is of high importance. In 2015, Luo *et al.* reported the synthesis of a Zn(II) MOF containing 1D channels functionalised with acylamide and carboxyl groups (Figure 1.13).[97] Activated samples of this MOF, denoted Zn(HBTC)(L), were added to solutions containing U(VI) ions to evaluate its adsorption capacity.

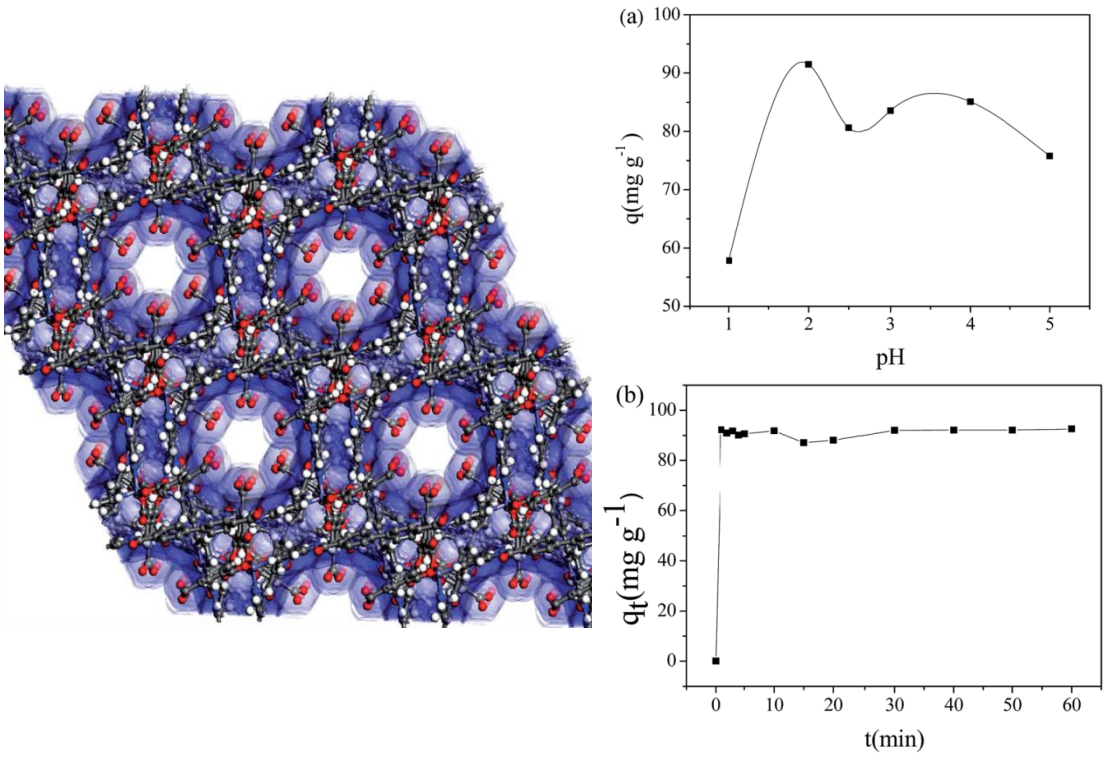


Figure 1.13. View of the 1D channel along the *c*-axis of Zn(HBTC)(L) (left) and the uptake of U(VI) ions with respect to pH and time using 100 ppm solutions of U(VI) and 10 mg of MOF at 298 K (right). Reproduced from reference 97.

A series of experiments were set up varying pH, contact time, temperature and U(VI) concentration to investigate the effects of these parameters on U(VI) uptake. It should be noted that whilst uranium speciation is known to vary with pH, the predominant species over the pH range used was UO_2^{2+}. As shown in Figure 1.13, the pH has a dramatic effect on the uptake, increasing from 55 mg g^{-1} to 92 mg g^{-1} between pH 1 and pH 2 and then reducing with further increases in pH. The maximum adsorption capacity of 92 mg g^{-1} is significantly lower than the 217 mg g^{-1} reported by Lin *et al.* in a similar series of experiments with Zr(IV) based MOFs.[96] However, the uptake time of just one minute shows that Zn(HBTC)(L) has great potential for quick and efficient scavenging of UO_2^{2+}. This quick adsorption is driven

by the interactions between UO_2^{2+} ions and the free functional groups of the MOF, as determined from IR experiments.[97]

1.4.3 Heavy Metal Ions

Heavy metal such as Hg and Pb are a significant health concern when released into the environment as they have the potential to accumulate in the human body.[102] As a result, their removal and recovery from industrial waste streams, and even drinking water in less developed countries, is a necessity.[102] A number of MOFs have been tested for their Hg(II) uptake capacity in recent years,[102-106] with the first known example published in 2011 by Che *et al.* using a thioether functionalised MOF-5 analogue for the removal of $HgCl_2$ from ethanol solutions.[107] The first example of a MOF capable of Hg(II) extraction from an aqueous solution was reported in the same year using thiol functionalised HKUST-1, a water-stable Cu(II) MOF containing benzenetricarboxylate linkers.[102] The thiol functional groups were added to the MOF post-synthetically. This was performed by heating HKUST-1 under vacuum to give open Cu(II) sites, followed by stirring in a toluene/dithioglycol mixture to graft dithioglycol moieties to the Cu(II) ions (Figure 1.14). Three different compositions of the MOF after post-synthetic modification were determined using energy-dispersive X-ray spectroscopy (EDX); **A**, Cu-BTC-DTG-0.18, **B** Cu-BTC-DTG-0.92 and **C** Cu-BTC-DTG-1.52 (BTC = benzene tricarboxylate, DTG = dithioglycol).[102]

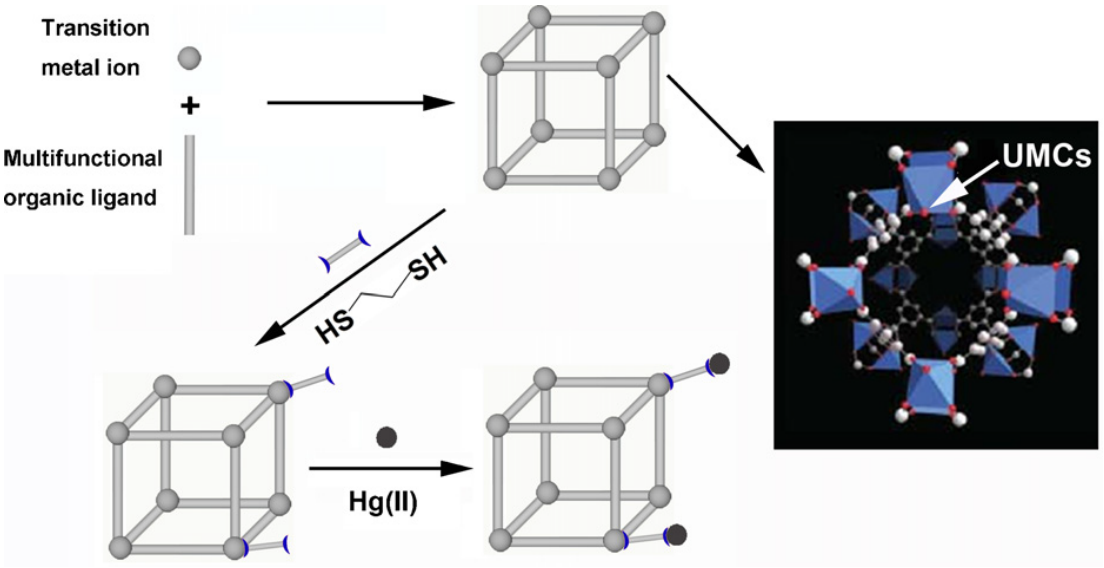


Figure 1.14. A schematic illustration of the coordination of thiol functional groups to free Cu(II) metal sites in HKUST-1. Reproduced from reference 102.

Mercury extraction experiments using these materials were performed in water over the course of 24 hours using a wide range of concentrations (from 0.1 to ~1500 ppm). The initial and final solution concentrations were analysed using atomic fluorescence spectroscopy (AFS) and a % uptake and adsorption capacity (in mg g^{-1}) were calculated for each sample. Sample **B**, Cu-BTC-DTG-0.92, exhibited the greatest Hg^{2+} adsorption capacity at all concentrations, showing an excellent maximum capacity of 714 mg g^{-1} and a 99.8% uptake. This compared very favourably to other porous adsorbents such as functionalised silica gels which generally exhibit a capacity of ~100 mg g^{-1} under similar conditions.[108,109] More importantly, **B** still exhibited 90% uptake at much lower concentrations of around 100 ppb (a more realistic real world concentration). Unfunctionalised HKUST-1 samples were found to exhibit no uptake capacity for Hg^{2+} ions under the same conditions, strongly suggesting that the extraction is entirely a result of interactions between the thiol groups and the metal ions.[102]

1.4.4 Precious Metals

The vast majority of MOF research concerning precious metals involves the encapsulation of Au, Ag, Ir, Pd and Pt nanoparticles for a variety of catalytic applications.[110-116] However, as stated previously, very few papers have reported MOFs with the ability to sense or scavenge precious metals from solution. In 2013, Xu *et al.* reported the synthesis of a MOF-5 analogue functionalised with allyl and sulfanyl groups, denoted ASMOF-5, for detection of precious metals from solution.[117] The sulfur groups were added to provide a conjugated photoluminescent aromatic core and the alkene was used to provide π-donor and π-acceptor character for preferential binding of noble metal ions. As noble metal ions are chemically soft species, they were also expected to interact with the thioether moieties, producing a substantial quenching of photoluminescence.[117] Upon immersion of ASMOF-5 in a solution of $Pd(MeCN)_2Cl_2$ in MeCN (0.25% w/w), the crystals exhibit a distinct colour change from light yellow to dark red within minutes (Figure 1.15). ICP-OES analysis showed a Zn:Pd ratio of 6.25 : 1 in the framework, equivalent to 0.64 Pd(II) ions per functionalised cage.

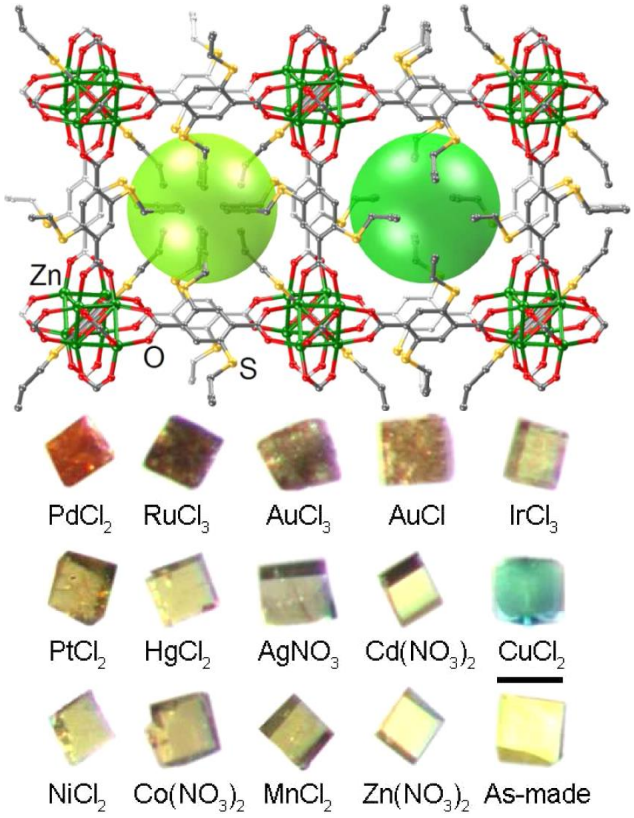


Figure 1.15. A view of the cage structure of ASMOF-5 (left) and the colour changes exhibited upon immersion in a variety of metal ion solutions (right). Reproduced from reference 117.

ASMOF-5 was also immersed in solutions of other precious metals and transition metals, giving a colour change in each case (Figure 1.15). As none of these colour changes are particularly distinct, ASMOF-5 therefore provides a simple method of detecting Pd(II) in the presence of other metal ions. Unfortunately ASMOF-5 was found to be unstable in water and the Pd-doped samples began to degrade in air within hours.[117]

The first example of a MOF designed specifically for the removal of PGMs from water was published by Amini *et al.* in 2012.[118] This involved the preparation of HKUST-1 incorporating immobilised Fe_3O_4 nanoparticles functionalised with amide

and pyridyl groups in the pores, for the removal of Pd(II) from seawater (Figure 1.16).

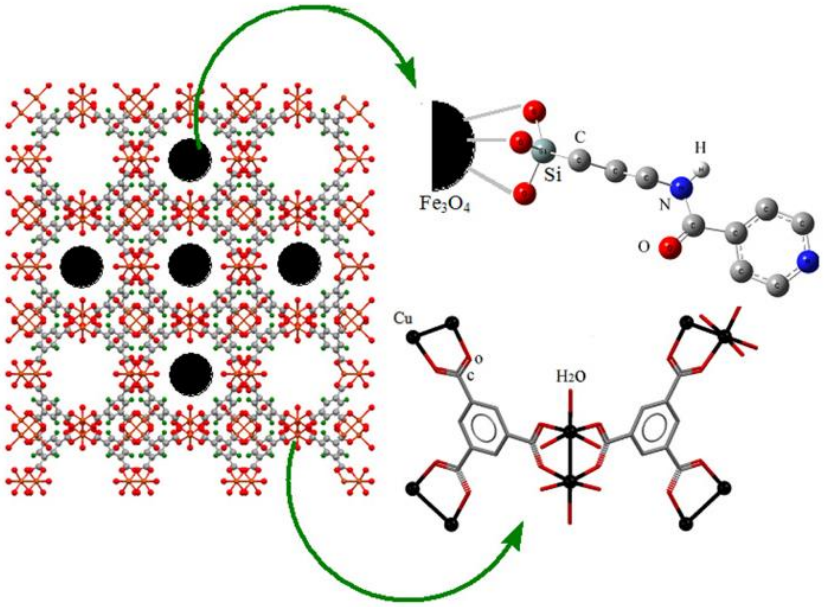


Figure 1.16. A schematic illustration of the functionalisation of HKUST-1 with Fe_3O_4 nanoparticles. Reproduced from reference 118.

Pd(II) extraction was investigated using batch experiments in 15 ml of de-ionised water with 30 µg of Pd^{2+} ions, whilst the pH was adjusted using dropwise addition of NaOH or HCl solutions. Once the extraction was complete, the concentration of the solution before and after was calculated using flame atomic absorption spectroscopy (FAAS) and converted into a % of Pd removed from solution. Under optimised conditions the MOF exhibited 100% adsorption of Pd(II) from solution with a maximum capacity of 105.1 mg g^{-1}. However, this was only successful when using a trace amount of Pd(II) and the MOF exhibited no adsorption of Pd(II) from HCl solutions, which is by far the most common medium for PGM dissolution.[118]

In 2015, Xu and co-workers reported the extraction of Pd(II) from aqueous acidic waste solutions using a Zr(IV) analogue of the sulfur and alkene-functionalised

Zn(II) MOF described earlier.[119] The framework consists of Zr-oxo clusters bridged by the organic linkers to give a structure containing cages decorated by the functional groups (Figure 1.17). As Zr(IV) is very oxophilic, it produces MOFs with high levels of thermal and chemical stability including stability in acidic solutions in which the majority of MOFs would decompose. To carry out the extraction, 300 mg of the MOF, denoted ASUiO-66 was added to simulated liquid waste containing 20 metal ions of different concentrations.

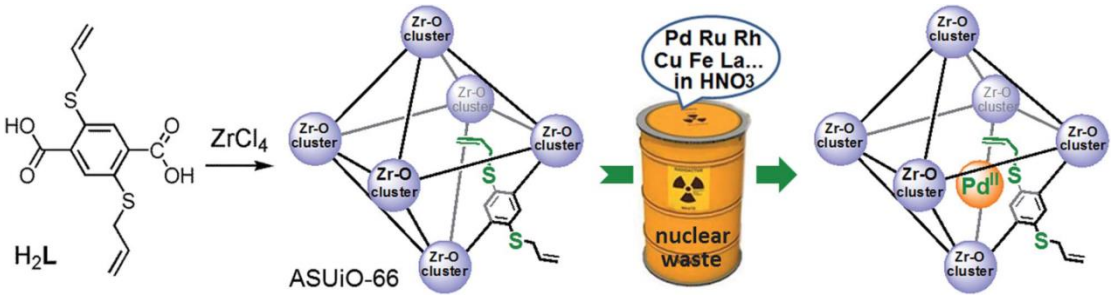


Figure 1.17. A schematic illustration of the synthesis of ASUiO-66 and the removal of Pd(II) from nuclear waste. Reproduced from reference 119.

After shaking for one hour in 40 ml of the 1 M HNO_3 solution, ICP-AES analysis showed a 95% reduction in Pd(II) concentration and importantly, uptake of the majority of the other metals was negligible. Whilst uptake of Ag(I) and Se(II) was observed (Figure 1.18), ASUiO-66 still exhibits excellent selectivity for Pd(II) over a wide range of metal ions. It is also important to note that the same extraction performed with unfunctionalised UiO-66 gave a Pd(II) uptake of just 1.4%, highlighting the key role of the functional groups in this process. The retrieval of Pd(II) from ASUiO-66 was demonstrated by stirring Pd@ASUiO-66 samples in a mixture of HNO_3/thiourea at 50 °C, releasing 85% of the Pd from the pores. It was possible to repeat this cycle of uptake/retrieval without a significant loss of efficiency (40.8 mg g^{-1} to 37.9 mg g^{-1} after 5 cycles).[119]

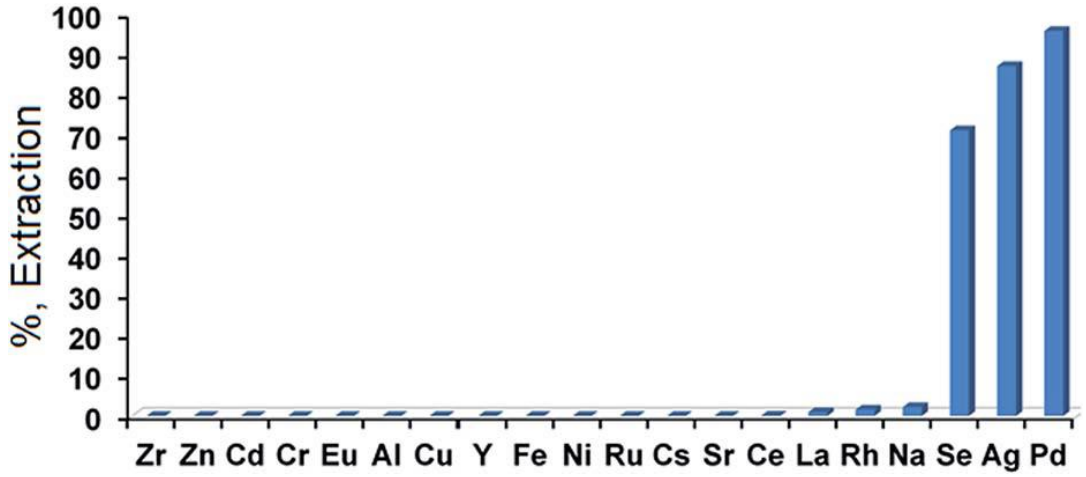


Figure 1.18. Percentage of the metal ions adsorbed by ASUiO-66 from a simulated aqueous waste solution. Reproduced from reference 119.

The first reports of MOFs capable of recovering PGM chlorides from aqueous solutions were published in 2014.[120,121] Huang *et al.* investigated the extraction of $PtCl_4^{2-}$, in the form of K_2PtCl_4, from aqueous solutions using a series of isoreticular Zr(IV) UiO-66 frameworks functionalised with -NH_2, -F, -OMe and -NO_2 groups.[120] Uptake of the anion was monitored *in-situ* using X-ray absorption spectroscopy (XAS). Each MOF was dispersed in a K_2PtCl_4/H_2O solution, sealed in a liquid cell and placed into the X-ray beam. XAS spectra were then collected periodically over the course of 36 hours. The results showed that UiO-66-NH_2 exhibited the greatest sorption capacity for $PtCl_4^{2-}$ (94%) with the other frameworks performing poorly (between 16% and 29% uptake).[120] Fitting of the spectra allowed the coordination of Pt within UiO-66-NH_2 to be monitored over time, showing a rapid decrease in Pt-Cl coordination from 4 to 2 and a concomitant increase in Pt-N coordination from 0 to 2 (Figure 1.19). This confirms that the coordination number remained at 4 and suggests that the square planar geometry of Pt(II) is maintained with 2 NH_2 groups of the MOF binding a $PtCl_2$ molecule within the pore.

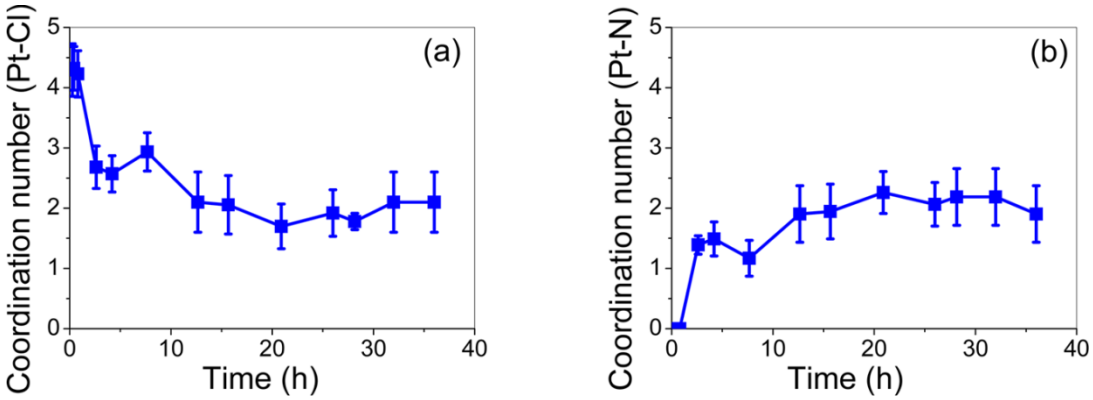


Figure 1.19. The time dependence of Pt coordination with Cl (left) and N (right). Reproduced from reference 120.

A similar coordination trend was observed for UiO-66 and the $–NO_2$, -OMe and –F functionalised MOFs. The Pt-Cl coordination reduced from 4 to 2.5 with a rise of 0 to 1.5 in Pt-O coordination, strongly suggesting that the Pt complex binds with the framework carboxyl groups in the absence of an NH_2 group. A DRIFTS study also showed a suppression of the carboxyl vibrations upon Pt loading, giving further evidence for this theory.[120] Following this work, the same group published a more detailed report focussing on the use of UiO-66-NH_2 as an extractant for $PtCl_4^{2-}$.[121] This will be discussed in more detail in the introduction section of Chapter 2.

1.5 Scope of this Work

The key aim of this work was to explore the use of MOFs for the recovery of PGMs from aqueous and organic solutions. A specific focus was on the design and preparation of MOFs with pendant functional groups capable of selectively binding to these metal complexes.

Chapter 2 focuses on the synthesis of ligands for the preparation of highly stable Zr(IV) MOFs for the removal of PGM chlorides, particularly $PtCl_6^{2-}$, from aqueous and acidic solutions. These frameworks incorporate amine groups to bind to the

chloride groups of the PGM and the sorption capacity was compared to that of non-functionalised analogues as well as industrially used sorbent materials. The uptake into each material is examined using ICP-OES and UV-vis spectroscopy and the doped MOF materials are characterised using a combination of solid state NMR, ICP-OES and X-ray photoelectron spectroscopy (XPS).

Chapter 3 is based around the retrieval of three important PGM compounds, $Pd(OAc)_2$, $PtCl_4$ and $Rh_2(OAc)_4$ from organic solvents. For this purpose, a series of Cu(II) frameworks has been synthesised and their sorption capacity is analysed by ICP-OES and XPS techniques. The design of the series allows for a direct comparison between different functional groups (amine, oxamide and methyl) in addition to exploring the effect of different topological structures and pore sizes on guest encapsulation.

Chapter 4 focuses on the synthesis of novel MOFs based around a nitrogen-rich triazine core and their use for PGM extraction and gas storage/separation applications. The gas adsorption and separation properties of a new, highly porous MOF, denoted NOTT-160, are examined and compared to similar materials previously reported in the literature. In particular, high pressure CH_4 sorption and low pressure separation of CH_4 from C_2 hydrocarbons in NOTT-160 is discussed, with Langmuir-Freundlich fittings applied to the isotherms and the use of Henry's law and the IAST model to predict selectivities for one gas over another.

1.6 ICP-OES

Inductively coupled plasma optical emission spectrometry (ICP-OES) is a powerful analytical technique for the determination of trace elements within a sample. The instrument consists of an excitation source which contains a torch consisting of three

concentric tubes made of quartz and another suitable material.[122] A copper coil, called the load coil, surrounds the top of the torch and is connected to a radio frequency (RF) generator.[122] Argon gas is passed through the torch, RF energy is applied to the load coil and a spark is added to the highly energised Ar atoms, which are stripped of electrons, forming plasma. Further agitation of these Ar ions and electrons by the RF field increases the plasma temperature to approximately 10,000 K.[123] The sample, in liquid form, is converted to an aerosol using a nebuliser and directed into the centre of the plasma. The aerosol is quickly vaporised and the atoms/ions from the sample are promoted to excited states.[122] Relaxation of these excited states to the ground state may occur through the emission of photons, which are then separated into their component wavelengths through a diffraction grating. As each element has a characteristic set of emission wavelengths, the wavelength of the photon emission can be used to determine the element from which it originated. As the number of photons is directly proportional to the quantity of an element within a sample, ICP-OES is a very accurate technique to determine the concentration of an element in solution. There are many advantages to ICP-OES over similar techniques such as direct current plasma (DCP), microwave-induced plasma (MIP) and laser-induced plasma (LIP). For example, the very high temperature of the plasma means that ICP-OES gives efficient and reproducible vaporisation, excitation and ionisation of a huge range of elements from different matrices.[123] This is particularly useful for the excitation of metals with very high melting points. ICP-OES gives low background noise, low levels of chemical interference, has a highly stable, highly electron dense source and is better able to handle liquid samples than other techniques, all of which lead to excellent accuracy.[123] It also exhibits very low detection limits for the majority of elements, with some detected in concentrations as

low as 0.1 ppb (0.1 ng L^{-1}).[123] Thus ICP-OES was the ideal technique to use to monitor changes in PGM concentration in solution during the extraction process.

1.7 General Experimental Methods

1.7.1 Reagents and Analytical Techniques

All solvents and reagents were purchased from Sigma-Aldrich, Alfa Aesar, Fisher Scientific or Frontier Scientific and were used without further purification unless stated. The specific details of the synthesis of organic linkers are described in the experimental section of each chapter. MOF materials were prepared using a solvothermal method in a variety of different vessels – 250 ml Schott bottles, 45 ml stainless steel Parr autoclaves, 15 ml pressure tubes or 8 ml Wheaton pressure vials.

^{1}H and ^{13}C NMR spectra were recorded on Bruker DPX-300, DPX-400 and AV-400 spectrometers. Mass spectra (ESI) were recorded on a Bruker MALDI-TOF spectrometer. Elemental analyses were performed on a CE-440 elemental analyser at the University of Nottingham. Powder X-ray diffractograms were measured on a PANalytical X'Pert PRO diffractometer using Cu-*Kα* radiation (λ = 1.5418 Å). Thermogravimetric analyses were performed under a flow of air (20 ml/min) from 25 – 600 °C using a heating rate of 5 °C/min on a TA SDT-600 thermogravimetric analyser. Infra-red spectra were recorded on a Thermoscientific Nicolet iS5 FT-IR spectrometer at the University of Nottingham. UV-vis spectra were recorded on an Ocean Optics USB2000+ UV-VIS ES spectrometer using a DT-MINI-2-GS light source. ICP-OES spectra were measured using an Optima 2000 DV ICP-OES with S10 autosampler. In all cases the samples were measured against 0, 20, 40, 60 and 100 ppm calibration standards containing the elements of interest. XPS analysis was performed by collaborators at Johnson Matthey Technology Centre (JMTC) using a

Thermo Escalab 250 instrument with monochromated Al-*Kα* radiation (1486.6eV) with a spot size of 650 μm. SS-NMR spectra were also acquired at JMTC at a static magnetic field strength of 9.4 T (ν0(1H) = 400.16 MHz) on a Bruker Avance III console using a widebore Bruker 4 mm BB/1H WVT MAS probe and TopSpin 3.1 software. For ^{13}C, the probe was tuned to 100.63 MHz and the spectra referenced to the alanine CH_3 signal at 20.5 ppm

1.7.2 Single Crystal X-ray Diffraction

In-house single crystal X-ray diffraction experiments were run on Bruker APEX, Agilent Technologies Supernova and Agilent Technologies Supernova II diffractometers using Cu-*Kα* radiation (λ = 1.5418 Å). As a result of weak diffraction, several structures were solved from data collected at Diamond Light Source, beamline I19, using synchrotron radiation (λ = 0.6889 Å). Data was refined using CrysAlis Pro and all structures were solved using the Olex2[124] and SHELX[125] software packages. Where necessary, PLATON/SQUEEZE[126] was employed to remove residual electron density associated with disordered solvent molecules to give a set of solvent-free diffraction intensities.

1.7.3 Gas Adsorption Isotherms

Low pressure N_2 isotherms at 77 K were carried out on a Quantachrome Autosorb, a Micromeritics 3Flex Surface Characterisation Analyser system and a Tristar II Surface Characterisation Analyser system using high purity (99.999%) research grade N_2. Gas sorption isotherms from 0-20 bar were carried out on a Hiden intelligent gravimetric analyser (IGA). Prior to all measurements, approximately 100 mg of solvent exchanged MOF was loaded into the sample holder and outgassed at 100-120 °C under high vacuum for 20 hours to remove all guest molecules. For H_2 adsorption experiments, ultra-pure grade H_2 (99.9995%) was purified further by

passing through a zeolite to remove trace impurities before entering the sample chamber. This same process was adhered to for the purification of C_2H_2. High pressure (0-80 bar) CH_4 adsorption experiments were carried out by collaborators at General Motors.

1.8 References

1. Bernardis, F. L.; Grant, R. A.; Sherrington, D. C., *React. Funct. Polym.*, **2005**, *65*, 205.
2. Seymore, R. J.; O'Farrelly, J. I.; Potter, L. C., *Encyclopedia of Chemical Technology*, Wiley, **1998**, *19*, 367.
3. Edwards, R. I.; te Riele, W. A. M.; Bernfield, G. J., *Gmelin Handbook of Inorganic Chemistry*, Springer, **1986**, 1.
4. Grant, R. *Proceedings of IPMI Seminar on Precious Metals Recovery and Refining*, Scottsdale, AZ, USA, **1989**.
5. Willard, H.; Merrit, L.; Dean, J.; Settle, F., *Instrumental Methods of Analysis*, Wadsworth, **1988**, 636.
6. Alguacil, F. T.; Cobo, A.; Coedo, A. G.; Dorado, M. T.; Sastre, A., *Hydrometallurgy*, **1997**, *44*, 203.
7. Lee, J. Y.; Kumar, J. R.; Kim, J. S.; Park, H. K.; Yoon, H. S., *J. Hazard. Mater.*, **2009**, *168*, 424.
8. Reddy, B. R.; Raju, B.; Lee, J. Y.; Park, H. K., *J. Hazard. Mater.*, **2010**, *180*, 253.
9. Warr, R. J.; Westra, A. N.; Bell, K. J.; Chartres, J.; Ellis, R.; Tong, C. C.; Simmance, T. G.; Gadzhieva, A.; Blake, A. J.; Tasker, P. A.; Schröder, M., *Chem. Eur. J.*, **2009**, *15*, 4836.
10. Charlesworth, P., *Platinum Met. Rev.*, **1981**, *25*, 106.
11. Bell, K. J.; Westra, A. N.; Warr, R. J.; Chartres, J.; Ellis, R.; Tong, C. C.; Blake, A. J.; Tasker, P. A.; Schröder, M., *Angew. Chem., Int. Ed.*, **2008**, *47*, 1745.
12. Mladenova, E.; Karadjova, I.; Tsalev, D. L. *J. Sep. Sci.* **2012**, *35*, 1249.
13. Robin, A. Y.; Fromm, K. M., *Coord. Chem. Rev.*, **2006**, *250*, 2127.
14. Yang, S.; Sun, J. L.; Ramirez-Cuesta, A. J.; Callear, S. K.; David, W. I. F.; Anderson, D. P.; Newby, R.; Blake, A. J.; Parker, J. E.; Tang, C. C.; Schröder, M., *Nature Chem.*, **2012**, *4*, 887.
15. Lin, X.; Jia, J.; Zhao, X.; Thomas, K. M.; Blake, A. J.; Walker, G. S.; Champness, N. R.; Hubberstey, P.; Schröder, M., *Angew. Chem., Int. Ed.*, **2006**, *45*, 7358.

16. Lin, X.; Telepini, I.; Blake, A. J.; Dailly, A.; Brown, C. M.; Simmons, J. M.; Zoppi, M.; Walker, G. S.; Thomas, K. M.; Mays, T. J.; Hubberstey, P.; Champness, N. R.; Schröder, M., *J. Am. Chem. Soc.*, **2009**, *131*, 2159.
17. Farha, O. K.; Yazaydin, A. Ö.; Eryazici, I.; Milliakas, C. D.; Hauser, B. G.; Kanatzidis, M. G.; Nguyen, S. T.; Snurr, R. Q.; Hupp, J. T., *Nature Chem.*, **2010**, *2*, 944.
18. Dinca, M.; Dailly, A.; Liu, Y.; Brown, C. M.; Neumann, D. A.; Long, J. R., *J. Am. Chem. Soc.*, **2006**, *128*, 16876.
19. Dinca, M.; Long, J. R., *J. Am. Chem. Soc.*, **2005**, *127*, 9376.
20. Rowsell, J. R.; Yaghi, O. M., *Angew. Chem., Int. Ed.*, **2005**, *44*, 4670.
21. Millward, A. R.; Yaghi, O. M., *J. Am. Chem. Soc.*, **2005**, *127*, 17998.
22. Ma, S. Q.; Sun, D. F.; Simmons, J. M.; Collier, C. D.; Yuan, D. Q.; Zhou, H-C., *J. Am. Chem. Soc.*, **2008**, *130*, 1012.
23. Furukawa, H.; Ko, N.; Go, Y. B.; Aratani, N.; Choi, S. B.; Choi, E.; Yazaydin, A. Ö.; Snurr, R. Q.; O'Keeffe, M.; Kim, J.; Yaghi, O. M., *Science*, **2010**, *329*, 424.
24. Li, J. R.; Kuppler, J. R.; Zhou, H-C., *Chem. Soc. Rev.*, **2009**, *38*, 1477.
25. Li, J. R.; Ma, Y.; McCarthy, M. C.; Sculley, J.; Yu, J.; Jeong, H-K.; Balbuena, P. B.; Zhou, H-C., *Coord. Chem. Rev.*, **2011**, *255*, 1791.
26. Li, J. R.; Sculley, J.; Zhou, H-C., *Chem. Rev.*, **2012**, *112*, 869.
27. Britt, D.; Furukawa, H.; Wang, B.; Glover, G.; Yaghi, O. M., *PNAS*, **2009**, *106*, 20637.
28. Matsuda, R.; Kitaura, R.; Kitagawa, S.; Kubota, Y.; Belosludov, R. V.; Kobayashi, T. C.; Sakamoto, H.; Chiba, T.; Takata, M.; Kawazoe, Y.; Mita, Y., *Nature*, **2005**, *436*, 238.
29. Bloch, E. D.; Queen, W. L.; Krishna, R.; Zadrozny, J. M.; Brown, C. M.; Long, J. R., *Science*, **2012**, *335*, 1606.
30. Yang, S.; Ramirez-Cuesta, A. J.; Newby, R.; Garcia Sakai, V.; Manuel, P.; Callear, S. K.; Campbell, S. I.; Tang, C. C.; Schröder, M., *Nature Chem.*, **2015**, *7*, 121.
31. Yang, W.; Davies, A. J.; Lin, X.; Suyetin, M.; Matsuda, R.; Blake, A. J.; Wilson, C.; Lewis, W.; Parker, J. E.; Tang, C. C.; George, M. W.; Hubberstey, P.; Kitagawa, S.; Sakamoto, H.; Bichoutskaia, E.; Champness, N. R.; Yang, S.; Schröder, M., *Chem. Sci.*, **2012**, *3*, 2993.
32. Yang, S.; Lin, X.; Lewis, W.; Suyetin, M.; Bichoutskaia, E.; Parker, J. E.; Tang, C. C.; Allan, D. R.; Rizkallah, P. J.; Hubberstey, P.; Champness, N. R.; Thomas, M. K.; Blake, A. J.; Schröder, M., *Nature Mater.*, **2012**, *11*, 710.
33. Bae, Y-S.; Mulfort, K. L.; Frost, H.; Ryan, P.; Punnathanam, S.; Broadbelt, L. J; Hupp, J. T.; Snurr, R. Q., *Langmuir*, **2008**, *24*, 8592.

34. An, J.; Geib, S. J.; Rosi, N. L., *J. Am. Chem. Soc.*, **2010**, *132*, 38.
35. Chen, B.; Ma, S. Q.; Zapata, F.; Fronczek, F. R.; Lobkovsky, E. B.; Zhou, H-C., *Inorg. Chem.*, **2007**, *46*, 1233.
36. Lee, J.; Farha, O. K.; Roberts, J.; Scheidt, K. A.; Nguyen, S. T.; Hupp, J. T., *Chem. Soc. Rev.*, **2009**, *38*, 1450.
37. Wu, C. D.; Hu, A.; Zhang, L.; Lin, W., *J. Am. Chem. Soc.*, **2005**, *127*, 8940.
38. Liu, Y.; Xuan, W. M.; Cui, Y., *Adv. Mater.*, **2010**, *22*, 4112.
39. Hong, D. Y.; Hwang, Y. K.; Serre, C.; Férey, G.; Chang, J. S., *Adv. Funct. Mater.*, **2009**, *19*, 1537.
40. Dang, D. B.; Wu, P. Y.; He, C.; Xie, Z.; Duan, C. Y., *J. Am. Chem. Soc.*, **2010**, *132*, 14321.
41. An, J.; Geib, S. J.; Rosi, N. L., *J. Am. Chem. Soc.*, **2009**, *131*, 8376.
42. Huxford, R. C.; Della Rocca, J.; Lin, W. B., *Curr.Opin. Chem. Biol.*, **2010**, *14*, 262.
43. McKinlay, A. C.; Xiao, B.; Wragg, D. S.; Wheatley, P. S.; Megson, I. L.; Morris, R. E., *J. Am. Chem. Soc.*, **2008**, *130*, 10440.
44. Sun, C. Y.; Qin, C.; Wang, C-G.; Su, Z-M.; Wang, S.; Wang, X-L.; Yang, G-S.; Shao, K-Z.; Lan, Y. Q.; Wang, E. B., *Adv. Mater.*, **2011**, *23*, 5629.
45. Ke, F.; Yuan, Y-P.; Qiu, L-Q.; Shen, Y-H.; Xie, A. J.; Zhu, J-F.; Tian, X-Y.; Zhang, L-D., *J. Mater. Chem.*, **2011**, *21*, 3843.
46. Paseta, L.; Potier, G.; Abbott, S.; Coronas, J., *Org. Biomol. Chem.*, **2015**, *13*, 1724.
47. Chen, B.; Xiang, S.; Qian, G., *Acc. Chem. Res.*, **2010**, *43*, 1115.
48. Lu, Z-Z.; Zhang, R.; Li, Y-Z.; Guo, Z-J.; Zheng, H-G., *J. Am. Chem. Soc.*, **2011**, *133*, 4172.
49. Hu, Z.; Deibert, B. J.; Li, J., *Chem. Soc. Rev.*, **2014**, *43*, 5815.
50. Gole, B.; Bar, A. K.; Mukherjee, P. S., *Chem. Commun.*, **2011**, *47*, 12137.
51. Zhang, C.; Sun, L.; Yan, Y.; Li, Y.; Song, X.; Liu, Y.; Liang, Z., *Dalton Trans.*, **2015**, *44*, 230.
52. Mallick, A.; Garai, B.; Addicoat, M. A.; Petkov, P. S.; Heine, T.; Banerjee, R., *Chem. Sci.*, **2015**, *6*, 1420.
53. Hurd, J. A.; Vaidhyanathan, R.; Thangadurai, V.; Ratcliffe, C. I.; Moudrakovski, I. L.; Shimizu, G. K. H., *Nature Chem.*, **2009**, *1*, 705.
54. Sadakiyo, M.; Yamada, T.; Kitagawa, H., *J. Am. Chem. Soc.*, **2009**, *131*, 9906.
55. Nagarkar, S. S.; Unni, S. M.; Sharma, A.; Kurungot, S.; Ghosh, S. K., *Angew. Chem., Int. Ed.*, **2014**, *53*, 2638.
56. Bao, S. S.; Otsubo, K.; Taylor, J. M.; Jiang, Z.; Zheng, L. M. Kitagawa, H., *J. Am. Chem. Soc.*, **2014**, *136*, 9292.
57. Sadakiyo, M.; Yamada, T.; Kitagawa, H., *J. Am. Chem. Soc.*, **2014**, *136*, 13166.

58. Zheng, G-L.; Yang, G-C.; Song, S-Y.; Song, X-Z.; Zhang, H-J., *Cryst. Eng. Comm.*, **2014**, *16*, 64.
59. Farha, O. K.; Eryazici, I.; Jeong, N. C.; Hauser, B. G.; Wilmer, C. E.; Sarjeant, A. A.; Snurr, R. Q.; Nguyen, S. T.; Yazaydin, A, Ö.; Hupp, J. T., *J. Am. Chem. Soc.*, **2012**, *134*, 15016.
60. Férey, G., *Chem. Soc. Rev.*, **2008**, *37*, 191.
61. Ni, Z.; Masel, R. I., *J. Am. Chem. Soc.*, **2006**, *128*, 12394.
62. Klimakow, M.; Klobes, P.; Thünemann, A. F.; Rademann, K.; Emmerling, F., *Chem. Mater.*, **2010**, *22*, 5216.
63. Bayliss, P. A.; Ibarra, I. A.; Pérez, E.; Yang, S.; Tang, C. C.; Poliakoff, M.; Schröder, M., *Green Chem.*, **2014**, *16*, 3796.
64. Cook, T. R.; Zheng, Y-R.; Stang, P. J., *Chem. Rev.*, **2013**, *113*, 734.
65. Kim, J.; Chen, B.; Reineke, T. M.; Li, H. L.; Eddaoudi, M.; Moler, D. B.; O'Keeffe, M.; Yaghi, O. M., *J. Am. Chem. Soc.*, **2001**, *123*, 8239.
66. Eddaoudi, M.; Moler, D. B.; Li, H.; Chen, B.; Reineke, T. M.; O'Keeffe, M.; Yaghi, O. M., *Acc. Chem. Res.*, **2001**, *34*, 319.
67. Perry IV, J. J.; Perman, J. A.; Zawarotko, M. J., *Chem. Soc. Rev.*, **2009**, *38*, 1400.
68. Liu, Y.; Eubank, J. F.; Cairns, A. J.; Eckert, J.; Kravstov, V. C.; Luebke, R.; Eddaoudi, M., *Angew. Chem., Int. Ed.*, **2007**, *46*, 3278.
69. Ockwig, N. W.; Delgado-Friedrichs, O.; O'Keeffe, M.; Yaghi, O. M., *Acc. Chem. Res.*, **2005**, *38*, 176.
70. Eddaoudi, M.; Kim, J.; Rosi, N. L.; Vodak, D.; Wachter, J.; O'Keeffe, M.; Yaghi, O. M., *Science*, **2002**, *295*, 469.
71. Yaghi, O. M.; O'Keeffe, M.; Ockwig, N. W.; Chae, H. K.; Eddaoudi, M.; Kim, J., *Nature*, **2003**, *423*, 705.
72. Yuan, D.; Zhao, D.; Sun, D.; Zhou, H-C., *Angew. Chem., Int. Ed.*, **2010**, *49*, 5357.
73. Banerjee, R.; Furukawa, H.; Britt, D.; Knobler, C.; O'Keeffe, M.; Yaghi, O. M., *J. Am. Chem. Soc.*, **2009**, *131*, 3875.
74. Deng, H.; Grunder, S.; Cordova, K. E.; Valente, C.; Furukawa, H.; Hmadeh, M.; Gàndara, F.; Whalley, A. C.; Liu, Z.; Asahina, S.; Kazumori, H.; O'Keeffe, M.; Terasaki, O.; Stoddart, J. F.; Yaghi, O. M., *Science*, **2012**, *336*, 1018.
75. McDonald, T. M.; Lee, W. R.; Mason, J. A.; Wiers, B. M.; Hong, C. S.; Long, J. R., *J. Am. Chem. Soc.*, **2012**, *134*, 7056.
76. Torrisi, A.; Bell, R. G.; Mellot-Draznieks, C., *Cryst. Growth Des.*, **2010**, *10*, 2839.
77. Panda, T.; Pachfule, P.; Chen, Y.; Jiang, J.; Banerjee, R., *Chem. Commun.*, **2011**, *47*, 2011.
78. Park, J.; Feng, D.; Zhou, H-C., *J. Am. Chem. Soc.*, **2015**, *137*, 11801.

79. Zlotea, C.; Phanon, D.; Mazaj, M.; Heurtaux, D.; Guillerm, V.; Serre, C.; Horcajada, P.; Devic, T.; Magnier, E.; Cuevas, F.; Férey, G.; Llewellyn, P. L.; Latroche, M., *Dalton Trans.*, **2011**, *40*, 4879.
80. Lu, W.; Wei, Z.; Gu, Z-Y.; Liu, T-F.; Park, J.; Park, J.; Tian, J.; Zhang, M.; Zhang, Q.; Gentle III, T.; Bosch, M.; Zhou, H-C., *Chem. Soc. Rev.*, **2014**, *43*, 5561.
81. Neofotistou, E.; Malliakas, C. D.; Trikalitis, P. N., *Chem. Eur. J.*, **2009**, *15*, 4523.
82. Yang, C-X.; Ren, H-B.; Yan, X-P., *Anal. Chem.*, **2013**, *85*, 7441.
83. Zhou, X-H.; Li, L.; Li, H-H.; Li, A.; Yang, T.; Huang, W., *Dalton Trans.*, **2013**, *42*, 12403.
84. Dang, S.; Ma, E.; Sun, Z-M.; Zhang, H., *J. Mater. Chem.*, **2012**, *22*, 16920.
85. Zalomaeva, O. V.; Kovalenko, K. A.; Chesalov, Y. A.; Mel'gunov, M. S.; Zaikovskii, V. I.; Kaichev, V. V.; Sorokin, A. B.; Kholdeeva, O. A.; Fedin, V. P., *Dalton Trans.*, **2011**, *40*, 1441.
86. Meng, X.; Zhong, R-L.; Song, X-Z.; Song, S. Y.; Mao, Z-M.; Zhu, M.; Zhao, S-N.; Zhang, H-J., *Chem. Commun.*, **2014**, *50*, 6406.
87. Chen, B.; Wang, L.; Xiao, Y.; Fronczek, F. R.; Xue, M.; Cui, Y.; Qian, G., *Angew. Chem., Int. Ed.*, **2009**, *48*, 500.
88. Hao, Z.; Song, X.; Zhu, M.; Meng, X.; Zhao, S.; Su, B.; Yang, W.; Song, S.; Zhang, H., *J. Mater. Chem. A*, **2013**, *1*, 11043.
89. Xiao, Y.; Cui, Y.; Zheng, Q.; Xiang, S.; Qian, G.; Chen, B., *Chem. Commun.*, **2010**, *46*, 5503.
90. Chen, C-X.; Liu, Q-K.; Ma, J-P.; Dong, Y-B., *J. Mater. Chem.*, **2012**, *22*, 9027.
91. Wang, Y.; Yang, J.; Liu, Y-Y.; Ma, J-F., *Chem. Eur. J.*, **2013**, *19*, 14591.
92. Lan, Y-Q.; Jiang, H-L.; Li, S-L.; Xu, Q., *Adv. Mater.*, **2011**, *23*, 5015.
93. An, J.; Shade, C. M.; Chengelis-Czegan, D. A.; Petoud, S.; Rosi, N. L., *J. Am. Chem. Soc.*, **2011**, *133*, 1220.
94. Zhao, S-N.; Song, X-Z.; Zhu, M.; Meng, X.; Wu, L-L.; Feng, J.; Song, S-Y.; Zhang, H-L., *Chem. Eur. J.*, **2015**, *21*, 9748.
95. Qin, J-S.; Zhang, S-R.; Du, D-Y.; Shen, P.; Bao, S-J.; Lan, Y-Q.; Su, Z-M., *Chem. Eur. J.*, **2014**, *20*, 5625.
96. Carboni, M.; Abney, C. W.; Liu, S.; Lin, W., *Chem. Sci.*, **2013**, *4*, 2396.
97. Wang, L. L.; Luo, F.; Dang, L-L.; Li, J. Q.; Wu, X-L.; Liu, S. J.; Luo, M. B., *J. Mater. Chem. A*, **2015**, *3*, 13724.
98. Abney, C. W.; Taylor-Pashow, K. M. L.; Russell, S. R.; Chen, Y.; Samantaray, R.; Lockard, J. V.; Lin, W., *Chem. Mater.*, **2014**, *26*, 5231.
99. Yang, W.; Bai, Z-Q.; Shi, W-Q.; Yuan, L-Y.; Tian, T.; Chai, Z-F.; Wang, H.; Sun, Z-M., *Chem. Commun.*, **2013**, *49*, 10415.

100. Bai, Z-Q.; Yuan, L-Y.; Zhu, L.; Liu, Z-R.; Shu, S-Q.; Zheng, L-R.; Zhang, J.; Chai, Z-F.; Shi, W-Q., *J. Mater. Chem. A*, **2015**, *3*, 525.
101. Yue, Y. F.; Sun, X. G.; Mayes, R. T.; Kim, J. S.; Fulvio, P. F.; Qiao, Z. A.; Brown S.; Dai, D., *Sci. China: Chem.*, **2013**, *56*, 1510.
102. Ke, F.; Qiu, L-G.; Yuan, Y-P.; Peng, F-M.; Jiang, X.; Xie, A-J.; Shen, Y-H.; Zhu, J-F., *J. Hazard. Mat.*, **2011**, *196*, 36.
103. Liu, T.; Che, J-X.; Hu, Y-Z.; Dong, X-W.; Liu, X-Y.; Che, C-M., *Chem. Eur. J.*, **2014**, *20*, 14090.
104. Abney, C. W.; Gilhula, J. C.; Lu, K.; Lin, W., *Adv. Mater.*, **2014**, *26*, 7993.
105. Tan, H.; Liu, B.; Chen, Y., *ACS Nano*, **2012**, *6*, 10505.
106. Yee, K-K.; Reimer, N.; Liu, J.; Cheng, S-Y.; Yiu, S-M.; Weber, J.; Stock, N.; Xu, Z., *J. Am. Chem. Soc.*, **2013**, *135*, 7795.
107. He, J.; Yee, K-K.; Xu, Z.; Zeller, M.; Hunter, A. D.; Chui, S. S-Y.; Che, C-M., *Chem. Mater.*, **2011**, *23*, 2940.
108. Qu, R.; Wang, M.; Song, R.; Sun, C.; Zhang, Y.; Sun, X.; Ji, C.; Wang, C.; Yin, P., *J. Chem. Eng. Data*, **2011**, *56*, 1982.
109. Sun, C.; Ma, F.; Zhang, G.; Qu, R.; Zhang, Y., *J. Chem. Eng. Data*, **2011**, *56*, 4407.
110. Hermannsdörfer, J.; Kempe, R., *Chem. Eur. J.*, **2011**, *17*, 8071.
111. Yuan, B.; Pan, Y.; Li, Y.; Yin, B.; Jiang, H., *Angew. Chem., Int. Ed.*, **2010**, *49*, 4054.
112. Aijaz, A.; Karkamkov, A.; Choi, Y. J.; Tsumori, N.; Rönnebro, E.; Autrey, T.; Shioyama, H.; Xu, Q., *J. Am. Chem. Soc.*, **2012**, *134*, 13926.
113. Zahmakiran, M., *Dalton Trans.*, **2012**, *41*, 12690.
114. Ke, F.; Zhu, J.; Qui, L-G.; Jiang, X., *Chem. Commun.*, **2013**, *49*, 1267.
115. Zhu, Q-L.; Li, J.; Xu, Q., *J. Am. Chem. Soc.*, **2013**, *135*, 10210.
116. Houk, R. J. T.; Jacobs, B. W.; Gabaly, F. E.; Chang, N. N.; Talin, A. A.; Graham, D. D.; House, S. D.; Robertson, I. M.; Allendorf, M. D., *Nano Lett.*, **2009**, *9*, 3413.
117. He, J.; Zha, M.; Cui, J.; Zeller, M.; Hunter, A. D.; Yun, S-M.; Lee, S-T.; Xu, Z., *J. Am. Chem. Soc.*, **2013**, *135*, 7807.
118. Bagheri, A.; Taghizadeh, M.; Behbahani, M.; Asgharinezhad, A. A.; Salarian, M.; Dehghani, A.; Ebrahimzadeh, H.; Amini, M. M., *Talanta*, **2012**, *99*, 132.
119. Zha, M.; Liu, J.; Wong, Y-L.; Xu, Z., *J. Mater. Chem. A*, **2015**, *3*, 3928.
120. Xiao, C.; Goh, T. W.; Brashler, K.; Pei, Y.; Guo, Z.; Huang, W., *J. Phys. Chem. B*, **2014**, *118*, 14168.
121. Guo, Z.; Kobayashi, T.; Wang, L-L.; Goh, T. W.; Xiao, C.; Caporini, M. A.; Rosay, M.; Johnson, D. D.; Pruski, M.; Huang, W., *Chem. Eur. J.*, **2014**, *20*, 16308.
122. Boss, C. B.; Fredeen, K. J., *Concept, Instrumentation and Techniques in Inductively Coupled Plasma Optical Emission Spectrometry*, **1997**, 2nd edition, Perkin-Elmer.

123. Hou, X.; Jones, B. T., *Encyclopedia of Analytical Chemistry*, **2000**, 9468.
124. Dolomanov, O. V.; Bourhis, L. J.; Gildea, R. J.; Howard, J. A. K.; Puschmann, H., *J. Appl. Cryst.*, **2009**, *42*, 339.
125. Sheldrick, G. M., *Acta Cryst.*, **2008**, *A64*, 112.
126. Spek, A. L., *Acta Cryst*., **2015**, *C71*, 9.

Chapter 2

Water-Stable Zr(IV) MOFs for PGM Anion Extraction

2.1 Introduction

In recent years Zr(IV) based metal-organic frameworks have garnered much attention largely as a result of their high chemical and thermal stability as well as being stable upon exposure to moisture and water.[1] The first Zr(IV) MOFs, UiO-66, UiO-67 and UiO-68, were reported by Lillerud *et al.* in 2008, with structures consisting of linear dicarboxylate linkers in combination with a Zr_6 cluster (Figure 2.1).[2]

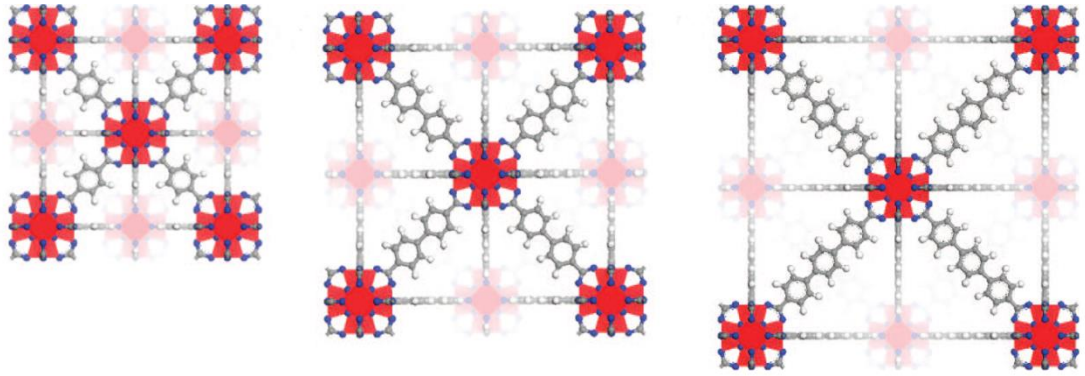


Figure 2.1. Structures of UiO-66 (left), UiO-67 (centre) and UiO-68 (right). Reproduced from reference 2.

It is this Zr_6 cluster that is responsible for the exceptional stability of Zr(IV) MOFs. The cluster contains an inner core of $Zr_6O_4(OH)_4$ in which the Zr(IV) ions are arranged octahedrally with alternating μ_3-O and μ_3-OH groups capping the triangular faces of this octahedron. With the linker taken into consideration, this core becomes a $\{Zr_6O_4(OH)_4(CO_2)_{12}\}$ cluster in which all of the polyhedron edges are bridged by -CO_2 groups from the linker with each Zr(IV) ion coordinated to eight oxygen atoms in a square antiprismatic geometry (Figure 2.2).

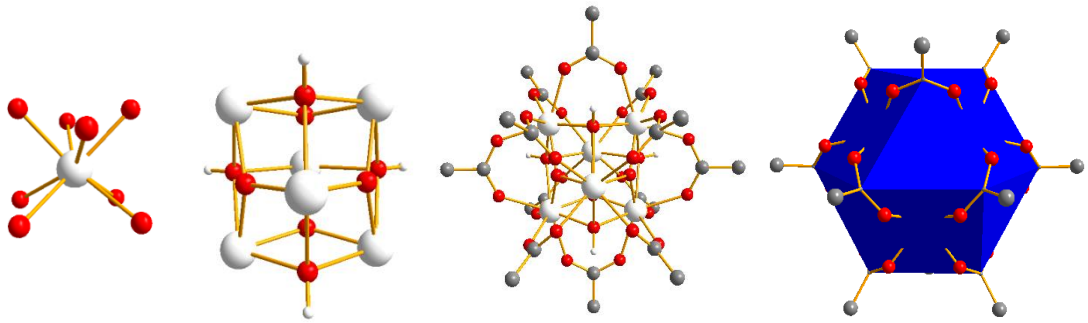


Figure 2.2. Left to right – Square antiprismatic geometry around a Zr(IV) ion, the inner $Zr_6O_4(OH)_4$ cluster, the $Zr_6O_4(OH)_4(CO_2)_{12}$ cluster with bound linkers, the alternating triangular and square faces of the cluster as determined by the points of extension of the linker. Reproduced from reference 2.

While gas adsorption in Zr(IV) MOFs has been studied, the lack of open metal sites inhibits their effectiveness for such applications. However, their robust nature has led to much work in areas previously unexplored with less stable MOFs. For example, in 2014 Yaghi and co-workers reported the water adsorption properties of a series of Zr(IV) MOFs for applications such as dehumidification, thermal batteries and delivery of drinking water (Figure 2.3).[3]

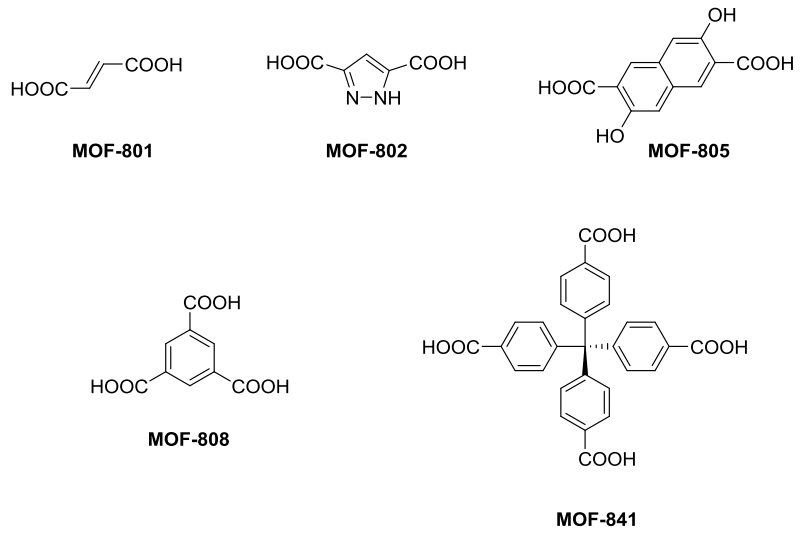


Figure 2.3. Structures of the linkers and the corresponding MOF nomenclature used by Yaghi *et al.* in Zr(IV) MOFs for adsorption of water.[3]

Each framework retained its phase and crystallinity after water adsorption and demonstrated almost constant uptake capacities over five cycles with a facile and low energy cost of regenerating the material. MOF-801 exhibited an excellent low pressure capacity for H_2O of 22.5 wt% at 0.1 bar and MOF-841 showed an uptake of 44 wt% at 0.3 bar.[3] The authors suggest that these characteristics make MOF-801 a suitable material for use in advanced thermal batteries and that MOF-841 may be used for storage and release of water in remote desert areas.

In addition to water stability, Zr(IV) MOFs have recently been used for the destruction of nerve agent and mustard gas simulants.[4-7] Most notably, in 2015, Farha and co-workers reported the use of NU-1000 (Figure 2.4) for the degradation of the nerve agent simulant dimethyl-4-nitrophenyl phosphate (DMNP) and the highly toxic chemical warfare agent Soman (O-pinacolyl methylphosphonofluoridate).[4]

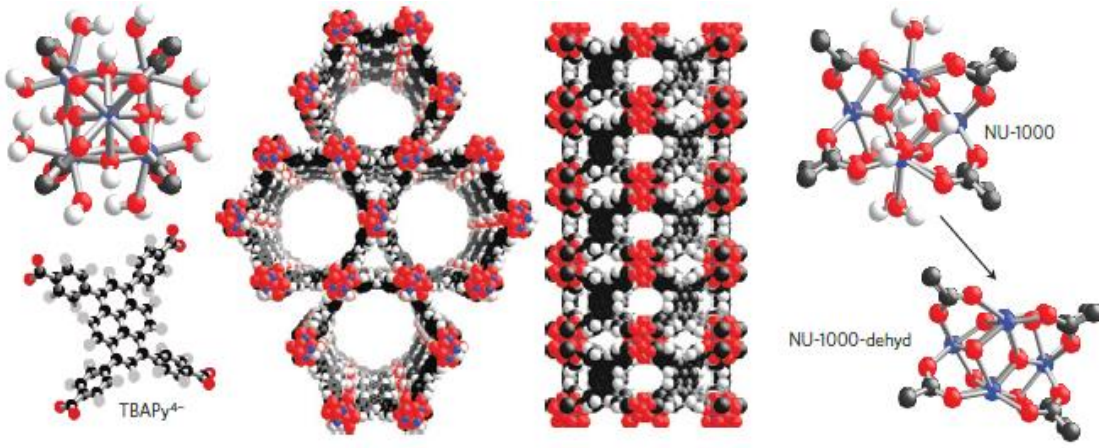


Figure 2.4. View of the linker (left), pore structure (centre) and metal nodes (right) present in NU-1000. Reproduced from reference 4.

NU-1000 is composed of eight-connected $\{Zr_6(\mu_3\text{-}O)_4(\mu_3\text{-}OH)_4(H_2O)_4(OH)_4\}$ nodes bridged by 4-connected pyrene-containing linkers. This creates very large channels of 31 Å in diameter within the structure with terminal hydroxo and aquo ligands directed into the channel. Upon heating under vacuum, these ligands are removed to give open Zr metal sites in NU-1000-dehyd, (Figure 2.4). The degradation of DMNP *via* the cleavage of a P-O bond was carried out in an aqueous buffered solution of N-ethylmorpholine and monitored by ^{31}P NMR and UV-vis spectroscopy. The degradation of Soman was also followed by ^{31}P NMR. NU-1000 was found to exhibit remarkable activity for the destruction of both compounds, with a $T_{1/2}$ of 15 minutes for the hydrolysis of DNMP and a $T_{1/2}$ of just 1.5 minutes when using NU-1000-dehyd.[4] Similarly the $T_{1/2}$ for Soman degradation was 36 minutes using NU-1000 and 3 minutes using NU-1000-dehyd, comparable to the best reported solid state materials used for nerve agent destruction.[8,9]

Another relatively new application for Zr(IV) MOFs is the sensing and adsorption of small molecules from solution.[10-16] In 2013, Serre *et al.* reported the encapsulation of caffeine (amphiphilic) and the analgesic ibuprofen (hydrophobic) in a series of UiO-

66-X MOFs, where X denotes a functional group.[10] Both drugs were encapsulated in the frameworks using an impregnation method with 10 mg L^{-1} of caffeine in H_2O (drug:MOF ratio of 2:1) and 20 mg L^{-1} of ibuprofen in EtOH (drug:MOF ratio of 4:1). After soaking in the solution for 24 hours, the MOFs were dried under vacuum and the quantity of drug adsorbed by each framework was calculated using a combination of HPLC, elemental analysis and TGA.[10]

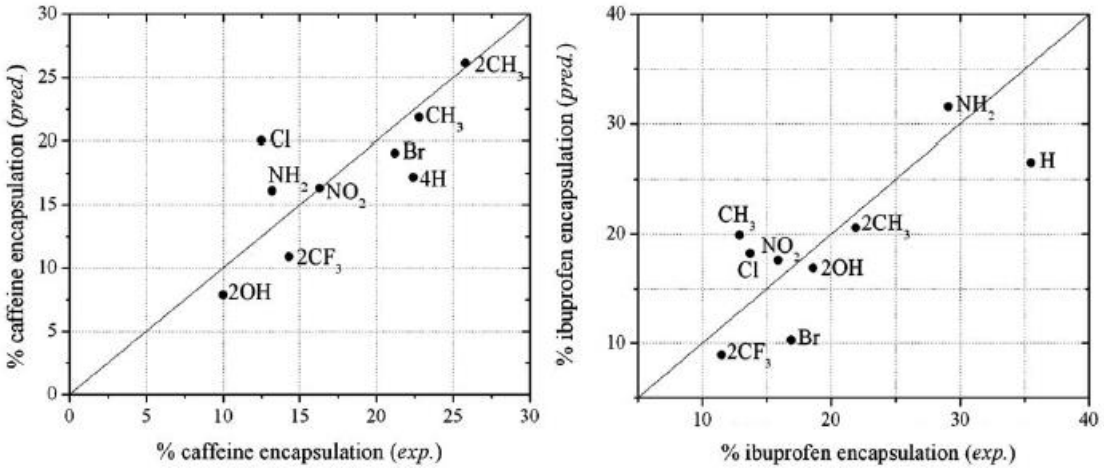


Figure 2.5. Predicted and experimental caffeine and ibuprofen adsorption in a series of functionalised Zr MOFs. Reproduced from reference 10.

Experimentally, caffeine encapsulation was shown to be greatest with lipophilic CH_3 groups in the framework or with a polarised Br group, which is in reasonable agreement with the results predicted using a quantitative structure-activity relationship (QSAR) (Figure 2.5). This was attributed to the favourable interactions of the frameworks with the caffeine molecules rather than the solvent water molecules which were adsorbed preferentially in the more hydrophilic MOFs, leading to a lower caffeine uptake. However, even the lowest uptake of 10.0% in UiO-66-OH is greater than those generally observed for polymer-based delivery systems. Ibuprofen adsorption was much greater in UiO-66 and UiO-66-NH_2 than

with any other functional groups, attributed largely to the greater BET surface area of these frameworks. Figure 2.5 shows clearly that the uptake into the MOFs with larger functional groups such as -CF_3, -Br, -NO_2 and –Cl is poor.[10]

Of particular interest to the work presented in this Chapter is the use of Zr(IV) MOFs for encapsulation of metal species from solution. In 2013, Lin and co-workers reported the use of post-synthetically modified UiO-68-NH_2 frameworks containing phosphorylurea groups for the removal of uranium from artificial seawater.[17] The three MOFs used were the parent UiO-68-NH_2 material, MOF **1**, a diethoxyphosphorylurea functionalised material, MOF **2**, and a dihydroxyphosphorylurea functionalised material, MOF **3** (Figure 2.6).

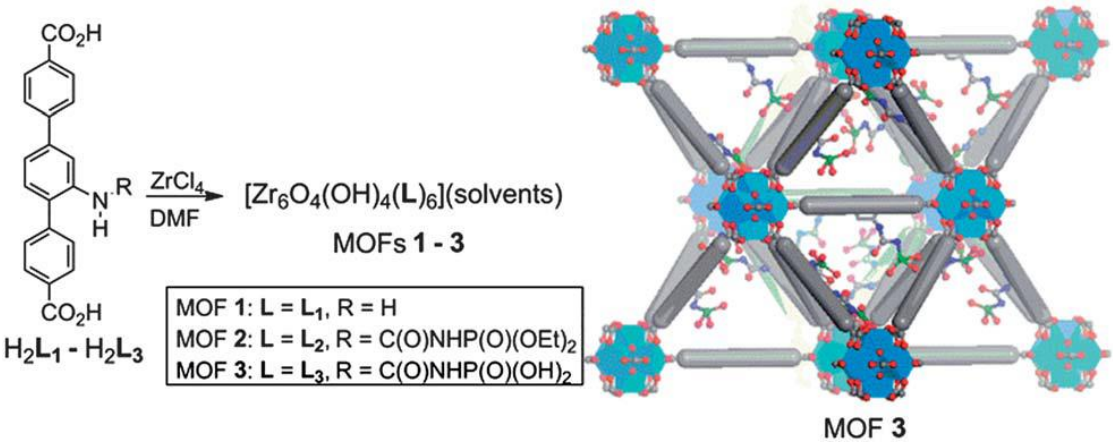


Figure 2.6. The structure of UiO-68-NH_2 derivatives used for the removal of UO^{2+} from solution. Reproduced from reference 17.

Uranium extraction experiments were carried out in both water and simulated seawater containing NaCl, Na_2SO_4, KCl, $NaHCO_3$, $MgCl_2{\cdot}6H_2O$ and $CaCl_2$.[18,19] In each extraction, 10 mg of MOF was added to 10 ml of a 100 ppm solution containing uranyl acetate, ($UO_2(OAc)_2{\cdot}2H_2O$). After shaking for one hour and removing the sorbent, the uranium concentration of the solution was analysed by UV-Vis

spectroscopy and ICP-MS. Each MOF was then washed with HCl to investigate the ease of removal of uranium from the material post-extraction. While MOF **1** was found to adsorb no UO_2^{2+} under these conditions, both MOFs **2** and **3** removed almost all of the uranium from solution. The highest uptake capacity of MOF **2** was 217 mg g^{-1} in water and 188 mg g^{-1} in artificial seawater in comparison to 54 mg g^{-1} in the Amidoxime fibres used as a comparison.[17] The uptake of 217 mg g^{-1} in MOF **2** corresponded to approximately one UO_2^{2+} ion bound per two ligands. Whilst washing with 1 M HCl removed a significant quantity of the uranium from the pores of MOFs **2** and **3**, a reasonable proportion remained in the pores, suggesting a strong interaction between the metal ions and the frameworks. This work represented the first use of a MOF for the removal of radionuclides from aqueous media.[17]

In 2015 Zhong *et al.* reported the selective uptake of Cu^{2+} over Ni^{2+} from an aqueous solution using a UiO-66-X series in which X = H, Br, NH_2, $NH(CH_2)_2$-SO_3H, $(COOH)_2$.[20] In each experiment, 10 mg of MOF were added to a 10 ml solution containing a 1:1 mass ratio of Cu:Ni which was spun at 130 rpm for 10 hours. After removal of the sorbent, the concentration of each metal in solution was determined by ICP-OES. This determined that UiO-66-$(COOH)_2$ was the most effective framework for the separation of Cu^{2+} from Ni^{2+}, with the higher uptake of Cu^{2+} ascribed to the Jahn-Teller effect enhancing the coordination ability of Cu^{2+}. The calculated selectivity of 27:1 for Cu:Ni makes UiO-66-$(COOH)_2$ the best material to date for this separation which is of great importance for the recycling of transition metal ions.[20]

The encapsulation of platinum group metals (PGMs) by Zr(IV) MOFs has been reported, usually in the form of Pd or Pt nanoparticles for catalysis applications.[21-24] However, of greater relevance to the work in this Chapter is the uptake of $PtCl_4^{2-}$ and

$CuCl_2$ from aqueous solutions using UiO-66 derivatives reported by Huang *et al.* in 2014.[15,16] This involved the addition of 100 mg of activated MOF to 12 ml of H_2O to which K_2PtCl_4 or $CuCl_2$ were added. A combination of ^{15}N DNP SS-NMR spectroscopy, ICP-OES and XAS analysis along with DFT was used to calculate the uptake of metal ions and determine the coordination of the Pt(II) species in the MOF cavities.[16] An efficiency of 70-100% for Pt uptake into UiO-66-NH_2 was reported with just a 6% uptake of Cu. In contrast, UiO-66 exhibited an 18% uptake of Pt.

^{15}N DNP SS-NMR spectroscopy of Pt-doped UiO-66-NH_2 clearly showed the growth of a peak associated with the interaction between the NH_2 groups of UiO-66-NH_2 and the encapsulated Pt (Figure 2.7).[16]

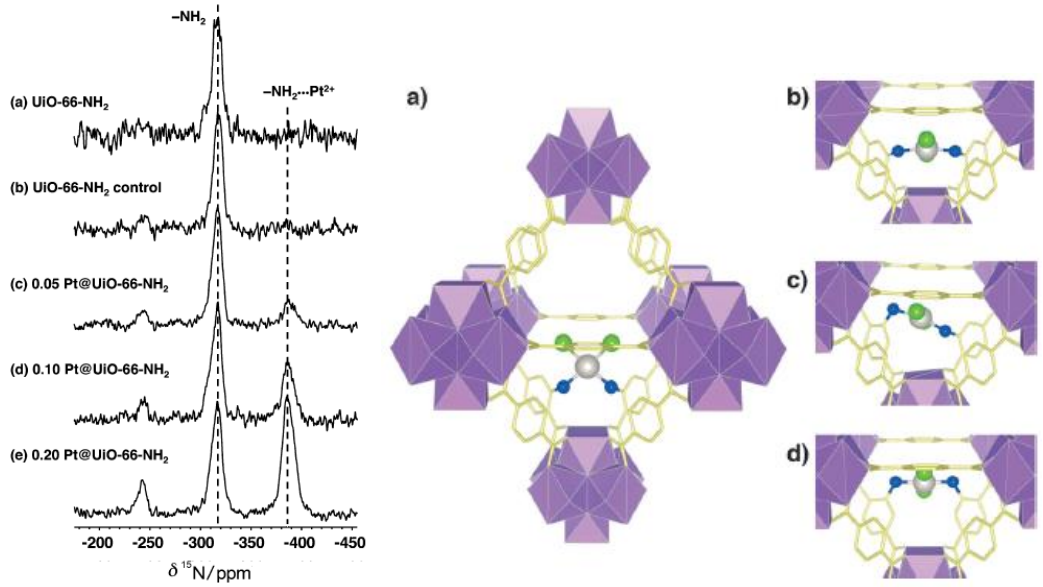


Figure 2.7. ^{15}N DNP SS-NMR spectra of Pt-doped samples of UiO-66-NH_2 (left) and the stable configurations of $PtCl_2$ encapsulated in the MOF (right), a) – (2,2)-*cis*, b) (2,2)-*trans*, c) (2,3)-*trans*, d) (3,3)-*trans*. Reproduced from reference 16.

Furthermore, EXAFS data proved that the encapsulated species was not a $PtCl_4^{2-}$ ion but a neutral $PtCl_2$ species. DFT modelling suggested that two NH_2 groups were

bound to each $PtCl_2$ with a (3,3)-*trans* configuration being the most stable, although the energy difference between this and the (2,2)-*cis* and (2,3)-*trans* configurations was small. This modelling fitted the experimental ICP-OES analysis of the doped UiO-66-NH_2 materials which gave a ratio of between 1.9 and 2.5 NH_2 groups per encapsulated $PtCl_2$. To the best of our knowledge this is the first known literature example of a metal-organic framework used for the extraction of a PGM chloride from an aqueous solution.

2.2 Aims of this Work

The aims of this work were to investigate the extraction of PGM anions from aqueous and acidic (HCl) solutions, using metal-organic frameworks, with particular focus on the hexachloroplatinate anion, $PtCl_6^{2-}$. As Zr(IV) MOFs are well known to be highly chemically stable and have been used for similar applications, as described above, Zr(IV) was our metal of choice when considering the design of MOFs for PGM extraction. Also of key concern was the presence of an amine or amide functional group to interact with the chloride groups of the PGM.[25,26] These protonatable hydrogen bond donors are capable of forming ion pairs with the $PtCl_6^{2-}$ anion and encapsulating it within the framework, as shown in previous work in the Schröder group.[25,26] The general process carried out in the course of this work is outlined in Figure 2.8.

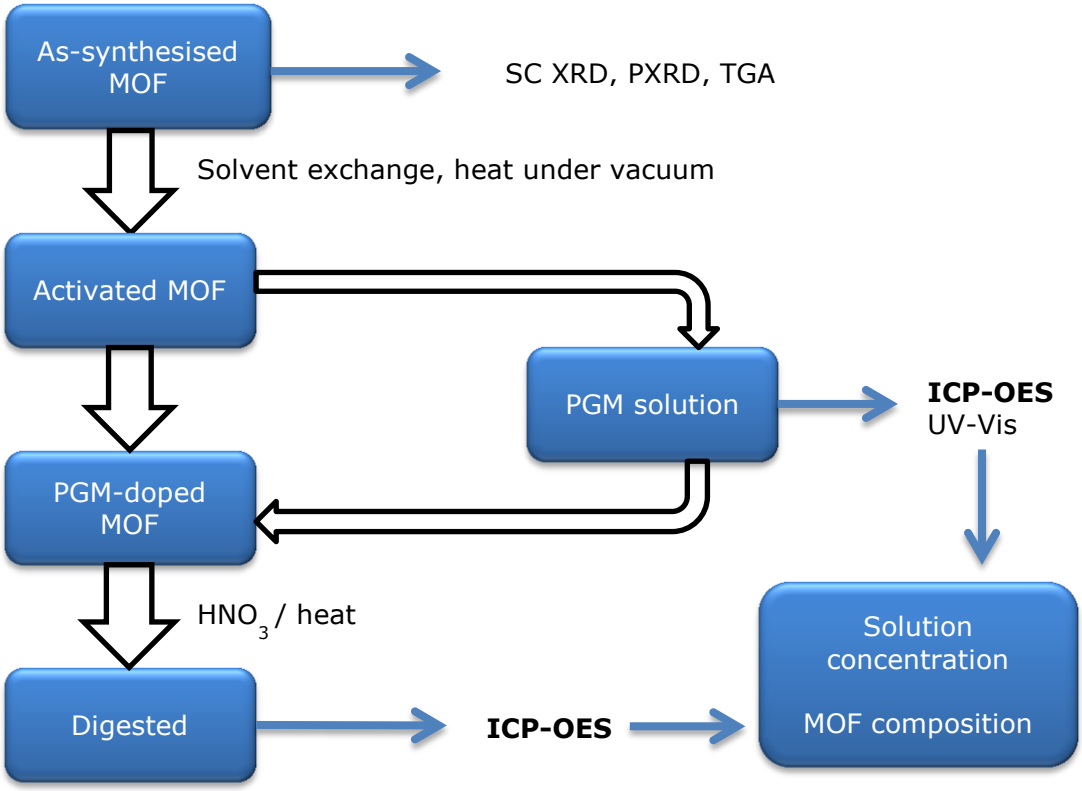


Figure 2.8. A scheme showing the steps taken from MOF synthesis to the encapsulation of PGM species and subsequent analyses.

The first step is to design and synthesise the desired MOF and to fully characterise it using single crystal X-ray diffraction (SCXRD), powder X-ray diffraction (PXRD) and thermogravimetric analysis (TGA). Having elucidated the structure and shown the bulk material to be phase pure and thermally stable, the synthesis solvent is replaced with a more volatile solvent (usually acetone) by exchanging the solvent several times over the course of 5 days. The material is then "activated" by heating under vacuum to remove all solvent and guest molecules from the pores. Once activated, the MOF is placed into the PGM-containing solution and left at room temperature without stirring. It should be noted that test extraction experiments were carried out with stirring, however this lead to the dissolution of the MOF materials. As the extraction is taking place, the concentration of the solution can be monitored by ICP-OES and UV-Vis spectroscopy. Once the extraction is complete, the MOF is

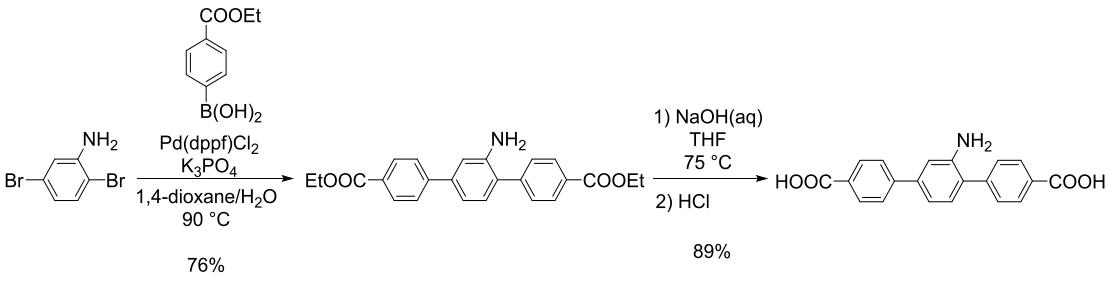
removed from the solution, dried and digested in HNO_3 and analysed by ICP-OES to give the ratio of encapsulated metal (Pt) to framework metal (Zr).

2.3 Results and Discussion

2.3.1 UiO-68-NH_2

2.3.1.1 Synthesis

In addition to chemical stability and an amine functional group, the desired features when selecting a MOF for aqueous extraction of precious metals were a high BET surface area and large cavities within the framework in which to encapsulate the metal anions. For these reasons, UiO-68-NH_2 was chosen as a suitable material with which to carry out these extractions.[27] The amine functionalised triphenyl linker of UiO-68-NH_2, H_2L^1 (Scheme 2.1), was synthesised *via* a Suzuki cross-coupling reaction between 2,5-dibromoaniline and (4-(ethoxycarbonyl)phenyl)boronic acid. These reagents were heated at 90 °C with Pd(dppf)Cl_2 and K_3PO_4 in a mixture of 1,4-dioxane/DMF in an argon atmosphere for 24 hours. Following extraction into $CHCl_3$ and purification through a plug of silica gel, the diester product was obtained in good yield (76%). This ester was then hydrolysed in NaOH(aq), acidified to pH~1 with 37% HCl and recrystallised from hot DMF to give the pure ligand H_2L^1.



Scheme 2.1. The synthetic route to H_2L^1.

H_2L^1 was then reacted with $ZrCl_4$ in DMF at 120 °C using PhCOOH as a modulator to give colourless octahedral crystals of UiO-68-NH_2. The use of PhCOOH as a competitive modulator is essential as the oxophilic nature of Zr(IV) makes reversible self-assembly very difficult and may lead to the formation of many unwanted side products or amorphous phases without modulation. Single crystal diffraction on the in-house GV1000 diffractometers and at beamline I19 of Diamond Light Source was too weak to afford the single crystal structure. However, the powder X-ray diffractogram (Figure 2.9) of the as-synthesised material was successfully indexed to the same unit cell as that reported by Behrens *et al.* (*F*-43*m*; *a* = 32.7767(5) Å).[27]

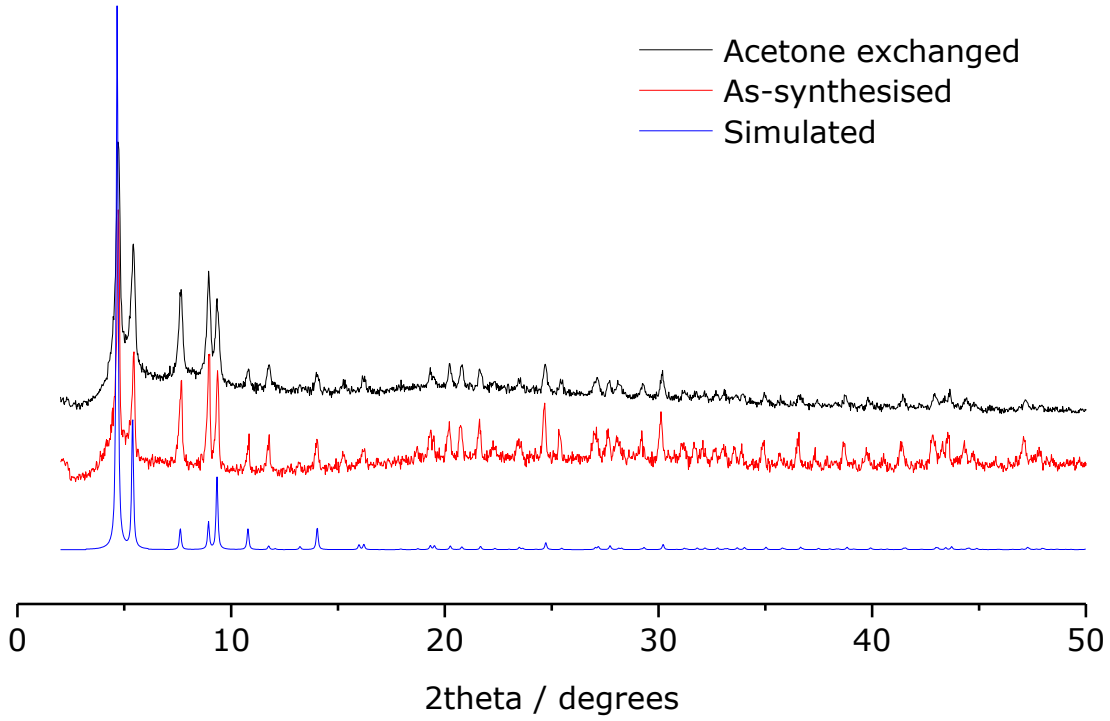


Figure 2.9. PXRD patterns of simulated, as-synthesised and acetone exchanged UiO-68-NH_2.

2.3.1.2 Structural Analysis

The structure of UiO-68-NH_2 consists of ZrO_8 clusters each connected to 12 separate dicarboxylate linkers to give a 3D structure. The framework consists of two types of cage – one octahedral and one tetrahedral (Figure 2.10). The cif file from which Figure 2.10 was constructed was taken from the paper in which the structure of UiO-68-NH_2 is originally reported.[27]

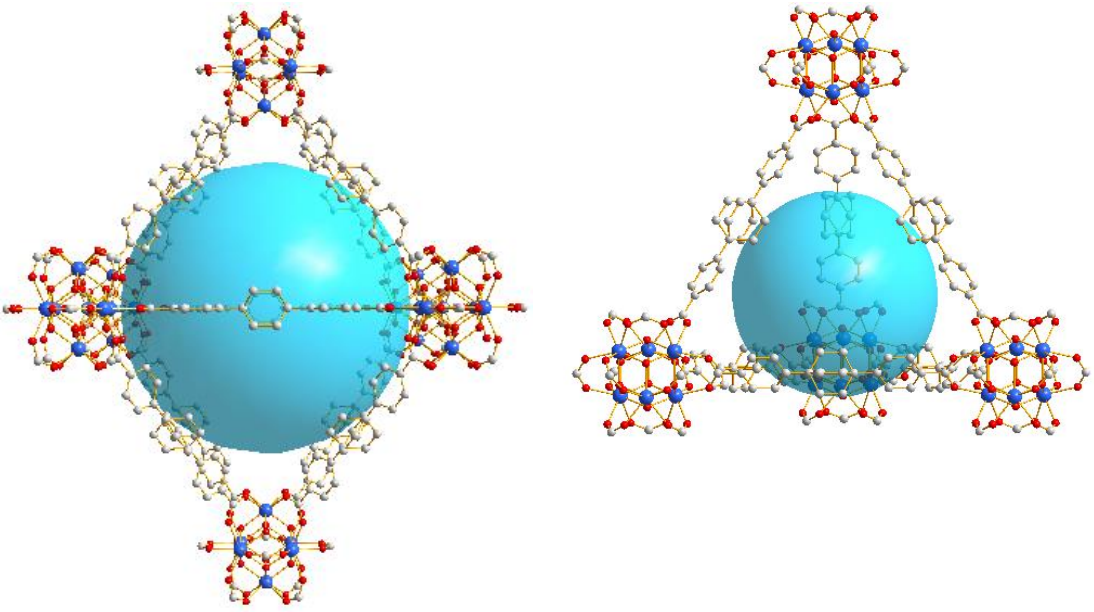


Figure 2.10. View of the octahedral and tetrahedral cavities present in UiO-68-NH_2. For clarity the NH_2 groups have been removed from the structure as they exhibit 8-fold positional disorder.

The larger octahedral cavity is ~20 Å in diameter with accessible windows of 10 Å. The smaller tetrahedral cage is 13.5 Å in diameter with accessible pore windows of 7 Å. The cavity diameters were calculated by fitting a sphere from the centre of the cage to its walls, taking into account van der Waals radii and the window diameters were estimated from the largest sphere able to pass through the window. The diameter of a $PtCl_6^{2-}$ anion has been reported as 4.6 Å,[28] meaning that it should

comfortably pass through the cavity windows in UiO-68-NH_2. The central phenyl ring of the linker exhibits two-fold positional disorder with a torsional angle of 48° between each conformation and the planar carboxylate groups. The amine moieties are consequently disordered over 8 positions and have therefore been removed from the structure shown in Figure 2.10 for clarity.

2.3.1.3 Thermal Stability and N_2 Sorption

After synthesis, samples of UiO-68-NH_2 were washed with fresh DMF to remove any benzoic acid or unreacted linker. The crystals were then kept in acetone which was replaced twice a day over the course of five days. To confirm that the material exhibited permanent porosity, the acetone exchanged sample was heated under vacuum at 120 °C for 16 hours and a nitrogen isotherm was measured from 0-1 bar at 77 K. This showed a reversible type-I sorption profile with a total uptake of 697 cc g^{-1} at 1 bar (Figure 2.11).

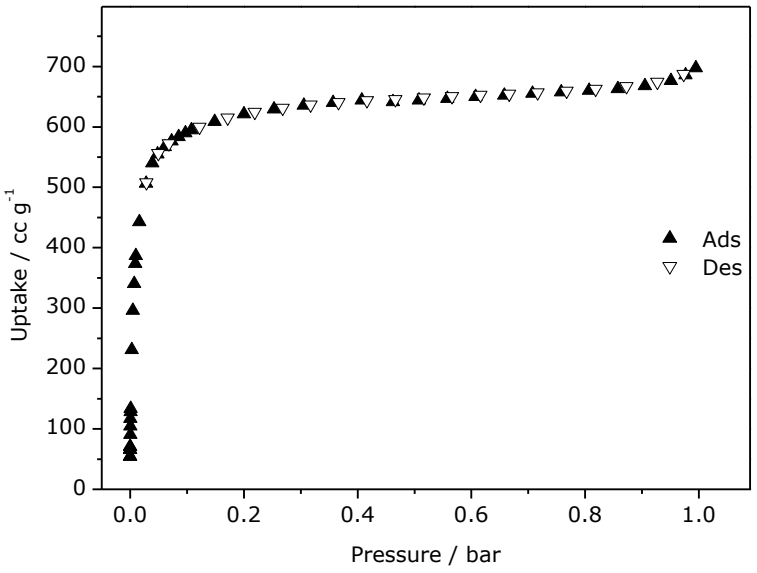


Figure 2.11. N_2 isotherm for UiO-68-NH_2 at 77 K from 0-1 bar after acetone exchange and sample activation.

The estimated Braun-Emmett-Teller (BET) surface area of desolvated UiO-68-NH_2 as calculated from this isotherm was 2553 m^2 g^{-1} with a total pore volume of 1.01 cm^3 g^{-1}.

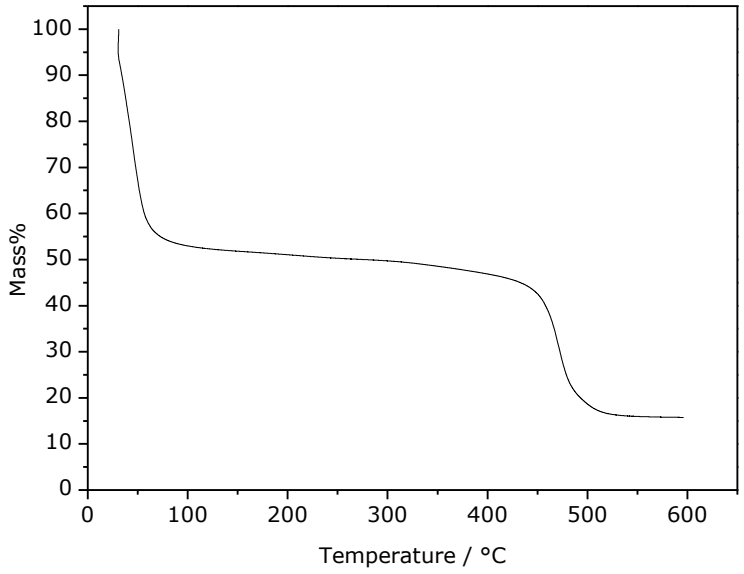


Figure 2.12. TGA trace of acetone exchanged UiO-68-NH_2 in air.

Thermogravimetric analysis of the acetone exchanged sample in air showed solvent loss below 100 °C, with the material then stable up to ~450 °C, beyond which point a mass loss corresponding to framework decomposition is observed (Figure 2.12). This is consistent with previous reports on the thermal stability of UiO-68-NH_2.[17]

2.3.1.4 Aqueous Extraction of K_2PtCl_6

As platinum is the most abundant and widely used PGM along with palladium,[29] the initial experiments focused on the extraction of Pt(IV), in the form of $PtCl_6^{2-}$, from aqueous solutions. This involved the addition of 20 mg of activated UiO-68-NH_2 to 100 ml solutions of varying Pt concentration and monitoring changes in this concentration over time. As ppm (mg L^{-1}) is both a common unit of measure for

PGM concentration in industrial applications and the concentration measurement calculated by the ICP spectrometer, all solutions concentrations were measured in ppm rather than in mol dm^{-3}. To determine the concentration as a function of time, 1 ml aliquots of the Pt solution were removed periodically and diluted with 9 ml of ultrapure de-ionised water. This solution was then analysed by ICP-OES and the concentration was compared with that of the original solution, from which a % of extraction can be calculated.

Errors resulting from the use of pipettes, volumetric flasks, measuring cylinders and from measuring the mass of MOF and PGM were taken into account and a propagation of uncertainty was calculated as the square root of the sum of the squared errors. As the % uptake was calculated using eqn (1) shown below, the uncertainty of the % uptake was calculated by summing the errors of each part (eqn (2)), where *Ei* and *Ef* are the errors associated with the initial and final concentrations respectively.

$$\%\, uptake = \frac{initial\ conc. - final\ conc.}{initial\ conc.} * 100 \qquad \textbf{eqn(1)}$$

$$\%\, uptake\ uncertainty = Ei + Ef + Ei \qquad \textbf{eqn(2)}$$

Furthermore, the periodic removal of 1 ml aliquots leads to additional uncertainty as the % uptake is overestimated in each case by x %, where x is the number of aliquots removed from the 100 ml solution. This is accounted for in each plot and results in an asymmetric error.

The first extraction was carried out using 100 ml of a 100 ppm solution of K_2PtCl_6 in H_2O and 20 mg UiO-68-NH_2. This corresponds to a ratio of 0.88 NH_2 groups per

$PtCl_6^{2-}$ anion, where the molecular mass of UiO-68-NH_2 is taken to be that of one complete linker plus 1/6th of a Zr_6O_8 cluster ($Zr_1C_{20}H_{13}N_1O_{16/3}$ = 443.56 g mol^{-1}). The MOF exhibits fast initial uptake of the PGM (28% extraction from solution after 3 hours) which begins to plateau at around 24 hours, leading to a total extraction of 51% after 120 hours (Figure 2.13).

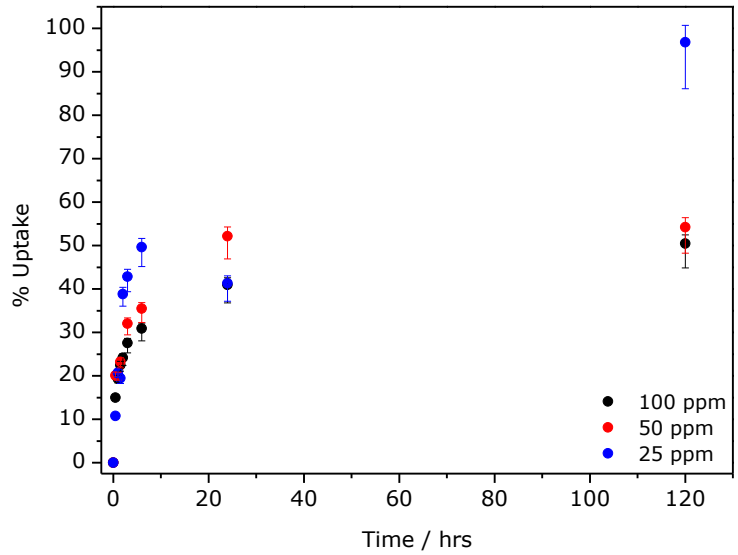


Figure 2.13. Extraction of K_2PtCl_6 from 100, 50 and 25 ppm Pt solutions using UiO-68-NH_2.

This uptake corresponds to 1.75 NH_2 moieties per $PtCl_6^{2-}$ anion. In comparison to the 2 NH_2 groups per $PtCl_4^{2-}$ required in UiO-66-NH_2, as reported by Huang *et al.*, our result suggests that UiO-68-NH_2 is potentially a very effective and efficient sorbent material for $PtCl_6^{2-}$.[16]

These conditions were then repeated using a 50 ppm solution of K_2PtCl_6, corresponding to a ratio of 1.76 NH_2 groups per $PtCl_6^{2-}$ anion. Interestingly, the total extraction has only increased from 51% to 54% and whilst the initial uptake once again accounts for the majority of the extraction, the uptake after 3 hours has only

increased from 28% to 32%. The ratio of NH_2:$PtCl_6^{2-}$ in the material calculated from the 54% extraction is 3.23:1.

Finally, these conditions were repeated with a 25 ppm solution of K_2PtCl_6, corresponding to a ratio of 3.52 NH_2 groups per $PtCl_6^{2-}$ anion. Figure 2.13 shows that the 20 mg sample of UiO-68-NH_2 removed 97% of the Pt from the solution by 120 hours and the uptake after 3 hours had increased from 32% in the 50 ppm case to 43%. The total uptake of 97% corresponds to 3.57 NH_2 groups per $PtCl_6^{2-}$ anion. This shows clearly that the number of $PtCl_6^{2-}$ anions extracted per NH_2 decreases as the concentration of the initial solution decreases. This is most likely to be a result of an equilibrium between the solvated and encapsulated anions, thus obeying Le Châtelier's principle.

In addition to determining solution concentration by ICP-OES, UV-vis spectroscopy was also employed (Figure 2.14) to monitor the change in the intensity of the bands associated with $PtCl_6^{2-}$ from the initial solution to the final solution (after 120 hours). This was carried out for the three cases described previously (100, 50 and 25 ppm Pt solutions) and shows clearly that in each instance there is a reduction in intensity of the $PtCl_6^{2-}$ bands during the experiment. In accordance with the Beer-Lambert law, $A = \varepsilon lc$, this is directly proportional to a reduction in solution concentration (where A represents absorbance, ε is the molar absorption coefficient, l is path length and c is solution concentration). As there is more than one band associated with the $PtCl_6^{2-}$, the reduction in peak intensity is not uniform over the wavelength range shown in Figure 2.14. The intensity used for comparison between spectra was therefore averaged over a series of points at around 300 nm, a wavelength at which the bands do not overlap as significantly. The spectra showed 39%, 62% and 94% concentration reductions for the 100, 50 and 25 ppm solutions respectively

(compared to 51%, 54% and 97% reductions from ICP-OES analysis). While these results agree in trend with the ICP-OES data, the values vary significantly depending on the wavelength of the chosen points. As such, the ICP-OES results were deemed to be of greater reliability.

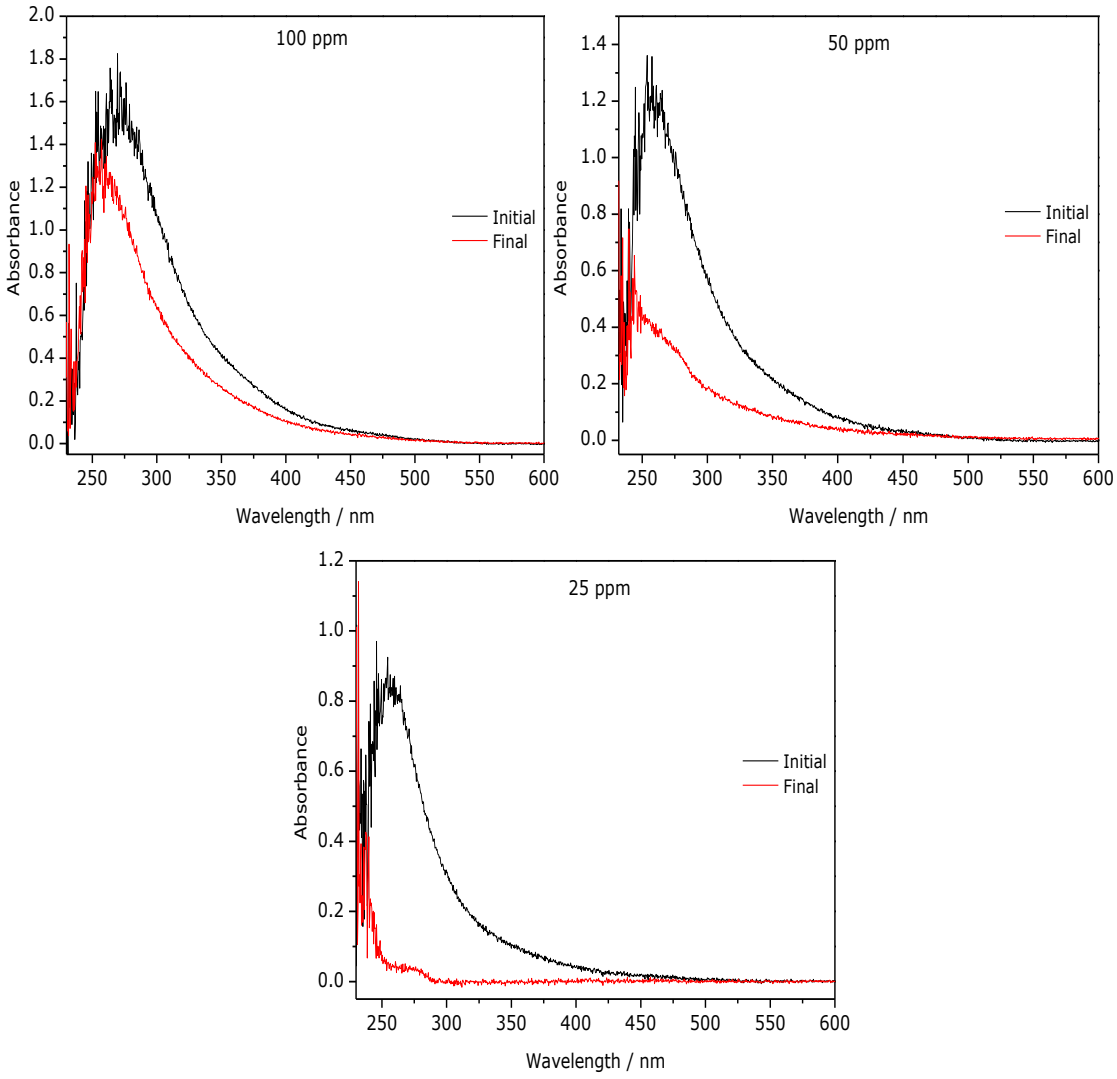


Figure 2.14. Initial and final UV-Vis spectra for 100 ppm (top left), 50 ppm (top right) and 25 ppm (bottom) solutions of $K_2PtCl_6^{2-}$ in H_2O.

Following each extraction, a small quantity (~5 mg) of the PGM-doped MOF material was digested by heating in 2 ml of 69% HNO_3 overnight at 70 °C. This was

then diluted with 10 ml of ultrapure de-ionised H_2O, filtered to remove undissolved linker and analysed by ICP-OES to determine the ratio of Pt to Zr in the sample. As the ratio of Zr:NH_2 in the framework is 1:1, the molar ratio of Pt:Zr calculated from the ICP-OES concentration is equal to the Pt:NH_2 ratio. The uptake of Pt determined from the earlier ICP-OES measurements is shown below in Table 2.1 along with the ratio of Pt:Zr expected from those results. For example, 51% of the 100 ppm Pt solution (0.02589 mmol) was removed using 20 mg (0.04509 mmol) of UiO-68-NH_2, giving an expected Pt:Zr ratio of 1:1.8. The "measured ratio" is the ratio determined from the ICP-OES analysis of the digested framework.

Table 2.1. Expected and measured ratios of Pt:Zr in UiO-68-NH_2 from extractions of $PtCl_6^{2-}$.

Initial conc / ppm	Uptake Pt / mmol	Zr / mmol	Expected Pt:Zr ratio	Measured Pt:Zr ratio
100	0.02589	0.04509	1:1.8	1:2.6
50	0.0139	0.04509	1:3.2	1:5.2
25	0.01241	0.04509	1:3.6	1:11.6

Analysis of the digested samples shows that the Pt content of the MOF is in agreement with the trend expected from the solution concentrations, *i.e.* Pt content decreases as the initial solution concentration decreases. However, in each case the measured Pt content is slightly lower than expected. This may be because the small quantity of MOF digested in HNO_3 was not representative of the bulk sample or possibly a proportion of the $PtCl_6^{2-}$ ions were still bound to the linker and were removed from the sample by filtration.

Additionally, extraction from a 10 ppm Pt solution was carried out with UiO-68-NH_2 (20 mg), as were a series of extractions from 25 ppm solutions using varying

quantities of MOF. The ICP-OES data for all UiO-68-NH_2 extractions are shown below in Figure 2.15 with each % uptake recorded after 120 hours.

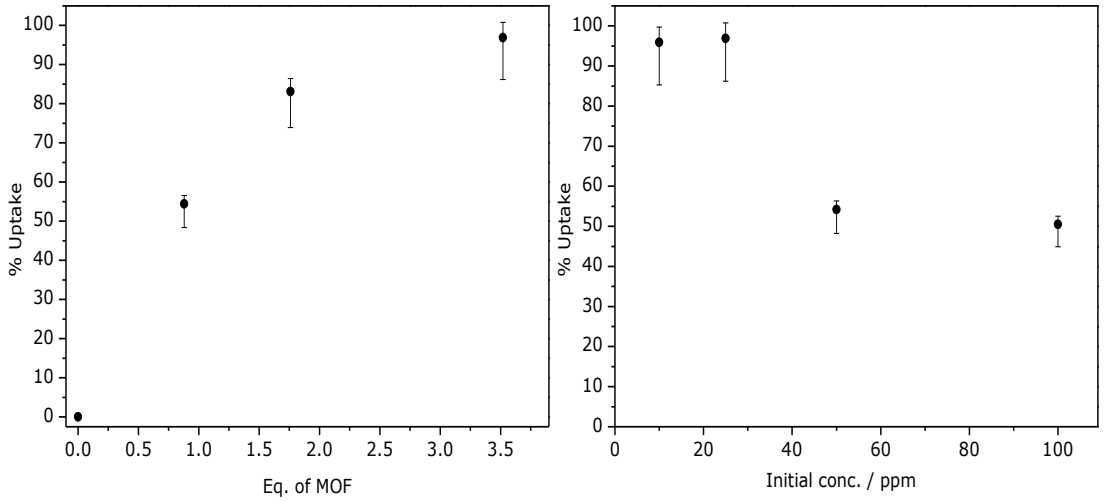


Figure 2.15. Extraction of 25 ppm of Pt from H_2O as a function of MOF quantity (left) and extraction into 20 mg of UiO-68-NH_2 as a function of initial Pt concentration (right).

This data shows that with just 0.88 eq. of MOF per $PtCl_6^{2-}$, 54% of the Pt is removed from the solution, rising to 83% with 1.76 eq. of material and ~100% with 3.52 eq. as described earlier. Clearly the uptake is increasing with the increase in MOF quantity, as expected. It also shows that the MOF exhibits very efficient $PtCl_6^{2-}$ uptake comparable with that of some of the most effective receptors used in solvent extraction, which require 3 equivalents to give ~85% extraction under similar conditions.[25] Lowering the initial solution concentration also leads to an increased extraction into UiO-68-NH_2.

As the MOF demonstrated very good capability for removal of $PtCl_6^{2-}$ from solution, a test extraction was undertaken using more industrially relevant conditions of $PtCl_6^{2-}$ in an acidic HCl solution. This was carried out with 20 mg of UiO-68-NH_2 in 100 ml of a 25 ppm K_2PtCl_6/2 M HCl solution from which 1 ml aliquots were removed

periodically to monitor the concentration. Unfortunately no measureable PGM uptake was observed and a powder X-ray diffractogram of the material post-extraction showed that it had become amorphous, strongly suggesting MOF decomposition in the acidic solution. As shown in Figure 2.16, the MOF retained its crystallinity and phase after extraction from H_2O but the material after extraction from HCl is clearly amorphous in character.

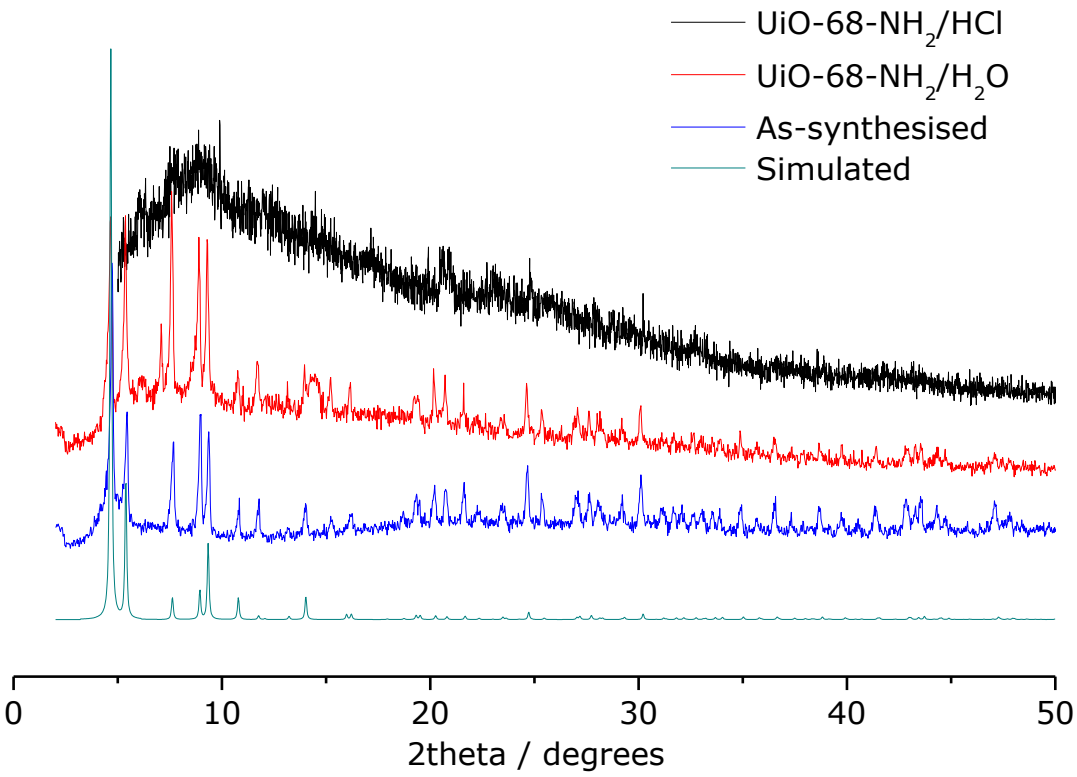


Figure 2.16. Powder X-ray diffractograms of UiO-68-NH_2 before and after extraction experiments.

2.3.2 UiO-66 and UiO-66-NH_2

2.3.2.1 Synthesis

This instability of UiO-68-NH_2 meant that a more chemically robust framework was required to carry out extractions from HCl. Therefore, the less porous but more stable UiO-66 and UiO-66-NH_2 MOFs were synthesised for this application. The non-

functionalised UiO-66 was used to provide an insight into the effect of the NH_2 group for $PtCl_6^{2-}$ binding. UiO-66-NH_2 was prepared by reacting 2-aminoterephthalic acid with $ZrCl_4$ in DMF in the presence of an excess of PhCOOH modulator. The product was washed with DMF and exchanged with fresh acetone several times over the course of five days before the material was activated at 120 °C under vacuum. UiO-66 was synthesised using an identical method with terephthalic acid as the linker in place of 2-aminoterephthalic acid.

2.3.2.2 Structural Analyses

Unlike UiO-68-NH_2, which features a ZrO_8 cluster, UiO-66 and UiO-66-NH_2 incorporate the hydroxylated $ZrO_4(OH)_4$ cluster described in the introduction to this Chapter. This cluster is linked to 12 terephthalic acid units to form a cubic close packed (CCP) structure with octahedral and tetrahedral cavities (Figure 2.17).

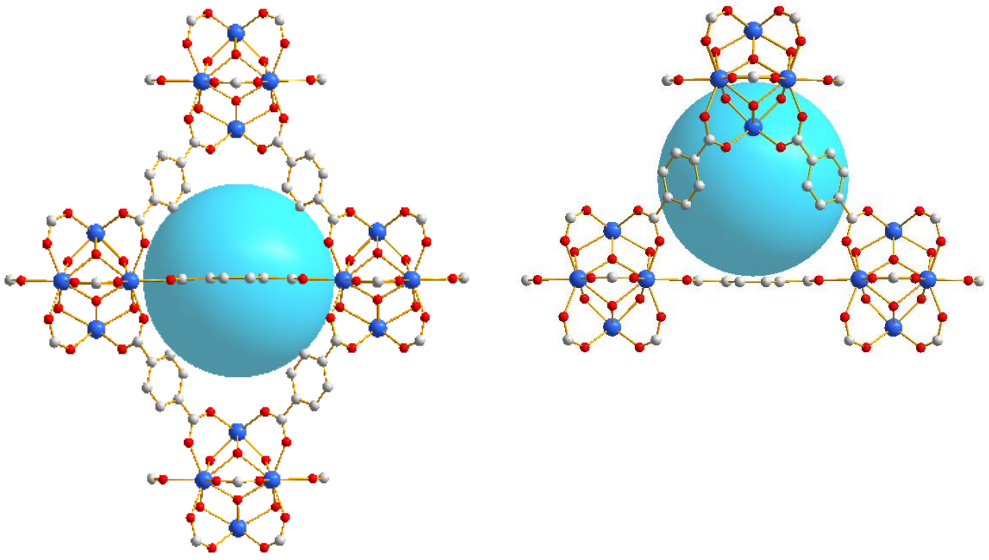


Figure 2.17. View of the octahedral and tetrahedral cavities observed in UiO-66.

Whereas in UiO-68-NH_2 the octahedral cage was much larger than the tetrahedral cage, the internal diameter of the two cages in UiO-66 is identical at 10.2 Å. The

windows to these cavities are 6.0 Å in diameter, which is large enough to incorporate a $PtCl_6^{2-}$ anion (4.6 Å).

2.3.2.3 Phase Purity, Thermal Stability and N_2 Sorption

Powder X-ray diffraction of both materials showed that they were phase pure and were indexed to the same unit cell as reported previously (*F-43m*; $a = b = c =$ 20.9784 Å).[30] The stability of UiO-66-NH_2 in acid was investigated by heating a small sample in 2 M HCl at 100 °C for 24 hours. The resulting powder pattern showed no phase change or loss of crystallinity (Figure 2.18), confirming that UiO-66-NH_2 is significantly more stable in acidic conditions than UiO-68-NH_2.

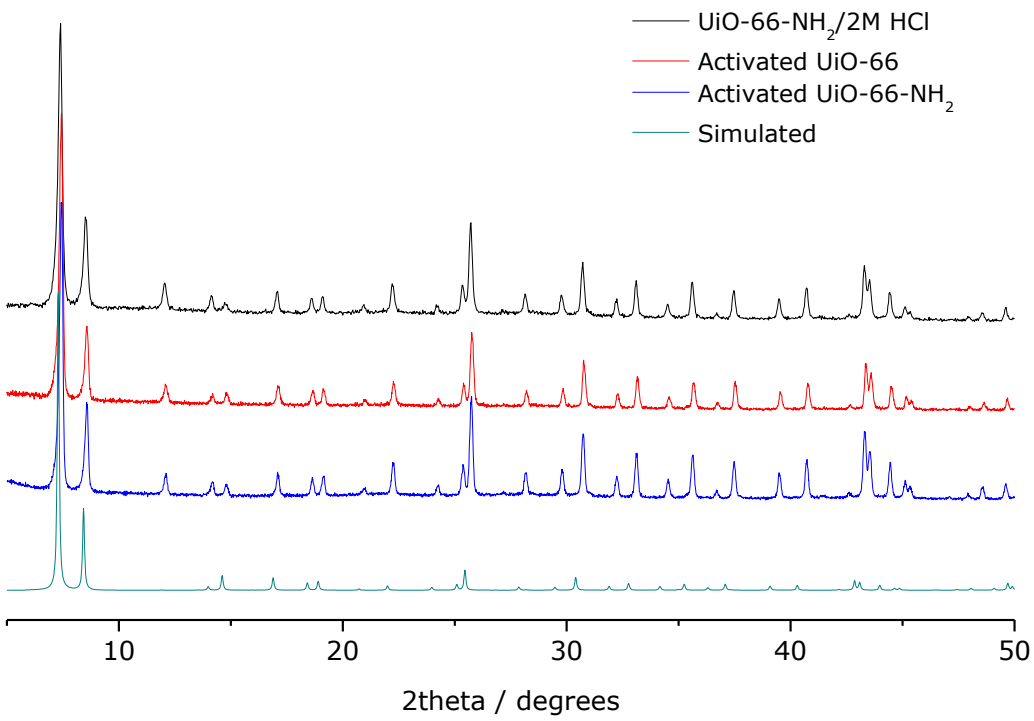


Figure 2.18. Powder X-ray diffractograms of activated UiO-66, activated UiO-66-NH_2 and UiO-66-NH_2 after heating in 2M HCl for 24 hours.

N_2 isotherms carried out at 77 K showed that UiO-66 and UiO-66-NH_2 both exhibit a typical reversible type-I sorption profile with an almost identical uptake of 369 cc g^{-1}

and 370 cc g^{-1} respectively at 1 bar (Figure 2.19). The BET surface area of UiO-66 was calculated to be 1358 m^2 g^{-1} with the BET surface area of UiO-66-NH_2 slightly lower than this at 1208 m^2 g^{-1}, these results are consistent with those reported previously.[31,32] Likewise, the N_2 uptake of UiO-66 was consistent with previous results, although the N_2 uptake of UiO-66-NH_2 was slightly higher than expected.[33]

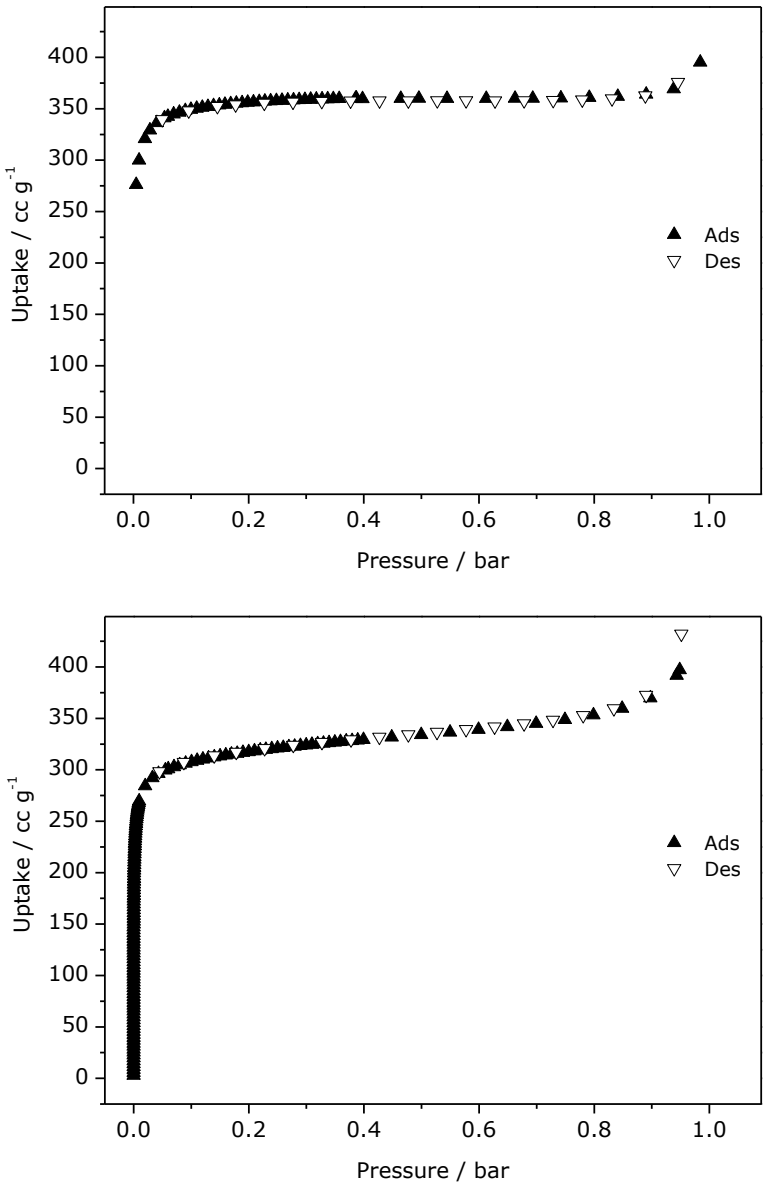


Figure 2.19. N_2 isotherms from 0-1 bar for UiO-66 (top) and UiO-66-NH_2 (bottom) at 77K.

Thermogravimetric analysis of acetone exchanged UiO-66 in air showed solvent loss corresponding to acetone and water below 100 °C, with the material then stable up to ~480 °C, beyond which point a mass loss corresponding to framework decomposition is observed (Figure 2.20). UiO-66-NH_2 also exhibits solvent loss below 100 °C followed by framework decomposition at ~340 °C. Both results are consistent with those reported in the literature,[34,35] with the lower stability of UiO-66-NH_2 attributable to the inductive electron withdrawing ability of the N atom weakening the neighbouring C-C bonds, leading to decomposition.[34]

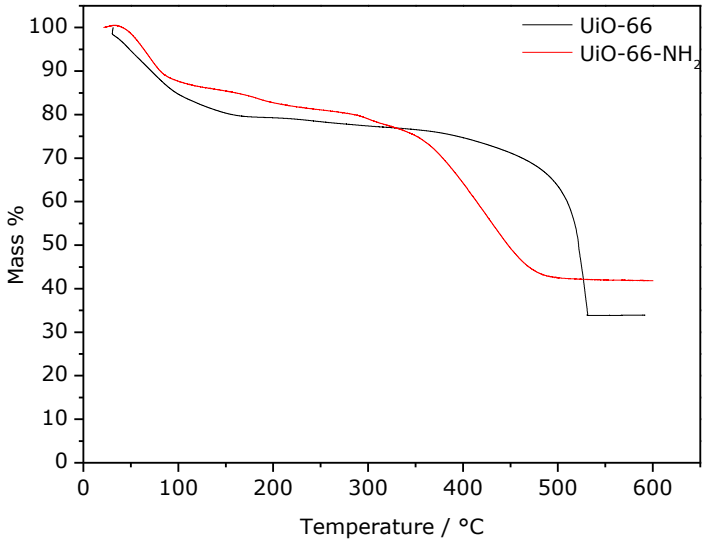


Figure 2.20. TGA traces of acetone exchanged UiO-66 and UiO-66-NH_2.

2.3.2.4 Comparison of K_2PtCl_6 Uptake in UiO-66-NH_2 and UiO-68-NH_2

To compare the sorption capacity of UiO-66-NH_2 to that of UiO-68-NH_2, the extractions performed using 20 mg of UiO-68-NH_2 were repeated with 13.2 mg of UiO-66-NH_2 (Figure 2.21). This gives an equimolar comparison between the two MOFs, with the molecular mass of UiO-66-NH_2 taken to be the mass of one linker plus 1/6th of a $Zr_6O_4(OH)_4$ cluster = $ZrC_8H_{17/3}NO_{16/3}$ = 292.33 g mol^{-1} (*i.e.* the same components as for UiO-68-NH_2).

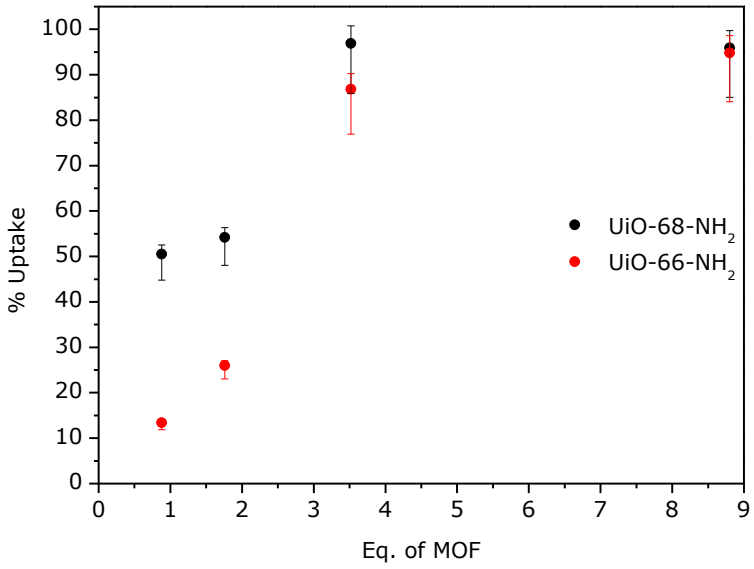


Figure 2.21. A comparison of $PtCl_6^{2-}$ uptake in equimolar quantities of UiO-66-NH_2 and UiO-68-NH_2.

As it has a much lower pore volume and BET surface area, the extraction capacity of UiO-66-NH_2 is unsurprisingly lower than that of UiO-68-NH_2. However, above a ratio of 2:1 MOF:PGM, UiO-66-NH_2 is a very effective sorbent material, exhibiting an 87% uptake of PGM from the initial solution when in 3.5:1 excess (97% for UiO-68-NH_2) and with 9 eq. of MOF, both frameworks show ~ 100% extraction.

2.3.2.5 Aqueous $PtCl_6^{2-}$ Extraction in UiO-66 and UiO-66-NH_2 *Versus* Industrial Materials

In order to determine the effectiveness of UiO-66-NH_2 and UiO-66 as sorbents for $PtCl_6^{2-}$, four industrially used materials supplied by Johnson Matthey, denoted as BP-1, WP-1, SMOPEX-105[36] and Quadrasil-AP,[37] were used as a comparison. BP-1 and WP-1 are silica composite materials functionalised with polyamines, BP-1 contains primary amines and WP-1 is a mixed primary, secondary and tertiary amine material. SMOPEX-105 is a polyolefin based fibre to which polymer chains containing

pyridinium hydrochloride functional groups have been grafted, *i.e.* the chains consist of poly-4-vinyl-pyridine. Quadrasil-AP is a functionalised silica material containing primary aminopropyl functional groups (Figure 2.22).



Figure 2.22. Functional groups present in SMOPEX-105 (left) and Quadrasil-AP (right).

For industrial purposes, Johnson Matthey are interested in a weight based comparison between materials rather than a molar comparison. As such, an initial test using 100 ml of a 10 ppm solution of K_2PtCl_6 in H_2O and 20 mg of each compound was carried out. The mixtures were left for 24 hours and a comparison between the initial solution concentration and final concentration by ICP-OES gave a % uptake for each material (Figure 2.23). Both MOFs showed a greater adsorption capacity than the industrial materials with UiO-66-NH_2 exhibiting 79% extraction after 24 hours and somewhat surprisingly 50% uptake into the non-functionalised UiO-66 was observed. Of the Johnson Matthey materials, WP-1 showed the highest uptake, followed by SMOPEX-105 and BP-1, with Quadrasil-AP extracting < 1% of the Pt from solution.

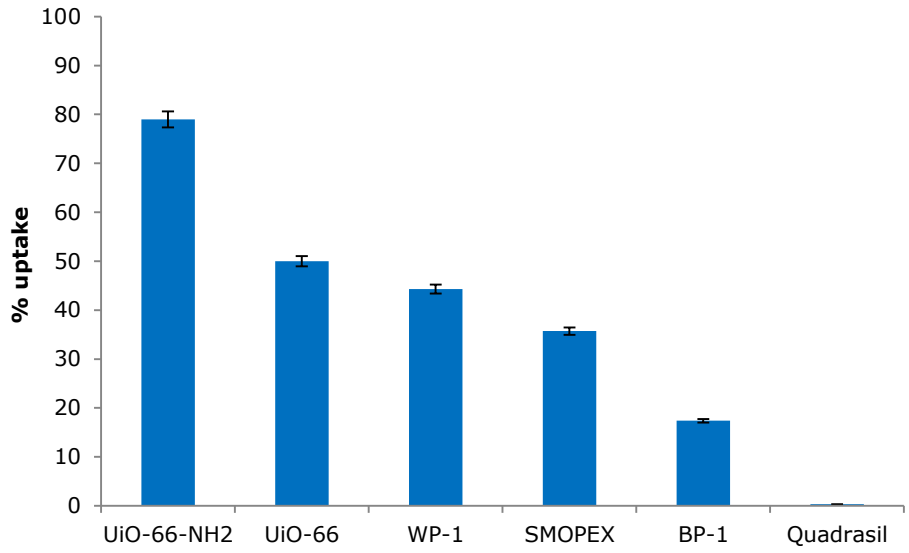


Figure 2.23. Extraction of a 10 ppm Pt solution of $PtCl_6^{2-}$ in H_2O using UiO-66, UiO-66-NH_2 and four industrially used materials.

Following this successful test, the sorption of $PtCl_6^{2-}$ into each of these materials was studied as a function of time, between 0 and 120 hours. As described previously, this was monitored by the periodic removal of 1 ml aliquots from each 100 ml solution and ICP-OES was used to determine the concentration at each point. Three separate comparisons were carried out using 100 ml of a 25 ppm Pt solution, with 20, 50 and 100 mg of each material. For UiO-66-NH_2, this corresponds to 5.34, 13.34 and 26.68 equivalents of the NH_2 group per $PtCl_6^{2-}$ anion respectively. The extractions carried out with 20 mg of sorbent are shown in Figure 2.24. WP-1 exhibits the greatest adsorption after 120 hours (92%), with UiO-66 and UiO-66-NH_2 showing 77% and 73% uptake respectively. However, the uptake profile observed for WP-1 shows that this extraction is slow, with only a 21% reduction in Pt concentration after 24 hours. In contrast, both MOFs show much greater capacity over a shorter time period, with 28% and 19% extraction into UiO-66 and UiO-66-NH_2 respectively after 3 hours and 51% and 46% after 24 hours. As a quick extraction process is highly desirable, the

greater sorption of Pt in UiO-66 and UiO-66-NH_2 between 0 and 3 hours demonstrates the potential of these materials.

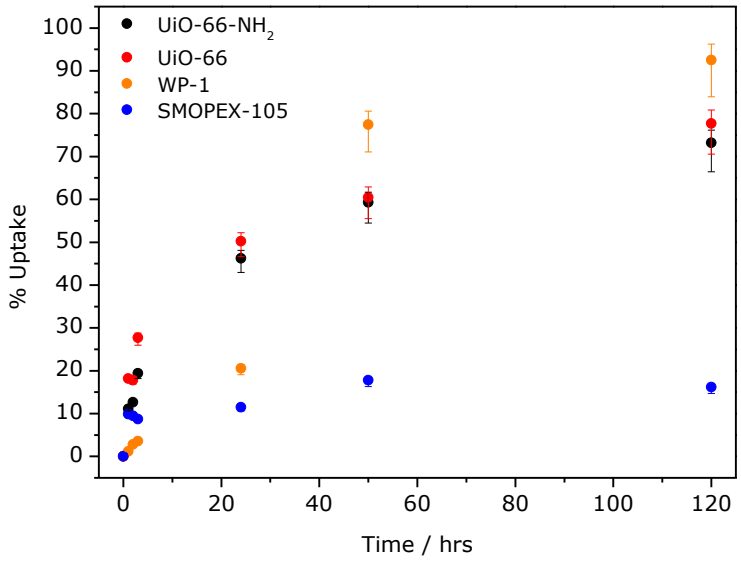


Figure 2.24. Uptake of $PtCl_6^{2-}$ from an aqueous 25 ppm Pt solution using 20 mg of each material. For clarity, only the most effective and least effective silica materials are displayed.

These experimental conditions were repeated using 50 mg of each material and the results are shown below in Figure 2.25. UiO-66-NH_2, UiO-66 and WP-1 now exhibit very similar uptake capacity after 120 hours (96%, 92% and 95% respectively) and once again the sorption capacity of both MOFs is far greater than each silica gel between 0 and 3 hours.

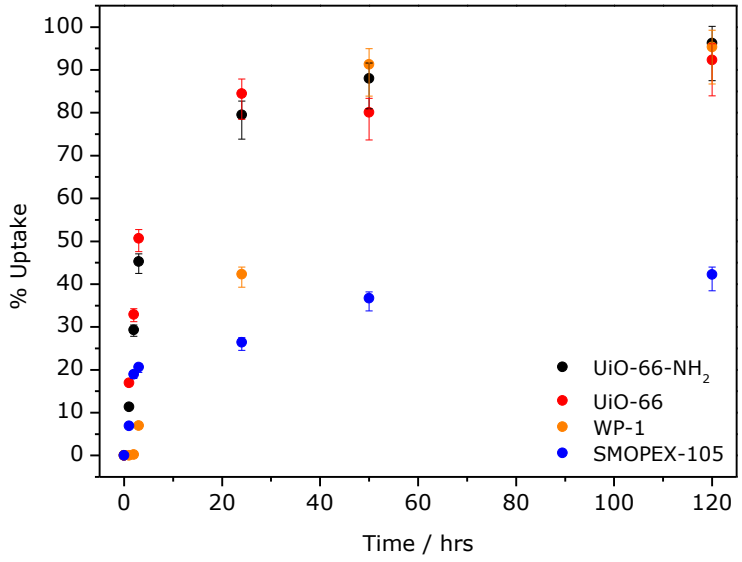


Figure 2.25. Uptake of $PtCl_6^{2-}$ from an aqueous 25 ppm Pt solution using 50 mg of each material. For clarity, only the most effective and least effective silica materials are displayed.

As in the 20 mg experiment, the unfunctionalised UiO-66 is more effective than UiO-66-NH_2 between 0 and 24 hours. This may be a result of the larger BET surface area of UiO-66 and a possible kinetic trapping effect in UiO-66-NH_2 resulting in slower transport of guest molecules through the structure.

However, when the mass of sorbent is increased to 100 mg (26.68 eq. of NH_2 per $PtCl_6^{2-}$), a huge improvement in the extraction capability of UiO-66-NH_2 is observed between 0 and 3 hours, as shown in Figure 2.26. The extraction reaches ~100% after just 24 hours and after one hour 58% of the PGM has been removed from solution (41% for UiO-66).

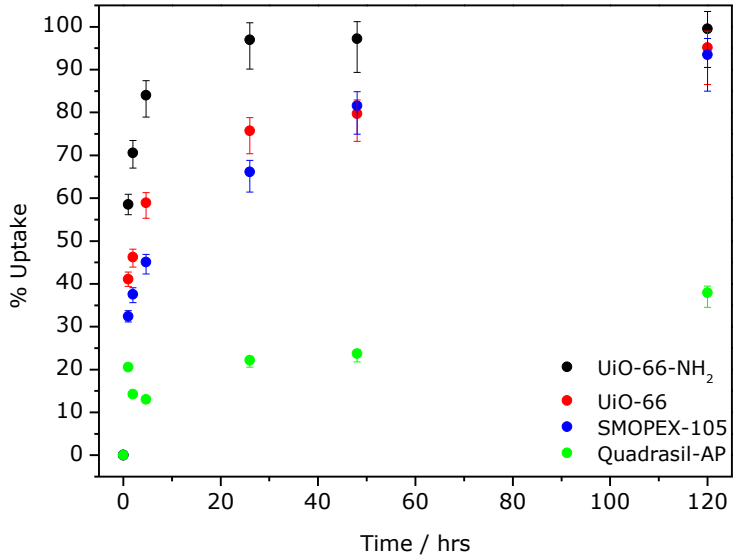


Figure 2.26. Uptake of $PtCl_6^{2-}$ from an aqueous 25 ppm Pt solution using 100 mg of each material. For clarity, only the most effective and least effective silica materials are displayed.

Both frameworks still display much quicker sorption than the silica materials, although interestingly SMOPEX-105 is now the most effective of those sorbents, having been the least effective in previous experiments. This is presumably a result of the hydrochloride functional groups increasing the acidity of the solution and thus strengthening the interaction between the PGM and the pyridyl functional groups.

Table 2.2. Expected and actual ratios of Pt:Zr in UiO-66-NH_2 and UiO-66 from extractions of $PtCl_6^{2-}$.

MOF (mass / mg)	Uptake Pt / mmol	Zr / mmol	Expected Pt:Zr ratio	Measured Pt:Zr ratio
UiO-66-NH_2 (20)	0.00939	0.0684	1 : 7.3	1 : 5.7
UiO-66-NH_2 (50)	0.0124	0.171	1 : 13.8	1 : 28.2
UiO-66-NH_2 (100)	0.0128	0.342	1 : 26.8	1 : 48.7
UiO-66 (20)	0.00995	0.0721	1 : 7.3	1 : 12.3
UiO-66 (50)	0.0118	0.18	1 : 15.2	1 : 18.2
UiO-66 (100)	0.0122	0.361	1 : 29.5	1 : 57.4

As with UiO-68-NH_2, analysis of the acid-digested PGM-doped frameworks shows that the Pt content of the MOFs is slightly lower than expected (Table 2.2). As this appears to be a consistently low value, it is likely to be the result of a small quantity of Pt being removed as the digested sample is filtered to remove undissolved linker.

2.3.2.6 Back-Extraction of $PtCl_6^{2-}$ from UiO-66-NH_2

Having demonstrated that UiO-66-NH_2 is capable of fast and efficient uptake of $PtCl_6^{2-}$ it was necessary to study the back-extraction of the PGM anion from the framework to recover the metal in a useable form. It was decided that the most facile method of removal would be a simple substitution of the bound PGM anions with chloride ions from HCl to release the $PtCl_6^{2-}$ in the form of hexachloroplatinic acid, H_2PtCl_6.

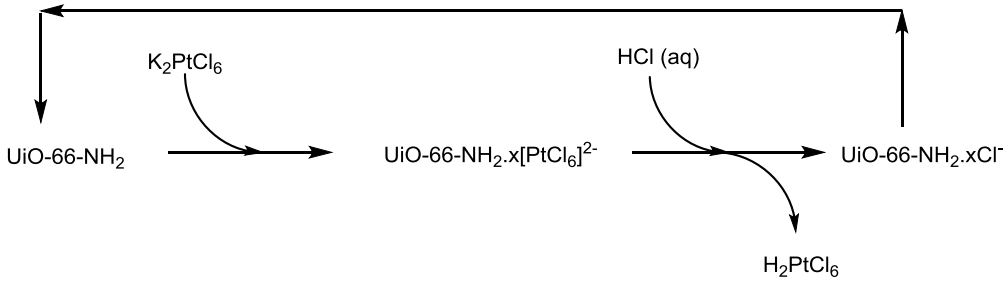


Figure 2.27. The predicted mechanism for $PtCl_6^{2-}$ removal from UiO-66-NH_2.

To investigate this, 6 mg portions of UiO-66-NH_2 from the 50 mg extraction experiment were added to 15 ml solutions of 0.1, 0.5, 1, 2 and 4 M HCl and heated overnight at 80 °C in a sealed vessel. A sample was also heated in ultrapure de-ionised H_2O to investigate whether heat was also a factor for PGM release. After filtration, the MOF samples were digested in 2 ml of 69% HNO_3 by heating at 70 °C for 16 hours and then diluted with 10 ml of ultrapure de-ionised H_2O upon cooling. The samples were then analysed by ICP-OES and the ratio of Pt:Zr was compared to

that of the sample before back-extraction. These ratios were converted into a % of Pt removed from the MOF (Figure 2.28).

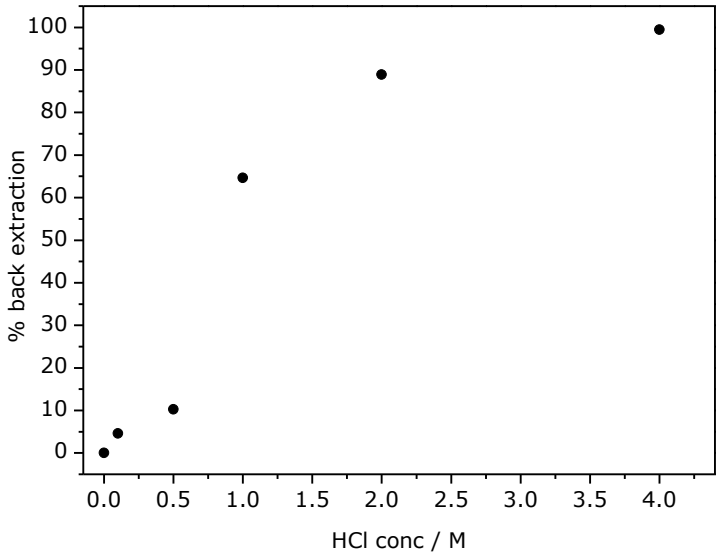


Figure 2.28. % of Pt back-extracted from samples of UiO-66-NH_2 as a function of HCl concentration.

The back-extractions performed in H_2O, 0.1 M and 0.5 M HCl are shown to be ineffective, with no back-extraction into H_2O observed and only 4.6% and 10.3% of Pt removed by 0.1 M and 0.5 M HCl respectively. However, when the HCl concentration is increased to 1 M, 65% of the PGM is back-extracted, rising to 89% in 2 M HCl and 99% in 4 M HCl. This demonstrates that the MOF is capable of $PtCl_6^{2-}$ uptake and subsequent release in very mild conditions. However, the fact that significant release of the anion occurs in 1 M HCl suggests that the framework has a high affinity for Cl^- ions. As the majority PGM extractions occur in acidic aqueous conditions (usually HCl), this high affinity for chloride ions may be problematic for selective removal of $PtCl_6^{2-}$.

2.3.2.7 Extraction of $PtCl_6^{2-}$ from Acidic Solutions

To study the performance of UiO-66-NH_2 under acidic conditions, an initial test using 100 ml/10 ppm solutions of K_2PtCl_6 in 2 M HCl and 20 mg samples of UiO-66, UiO-66-NH_2, BP-1, WP-1, SMOPEX-105 and Quadrasil-AP was carried out. Each solution was left at room temperature without stirring and the concentration after 24 hours was compared to the initial solution concentration and converted into a % uptake (Figure 2.29).

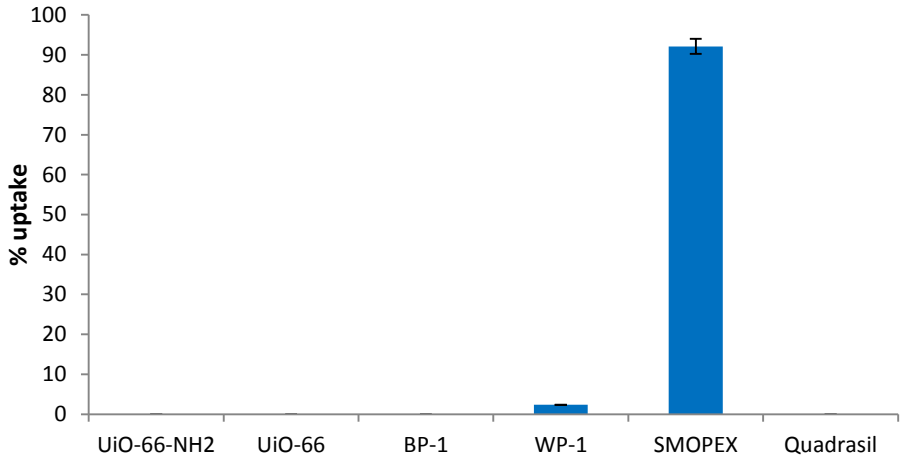


Figure 2.29. Extraction of a 10 ppm solution of $PtCl_6^{2-}$ in 2M HCl using UiO-66, UiO-66-NH_2 and four industrially used materials.

Under these conditions neither UiO-66 nor UiO-66-NH_2 is capable of extracting $PtCl_6^{2-}$ from solution. Of the Johnson Matthey materials, SMOPEX-105 exhibits a high sorption capacity (92%) and the uptake shown by BP-1, WP-1 and Quadrasil-AP is negligible. It was intended that the 20, 50 and 100 mg experiments performed with the solutions of K_2PtCl_6/H_2O would be repeated in 2 M HCl, however, the poor uptake from the 10 ppm solution meant that the loadings were increased to 50, 100 and 500 mg. Again, 1 ml aliquots were removed from the solutions periodically and the % uptake was calculated as a function of time. The results obtained using 50 mg

of each sorbent are shown below in Figure 2.30. SMOPEX-105 shows the greatest uptake (98%), followed by WP-1 (12%), while both MOFs perform poorly again (5.5% and 1.9% respectively for UiO-66-NH_2 and UiO-66).

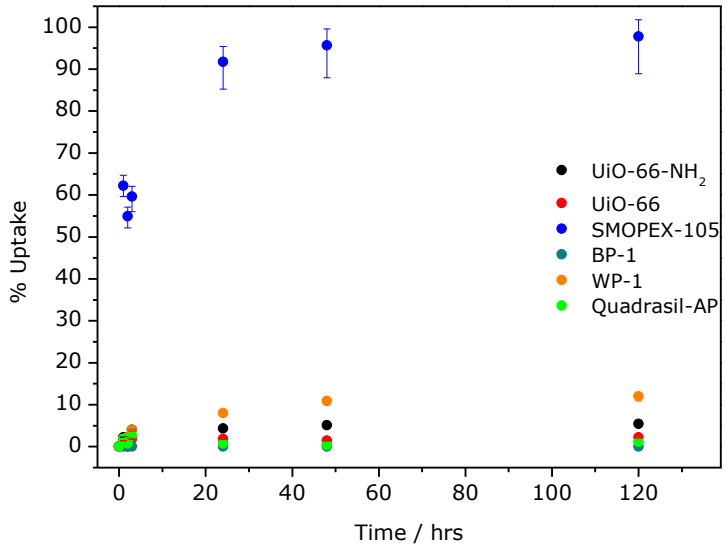


Figure 2.30. Uptake of $PtCl_6^{2-}$ from a 25 ppm Pt solution in 2 M HCl using 50 mg of each material.

2.3.2.8 BET Surface Area Comparison of Doped UiO-66-NH_2 Samples

To investigate the effect of the Cl^- ions on UiO-66-NH_2, the N_2 uptake of samples from K_2PtCl_6/H_2O and K_2PtCl_6/2 M HCl solutions was measured and compared to that of activated UiO-66-NH_2. The samples were both taken from the 50 mg Pt extraction experiments and were filtered and heated under vacuum at 120 °C before gas sorption. The results show that the low pressure uptake at 77 K has decreased considerably from 393 cc g^{-1} in the bare material to 260 cc g^{-1} for the sample from HCl and to 248 cc g^{-1} for the sample from H_2O, corresponding to 34% and 37% reductions in uptake respectively (Figure 2.31).

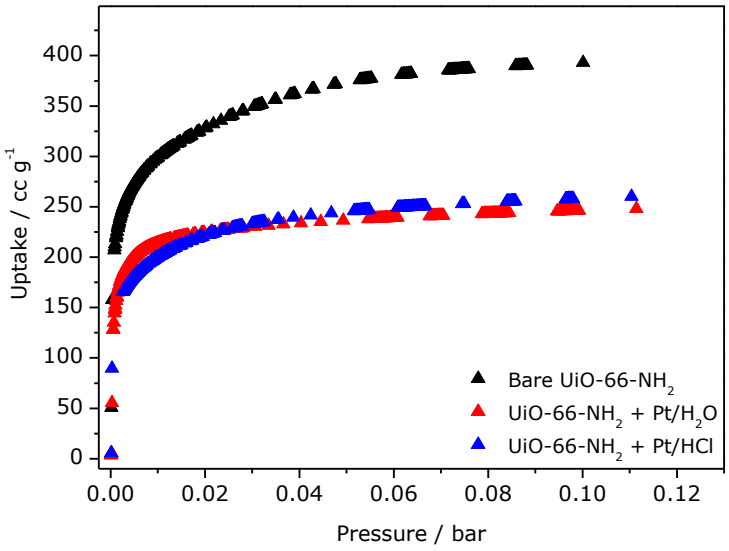


Figure 2.31. N_2 isotherms for activated and anion-doped samples of UiO-66-NH_2 at 77 K.

A concomitant decrease in BET surface area from 1478 m^2 g^{-1} in bare UiO-66-NH_2 to 977 m^2 g^{-1} and 927 m^2 g^{-1} is observed for the samples from HCl and H_2O respectively (as with the N_2 uptake this corresponds to reductions of 34% and 37%). The reduction in uptake and BET surface area were expected for the K_2PtCl_6/H_2O sample, which encapsulated 96% of the Pt from solution, explaining the reduction in BET surface area. The reduction in N_2 uptake and BET surface area for the K_2PtCl_6/HCl sample, which removed just 5% of the Pt from solution, is therefore assigned to the encapsulation of Cl^- anions blocking pore space.

This was confirmed by using X-ray photoelectron spectroscopy (XPS) analysis to calculate the ratios of Zr:Pt and Zr:Cl in both frameworks. The sample from H_2O showed a Zr:Pt ratio of 8.7:1 and a Zr:Cl ratio of 2.9:1 whereas the sample from HCl exhibited a Zr:Pt ratio of 142:1 and a Zr:Cl ratio of 1.6:1, showing clearly the high concentration of Cl^- within the pores. Interestingly, a series of XPS measurements on

the extraction samples from H_2O (20 mg, 50 mg and 100 mg) exhibited Pt:Cl ratios of 3:1, 3:1 and 3.5:1 respectively, suggesting that the encapsulated species within the MOF may be $PtCl_3(NH_2)_3$ or $PtCl_4(NH_2)_2$. This is consistent with the work of Huang and co-workers who demonstrated that the encapsulated species resulting from extraction of $PtCl_4^{2-}$ in UiO-66-NH_2 was likely to be $PtCl_2(NH_2)_2$.[16]

2.3.2.9 Investigating the Effect of HCl Concentration on $PtCl_6^{2-}$ Uptake

As the presence of Cl^- ions was clearly having a huge impact on the uptake capacity of UiO-66-NH_2 for $PtCl_6^{2-}$, the relationship between the concentration of HCl and extraction was studied in greater detail. Samples of UiO-66-NH_2 (20 mg) were added to 50 ml/25 ppm solutions of K_2PtCl_6 in various concentrations of HCl for 24 hours and the % uptake of the PGM was calculated from a comparison between the initial and final solution concentrations (Figure 2.32).

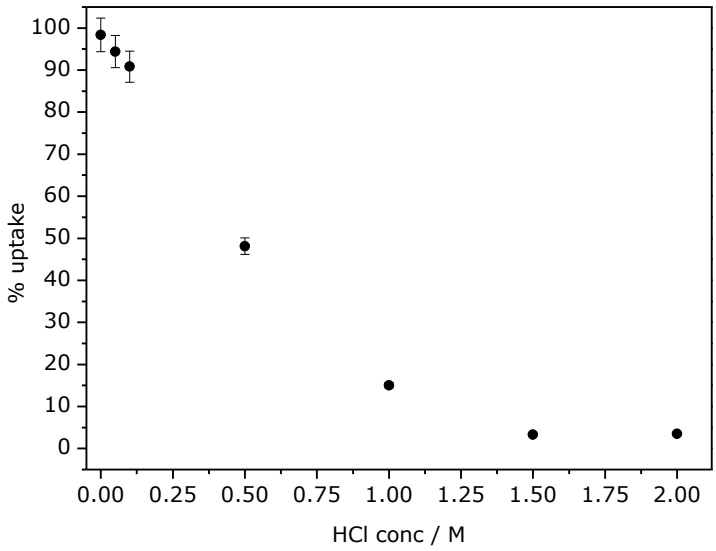


Figure 2.32. The effect of HCl concentration on the uptake of $PtCl_6^{2-}$ into UiO-66-NH_2 from a 25 ppm solution.

These results show clearly that low HCl concentration does not affect the PGM uptake to a great extent (98% to 90% from 0 M to 0.1 M HCl), however when the concentration is increased to 0.5 M, the uptake is reduced to 48%. This is consistent with the back-extraction experiments in which the removal of $PtCl_6^{2-}$ from the pores was found to dramatically increase between 0.1 M and 0.5 M concentrations. In the 1 M solution the uptake is reduced further to 15% and to ~3% in the 1.5 M and 2 M solutions. Whilst this severe reduction in uptake is problematic, it is worth noting that the 0.5 M solution contains 3,900 eq. of Cl^- per $PtCl_6^{2-}$ and 731 eq. of Cl^- per NH_2 moiety, suggesting that the 48% uptake of PGM actually represents *high* selectivity for $PtCl_6^{2-}$ over Cl^- in UiO-66-NH_2.

Following these results, two further studies were carried out in 2 M HCl using 100 and 500 mg of UiO-66 and UiO-66-NH_2 and a 25 ppm solution of K_2PtCl_6, with the solution volume reduced from 100 ml to 50 ml. Using 100 mg of UiO-66-NH_2 corresponds to 15,600 equivalents of Cl^- per $PtCl_6^{2-}$ but more importantly, only 292 eq. of Cl^- per NH_2 group and gives an NH_2:$PtCl_6^{2-}$ ratio of 53:1. With 500 mg of MOF, this becomes 58 Cl^- ions per NH_2 and an NH_2:$PtCl_6^{2-}$ ratio of 267:1.

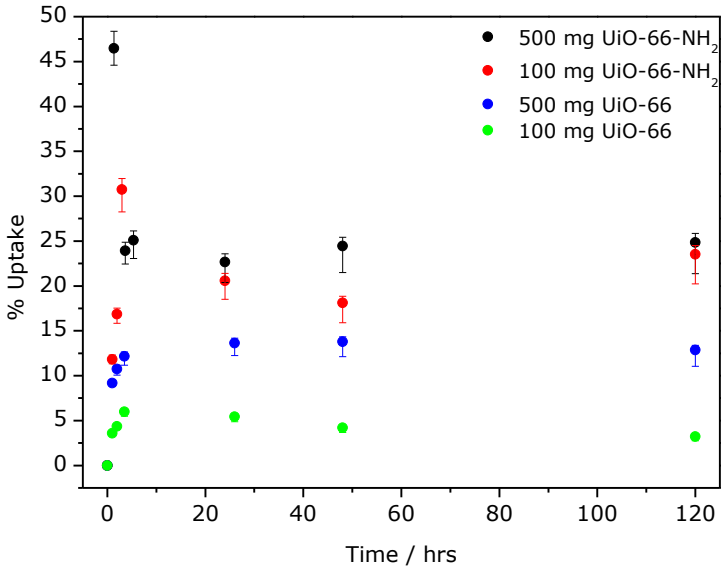


Figure 2.33. Uptake of $PtCl_6^{2-}$ from a 25 ppm Pt/2 M HCl solution into UiO-66 and UiO-66-NH_2.

The results show a much improved uptake with the increased masses of MOF, with both UiO-66-NH_2 samples extracting ~25% of the $PtCl_6^{2-}$ from solution after 120 hours (Figure 2.33). Interestingly, the initial uptake is good in both cases (46% after 1 hour with 500 mg of MOF), however this soon falls rapidly and plateaus at 25%. This may be due to an equilibrium process in which the larger, more negatively charged $PtCl_6^{2-}$ anions bind more quickly to the NH_2 groups but are then displaced over time by the large excess of Cl^- ions. The uptake of the PGM anion into UiO-66 is poor (3% with 100 mg and 13% with 500 mg after 120 hours). However, the uptake profile does not show the initial high uptake observed with UiO-66-NH_2, providing further evidence that competitive binding at the NH_2 group is the reason for the drop in uptake UiO-66-NH_2. The large difference in sorption capacity between UiO-66 and UiO-66-NH_2, which was not seen in the H_2O based extractions,

suggests that the lower pH of the acidic solution is improving the binding capability of the NH_2 group.

ICP-OES analysis of digested MOF samples post-extraction shows that the content of encapsulated Pt is higher than predicted in each case (Table 2.3). Whereas the low Pt content of samples from H_2O was assigned to incomplete digestion of Pt bound to the linker, the cause of this discrepancy is currently unknown.

Table 2.3. Expected and actual ratios of Pt:Zr in UiO-66-NH_2 and UiO-66 from extractions of $PtCl_6^{2-}$ from HCl.

MOF (mass / mg)	Uptake Pt / mmol	Zr / mmol	Expected Pt:Zr ratio	Measured Pt:Zr ratio
UiO-66-NH_2 (100)	1.49×10^{-3}	0.342	1 : 230.0	1 : 108.4
UiO-66-NH_2 (500)	1.59×10^{-3}	1.71	1 : 1076	1 : 209.5
UiO-66 (100)	8.21×10^{-4}	0.361	1 : 439.4	1 : 416.8
UiO-66 (500)	2.05×10^{-4}	1.8	1 : 8789	1 : 560.1

2.3.2.10 Extraction of $PdCl_6^{2-}$ from Acidic Solutions

Having demonstrated the potential of UiO-66-NH_2 as a sorbent material for Pt extraction, it was decided that the extraction of $PdCl_6^{2-}$, in the form of K_2PdCl_6, should also be studied for comparative purposes. As no Pd(IV) salts are soluble in H_2O, these extractions were carried out in 2 M HCl using 50 ml of 25 ppm solutions of Pd, while the mass of UiO-66-NH_2 was varied. Although the $PtCl_6^{2-}$ uptake under these conditions was poor, they were used for the $PdCl_6^{2-}$ experiments to give an accurate comparison between the extraction of both metals.

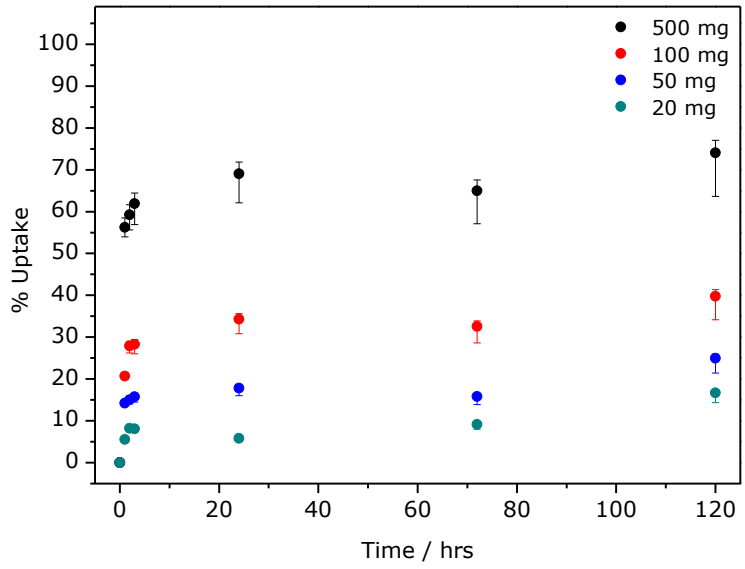


Figure 2.34. Uptake of $PdCl_6^{2-}$ with varying quantities of UiO-66-NH_2.

As shown above in Figure 2.34, the uptake of Pd(IV) is significantly greater than that observed for Pt(IV), from 17% when using 20 mg of MOF to 74% with 500 mg. As with Pt(IV), the uptake within the first three hours is good and unlike the Pt(IV) extraction, which then falls sharply, the Pd sorption continues to rise slowly until ~24 hours, at which point it plateaus.

The Pd and Zr content of the digested MOF samples is shown below in Table 2.4. As with the extractions of $PtCl_6^{2-}$ from HCl, the content of the PGM is considerably higher than predicted from the solution ICP-OES data. In the case of the 500 mg sample, the measured content of Pd was an order of magnitude greater than expected.

Table 2.4. Expected and actual ratios of Pd:Zr in UiO-66-NH_2 from extractions of $PdCl_6^{2-}$ from HCl.

Mass of MOF / mg	Uptake Pd / mmol	Zr / mmol	Expected Pd:Zr ratio	Measured Pd:Zr ratio
20	1.08×10^{-3}	0.0684	1 : 63.5	1 : 23.9
50	1.59×10^{-3}	0.171	1 : 107.6	1 : 30.1
100	2.56×10^{-3}	0.342	1 : 133.4	1 : 26.4
500	4.77×10^{-3}	1.71	1 : 358.6	1 : 38.8

2.3.2.11 ^{13}C Solid State NMR of PGM-Doped Samples of UiO-66-NH_2

To investigate the interaction between the framework and guest anions, ^{13}C CP-MAS solid state NMR was carried out by collaborators at Johnson Matthey on doped UiO-66-NH_2. Samples of UiO-66-NH_2 (100 mg) were soaked in 50 ml solutions of 2 M HCl, K_2PtCl_6/2 M HCl, K_2PtCl_6/H_2O and K_2PdCl_6/2 M HCl, with the PGM anions present in a 3:1 ratio of PGM:NH_2 in each case. Having been left to soak for one week the samples were isolated by filtration and heated under vacuum to remove the solvent. The SS-NMR spectrum of each sample was then compared to that of activated UiO-66-NH_2 (Figure 2.35). It should be noted that the spectrum of the activated material contains additional peaks from trace impurities of DMF and benzoic acid from synthesis.

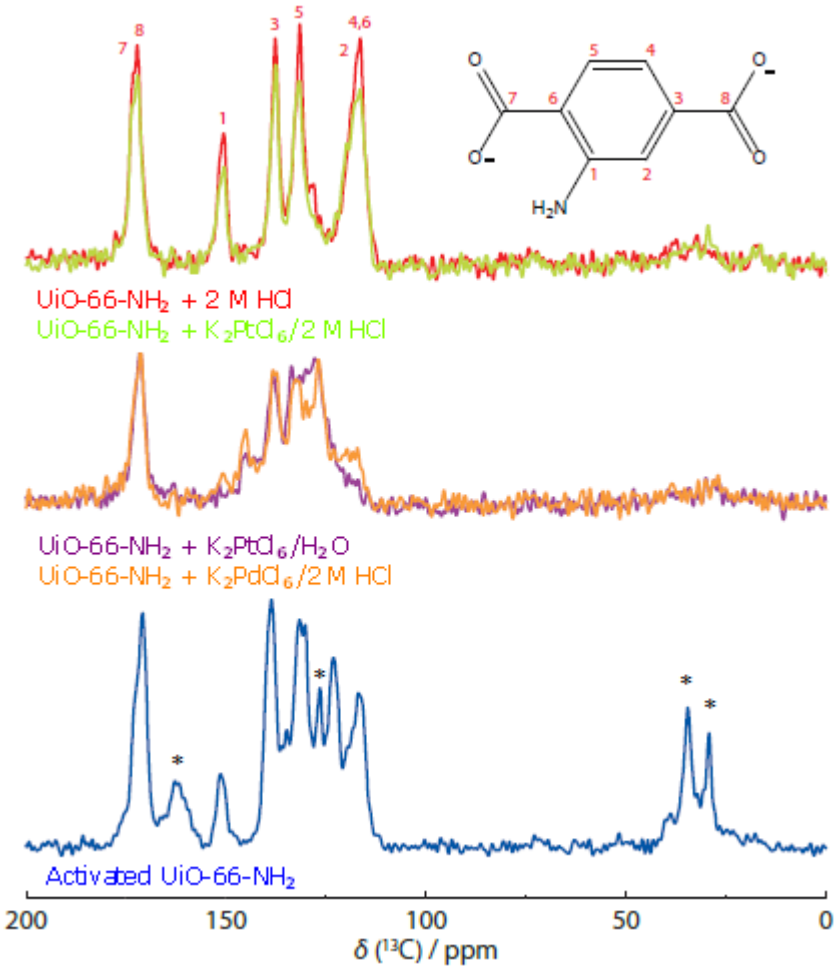


Figure 2.35. ^{13}C solid state CP-MAS NMR spectra of UiO-66-NH_2 doped with $PtCl_6^{2-}$, $PdCl_6^{2-}$ and Cl^-. Asterisks on the activated UiO-66-NH_2 spectrum indicate peaks from trace impurities. Peak assignments are based on those reported in reference 38.

Both the sample from 2 M HCl and the sample from the K_2PtCl_6/2 M HCl mixture only exhibit peaks that correspond to the activated framework (the residual DMF and PhCOOH have been removed from the pores). This result is consistent with ICP-OES analysis which showed no uptake of $PtCl_6^{2-}$ from the 2 M HCl solution. Interestingly these spectra show no shift in the peak corresponding to C_1 (the C atom

bound to the NH_2 group) at ~150 ppm, suggesting that protonation of the NH_2 and the presence of a Cl^- counter-ion in the pores is unlikely.

In contrast, the spectra of samples removed from K_2PtCl_6/H_2O and K_2PdCl_6/2 M HCl solutions show a clear shift upfield of the peak associated with C_1. This strongly suggests an interaction between the NH_2 group and the PGM anions, as was expected. Furthermore, the peaks corresponding to C_2 and C_4 have shifted downfield, which is also consistent with either a hydrogen bond between the NH_2 group and the chloride groups of the Pt anion or with a covalent bond between the NH_2 and the Pt centre. The ICP-OES analysis shows that, in the case of K_2PtCl_6/H_2O, the NH_2 groups are fully saturated with $PtCl_6^{2-}$, *i.e.* the PGM:NH_2 ratio is greater than 1:1 (1.01:1). This is shown in the ^{13}C NMR spectrum above as the original C_1 peak from the activated material has disappeared completely, suggesting that all of the NH_2 groups are interacting with the PGM. As XPS analysis suggested that the encapsulated species may be present in the form of $PtCl_3(NH_2)_3$ or $PtCl_4(NH_2)_2$, the 1.01:1 ratio of PGM:NH_2 shows that a proportion of the uptake must be a result of the interaction of $PtCl_6^{2-}$ with other components of the framework. For example, this could indicate van der Waals interactions between $PtCl_6^{2-}$ and aromatic protons of the linker or oxygen atoms in the Zr cluster, which would explain the unexpected uptake in the unfunctionalised UiO-66 material. In the case of $PdCl_6^{2-}$, ICP-OES analysis shows a PGM:NH_2 ratio of 0.55:1, suggesting that some of the NH_2 groups are not interacting with the $PdCl_6^{2-}$ guests. Again this is in agreement with the SS-NMR spectrum, in which the C_1 peak has clearly reduced in intensity but is still visible.

In an attempt to crystallographically determine the nature of the interactions between the framework and the PGM anions, these samples were sent to the I11 beamline at

Diamond Light Source for high-resolution powder X-ray diffraction scans. Unfortunately, despite the high quality data that was obtained, the positions of the various guest species could not be refined. This was partly because the high symmetry of the MOF made differentiating between real and symmetry-generated regions of electron density very difficult. Additionally, the disordered NH_2 group was difficult to model and may have resulted in very low occupancies of $PtCl_6^{2-}$ ions bound within the cavities.

2.3.2.12 Separation of $PdCl_6^{2-}$ from $PtCl_6^{2-}$

As the uptake of $PdCl_6^{2-}$ from 2 M HCl is much greater than that of $PtCl_6^{2-}$, it was expected that separation of Pd and Pt from a mixed solution of both metals would be observed. To investigate this, 50 ml solutions of 1 M HCl containing 25 ppm of Pt and Pd were prepared and extractions with 50 mg and 100 mg of UiO-66-NH_2 were carried out. The HCl concentration was reduced from 2 M to 1 M to improve the uptake of both metals and provide a clearer comparison between them. As seen below in Figure 2.36, the uptake of Pd is considerably higher than that of Pt in both experiments - 96% and 59% removal of Pd with 100 mg and 50 mg respectively compared to 31% and 9% uptake of Pt.

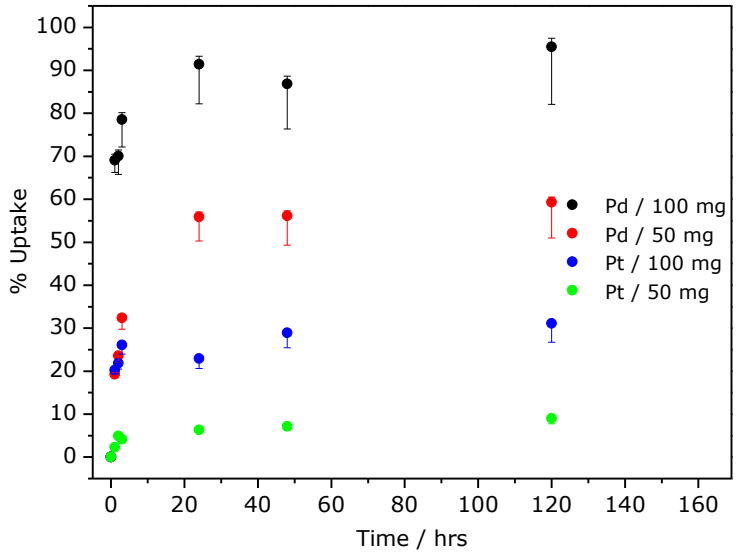


Figure 2.36. Extraction of Pd and Pt from mixed metal solutions using UiO-66-NH_2.

This corresponds to 3.1:1 and 6.6:1 selectivities (by weight) for Pd over Pt after 120 hours and of 5.7:1 and 12.1:1 when converted to a molar ratio.

Having earlier established that HCl concentration plays a huge role in the uptake of the hexachloroplatinate anion, a series of Pd/Pt separations in different HCl concentrations (0.1 M – 6 M) were carried out. In each case 50 mg of UiO-66-NH_2 was added to 50 ml of a 25 ppm solution of Pd and Pt and the extraction was monitored over the course of 120 hours. The selectivity of these separations is shown below in Figure 2.37. Plots of each individual data set are shown in the Appendices (Figures A1.1-A1.3).

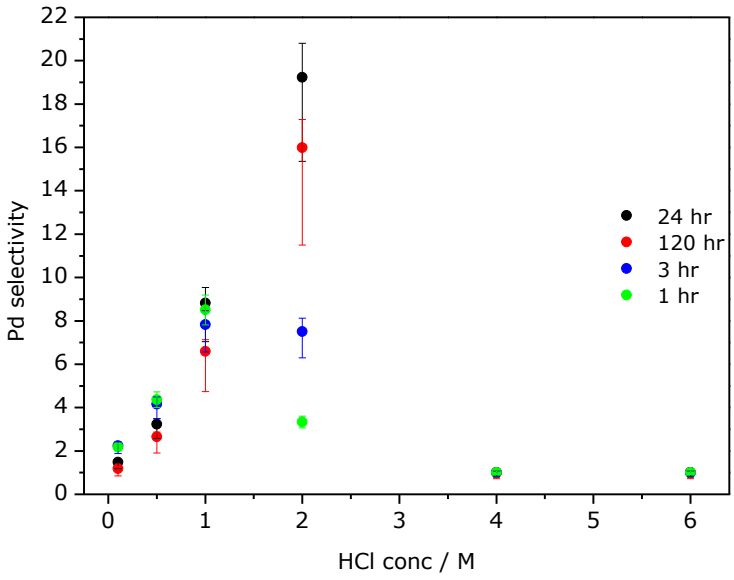


Figure 2.37. Selectivity for Pd over Pt as a function of both time and HCl concentration using UiO-66-NH_2.

In 0.1 M HCl, limited separation of Pd over Pt is observed (~1.2:1 after one hour), which then increases to 2.7:1 in 0.5 M HCl. However, this increases dramatically to 6.6:1 in 1 M HCl and to 15.9:1 in 2 M HCl. No uptake of either PGM was observed from the 4M and 6M solutions. Interestingly, it was noted that in addition to dependence on HCl concentration, this selectivity also exhibited time dependence. In 0.1 M and 0.5 M HCl, the separation of Pd from Pt is approximately halved between one and 120 hours. However, in the 1 M solution, the selectivity for Pd after 24 hours (8.8:1) is greater than the selectivity observed after one and three hours (8.5:1 and 7.8:1 respectively). In the 2 M solution, the selectivity after one and three hours is reduced but greatly increases at 24 and 120 hours, peaking at a 20:1 Pd:Pt ratio after 24 hours. These changes in selectivity are a result of the equilibrium effect described earlier for the extraction of Pt from HCl solutions. In the more concentrated solutions, the initial uptake of Pt quickly declines and plateaus at around 24 hours, whereas the extraction of Pd continues to increase over time.

2.3.2.13 Separation of PGM Anions from Base Metals

In addition to separation between PGMs it is also of great importance to separate PGMs from transition metal compounds, particularly chlorides and sulfates.[39,40] As Cu is one of the major transition metal impurities in PGM-containing ores,[41] we examined the separation of $PtCl_6^{2-}$ from $CuCl_2$ and $CuSO_4$ from 1 M HCl solutions containing 25 ppm of both metals. As with the extractions described previously, a 24 hour test was undertaken using 50 mg of UiO-66 and UiO-66-NH_2 in 50 ml/25 ppm solutions of Pt and Cu. The initial concentration of the solution was compared to the concentration after 24 hours by ICP-OES and converted into a % uptake of both metals (Figure 2.38).

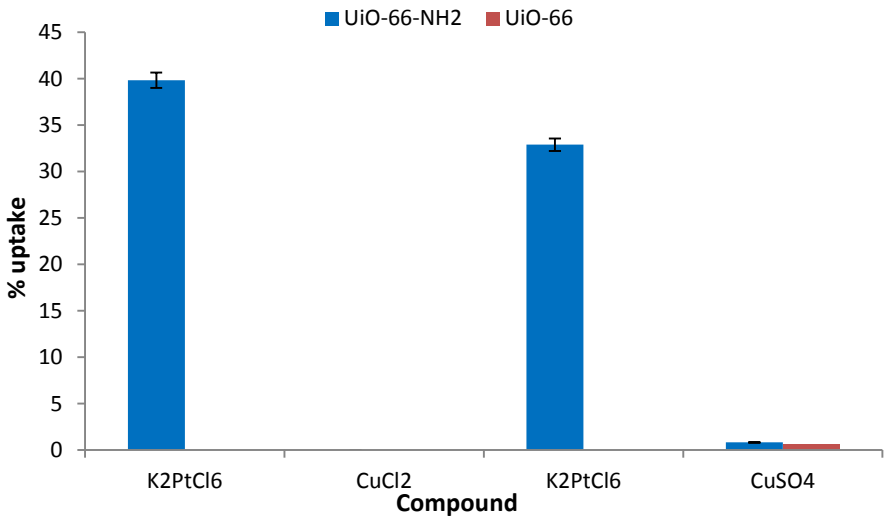


Figure 2.38. Uptake of Pt and Cu compounds from mixed solutions of $K_2PtCl_6/CuCl_2$ (left) and $K_2PtCl_6/CuSO_4$ (right).

The results show clearly that UiO-66-NH_2 exhibits 100% selectivity for $PtCl_6^{2-}$ over $CuCl_2$ as no uptake of Cu is observed over 24 hours and the Pt concentration in solution was reduced by 39%. The uptake of $PtCl_6^{2-}$ from the $K_2PtCl_6/CuSO_4$ mixture is slightly lower (33%) and 0.8% of the $CuSO_4$ is removed from solution but this still

equates to an excellent selectivity ratio for Pt over Cu of 37:1. Unlike the amine-functionalised MOF, UiO-66 exhibited negligible uptake of $PtCl_6^{2-}$, $CuCl_2$ and $CuSO_4$, demonstrating the importance of the NH_2 moiety for extractions from these acidic conditions.

Following these successful results, UiO-66-NH_2 (50 mg) was added to mixed metal 1 M HCl solutions containing 25 ppm of Pt and 25, 250 and 2500 ppm $CuCl_2$. In each case ~100% selectivity for Pt over Cu was observed, even in the presence of a 100-fold excess of Cu (Figure 2.39).

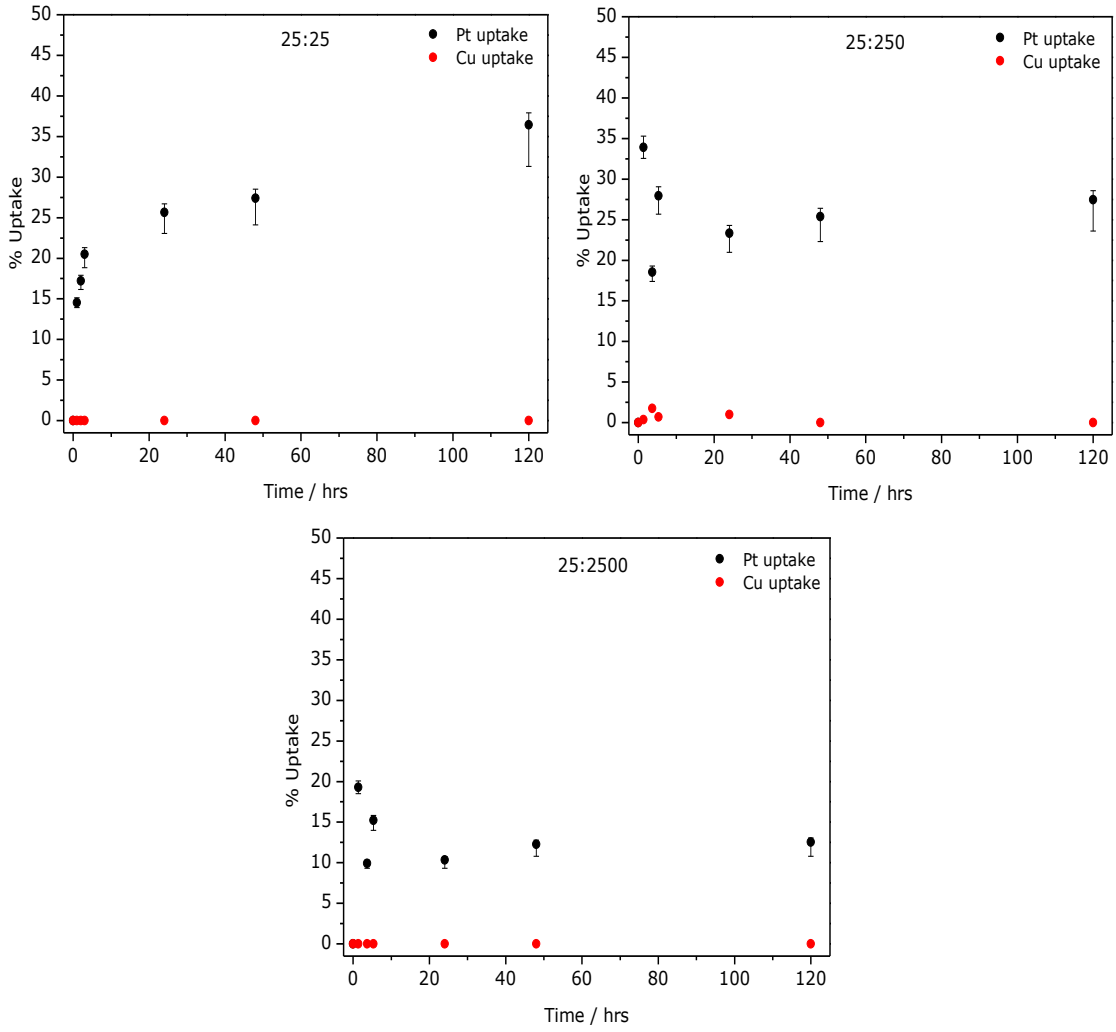


Figure 2.39. Uptake of Pt and Cu from mixed solutions of $K_2PtCl_6/CuCl_2$ of 25:25 ppm (top left), 25:250 ppm (top right) and 25:2500 ppm (bottom).

Despite the relatively low total uptake of $PtCl_6^{2-}$ (36%, 29%, 13% respectively for the 1:1, 1:10 and 1:100 ratio solutions of Pt:Cu), the uptake between 0 and 3 hours is good. This suggests that UiO-66-NH_2 is a useful material for quick and selective removal of $PtCl_6^{2-}$ from base metal solutions. It is worth noting that the extraction from the 25:25 ppm solution of Pt:Cu (Figure 2.39, top left) was performed using a different batch of MOF to the extractions from 25:250 ppm and 25:2500 ppm solutions. This may be the cause of the very different uptake profile observed for this experiment.

These conditions were then repeated using $CuSO_4$ in place of $CuCl_2$ (Figure 2.40). Again, 100% selectivity for Pt over Cu is observed, although the uptake of Pt is greatly reduced to 13% and 8% with 25 ppm and 250 ppm of Cu respectively. No uptake of Pt is observed when Cu is in 100 times excess. This may be the result of a kinetic competition effect between the $PtCl_6^{2-}$ anions and the Cu species which increases with the increasing content of Cu in solution.

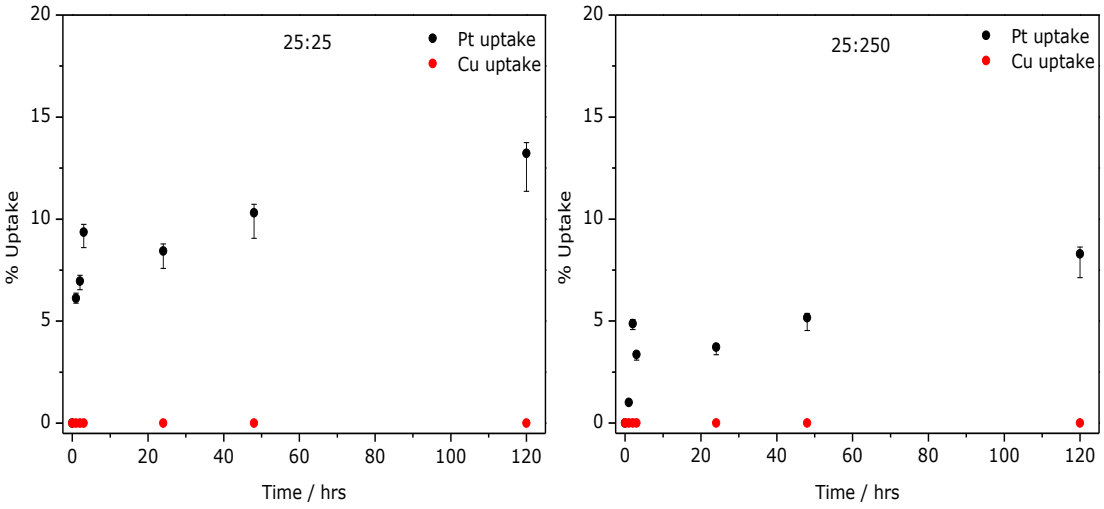


Figure 2.40. Uptake of Pt and Cu from mixed solutions of $K_2PtCl_6/CuSO_4$ of 25:25 ppm (left) and 25:250 ppm (right).

It should also be noted that the uptake of $PtCl_6^{2-}$ from the 25:25 ppm solution is now much lower than that observed from the initial test under the same conditions. The reason for this is unclear, although the batch of UiO-66-NH_2 used in this case was different to the batch used in the initial tests.The separation of $PdCl_6^{2-}$ from $CuCl_2$ and $CuSO_4$ was investigated using the same set of experimental conditions. The extractions of $PdCl_6^{2-}$ from $CuCl_2$ shown in Figure 2.41 exhibit 100% selectivity for Pd over Cu from the 25:25, 25:250 and 25:2500 ppm solutions. Unlike the $PtCl_6^{2-}$ /$CuCl_2$ separations, the 120 hour sorption of $PdCl_6^{2-}$ was not affected by the concentration of Cu in the solution, remaining almost constant at 76%, 80% and 76% for the three concentrations. However, the extraction of $PdCl_6^{2-}$ over the first three hours does reduce from 63% to 50% to 46% as the Cu concentration is increased ten-fold each time. Again this suggests a competitive kinetic effect brought about by the increased concentration of Cu in solution.

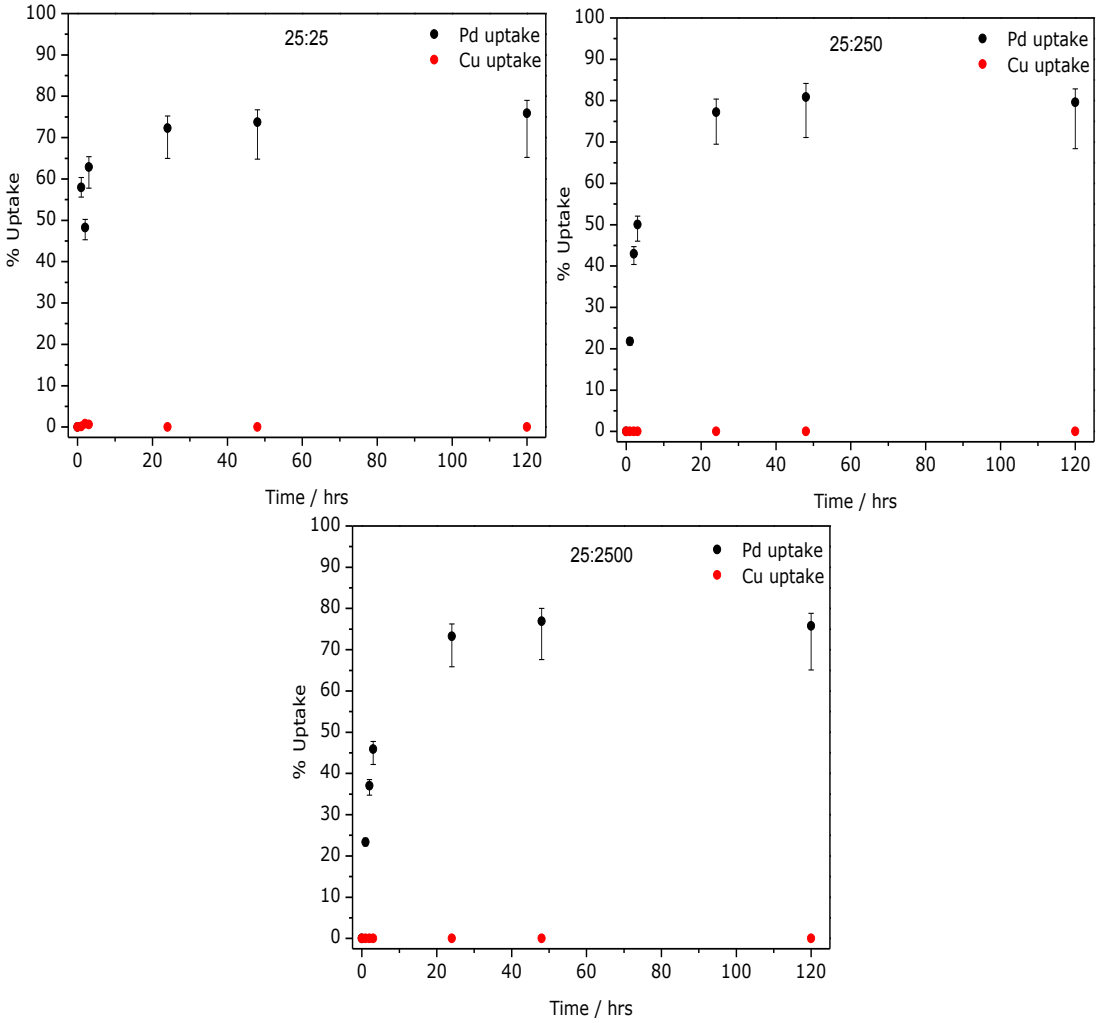


Figure 2.41. Uptake of Pd and Cu from mixed solutions of $K_2PdCl_6/CuCl_2$ of 25:25 ppm (top left), 25:250 ppm (top right) and 25:2500 ppm (bottom).

Similar results are also observed for the separation of Pd from $CuSO_4$ (Figure 2.42). Uptake of $PdCl_6^{2-}$ from a mixed 25:25 ppm Pd:Cu solution is 100% selective for Pd, with 75% $PdCl_6^{2-}$ uptake and no measureable extraction of $CuSO_4$. A very slight reduction in Cu concentration is observed from the 25:250 ppm solution, however this still corresponds to a 182:1 molar selectivity for Pd:Cu and an 18:1 ratio when the ten-fold mass difference between Cu and Pd is taken into account. The extraction of Pd from the 25:2500 ppm solution decreases to 38%, although the Cu uptake is just 1%, corresponding to a 33:1 ratio of Pd:Cu. Of greater importance is the fact that 75% of this Pd extraction occurs within the first three hours and over this time there

is no observable uptake of Cu. This means that UiO-66-NH_2 has the potential for quick and 100% selective uptake of Pd from sulfate solutions even in the presence of a large excess of Cu.

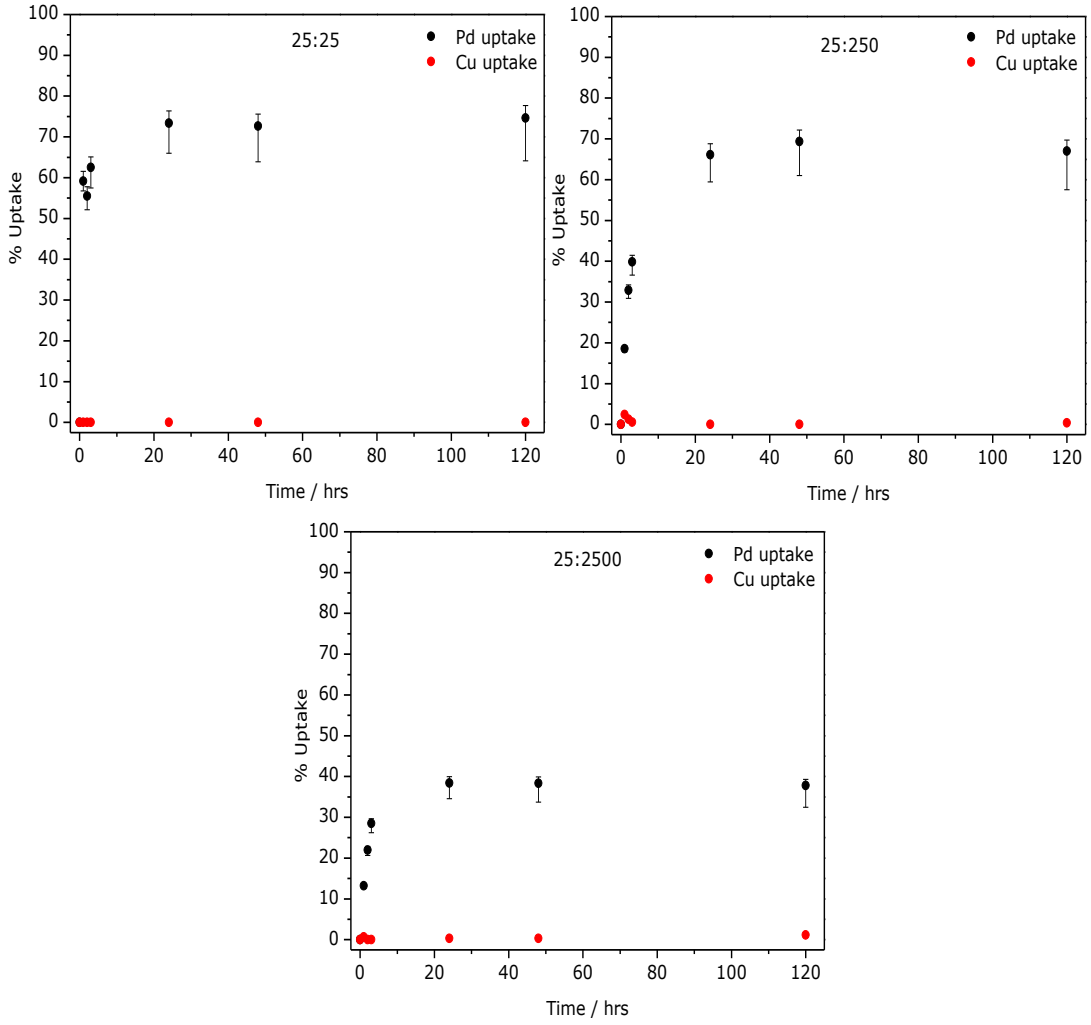


Figure 2.42. Uptake of Pd and Cu from mixed solutions of $K_2PdCl_6/CuSO_4$ of 25:25 ppm (top left), 25:250 ppm (top right) and 25:2500 ppm (bottom).

ICP-OES analysis of the digested MOFs from these mixed Pt/Cu and Pd/Cu experiments is in agreement with the results from solution as only trace amounts of Cu were found to be present in each case.

After every extraction experiment carried out using UiO-66-NH_2, PXRD patterns were recorded to confirm the stability of the MOF in the different solutions used.

Figure 2.43 shows that the MOF retains its crystallinity and phase after extraction and crucially that it exhibits no sign of amorphous character after the back-extraction of $PtCl_6^{2-}$ at 80 °C in 4 M HCl described earlier in the Chapter.

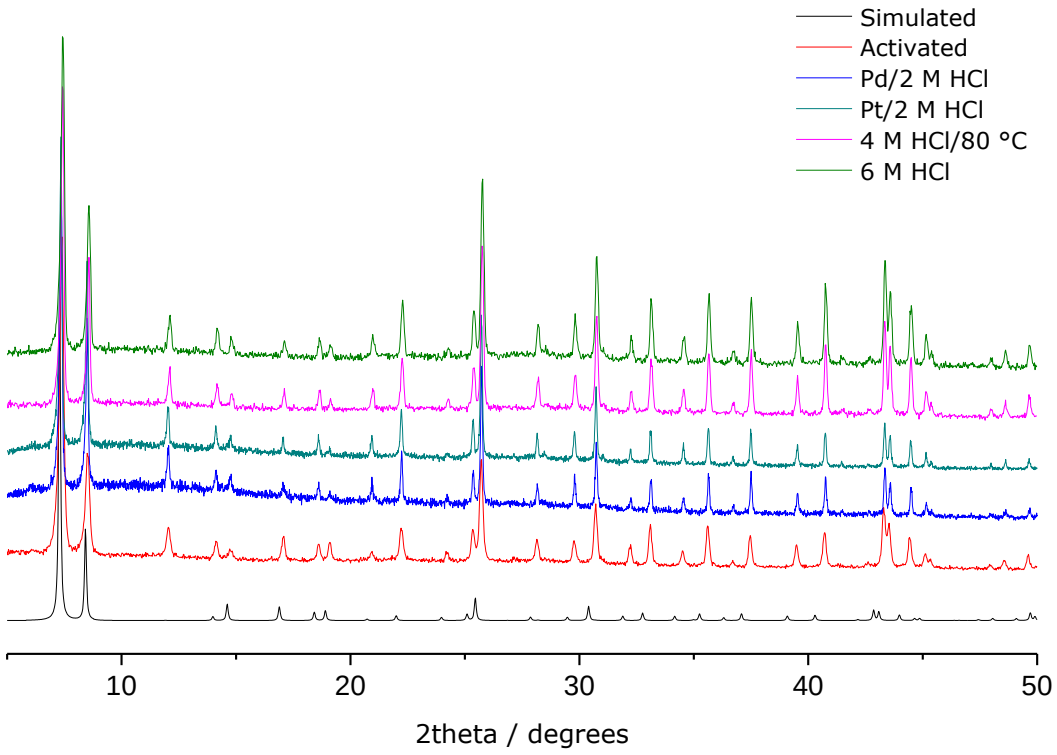


Figure 2.43. PXRD patterns showing the stability of UiO-66-NH_2 in HCl solutions.

Further work to be carried out with UiO-66-NH_2 will include ^{15}N DNP SS-NMR spectroscopy of the Pt and Pd-doped frameworks to provide additional information on the species encapsulated in the pore. This will be used to determine whether the interactions between the framework and the metal are hydrogen bonds from the NH_2 to the chloride groups of the PGM or covalent bonds from the NH_2 to the Pt/Pd centre. The separation of Ni from Pt and Pd will also be investigated as it is a major impurity in PGM-containing ores. Finally, the separation of Pd(II) species such as

$PdCl_2$ from $PtCl_6^{2-}$ will be examined as Pd(II) is the most common oxidation state of Pd used in industrial applications.

2.4 Current and Future Work

2.4.1 NOTT-300(Al) vs UiO-66

Whilst the presence of an NH_2 group within a MOF is clearly a big factor for the uptake of metal ions, the structure of the framework may also play a role. As shown with the extraction of $PtCl_6^{2-}$ from water into UiO-66, the lack of a functional group does not always inhibit the encapsulation of guest metal ions. Thus it was hypothesised that the cage structure within UiO-66 was responsible for the encapsulation of $PtCl_6^{2-}$ in the absence of a functional group. In particular, the potential for van der Waals interactions between the metal ions and the aromatic protons of the linkers and the oxygen atoms of the Zr-O clusters within the cage were thought to be responsible for the observed metal uptake. To establish a relationship between MOF structure and metal encapsulation, the uptake of UiO-66 was compared to that of a framework containing 1D channels, NOTT-300(Al), a MOF first reported by the Schröder group in 2012.[42] NOTT-300(Al) was chosen because, like UiO-66, it contains a non-functionalised linker and is stable to aqueous and acidic conditions (the framework does contain accessible OH groups, however they are not expected to contribute to metal encapsulation). The structure is comprised of octahedral 6-coordinate Al(III) ions bound to four carboxylate groups from the biphenyl tetracarboxylic acid linker and to two bridging OH groups. This gives rise to 1D channels, lined by the ligand, of 6.5 x 6.5 Å in diameter (Figure 2.44).

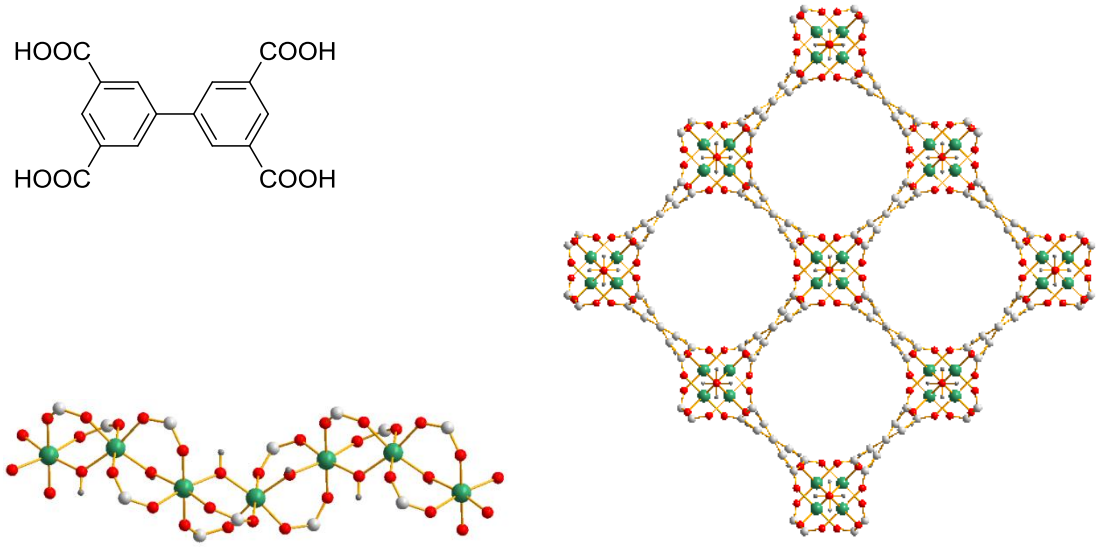


Figure 2.44. The linker (top left), Al(III) chain (bottom left) and 1D channels (right) present in NOTT-300(Al).[42]

These channels make NOTT-300(Al) an excellent comparative material for UiO-66 as the 6.5 Å diameter of the channels closely matches the 6.0 Å cavity windows in UiO-66. As the cages in UiO-66 provide a much larger number of aromatic protons to interact with the PGM in comparison to NOTT-300(Al), it was predicted that the uptake of $PtCl_6^{2-}$ from H_2O would be considerably lower in NOTT-300(Al) than that of the UiO MOFs. However, for the same reason we predicted that the uptake of $PtCl_6^{2-}$ from HCl in NOTT-300(Al) would not be greatly affected by the presence of Cl^- ions in solution as the vdW interactions between the framework and Cl^- would be much weaker than in UiO-66. The uptake of $PtCl_6^{2-}$ from 50 ml/25 ppm solutions in H_2O and 2 M HCl into 20 mg of NOTT-300(Al) is shown below in Figure 2.45.

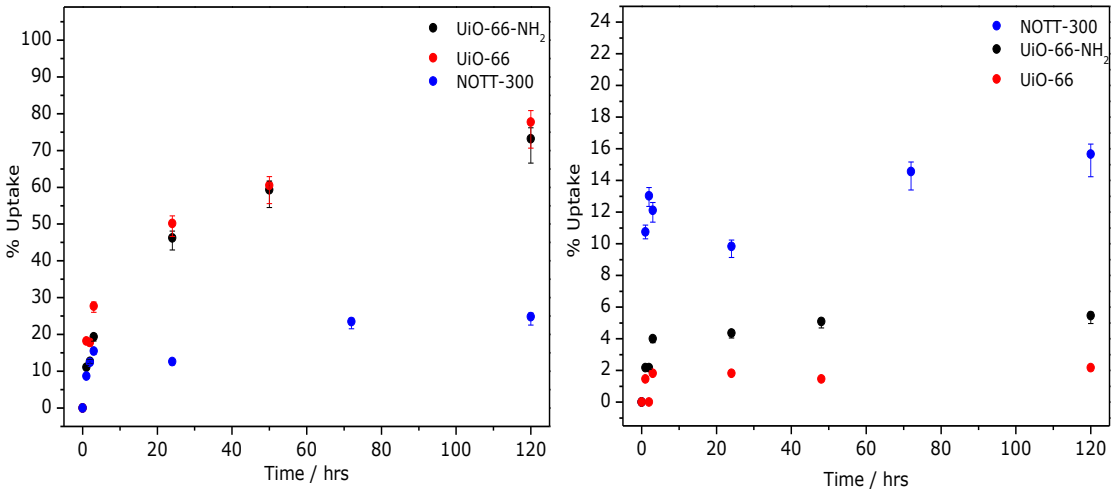


Figure 2.45. Comparison of $PtCl_6^{2-}$ extraction from 25 ppm solutions in H_2O (left) and 2M HCl (left) using UiO-66, UiO-66-NH_2 and NOTT-300(Al) as measured by ICP-OES.

As expected, the extraction from H_2O (25% after 120 hours) using NOTT-300(Al) is much lower than observed for UiO-66 and UiO-66-NH_2. However, whilst the uptake from 2 M HCl is just 16%, this is a 36% reduction from the H_2O experiment compared with the reductions of 97% and 93% for UiO-66 and UiO-66-NH_2 respectively. While NOTT-300(Al) may not be a good candidate for PGM extraction from HCl, this result strongly suggests that future work towards an amine-functionalised framework containing 1D channels may show great promise for this application.

2.4.2 Synthesis of New Amine-Containing Ligands

In addition to the metal scavenging described above, this work has also been focused on the organic synthesis of novel amine-functionalised linkers (Figure 2.46).

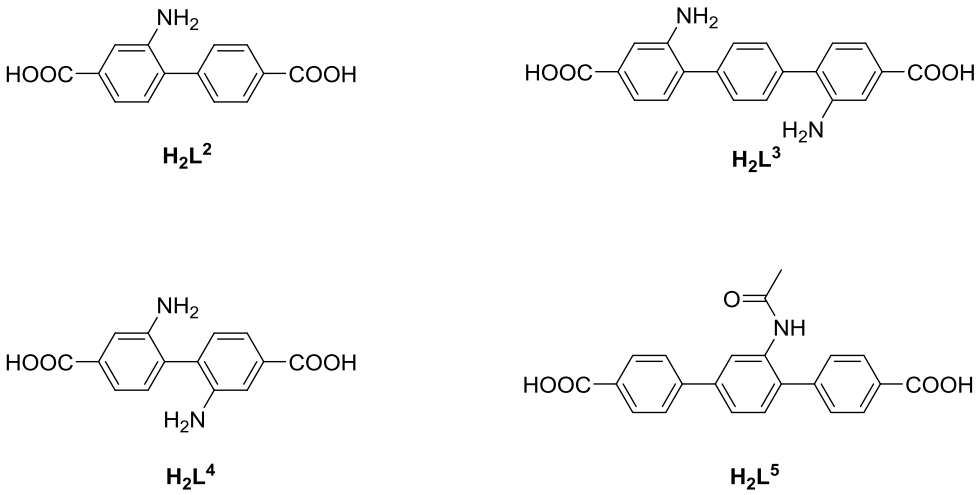
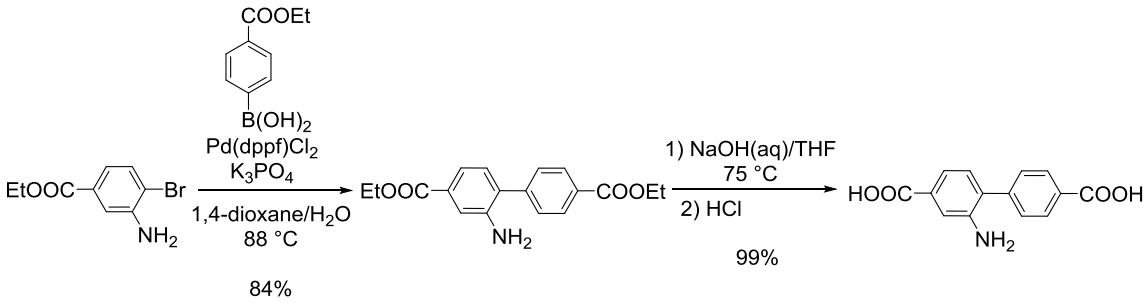


Figure 2.46. Amine-functionalised linkers for the synthesis of novel metal-organic frameworks.

These linkers will then be used for the preparation of new functionalised Zr(IV) MOFs. This work is currently on-going.

2.4.2.1 Synthesis of H_2L^2

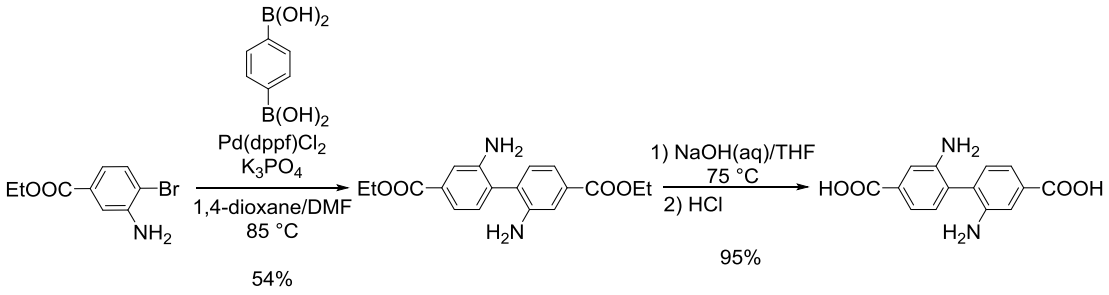
The first step in the synthesis of H_2L^2 was the esterification of 3-amino-4-bromobenzoic acid in acidified ethanol, followed by a Suzuki coupling of this ester with (4-(ethoxycarbonyl)phenyl)boronic acid (Scheme 2.2). These reagents were added to a mixture of 1,4-dioxane and DMF containing K_3PO_4 and $Pd(dppf)Cl_2$ and heated in a microwave reactor at 88 °C. The diester product resulting from this reaction was hydrolysed in NaOH(aq) and acidified with HCl to give H_2L^2.



Scheme 2.2. Synthesis of H_2L^2.

2.4.2.2 Synthesis of H_2L^3 and H_2L^4

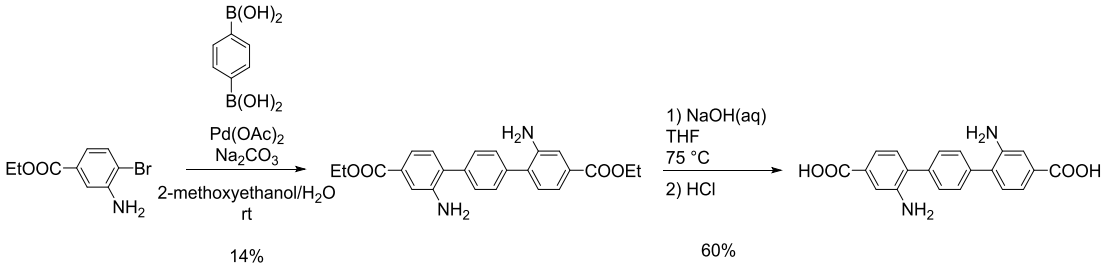
The synthesis of H_2L^3 was attempted as a facile way to increase the number of amine moieties on the dicarboxylate linker. The preparation involved the reaction of a diboronic acid with ethyl 3-amino-4-bromobenzoate using Pd(dppf)Cl_2 and K_3PO_4 in a mixture of 1,4-dioxane and DMF at 85 °C in a microwave reactor. However, upon analysis of the product there was no evidence of the desired triphenyl ester from ^{1}H NMR, ^{13}C NMR or MS. The synthesised product was determined to be a homocoupled diester (Scheme 2.3). Hydrolysis and subsequent acidification of this product gave a dicarboxylic acid, denoted as H_2L^4.



Scheme 2.3. Homocoupling reaction to produce H_2L^4.

Interestingly, the preparation of the homocoupled product was not possible without the addition of the boronic acid. Presumably the boronic acid was required to facilitate the reduction of the Pd(II) catalyst to the catalytically active Pd(0) species. In an attempt to prepare the desired H_2L^3 product, the reaction was repeated using

$Pd(OAc)_2$, Na_2CO_3 in a 2-methoxyethanol/H_2O mixture at room temperature (Scheme 2.4).

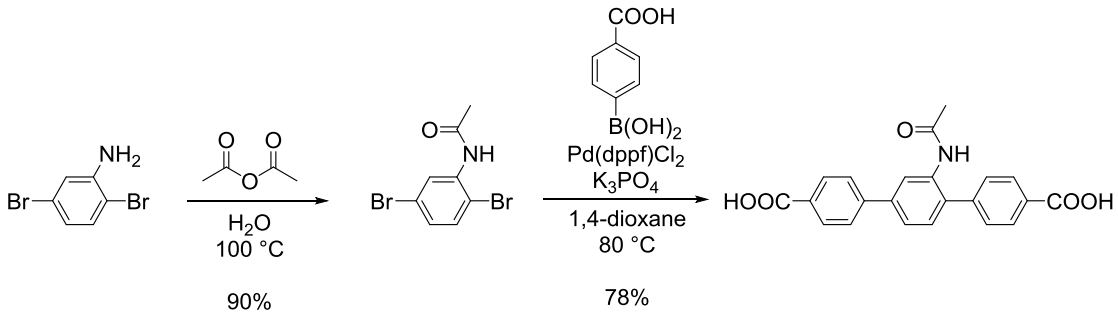


Scheme 2.4. Successful preparation of H_2L^3.

These conditions were adapted from a paper by Miyaura *et al.* in which the production of a homocoupled by-product was avoided using milder reagents and lower temperature.[43] These conditions did result in the formation of the desired product, albeit in low yield, as a brown solid, which was recrystallised from hot ethanol to give pure H_2L^3.

2.4.2.3 Synthesis of H_2L^5

The amide-functionalised H_2L^5 was synthesised to compare the effect of an amide group to that of an amine group for the extraction of $PtCl_6^{2-}$. The synthetic route involved the reaction of 2,5-dibromoaniline with acetic anhydride to give N-(2,5-dibromophenyl) acetamide in good yield (90%). This was then reacted with 4-carboxyphenyl boronic acid using K_3PO_4 base and $Pd(dppf)Cl_2$ catalyst in 1,4-dioxane at 80 °C (Scheme 2.5). The product was isolated after removing the solvent under vacuum, washed with $CHCl_3$, acidified with HCl and dried to give pure H_2L^5.



Scheme 2.5. Synthesis of H_2L^5.

The Suzuki coupling reaction was previously carried out using (4-(ethoxycarbonyl)phenyl)boronic acid, however the hydrolysis of the ethyl ester also partially cleaved the N-C amide bond, even under mild conditions at room temperature.

Unfortunately no successful reaction conditions for the formation of novel Zr(IV) MOFs with H_2L^2-H_2L^5 have yet been found. Reactions have produced either no product or amorphous powders as determined by PXRD.

2.5 Conclusions

In this Chapter we have demonstrated the capability of three Zr MOFs; UiO-68-NH_2, UiO-66-NH_2 and UiO-66 for the removal of PGMs from solution using ICP-OES and UV-vis absorption techniques. In particular, UiO-66-NH_2 exhibited an exceptional capacity for $PtCl_6^{2-}$ extraction from water in comparison to industrially used silica gels. This framework also showed good sorption capacity for $PtCl_6^{2-}$ and $PdCl_6^{2-}$ from acidic HCl solutions, which represents the first example of a MOF successfully being used for this application. Furthermore, a solid state NMR study showed clear evidence of the interaction between the MOF and these PGM anions. Sorption experiments on mixed metal solutions showed that UiO-66-NH_2 was able to separate Pd(IV) from Pt(IV) very efficiently (20:1 uptake of Pd:Pt). In addition to

Pd:Pt separations, UiO-66-NH_2 demonstrated 100% selective sorption of $PtCl_6^{2-}$ and $PdCl_6^{2-}$ over both $CuCl_2$ and $CuSO_4$ including cases in which Cu was in 100-fold excess.

More recent work on NOTT-300(Al) has shown that the design of a MOF to incorporate NH_2-functionalised 1D channels may greatly enhance the sorption of PGM chlorides from HCl solutions. We have also synthesised a series of amine and amide-functionalised linkers and work to trial reaction conditions for the successful synthesis of novel Zr(IV) MOFs is ongoing.

2.6 Experimental

Synthesis of (4-(ethoxycarbonyl)phenyl)boronic acid

4-Carboxybenzene boronic acid (20 g, 120.5 mmol) was dissolved in a mixture of ethanol (250 ml) and 95% sulfuric acid (8 ml) and heated at 85 °C for 16 h. Upon cooling, the solvent volume was reduced to ~ 75 ml under vacuum and H_2O (200 ml) was added to precipitate the product as a white solid. This solid was isolated by filtration, washed with H_2O (3 x 25 ml) and dried under vacuum to give the pure product (22.1 g, 95%). ^{1}H NMR (400 MHz, dmso-d_6) δ = 7.92 (s, 4H), 4.32 (q, 2H, *J* = 7.0 Hz), 1.33 (t, 3H, *J* = 7.0 Hz); ^{13}C{^{1}H} NMR (100 MHz, dmso-d_6) δ = 166.4, 134.7, 131.6, 128.4, 61.2, 14.6. MS(ESI) m/z 195 (M + H). Anal. Calcd (Found) for $C_9H_{11}BO_4$: C, 55.72 (55.77); H, 5.72 (5.79)%.

Synthesis of H_2L^1

(4-(Ethoxycarbonyl)phenyl)boronic acid (2.80 g, 14.43 mmol) was added to a mixture of 2,5-dibromoaniline (1.50 g, 5.98 mmol) and K_3PO_4 (3.06 g, 14.43 mmol) in 1,4-dioxane/H_2O (55 ml; 10:1 v/v). Pd(dppf)Cl_2 (60 mg) was then added under an

argon atmosphere and the vessel was heated under argon at 90 °C for 24 h. Once the reaction was complete, the solvent was removed under reduced pressure and the resulting residue was extracted into $CHCl_3$. The $CHCl_3$ was removed under reduced pressure to give a brown oil. This oil was then extracted into $CHCl_2$ and passed through a plug of silica gel. After evaporation of CH_2Cl_2, the pure product was isolated as a yellow solid (1.76 g, 4.52 mmol, 76%). ^{1}H NMR (270 MHz, dmso-d_6) δ = 8.04 (dd, 4H, *J* = 8.1, 1.4 Hz), 7.77 (d, 2H, *J* = 8.6 Hz), 7.64 (d, 2H, *J* = 8.4 Hz), 7.18 (s, 1H), 7.16 (d, 1H, *J* = 2.7 Hz), 7.01 (dd, 1H, *J* = 8.1, 1.6 Hz), 4.36 (q, 4H, *J* = 5.1 Hz), 1.34 (t, 6H, *J* = 7.0 Hz). MS(ESI) m/z 390 (M + H).

This diester (1.39 g, 3.57 mmol) was added to a solution of THF (30 ml) and 2 M NaOH(aq) (30 ml) and heated at 75 °C for 16 h. The aqueous layer was then separated and the organic layer washed with fresh 2 M NaOH(aq) (2 x 15 ml). The aqueous layers were combined and 37% HCl was added dropwise until pH~1, giving a yellow precipitate. This precipitate was filtered, dried and recrystallised from hot DMF to give H_2L^1 as a yellow solid (1.06 g, 3.18 mmol, 89%). ^{1}H NMR (400 MHz, dmso-d_6) δ = 12.98 (s, 2H) 8.04 (d, 4H, *J* = 8.0 Hz), 7.76 (d, 2H, *J* = 8.4 Hz), 7.63 (d, 2H, *J* = 8.4 Hz), 7.18 (d, 1H, *J* = 4.0 Hz), 7.17 (d, 1H, *J* = 2.0 Hz), 7.03 (dd, 1H, *J* = 8.0, 1.8 Hz), 5.13 (s, 2H); ^{13}C{^{1}H} NMR (100 MHz, dmso-d_6) δ = 167.7, 167.6, 146.3, 145.0, 144.3, 140.0, 131.3, 130.5, 130.4, 130.3, 129.2, 127.7, 127.0, 116.0, 114.3. MS(ESI) m/z 332 (M - H). Anal. Calcd (Found) for $C_{20}H_{15}N_1O_4$: C, 72.06 (71.39); H, 4.54 (4.42); N, 4.20 (3.97)%.

Synthesis of ethyl 3-amino-4-bromobenzoate

3-Amino-4-bromobenzoic acid (2 g, 9.26 mmol) was dissolved in a mixture of ethanol (40 ml) and 95% sulfuric acid (1.1 ml) and heated at 85 °C for 16 h. Upon

cooling, the solvent volume was reduced to ~ 20 ml and H_2O (100 ml) was added, forming a mass of white precipitate. This precipitate was isolated by filtration, washed with H_2O (3 x 25 ml) and dried under vacuum to give ethyl 3-amino-4-bromobenzoate as an off-white solid (1.41 g, 62%). ^{1}H NMR (400 MHz, dmso-d_6) δ = 7.47 (d, 1H, *J* = 8.4 Hz), 7.42 (d, 1H, *J* = 2.1 Hz), 7.03 (dd, 1H, *J* = 8.4, 2.0 Hz), 4.27 (q, 2H, *J* = 7.2 Hz), 1.34 (t, 3H, *J* = 7.2 Hz).

Synthesis of H_2L^2

Ethyl 3-amino-4-bromobenzoate (800 mg, 3.28 mmol), (4-(ethoxycarbonyl)phenyl) boronic acid (763 mg, 3.93 mmol, 1.2 eq.) and K_3PO_4 (3.47 g, 16.3 mmol, 5 eq.) were dissolved in a degassed mixture of 1,4-dioxane/H_2O (10:1; 55 ml). Pd(dppf)Cl_2 (30 mg) was added under an argon atmosphere and the solution was heated at 88 °C for 1 hour in a microwave reactor. Upon completion of the reaction, the solvent was removed under vacuum and the crude product was extracted into $CHCl_3$. After removal of $CHCl_3$ under reduced pressure, the product was dissolved in CH_2Cl_2 and passed through a plug of silica gel. After evaporation of CH_2Cl_2, a pale orange/yellow oil was isolated. Trituration of this oil with H_2O gave the product as a pale yellow solid (867 mg, 84%). ^{1}H NMR (400 MHz, dmso-d_6) δ = 8.05 (dd, 2H, *J* = 5.6, 1.8 Hz), 7.62 (dd, 2H, *J* = 7.0, 1.8 Hz), 7.45 (d, 1H, *J* = 1.6 Hz), 7.24 (dd, 1H, *J* = 7.8, 1.8 Hz), 7.16 (d, 1H, *J* = 8.0 Hz), 4.37 (q, 2H, *J* = 7.2 Hz), 4.32 (q, 2H, *J* = 7.2 Hz), 1.36 (t, 3H, *J* = 7.2 Hz), 1.32 (t, 3H, *J* = 7.2 Hz); ^{13}C{^{1}H} NMR (100 MHz, dmso-d_6) δ = 166.4, 166.0, 146.0, 144.1, 130.8, 130.1, 129.4, 129.1, 129.0, 117.6, 116.4, 61.2, 61.0, 14.7. MS(ESI) m/z 314 (M + H).

This diester (850 mg, 2.71 mmol) was dissolved in a mixture of THF (25 ml) and 2 M NaOH (25 ml) and heated at 75 °C for 16 h. Upon cooling, the aqueous layer was

separated and the organic layer washed with fresh 2 M NaOH(aq) (2 x 15 ml). The aqueous layers were combined and 37% HCl was added until pH~1 to give an off-white precipitate. This solid was isolated by filtration and washed with H_2O (30 ml) and EtOH (30 ml) and dried under vacuum to give H_2L^2 as an off-white solid (693 mg, 99%). ^{1}H NMR (400 MHz, dmso-d_6) δ = 8.05 (d, 2H, *J* = 8.0 Hz), 7.66 (m, 3H), 7.47 (d, 1H, *J* = 7.6 Hz), 7.28 (d, 1H, *J* = 7.6 Hz); ^{13}C{^{1}H} NMR (100 MHz, dmso-d_6) δ = 167.6, 167.5, 142.9, 131.7, 131.2, 130.5, 130.4, 130.3, 129.4, 127.7. MS(ESI) m/z 256 (M - H). Anal. Calcd (Found) for $C_{14}H_{11}N_1O_4$: C, 65.37 (64.68); H, 4.31 (4.26); N, 5.45 (4.83)%.

Synthesis of H_2L^3

Ethyl 3-amino-4-bromobenzoate (976 mg, 4.00 mmol), 1,4-benzene diboronic acid (1.59 mg, 9.60 mmol) and Na_2CO_3 (1.02 g, 9.60 mmol) were dissolved in a degassed mixture of 2-methoxyethanol/water (4:1; 40 ml). $Pd(OAc)_2$ (200 mg) was added under an argon atmosphere and the solution was left to stir at room temperature for 48 h. Once the reaction was complete, the solvent was removed under vacuum and the crude product was isolated as a dark brown oil. After triturating with water, the crude product was recrystallised from hot ethanol to give the product as a pale brown solid (233 mg, 14%).

This diester (200 mg) was dissolved in a mixture of THF (25 ml) and 2 M NaOH (25 ml) and heated at 75 °C for 16 h. Upon cooling, the aqueous layer was separated and the organic layer washed with fresh 2 M NaOH(aq) (2 x 15 ml). The aqueous layers were combined and 37% HCl was added until pH~1 to give an off-white precipitate. This solid was isolated by filtration and washed with H_2O (30 ml) and EtOH (30 ml) and dried under vacuum to give H_2L^3 as an off-white solid (104 mg, 60%). ^{1}H NMR

(400 MHz, dmso-d_6) δ = 7.91 (dd, 2H, *J* = 9.0 Hz, 2.0 Hz), 7.84 (s, 2H), 7.73 (dd, 2H, *J* = 5.6 Hz, 2.0 Hz), 7.68 (s, 4H); $^{13}C\{^1H\}$ NMR (100 MHz, dmso-d_6) δ = 167.2, 139.7, 137.2, 131.4, 130.1, 129.9, 127.6, 117.7, 116.3.

Synthesis of H_2L^4

Ethyl 3-amino-4-bromobenzoate (776 mg, 3.18 mmol), 1,4-benzene diboronic acid (285 mg, 1.72 mmol) and K_3PO_4 (1.12 g, 5.28 mmol) were dissolved in a degassed mixture of 1,4-dioxane/DMF (2:1; 30 ml) in a 35 ml microwave tube. Pd(dppf)Cl_2 (30 mg) was added under an argon atmosphere and the solution was heated at 85 °C in a microwave reactor for 30 mins. Once the reaction was complete, the solvent was removed under vacuum and the crude product was extracted into $CHCl_3$. After removal of $CHCl_3$ under reduced pressure, the product was dissolved in CH_2Cl_2 and passed through a plug of silica gel. After evaporation of CH_2Cl_2, a pale orange/yellow oil was isolated. Trituration of this oil with H_2O gave the product as a pale yellow solid (305 mg, 54%). ^1H NMR (300 MHz, dmso-d_6) δ = 7.48 (s, 1H), 7.45 (s, 1H), 7.42 (d, 2H, *J* = 2.1 Hz), 7.03 (d, 1H, *J* = 2.1 Hz), 7.01 (d, 1H, *J* = 2.1 Hz), 5.62 (s, 4H), 4.27 (q, 4H, *J* = 7.2 Hz), 1.27 (t, 6H, *J* = 7.2 Hz); $^{13}C\{^1H\}$ NMR (75 MHz, dmso-d_6) δ = 166.1, 146.6, 133.0, 130.4, 117.9, 115.9, 112.7, 61.1, 14.6. MS(ESI) m/z 329 (M + H).

This diester (300 mg) was dissolved in a mixture of THF (25 ml) and 2M NaOH (25 ml) and heated at 75 °C for 16 h. Upon cooling, the aqueous layer was separated and the organic layer washed with fresh 2 M NaOH(aq) (2 x 15 ml). The aqueous layers were combined and 37% HCl was added until pH~1 to give a white precipitate. This precipitate was isolated by filtration and washed with H_2O (30 ml) and EtOH (30 ml) and dried under vacuum to give H_2L^4 as an off-white solid (237 mg, 95%). ^1H NMR

(300 MHz, dmso-d_6) δ = 7.46 (s, 1H), 7.43 (s, 1H), 7.41 (d, 2H, *J* = 2.1 Hz), 7.03 (d, 1H, *J* = 2.1 Hz), 7.00 (d, 1H, *J* = 2.1 Hz); $^{13}C\{^1H\}$ NMR (75 MHz, dmso-d_6) δ = 167.6, 146.2, 132.8, 131.3, 118.4, 116.5, 112.5. MS(ESI) m/z 271 (M – H).

Synthesis of H_2L^5

2,5-Dibromoaniline (3.15 g, 12.55 mmol) was added to a mixture of acetic anhydride (11 ml) and H_2O (11 ml) and heated at 100 °C for 4 h. The resulting light brown precipitate was then added to water (100 ml) and stirred at room temperature for 1 hour. This solid was isolated by filtration and dried under vacuum giving N-(2,5-dibromophenyl)acetamide (3.31 g, 90%). ^1H NMR (400 MHz, dmso-d_6) δ = 9.59 (s, 1H), 7.87 (d, 1H, *J* = 2.4 Hz), 7.61 (d, 1H, *J* = 8.6 Hz), 7.32 (dd, 1H, *J* = 8.6, 2.4 Hz), 2.10 (s, 3H); $^{13}C\{^1H\}$ NMR (100 MHz, dmso-d_6) δ = 169.3, 138.4, 134.7, 129.7, 129.4, 120.7, 116.6, 23.8.

N-(2,5-dibromophenyl)acetamide (1.00 g, 3.41 mmol), 4-carboxyphenyl boronic acid (1.47 g, 8.86 mmol), K_3PO_4 (3.60 g, 16.98 mmol) and Pd(dppf)Cl_2 (14 mg) were added to degassed 1,4-dioxane (35 ml) and heated under argon at 80 °C for 48 h. Upon completion of the reaction, the solvent was removed under vacuum to give a light brown solid which was washed with $CHCl_3$, acidified with 37% HCl to pH~1 and dried to give the product as an off-white powder (1.23 g, 78%). ^1H NMR (270 MHz, dmso-d_6) δ = 9.50 (s, 1H), 8.03 (t, 4H, *J* = 8.5 Hz), 7.84 (t, 3H, *J* = 8.6 Hz), 7.69 (dd, 1H, *J* = 8.1, 1.5 Hz), 7.54 (dd, 2H, *J* = 6.8, 5.0 Hz), 7.49 (d, 1H, *J* = 8.0 Hz), 1.93 (s, 3H); $^{13}C\{^1H\}$ NMR (100 MHz, dmso-d_6) δ = 169.4, 167.7, 167.6, 143.7, 143.5, 139.4, 136.1, 135.8, 131.4, 130.6, 129.9, 129.3, 127.6, 127.2, 126.1, 124.9, 23.5. Anal. Calcd (Found) for $C_{22}H_{17}N_1O_5$: C, 70.39 (69.28); H, 4.56 (4.39); N, 3.73 (3.82)%.

Synthesis of [1,1'-biphenyl]-3,3',5,5'-tetracarboxylic acid

3,3',5,5'-Tetramethylbiphenyl (5 g, 23.06 mmol) and NaOH (3.69 g, 92.24 mmol) were dissolved in ^{t}BuOH/H_2O (1:1, 250 ml). The reaction mixture was heated to 50 °C with stirring and portions of $KMnO_4$ (totalling 44 g, 276.72 mmol) were added to the solution once the purple colour of the previous portion had faded. After 35 g of $KMnO_4$ had been added, the reaction temperature was increased to 70 °C and the addition of $KMnO_4$ continued until the purple colour persisted for over 3 h, indicating full oxidation of the methyl groups. Excess $KMnO_4$ was reduced by addition of IPA (100 ml) and the solution was filtered whilst hot. The MnO_2 cake was washed with boiling water (250 ml) and the aqueous filtrate was concentrated to ~ 50 ml by evaporation and acidified with 37% HCl to pH ~ 1. The resulting white precipitate was collected by filtration, recrystallised from hot DMF and washed with water to give pure [1,1'-biphenyl]-3,3',5,5'-tetracarboxylic acid as a white solid (5.79 g, 76%). ^{1}H NMR (400 MHz, dmso-d_6) δ = 13.51 (s, 4H), 8.53 (t, 2H, J = 1.6 Hz), 8.45 (d, 4H, J = 1.6 Hz); ^{13}C{^{1}H} NMR (100 MHz, dmso-d_6) δ = 166.8, 139.7, 132.8, 131.9, 130.0. Anal. Calcd (Found) for $C_{16}H_{10}O_8$: C, 58.19 (57.29); H, 3.05 (3.00); N, 0.00 (0.00)%.

Synthesis of UiO-66-NH_2

2-Aminoterephthalic acid (310 mg, 1.71 mmol), $ZrCl_4$ (400 mg, 1.71 mmol) and benzoic acid (6.25 g, 51.2 mmol) were dissolved in DMF (100 ml) and heated in a sealed round bottom pressure flask at 120 °C for 48 h. The resulting off-white precipitate was isolated by centrifugation and washed with fresh DMF which was exchanged with acetone over the course of 5 days. Removal of all volatiles under vacuum produced the final product as a pale yellow solid (455 mg, 91%). Anal.

Calcd (Found) for $Zr_6C_{48}H_{34}N_6O_{32}$: C, 32.87 (32.71); H, 1.95 (1.98); N, 4.79 (4.66)%.

Synthesis of UiO-66

Terephthalic acid (284 mg, 1.71 mmol), $ZrCl_4$ (400 mg, 1.71 mmol) and benzoic acid (6.25 g, 51.2 mmol) were dissolved in DMF (100 ml) and heated in a sealed round bottom pressure flask at 120 °C for 48 h. The resulting white precipitate was isolated by centrifugation and washed with fresh DMF which was exchanged with acetone over the course of 5 days. Removal of all volatiles under vacuum produced the final product as a white solid (372 mg, 78%). Anal. Calcd (Found) for $Zr_6C_{48}H_{28}O_{32}$: C, 34.65 (34.24); H, 1.70 (1.68); N, 0.00 (0.00)%.

Synthesis of UiO-68-NH_2·16DMF·2H_2O

H_2L^1 (20 mg, 0.06 mmol), $ZrCl_4$ (14 mg, 0.06 mmol) and benzoic acid (250 mg, 2.05 mmol) were dissolved in DMF (4 ml) and heated in a sealed 15 ml pressure tube at 120 °C for 72 h. The resulting colourless crystals were isolated by filtration, washed with hot DMF and dried in air to give the final product (32 mg, 83%) Anal. Calcd (Found) for $Zr_6C_{168}H_{194}N_{22}O_{50}$: C, 52.16 (51.83); H, 5.05 (4.81); N, 7.97 (7.99)%.

Synthesis of NOTT-300(Al)

Biphenyl tetracarboxylic acid (120 mg, 0.36 mmol), $Al(NO_3)_3·9H_2O$ (680 mg, 1.81 mmol) and piperazine (200 mg, 2.32 mmol) were added to a solution of HNO_3 (0.68 ml) and water (30 ml). This mixture was heated at 210 °C in a stainless steel autoclave for three days. Upon cooling, the solvent was decanted and the solid product was washed with hot DMF (25 ml x 3), hot methanol (25 ml x 3) and dried

under vacuum to give desolvated NOTT-300(Al) as a pale yellow powder (89 mg, 59%).

2.7 References

1. Bosch, M.; Zhang, M.; Zhou, H-C., *Adv. Chem.*, **2014**, *2014*, 1.
2. Cavka, J. H.; Jakobsen, S.; Olsbye, U.; Guillou, N.; Lamberti, C.; Bordiga, S.; Lillerud, K. P., *J. Am. Chem. Soc.*, **2008**, *130*, 13850.
3. Furukawa, H.; Gàndara, F.; Zhang, Y-B.; Jiang, J.; Queen, W. L.; Hudson, M. R.; Yaghi, O. M., *J. Am. Chem. Soc.*, **2014**, *136*, 4369.
4. Mondloch, J. E.; Katz, M. J.; Isley III, W. C.; Ghosh, P.; Liao, P.; Bury, W.; Wagner, G. W.; Hall, M. G.; DeCoste, J. B.; Peterson, G. W.; Snurr, R. Q.; Cramer, C. J.; Hupp, J. T.; Farha, O. K., *Nature Mater.*, **2015**, *14*, 512.
5. Liu, Y.; Howarth, A. J.; Hupp, J. T.; Farha, O. K., *Angew. Chem., Int. Ed.*, **2015**, *54*, 9001.
6. Moon, S-Y.; Liu, Y.; Hupp, J. T.; Farha, O. K., *Angew. Chem., Int. Ed.*, **2015**, *54*, 6795.
7. Katz, M. J.; Mondloch, J. E.; Totten, R. K.; Park, J. K.; Nguyen, S. T.; Farha, O. K.; Hupp, J. T., *Angew. Chem., Int. Ed.*, **2014**, *53*, 497.
8. Bandosz, T. J.; Laskoski, M.; Mahle, J.; Mogilevsky, G.; Peterson, G. W.; Rossin, J. A.; Wagner, G. W., *J. Phys. Chem. C*, **2012**, *116*, 11606.
9. Decoste, J. B.; Peterson, G. W., *Chem. Rev.*, **2014**, *114*, 5695.
10. Cunha, D.; Gaudin, C.; Colinet, I.; Horcajada, P.; Maurin, G.; Serre, C., *J. Mater. Chem.*, **2013**, *1*, 1101.
11. Cunha, D.; Yahia, M. B.; Hall, S.; Miller, S. R.; Chevreau, H.; Elkaïm, E.; Maurin, G.; Horcajada, P. Serre, C., *Chem. Mater.*, **2013**, *25*, 2767.
12. Abney, C. W.; Taylor-Pashow, K. M. L.; Russell, S. R.; Chen, Y.; Samantaray, R.; Lockard, J. V.; Lin, W., *Chem. Mater.*, **2014**, *26*, 5231.
13. Zhang, W.; Huang, H.; Liu, D.; Yang, Q.; Xiao, Y.; Ma, Q.; Zhong, C., *Micropor. Mesopor. Mat.*, **2013**, *171*, 118.
14. Yang, X-L.; Qiao, L-M.; Dai, W-L., *Micropor. Mesopor. Mat.*, **2015**, *211*, 73.
15. Xiao, C.; Goh, T. W.; Brashler, K.; Pei, Y.; Guo, Z.; Huang, W., *J. Phys. Chem. B*, **2014**, *118*, 14168.
16. Guo, Z.; Kobayashi, T.; Wang, L-L.; Goh, T. W.; Xiao, C.; Caporini, M. A.; Rosay, M.; Johnson, D. D.; Pruski, M.; Huang, W., *Chem. Eur. J.*, **2014**, *20*, 16308.
17. Carboni, M.; Abney, C. W.; Liu, S.; Lin, W., *Chem. Sci.*, **2013**, *4*, 2396.

18. Saito, K.; Miyauchi, T., *J. Nucl. Sci. Technol.*, **1982**, *19*, 145.
19. Kester, D. R.; Duedall, I. W.; Connors, D. N.; Pytkowicz, R. M., *Limnol. Oceanogr.*, **1967**, *12*, 176.
20. Zhang, Y.; Zhao, X.; Huang, H.; Li, Z.; Liu, D.; Zhong, C., *RSC Adv.*, **2015**, *5*, 72107.
21. Luz, I.; Rösler, C.; Epp, K.; Xamena, F. X. L.; Fischer, R. A., *Eur. J. Inorg. Chem.*, **2015**, 3904.
22. Xu, Z.; Yang, L.; Xu, C., *Anal. Chem.*, **2015**, *87*, 3438.
23. Guo, Z.; Xiao, C.; Maligal-Ganesh, R. V.; Zhou, L.; Goh, T. W.; Li, X.; Tesfagaber, D.; Thiel, A.; Huang, W., *ACS Catal.*, **2014**, *4*, 1340.
24. Wang, C.; deKrafft, K. E.; Lin, W., *J. Am. Chem. Soc.*, **2012**, *134*, 7211.
25. Bell, K. J.; Westra, A. N.; Warr, R. J.; Chartres, J.; Ellis, R.; Tong, C. C.; Blake, A. J.; Tasker, P. A.; Schröder, M., *Angew. Chem., Int. Ed.*, **2008**, *47*, 1745.
26. Warr, R. J.; Westra, A. N.; Bell, K. J.; Chartres, J.; Ellis, R.; Tong, C. C.; Simmance, T. G.; Gadzhieva, A.; Blake, A. J.; Tasker, P. A.; Schröder, M., *Chem. Eur. J.*, **2009**, *15*, 4836.
27. Schaate, A.; Roy, P.; Godt, A.; Lippke, J.; Waltz, F.; Wiebcke, M.; Behrens, P., *Chem. Eur. J.*, **2011**, *17*, 6643.
28. Schefer, J.; Schwarzenbach, D.; Fischer, P.; Koetzle, T.; Larsen, F. K.; Haussühl, S.; Rüdlinger, M.; McIntyre, G.; Bürkedal, H.; Bürgi, H-B., *Acta Cryst.*, **1998**, *54*, 121.
29. Pattou, L.; Lorand, J. P.; Gros, M., *Nature*, **1996**, *379*, 712.
30. Yang, Q.; Guillerm, V.; Ragon, F.; Wiersun, A. D.; Llewellyn, P. L.; Zhong, C.; Devic, T.; Serre, C.; Maurin, G., *Chem. Commun.*, **2012**, *48*, 9831.
31. Katz, M. J.; Brown, Z. J.; Colón, Y. J.; Siu, P. W.; Scheidt, K. A.; Snurr, R. Q.; Hupp, J. T.; Farha, O. K., *Chem. Commun.*, **2013**, *49*, 9449.
32. Kim, M.; Cahill, J. F.; Prather, K. A.; Cohen, S. M., *Chem Commun.*, **2011**, *47*, 7629.
33. Kandiah, M.; Usseglio, S.; Olsbye, U.; Lillerud, K. P.; Tilset, M., *J. Mater. Chem.*, **2010**, *20*, 9848.
34. DeCoste, J. B.; Peterson, G. W.; Jasuja, H.; Glover, T. G.; Huang, Y.; Walton, K. S., *J. Mater. Chem. A*, **2013**, *1*, 5642.
35. Vermootele, F.; Ameloot, R.; Vimont, A.; Serre, C.; De Vos, D., *Chem. Commun.*, **2011**, *47*, 1521.
36. US Pat., US2006237371A1, **2006**.
37. US Pat., US20130158210A1, **2013**.
38. Devautour-Vinot, S.; Maurin, G.; Serre, C.; Horcajada, P.; Cunha, D.; Guillerm, V.; de Souza Costa, E.; Taulelle, F.; Martineau, C., *Chem. Mater.*, **2012**, *24*, 2168.

39. Kramer, J.; Driessen, W. L.; Kock, K. R.; Reedijk, J., *Hydrometallurgy*, **2002**, *64*, 59.
40. Kononova, O. N.; Melnikov, A. M.; Demitrichenko, D. S., *Solvent Extr. Ion Exc.*, **2013**, *31*, 306.
41. Bernardis, F. L.; Grant, R. A.; Sherrington, D. C., *React. Funct. Polym.*, **2005**, *65*, 205.
42. Yang, S.; Sun, J.; Ramirez-Cuesta, A. J.; Callear, S. K.; David, W. I. F.; Anderson, D. P.; Newby, R.; Blake, A. J.; Parker, J. E.; Tang, C. C.; Schröder, M., *Nature Chem.*, **2012**, *4*, 887.
43. Ishiyama, T.; Murata, M.; Miyaura, N., *J. Org. Chem.*, **1995**, *60*, 7508.

Chapter 3

PGM Scavenging from Organic Solvents

Using Functionalised Cu(II) MOFs

3.1 Introduction

PGM-catalysed cross-coupling reactions for the formation of C-C bonds have arguably become the most important chemical processes used in industrial applications.[1] Procedures such as Heck,[2,3] Sonogashira,[4,5] Negishi[6,7] and Suzuki[8-11] cross-coupling reactions generally employ a Pd(II) or Pd(0) catalyst (Figure 3.1).[1,12] Likewise, Pt and Rh catalysts are also commonly used in C-C bond forming,[13,14] C-H activation[15,16] and direct borylation reactions.[17,18] Upon completion of these reactions, the catalyst must be separated from the product to avoid the loss of the PGM into a waste stream and to avoid contamination of the product, which is of particular importance for pharmaceuticals.[19] Heterogeneous catalysts may be easily removed from the final product, however cross-coupling reactions often use homogeneous catalysts which present significant separation problems.[19]

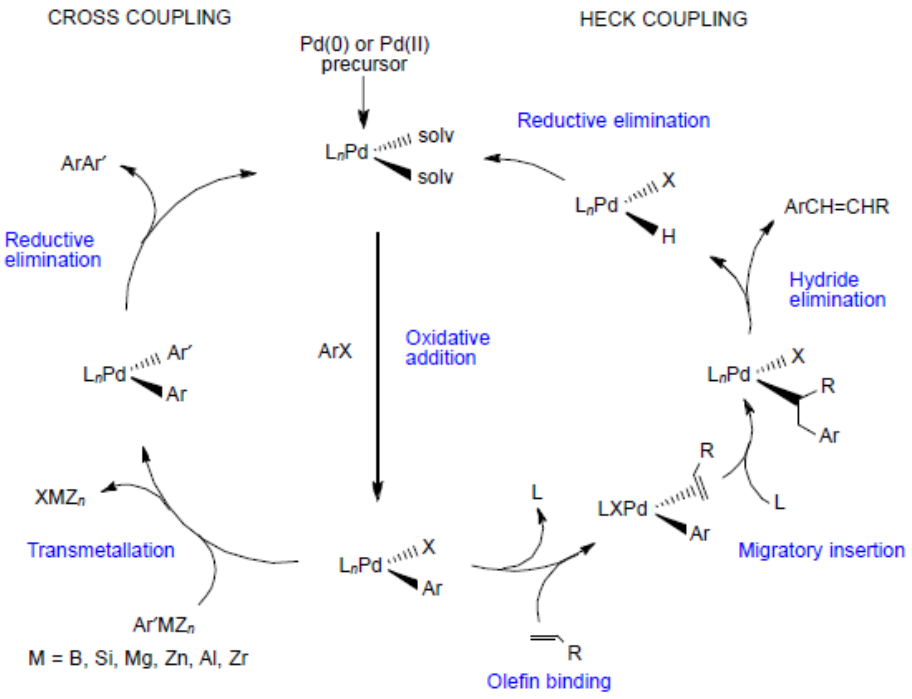


Figure 3.1. Mechanism of the Heck reaction and related cross-coupling reactions. Reproduced from reference 12.

These problems can be overcome by recrystallisation, although this often results in a significant loss of product.[1] An alternative to recrystallisation is to use a material capable of scavenging the residual catalyst from solution.[19] The key advantage of such materials is that their chemical functionality may be tuned specifically to afford high affinity for the residual metal.[20] For the selective uptake of PGM catalysts, these scavengers usually include amine and thiol functional groups. For example, trimercaptotriazine,[21,22] polystyrene-bound ethylenediamine[23] and Johnson Matthey's SMOPEX series of functionalised polyolefin fibres[1,24] (Figure 3.2) have been used successfully for the removal of Pd(II) and Pd(0) species from a range of organic solvents.

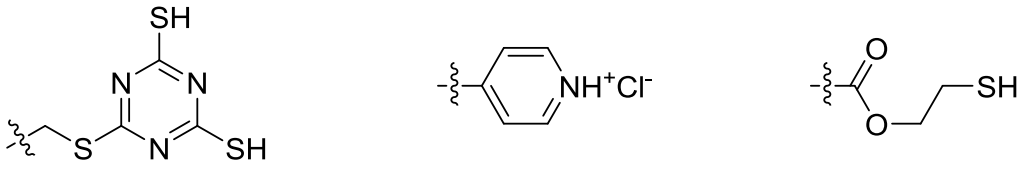


Figure 3.2. The structures of trimercaptotriazine (left), SMOPEX-105 (centre) and SMOPEX-234 (right).

Whilst the materials currently used for PGM scavenging show great efficiency for the removal of specific catalysts, the sheer number and variety of different catalysts and solvent mixtures means that no single compound is effective in every scenario. As such, we propose the use of MOFs as an alternative to the materials currently used, with the advantages of predictable structures, cage sizes and the ability to tune the relative positions and functionality of pendant groups within the pores. To the best of our knowledge, the use of MOFs for the recovery of PGM catalysts from solution has not previously been reported.

3.2 Aims of this Work

The aim of this work was to investigate the uptake of Pd, Pt and Rh complexes, specifically $Pd(OAc)_2$, $PtCl_4$ and $Rh_2(OAc)_4$, from organic solutions using functionalised MOFs. $Pd(OAc)_2$, $PtCl_4$ and $Rh_2(OAc)_4$ were chosen as they are of industrial interest to Johnson Matthey and are relatively small PGM species, thus more likely to fit through the pore windows of a MOF. As Cu(II) is well known to form a huge variety of different MOFs under mild conditions,[25-27] it was decided that a Cu(II) metal node would allow a variety of different ligands to be used to prepare MOFs on an appropriate scale to carry out a range of extraction experiments. To fully understand the factors dictating the encapsulation of these metal species, a comparison of different functional groups, topologies and cage sizes was required. As such, the linkers H_4L^6-H_4L^9 (Figure 3.3) and their corresponding Cu(II) MOFs were prepared. These linkers allow for a direct comparison between amine, oxamide and methyl functional groups and a comparison of the two different topologies given by the linear and V-shaped linker geometries.

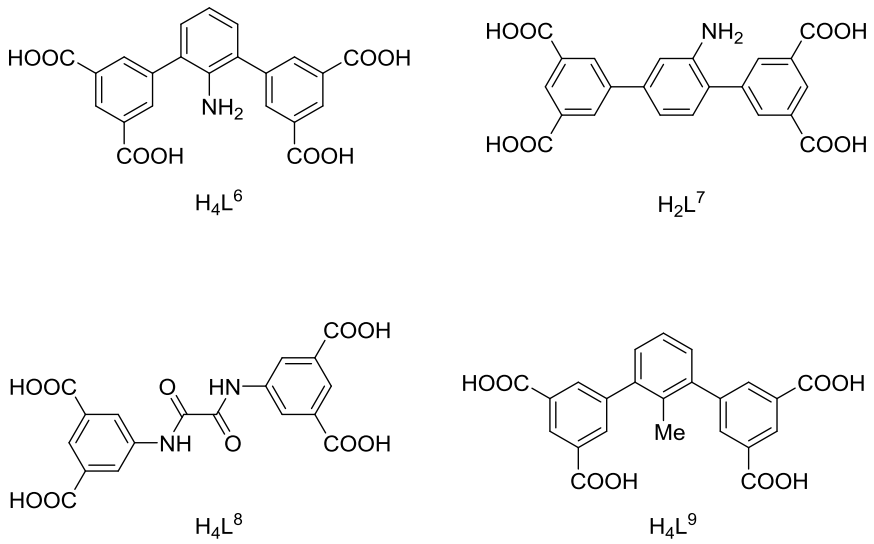


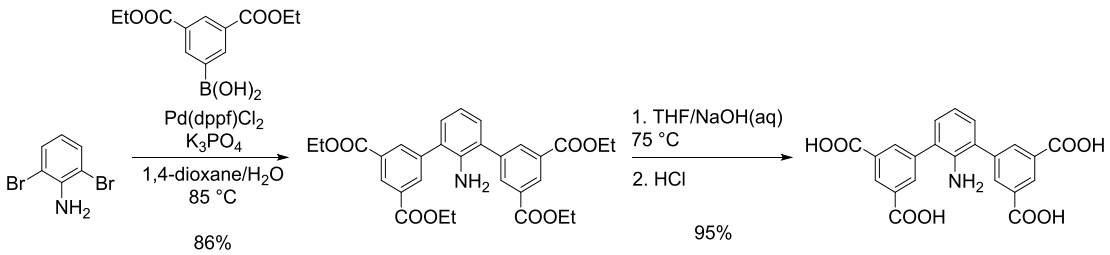
Figure 3.3. Structures of the functionalised tetracarboxylate linkers H_4L^6-H_4L^9.

3.3 Results and Discussion

3.3.1 NOTT-151

3.3.1.1 Synthesis of $[Cu_2(L^6)(H_2O)_2]\cdot 4DMF\cdot H_2O$ (NOTT-151)

The first of these frameworks to be synthesised was $[Cu_2(L^6)(H_2O)_2]\cdot 4DMF\cdot H_2O$ (denoted NOTT-151) prepared from the tetracarboxylate linker H_4L^6. H_4L^6 was synthesised *via* a Suzuki cross-coupling reaction of 2,6-dibromoaniline with (3,5-bis(ethoxycarbonyl)phenyl)boronic acid in a microwave reactor at 85 °C. A solution of these precursors together with K_3PO_4 and $Pd(dppf)Cl_2$ in a degassed mixture of 1,4-dioxane and water was heated with stirring for 1 hour at 85°C (Scheme 3.1). After work-up and column chromatography to give the pure tetraester, the compound was hydrolysed in a THF/NaOH solution and then acidified to pH~1 with 37% HCl to give the pure ligand as an off-white powder.



Scheme 3.1. Synthesis of H_4L^6.

The corresponding MOF, NOTT-151, was prepared *via* a solvothermal reaction of H_4L^6 and $Cu(NO_3)_2\cdot 3H_2O$ in acidified DMF at 80 °C for 20 hours in an 8 ml glass vial to give large, green plate crystals of $[Cu_2(L^6)(H_2O)_2]\cdot 4DMF\cdot H_2O$. Microcrystalline samples for metal scavenging were prepared using the same conditions on a larger scale in a 100 ml Schott bottle.

3.3.1.2 Structural Analysis

Single crystal X-ray diffraction reveals that NOTT-151 crystallises in the hexagonal space group $P6_3/mmc$ with unit cell dimensions a = 18.326(8) Å, c = 23.99(2) Å and V = 6977(8) Å^3. The framework is a 4,4-connected structure incorporating a Kagomé lattice, a common feature of many metal-organic frameworks[28,29] (Figure 3.4). However, the underlying **ssa** topology of NOTT-151 is much less common and to our knowledge is only exhibited in one other MOF, reported by Sun *et al.* in 2011.[30] The rarity of the **ssa** topology is a result of the need for a tetracarboxylate ligand in which both isophthalate moieties are almost perpendicular to the plane of the core. In NOTT-151, this is brought about by the central amine functionality sterically hindering the isophthalate units such that a torsion angle of 86.4 ° between the two ring systems is present. This topology introduces three distinct cavities into the MOF, denoted cages **A**, **B** and **C** (Figure 3.5). Most importantly, and in contrast to tetracarboxylate MOFs that do not possess **ssa** topology,[31,32] cage **A** features a triangular arrangement of three amine groups, ideally placed to maximise host-guest interactions. This is useful for gas storage applications but crucially for metal scavenging applications the accessible diameter of the cage is just 6.4 Å and the distance between adjacent NH_2 groups is 5.7 Å, *i.e.* large enough to accommodate a PGM complex whilst ensuring the available groups on the PGM are in close proximity to the amine moietiy. For reference, $Pd(OAc)_2$ is ~ 5.2 Å x 4.5 Å in diameter (8.1 Å x 2.3 Å in monodentate form)[33] and $PtCl_4$ is ~ 4.6 x 4.6 Å in diameter.[34] Cage **A** is comprised of six Cu(II) paddlewheels with three complete ligands bridging between them and the amine groups point directly into the centre of the cavity. Cage **B** is comprised of six Cu(II) paddlewheel units with six ligands bridging between opposing clusters and a further six isophthalates joining adjacent

paddlewheels. The six amine groups line the walls of the pore and the internal accessible diameter is 12.2 Å when axial water molecules are removed from the paddlewheels and the end-to-end distance is 18.0 Å. Cage **C** is not functionalised with amine groups and has an accessible internal diameter of 10.0 Å. All internal diameters were calculated by fitting a sphere from the centroid of the cage to its walls, taking into account Van der Waals radii.

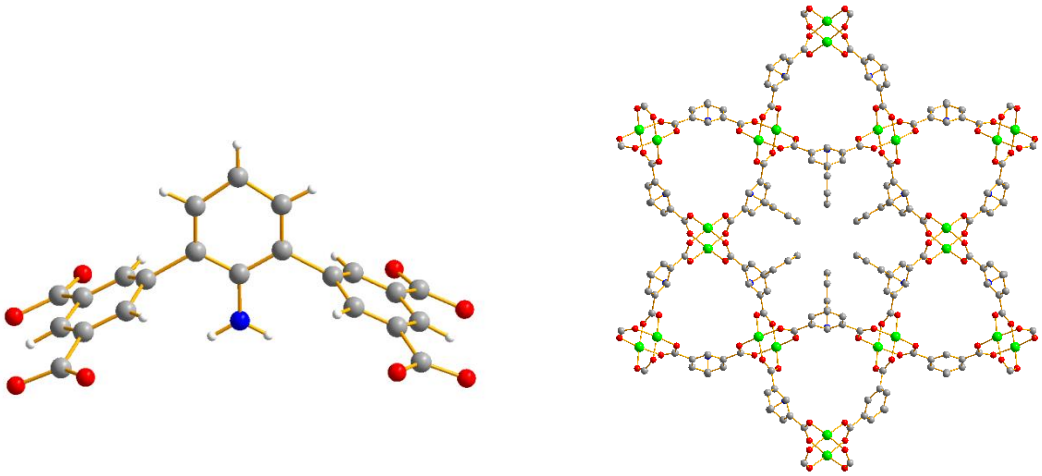


Figure 3.4. View of the linker conformation (left) and Kagomé lattice (right) observed in NOTT-151.

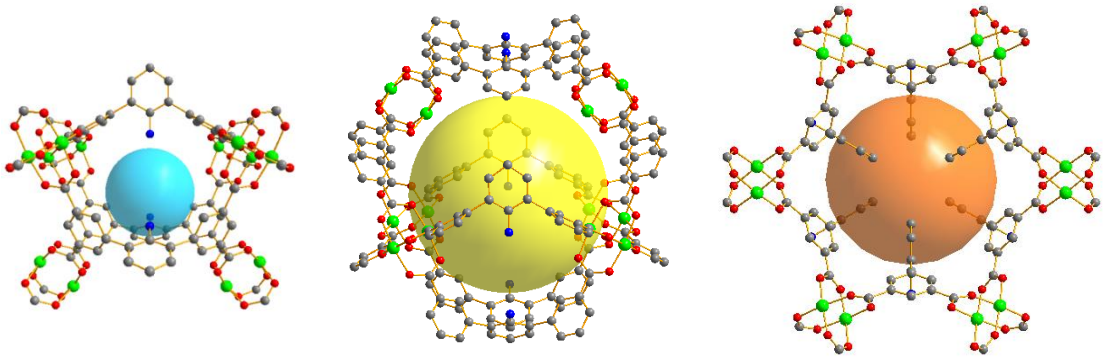


Figure 3.5. View of the polyhedral cages A (left), B (centre) and C (right) present in NOTT-151.

3.3.1.3 Phase Purity, Thermal Stability and N_2 Sorption

To confirm the phase purity of the bulk material, powder X-ray diffractograms of the as-synthesised and acetone exchanged MOF samples were recorded (Figure 3.6). and successfully indexed to the same unit cell as the single crystal structure.

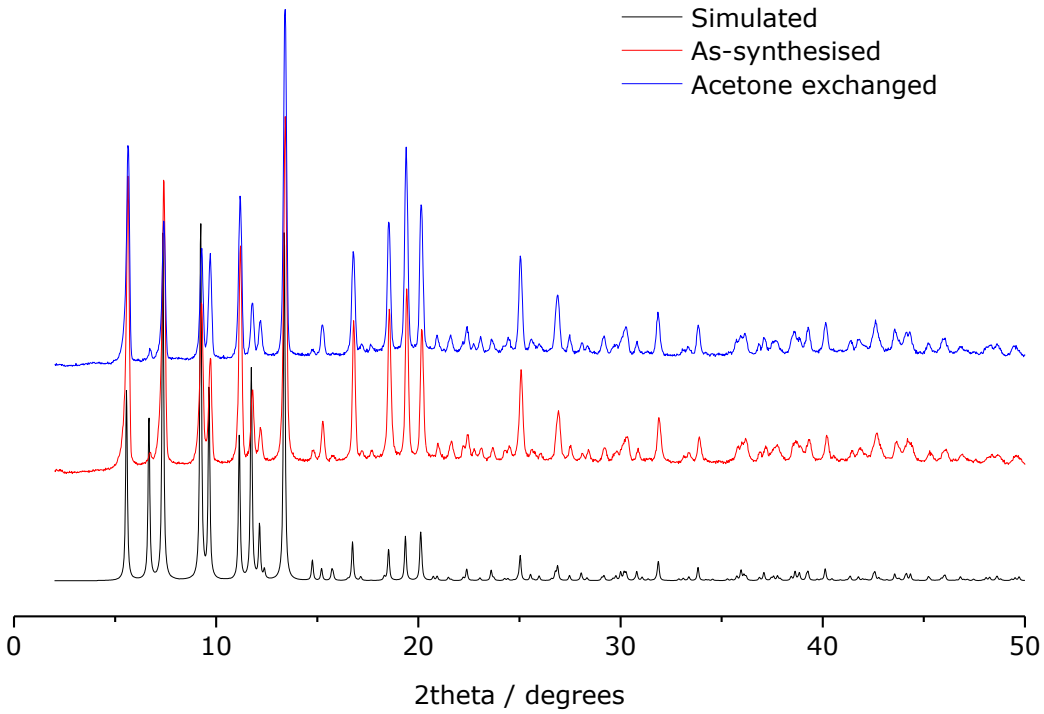


Figure 3.6. PXRD patterns of simulated, as-synthesised and acetone exchanged NOTT-151.

The potential accessible volume of the desolvated material is 68%, as calculated by the PLATON/VOID routine[35] after removal of all guest solvents and coordinated water molecules with a calculated crystal density of 0.807 g cm^{-3}. Thermogravimetric analysis of the as-synthesised sample of NOTT-151 in air showed solvent loss (DMF and H_2O) below 160 °C, with the material stable up to 270 °C, beyond which point a mass loss corresponding to framework decomposition is observed (Figure 3.7).

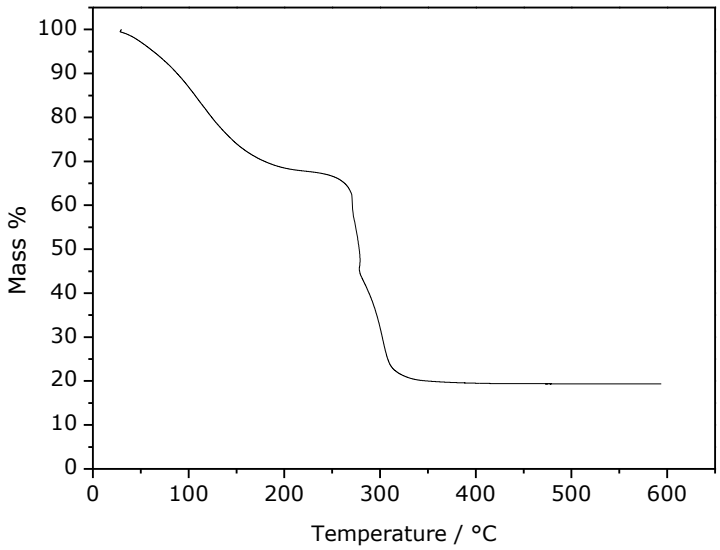


Figure 3.7. TGA trace of as-synthesised NOTT-151.

To prepare NOTT-151 for the metal scavenging experiments, the solvent of the as-synthesised sample was exchanged with fresh acetone twice daily for 5 days. This material was then heated under vacuum at 100 °C for 20 hours, to give the activated framework NOTT-151a and the permanent porosity was confirmed *via* an N_2 sorption isotherm performed at 77 K from 0-1 bar. This exhibited a reversible type-I sorption profile with a maximum uptake of 669 cc g^{-1} (Figure 3.8). The estimated BET surface area of the material, as calculated from this isotherm, was 1887 m^2 g^{-1} with a total pore volume of 0.88 cm^3 g^{-1}.

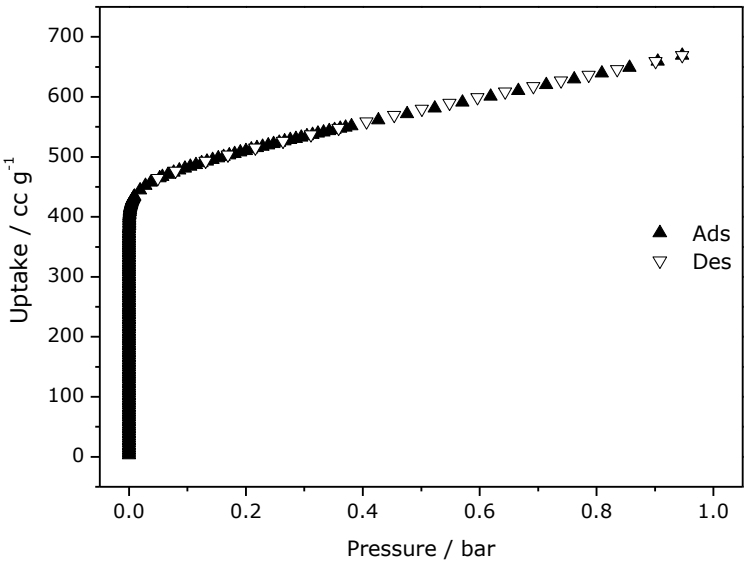
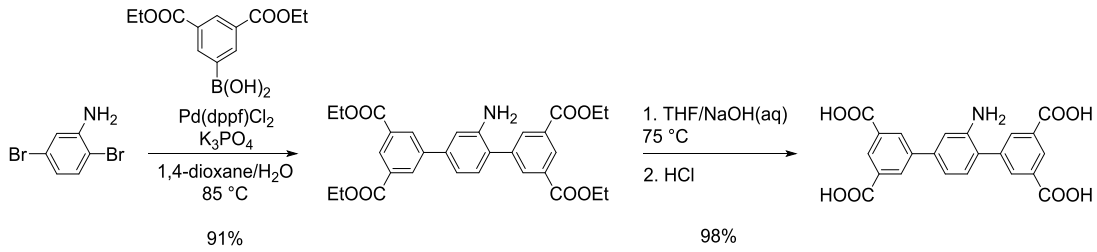


Figure 3.8. N_2 isotherm for NOTT-151a from 0-1 bar at 77K.

3.3.2 NOTT-155

3.3.2.1 Synthesis of $[Cu_2(L^7)(H_2O)_2]\cdot 7DMF\cdot H_2O$ (NOTT-155)

To study the effect of structure and cage size on PGM encapsulation, a linear analogue of H_4L^6 was synthesised with the aim of preparing a MOF of **fof** topology to compare with the **ssa** topology of NOTT-151. This linker, denoted H_4L^7, was synthesised *via* a Suzuki cross-coupling reaction of 2,5-dibromoaniline with (3,5-bis(ethoxycarbonyl)phenyl)boronic acid (Scheme 3.2). A solution of these precursors together with K_3PO_4 and $Pd(dppf)Cl_2$ in a degassed mixture of 1,4-dioxane and water was heated for 3 days at 85 °C. After work-up and column chromatography to give the pure tetraester, the compound was hydrolysed in a THF/NaOH solution and then acidified to pH~1 to give the pure ligand as a pale yellow powder.



Scheme 3.2. Synthesis of H_4L^7.

The corresponding MOF, NOTT-155, was prepared *via* a solvothermal reaction of H_4L^7 and $Cu(NO_3)_2{\cdot}3H_2O$ in acidified DMF/H_2O mixture at 80 °C for 20 hours in an 8 ml glass vial to give large, green plate crystals of $[Cu_2(L^7)(H_2O)_2]{\cdot}7DMF{\cdot}H_2O$. Microcrystalline samples for metal scavenging were prepared using the same conditions on a larger scale in a 100 ml Schott bottle.

3.3.2.2 Structural Analysis

Single crystal X-ray diffraction reveals that NOTT-155 crystallises in the trigonal space group *R*-3*m* with unit cell dimensions *a* = 18.6224(5) Å, *c* = 38.283(1) Å and *V* = 11497.8(7) $Å^3$. The framework is a 4,4-connected structure of **fof** topology which consists of two distinct cages, **A** and **B** (Figure 3.9). Cage **A** comprises 12 Cu(II) paddlewheels joined by six complete ligands to give an elliptical cavity measuring 23.8 Å x 11.3 Å. The windows to the cavity are 8.3 Å in diameter (the amine groups have been ignored in this measurement as four-fold disorder makes it impossible to accurately determine their position). Cage **B** consists of six paddlewheels arranged in two sets of three clusters. Six ligands bridge between the two clusters and the isophthalate units of six further ligands bridge between adjacent Cu(II) paddlewheels in the same cluster. The accessible internal diameter in cage **B** measures 12.8 Å and the windows to the cage measure 9.0 Å, again this is measured after disregarding the amine functional groups.

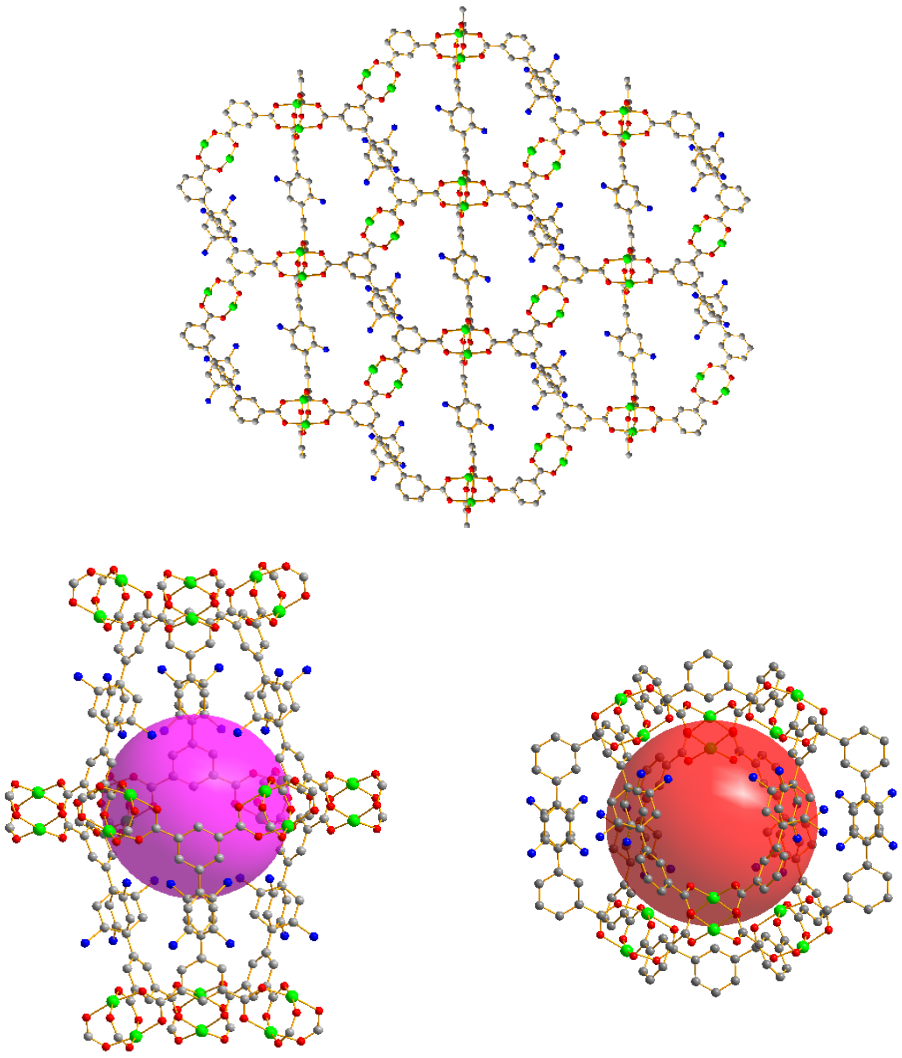


Figure 3.9. View down the *a*-axis (top) and of cages A (bottom left) and B (bottom right) seen in NOTT-155.

3.3.2.3 Phase Purity, Thermal Stability and N_2 Sorption

The phase purity of the bulk sample was confirmed from the powder patterns of the as-synthesised and acetone exchanged materials (Figure 3.10).

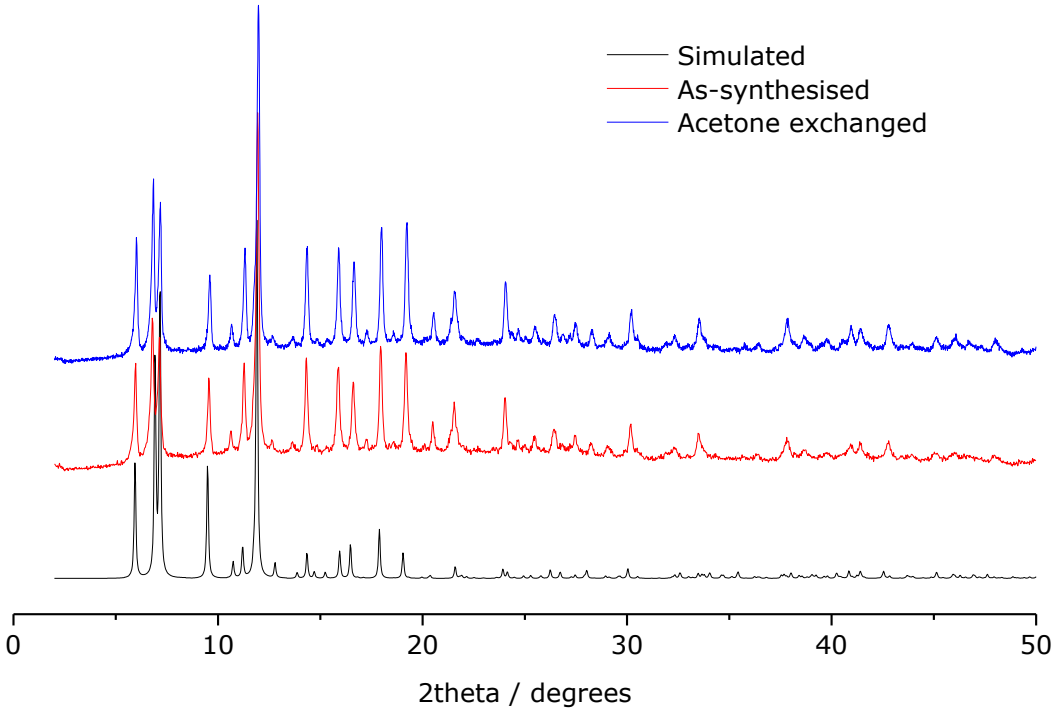


Figure 3.10. PXRD patterns of simulated, as-synthesised and acetone exchanged NOTT-155.

The potential accessible volume of the desolvated material is 71%, as calculated by the PLATON/VOID routine[35] after removal of all guest solvents and coordinated water molecules with a calculated crystal density of 0.779 g cm^{-3}. Thermogravimetric analysis of the as-synthesised sample in air shows a mass decrease corresponding to solvent loss below 240 °C, followed by a mass loss at 285 °C attributed to framework decomposition. The acetone exchanged sample exhibits much more rapid solvent loss followed by the same MOF decomposition temperature of 285 °C (Figure 3.11).

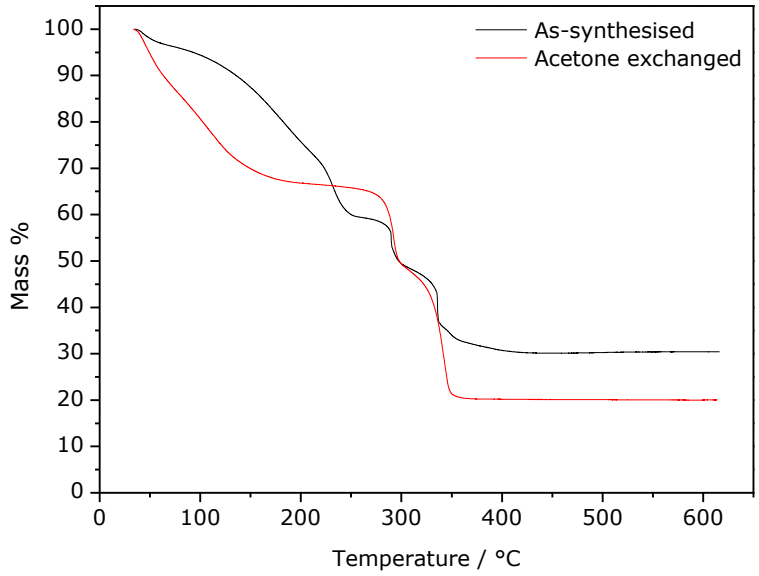


Figure 3.11. TGA trace of as-synthesised and acetone exchanged NOTT-155.

An N_2 isotherm at 77 K was then measured to confirm the permanent porosity of activated NOTT-155a (Figure 3.12). This exhibited typical reversible type-I behaviour with an uptake of 808 cc g^{-1}, a BET surface area of 2528 m^2 g^{-1} and a pore volume of 1.03 cm^3 g^{-1}.

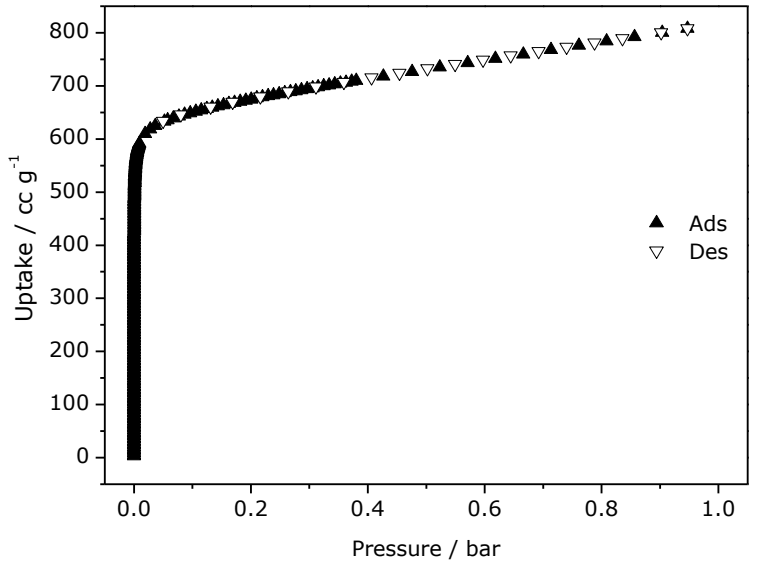
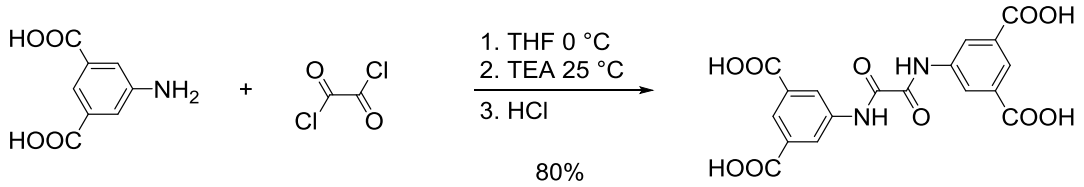


Figure 3.12. N_2 isotherm for NOTT-155a from 0-1 bar at 77K.

3.3.3 NOTT-125

3.3.3.1 Synthesis of $[Cu_2(L^8)(H_2O)_2]\cdot 3DMA\cdot 3H_2O$ (NOTT-125)

To compare between different H-bond donor groups, an oxamide-functionalised analogue of H_4L^7, denoted H_4L^8, was synthesised. This linker was known to give a Cu(II) framework isostructural to NOTT-155,[36] thus providing a direct comparison between amine and oxamide functional groups for PGM sorption. H_4L^8 was prepared by a nucleophilic substitution reaction between oxalyl chloride and 5-aminoisophthalic acid (Scheme 3.3).[36] The reactants were added to dry THF at 0 °C under argon and left to stir for an hour. Triethylamine (TEA) was then added and the solution was stirred at room temperature overnight. Following acidification to pH~1 and recrystallisation from hot methanol, the pure ligand was isolated in good yield (80%).



Scheme 3.3. Synthesis of H_4L^8.

The corresponding Cu(II) MOF, NOTT-125 was prepared *via* a solvothermal reaction between H_4L^8 and $Cu(NO)_3\cdot 3H_2O$ in a mixture of acidified dimethylacetamide (DMA) and H_2O at 70 °C in an 8 ml glass vial to give blue block crystals of $[Cu_2(L^8)(H_2O)_2]\cdot 3DMA\cdot 3H_2O$. Microcrystalline samples for metal scavenging were prepared using the same conditions on a larger scale in a 100 ml Schott bottle.

3.3.3.2 Structural Analysis

Single crystal X-ray diffraction reveals that NOTT-125 crystallises in the monoclinic space group $P2_1/c$ with unit cell dimensions a = 27.9161(6), b = 18.6627(4), c = 32.3643(8) Å, β = 112.655(3)° and V = 15560.5(7) Å^3. As seen in NOTT-155, NOTT-125 is a 4,4-connected framework of **fof** topology consisting of two cages, **A** and **B.** The cages are almost identical to those observed in NOTT-155, with the central functionality having changed from an aniline group to an oxamide group (Figure 3.13). Cage **A** consists of 12 Cu(II) paddlewheels joined by six complete ligands giving an elliptical cavity measuring 23.2 Å x 12.4 Å in diameter. The windows to this cavity measure 6.6 Å, 7.9 Å and 8.5 Å depending on the configurations of adjacent oxamide groups. Cage **B** is comprised of six Cu(II) paddlewheels arranged in two sets of three clusters. As in NOTT-155, six ligands bridge between the two clusters and the isophthalate units of six other ligands bridge between adjacent paddlewheels in the same cluster. The accessible internal diameter in cage **B** measures 12.8 Å and the windows to the cage measure 6.9 Å, 6.9 Å and 8.8 Å. Again, this is dependent on the relative configurations of adjacent oxamide groups.

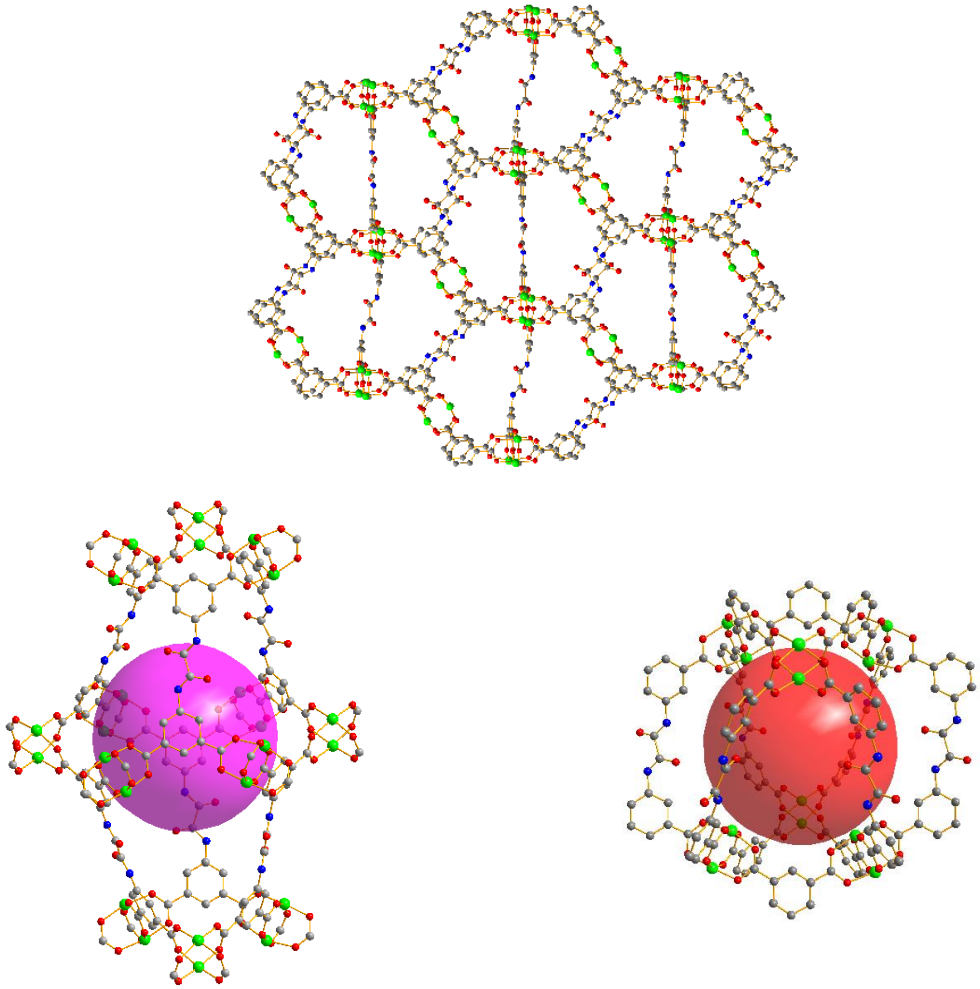


Figure 3.13. View down the *a*-axis (top) and of cages A (bottom left) and B (bottom right) seen in NOTT-125.

3.3.3.3 Phase Purity, Thermal Stability and N_2 Sorption

PXRD patterns were recorded to confirm the phase purity of as-synthesised and acetone exchanged samples of NOTT-125 (Figure 3.14) and both were indexed to the same unit cell as the single crystal structure

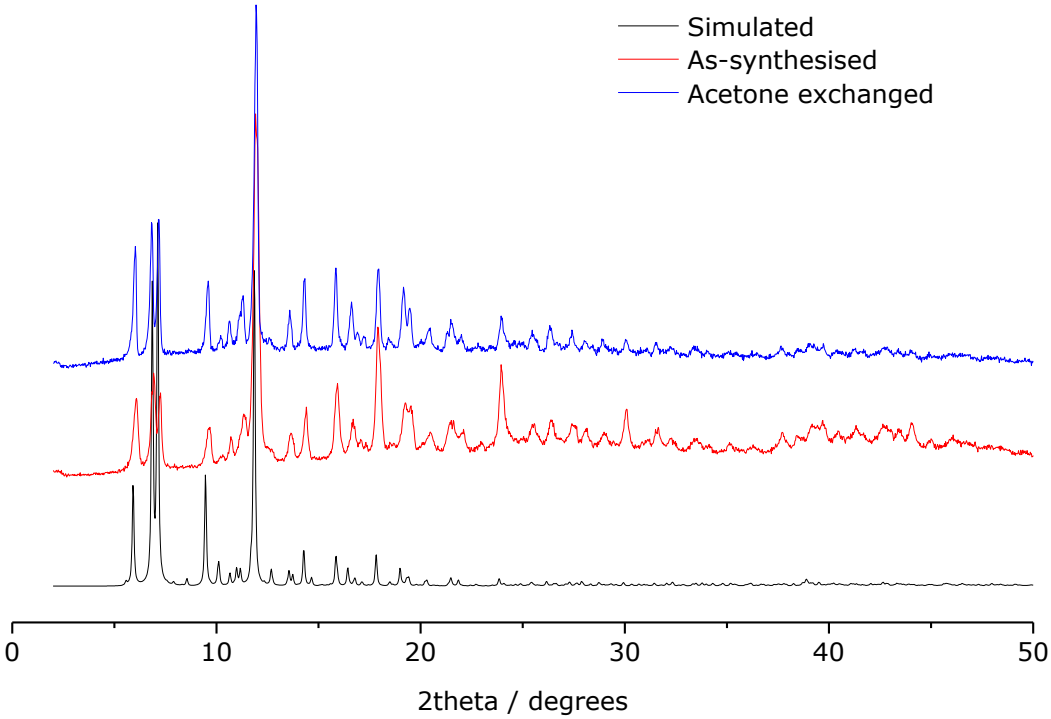


Figure 3.14. PXRD patterns of simulated, as-synthesised and acetone exchanged NOTT-125.

The potential accessible volume of the desolvated material is 71%, as calculated by the PLATON/VOID routine[35] after removal of all guest solvents and coordinated water molecules with a calculated crystal density of 0.672 g cm^{-3}. Thermogravimetric analysis of as-synthesised NOTT-125 exhibits solvent loss below 240 °C, with the material showing stability up to 340 °C, at which point a mass loss attributed to framework decomposition is observed (Figure 3.15).

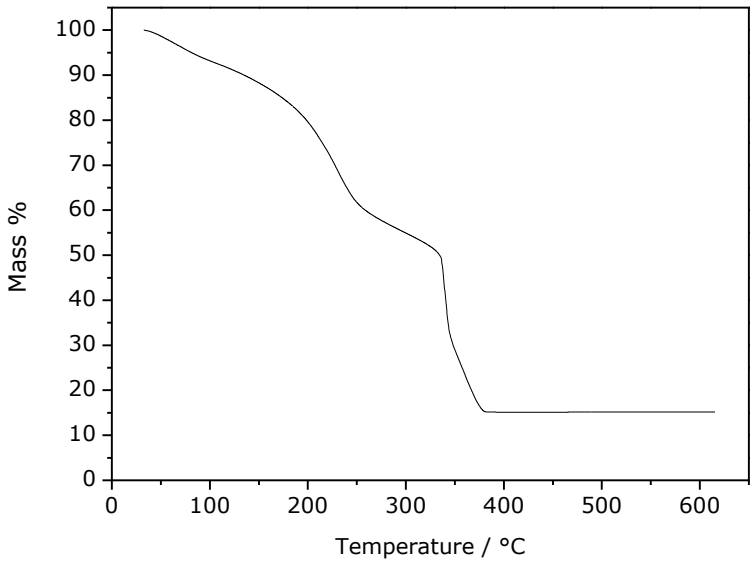


Figure 3.15. TGA trace of as-synthesised and acetone exchanged NOTT-125.

An N_2 isotherm from 0-1 bar was measured at 77 K to confirm the permanent porosity of activated NOTT-125a. As with NOTT-151a and NOTT-155a, this isotherm exhibits a reversible type-I sorption profile with a saturation uptake of 692 cc g^{-1} (Figure 3.16). The BET surface area was calculated to be 2419 m^2 g^{-1} with a total pore volume of 0.96 cm^3 g^{-1}.

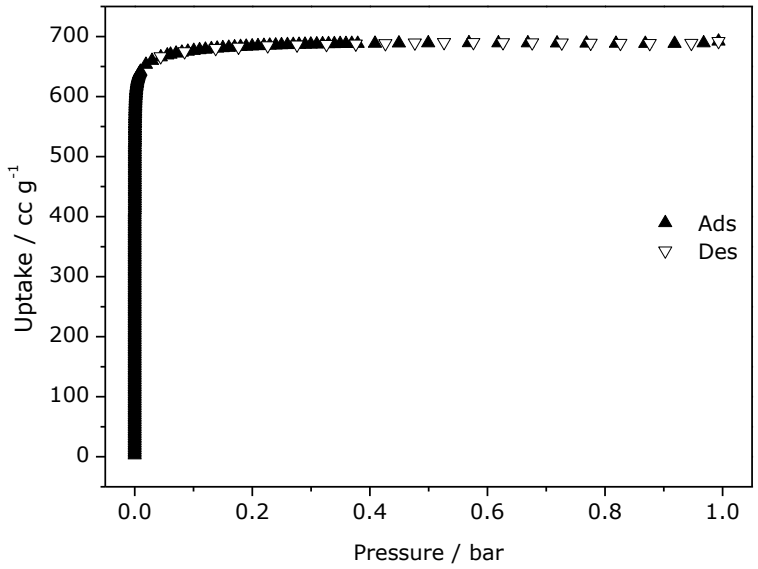
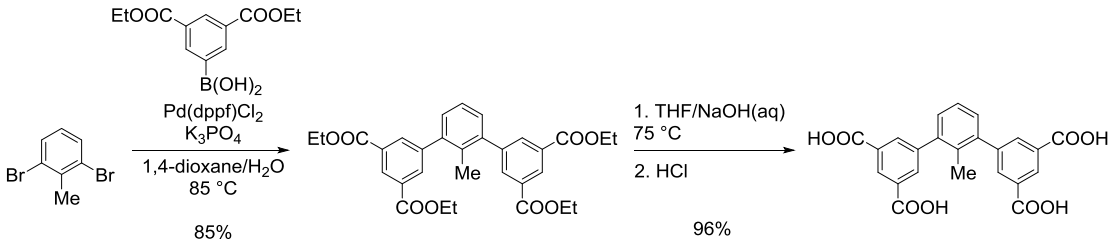


Figure 3.16. N_2 isotherm for NOTT-125a from 0-1 bar at 77K.

3.3.4 NOTT-150

3.3.4.1 Synthesis and Structural Analysis of $[Cu_2(L^9)(H_2O)_2]\cdot 5DMF\cdot 4H_2O$ (NOTT-150)

To investigate the effect of the amine functional group on PGM encapsulation, an analogue of NOTT-151 incorporating a methyl functional group, denoted NOTT-150, was synthesised for comparison. The linker, H_4L^9 was prepared *via* a Suzuki cross-coupling reaction between 2,6-dibromotoluene and (3,5-bis(ethoxycarbonyl)phenyl)boronic acid in 1,4-dioxane/H_2O. Pd(dppf)Cl_2 and K_3PO_4 were added and the mixture was heated under argon at 85 °C for 48 hours (Scheme 3.4). After purification through a plug of silica gel, the ester product was hydrolysed in NaOH and acidified with HCl to give the tetracarboxylic acid linker, H_4L^9, in good yield (96%). NOTT-150 was prepared *via* the reaction of H_4L^9 with $Cu(NO_3)_2\cdot 3H_2O$ in acidified DMF at 80 °C to yield blue block crystals.



Scheme 3.4. Synthesis of H_4L^9.

As with NOTT-151, NOTT-150 crystallises in the hexagonal space group $P6_3/mmc$ with unit cell dimensions a = 18.3894(4) Å, c = 23.8606(4) Å and V = 6981.1(4) Å^3. The framework is isostructural to NOTT-151, comprising the same three cages **A**, **B** and **C** (Figure 3.17) in which the NH_2 functional groups of NOTT-151 are replaced with methyl groups.

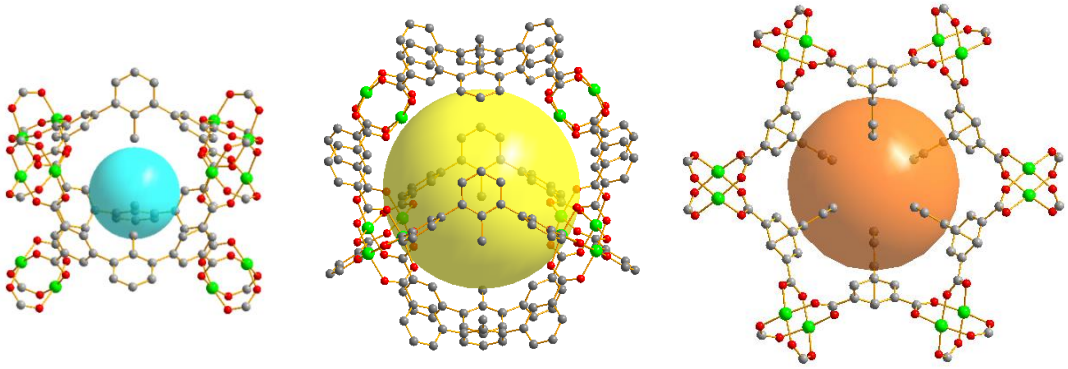


Figure 3.17. View of cages A (left), B (centre) and C (right) seen in NOTT-150.

3.3.4.2 Phase Purity, Thermal Stability and N_2 Sorption

PXRD was used to confirm the crystallinity and phase purity of the as-synthesised and acetone exchanged samples of NOTT-150 (Figure 3.18). Both powder patterns were successfully indexed to the unit cell observed from the single crystal structure.

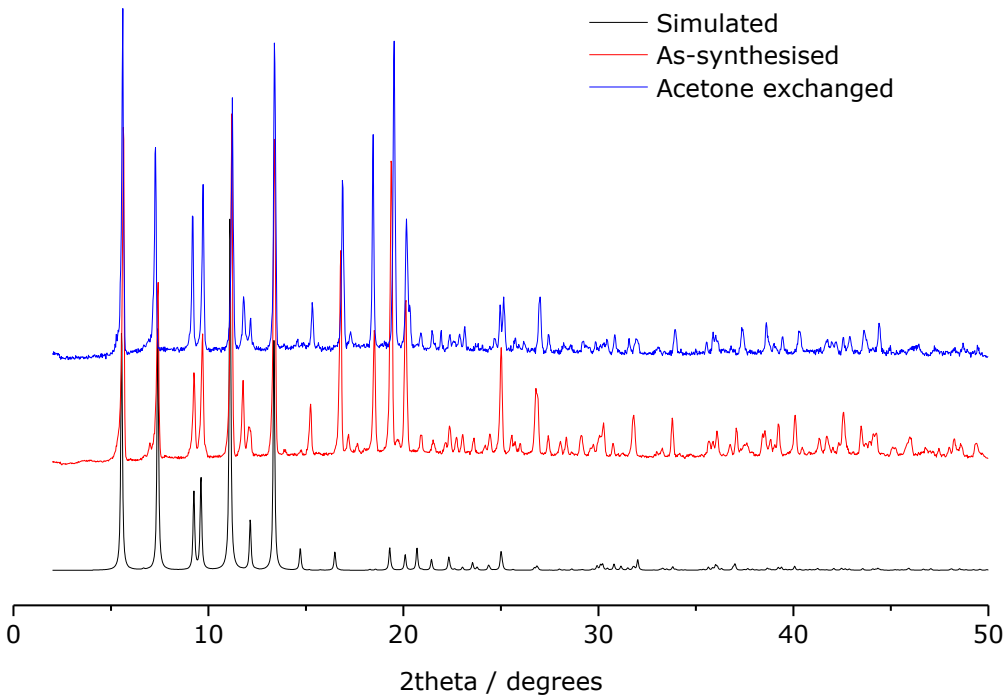


Figure 3.18. PXRD patterns of simulated, as-synthesised and acetone exchanged NOTT-150.

The potential accessible volume of the desolvated material is 68%, as calculated by the PLATON/VOID routine[35] (after removal of all guest solvents and coordinated water molecules) with a calculated crystal density of 0.758 g cm^{-3}. Thermogravimetric analysis of as-synthesised NOTT-150 exhibits solvent loss followed by a mass loss corresponding to framework decomposition at 315 °C (Figure 3.19). This is an increase of 45 °C in comparison to the isostructural amine-functionalised NOTT-151. The acetone exchanged sample exhibits rapid solvent loss followed by the same framework decomposition at 315 °C.

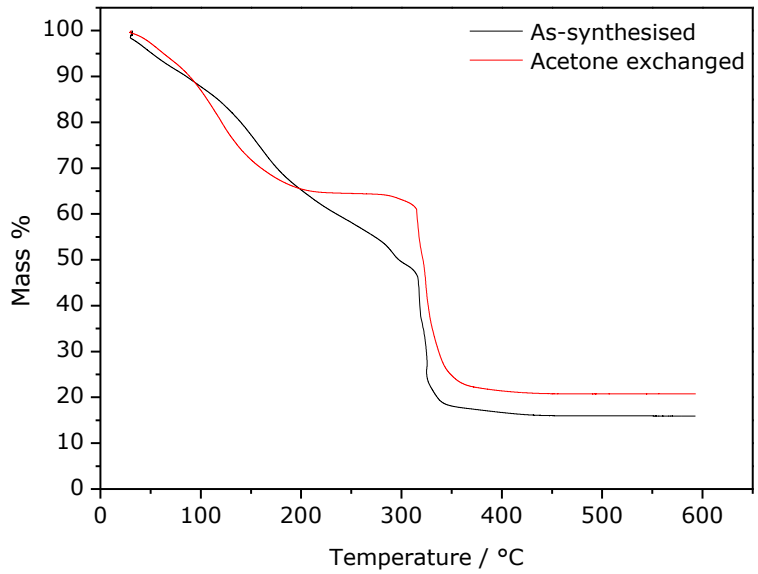


Figure 3.19. TGA trace of as-synthesised and acetone exchanged NOTT-150.

The permanent porosity of activated NOTT-150a was confirmed by measuring a nitrogen isotherm at 77 K (Figure 3.20). This exhibited reversible type-I behaviour with a saturation uptake of 592 cc g^{-1}, a calculated BET surface area of 2042 m^2 g^{-1} and a total pore volume of 0.73 cm^3 g^{-1}.

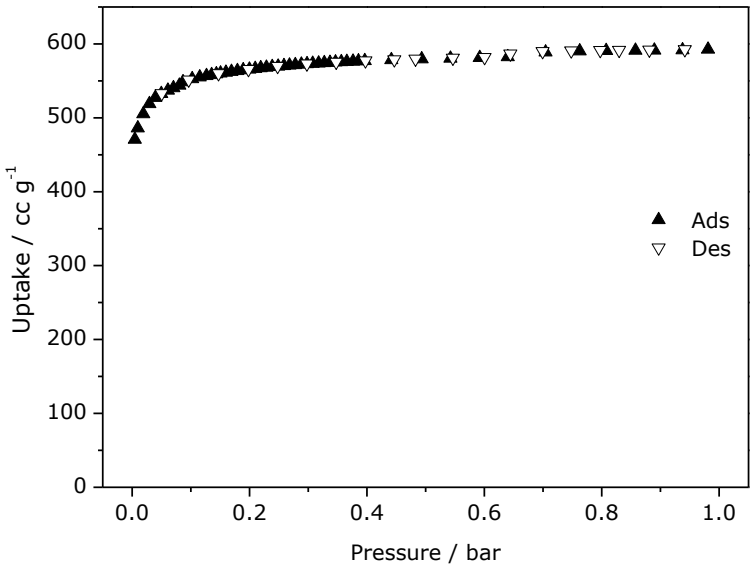


Figure 3.20. N_2 isotherm for NOTT-150a from 0-1 bar at 77K.

3.3.5 Structure Summary

To summarise, we have synthesised four Cu(II) MOFs to investigate the effects of structural and chemical features of a framework on the encapsulation of PGM complexes (Figure 3.21).

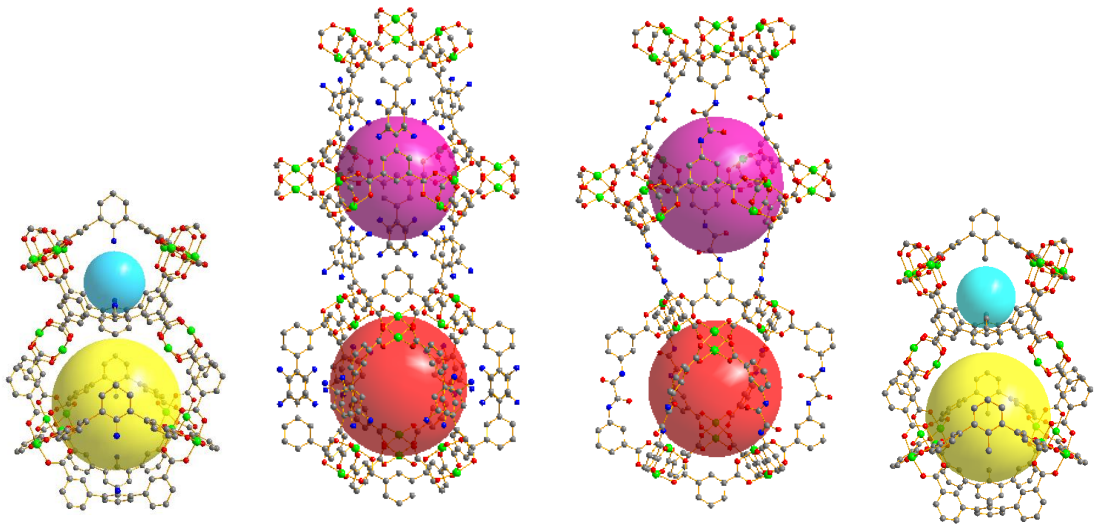


Figure 3.21. View of the functionalised cages in NOTT-151, NOTT-155, NOTT-125 and NOTT-150 (left to right).

The first of these frameworks, denoted NOTT-151, was prepared from a V-shaped linker (H_4L^6) which was combined with a Cu(II) paddlewheel motif to give a MOF of **ssa** topology. The twist of the ligand resulted in a small pore with three NH_2 groups in close proximity (5.7 Å apart) and a larger pore with NH_2 groups lining the pore openings. The overall porosity upon desolvation was calculated to be 68%, with a moderate BET surface area of 1887 m^2 g^{-1}. The linear analogue of H_4L^6, denoted H_4L^7, was used to prepare NOTT-155, a MOF of **fof** topology which exhibited greater porosity (71%) and a larger BET surface area (2528 m^2 g^{-1}) than NOTT-151. However, the spacing between NH_2 groups is increased. Thus, by simply changing the geometry of the linker, the MOF structure, porosity and position of the functional groups have been altered considerably. NOTT-125 was then synthesised as an oxamide-functionalised analogue of NOTT-155. As NOTT-125 and NOTT-155 have the same underlying topology, the same porosity and very similar BET surface areas, these two MOFs allow for a direct comparison of the effect of amine and oxamide functional groups on PGM encapsulation. Finally, a methyl-functionalised analogue of NOTT-151, denoted NOTT-150, was prepared. As the methyl functionality was not expected to interact strongly with the guest metal complexes, the comparison with NOTT-151 was designed to give a good indication of the effect of the NH_2 group in NOTT-151 on metal encapsulation. A V-shaped methyl-functionalised linker was chosen instead of the linear analogue as the closer proximity of the functional groups in the **ssa** topology in comparison to **fof** was expected to result in stronger interactions with the PGM. Thus it was considered that this comparison would better illustrate the importance of the NH_2 group for metal binding. The structural features of these frameworks relevant to PGM extraction are shown below in Table 3.1.

Table 3.1. A structural and chemical comparison of the four Cu(II) MOFs prepared for PGM encapsulation.

MOF	Linker geometry	Framework topology	Functional Group	BET surface area / $m^2 g^{-1}$	Accessible pore volume
NOTT-151	V-shaped	**ssa**	$-NH_2$	1887	68%
NOTT-155	Linear	**fof**	$-NH_2$	2528	71%
NOTT-125	Linear	**fof**	$-NH(CO)_2NH-$	2419	71%
NOTT-150	V-shaped	**ssa**	$-CH_3$	2042	68%

3.3.6 Extraction of $Pd(OAc)_2$, $PtCl_4$ and $Rh_2(OAc)_4$ from THF

After synthesis, each MOF was exchanged with acetone over the course of five days, with fresh acetone added daily. The acetone exchanged samples were then activated by heating under vacuum at 100 °C overnight and stored at room temperature under an inert argon atmosphere. A series of extractions using 10/25 ppm of the PGM in 50 ml of THF were set up and the mass of activated MOF added was varied between 10, 20 and 50 mg. THF was chosen as the matrix solvent as it allows for a close comparison to industrial conditions for PGM scavenging. Additionally, a series of test extractions showed that PGM scavenging from THF using these Cu(II) MOFs was more effective than from similar suitable solvents such as acetone and ethanol. Each experiment was left to stand at room temperature without stirring for 48 hours, at which point the MOF was recovered by filtration and a 10 ml aliquot of the solution was removed and the THF was left to evaporate. These conditions were chosen after initial test experiments showed that stirring resulted in dissolution of the MOF and that very little extraction was observed after 48 hours. The residues from the evaporated solutions were dissolved in 10 ml of 5% HNO_3 and the PGM concentration was analysed by ICP-OES. The same process was applied to the pre-extraction solution and the difference in concentration was converted into a % uptake for each framework. The PGM-doped MOFs were also digested in HNO_3 and diluted

with ultrapure de-ionised water and ICP-OES was used to determine the Cu:PGM ratio of the bulk sample. This can then be compared to the ratio expected from the solution results (Table 3.2). This "expected ratio" is calculated from the molar quantity of Cu in the MOF and the molar quantity of PGM removed from solution (given by the % uptake) to give a Cu:PGM ratio.

The first series of extractions were performed in a $Pd(OAc)_2$/THF mixture, with each MOF exhibiting a measureable uptake of Pd in every experiment (Table 3.2). The calculated % uptakes show clearly that the larger pore MOFs, NOTT-155 and NOTT-125, show a significantly greater extraction capacity than that of NOTT-151. As NOTT-155 and NOTT-151 contain the same functional group, the greater uptake in NOTT-155 is attributed to the higher porosity allowing it to more easily accommodate the PGM complexes.

Table 3.2. Uptake of $Pd(OAc)_2$ from THF into a series of Cu(II) MOFs. Values highlighted in bold text show the most effective material for each experiment.

MOF (mass / mg)	Pd conc / ppm	% uptake	Uptake / mg g^{-1}	Expected Cu:Pd ratio	Measured Cu:Pd ratio
NOTT-151 (20)	10	14.14	7.5	66 : 1	156 : 1
NOTT-151 (50)	10	11.93	2.5	195 : 1	146 : 1
NOTT-151 (10)	25	3.49	9.2	53 : 1	77 : 1
NOTT-151 (20)	25	2.87	3.8	130 : 1	142 : 1
NOTT-151 (50)	25	8.07	4.3	116 : 1	368 : 1
NOTT-155 (20)	10	**18.70**	**9.9**	**50 : 1**	49 : 1
NOTT-155 (50)	10	2.86	0.6	815 : 1	188 : 1
NOTT-155 (10)	25	0.69	1.8	270 : 1	162 : 1
NOTT-155 (20)	25	**33.15**	**43.7**	**11 : 1**	56 : 1
NOTT-155 (50)	25	18.72	9.9	50 : 1	292 : 1
NOTT-125 (20)	10	14.19	7.5	66 : 1	277 : 1
NOTT-125 (50)	10	**18.55**	**3.9**	**127 : 1**	220 : 1
NOTT-125 (10)	25	**13.12**	**34.6**	**14 : 1**	79 : 1
NOTT-125 (20)	25	14.11	18.6	27 : 1	101 : 1
NOTT-125 (50)	25	**27.63**	**14.6**	**34 : 1**	64 : 1
NOTT-150 (50)	10	7.37	1.6	317 : 1	207 : 1
NOTT-150 (50)	25	3.99	2.1	234 : 1	541 : 1

Although the extraction capacity of NOTT-151 is moderate, it is higher than that exhibited by both samples of methyl functionalised NOTT-150, suggesting that the NH_2 functional group in NOTT-151 is improving the adsorption of $Pd(OAc)_2$. The scavenging ability of NOTT-151 and NOTT-155 appear to be inconsistent between experiments, however NOTT-125 exhibits consistent uptake with a highest capacity of 34.6 mg g^{-1} from a 10 ppm solution (equivalent to 1 Pd complex per 7 oxamide groups). Despite these promising results, the ratio of Cu:Pd in the digested MOF samples is consistently lower than the expected value. This suggests that the PGM complex may be partially removed from solution when the digested mixture is filtered to remove undissolved linker.

To confirm the stability of each MOF in the $Pd(OAc)_2$/THF solution, PXRD patterns were recorded for the post-extraction samples (Figure 3.22). This shows clearly that the MOFs retain their phase and crystallinity throughout the course of the extraction.

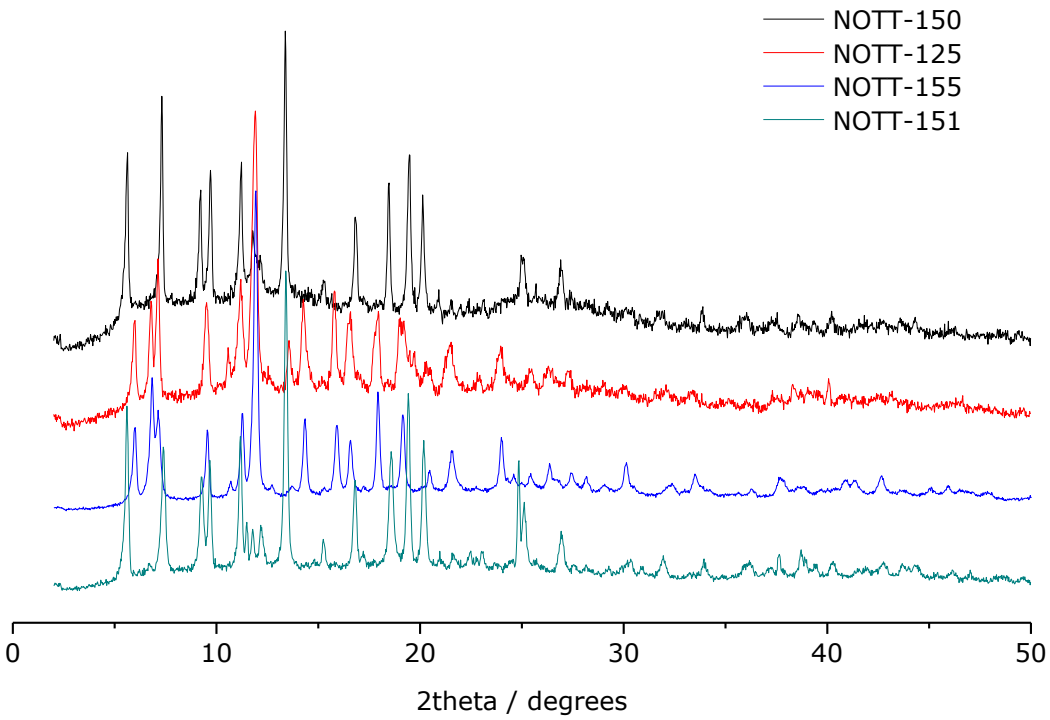


Figure 3.22. Post-extraction PXRD patterns of each Cu(II) MOF from the $Pd(OAc)_2$/THF mixture.

The same series of extractions was then carried out with a $PtCl_4$/THF mixture, with each MOF again exhibiting uptake of the PGM from solution (Table 3.3). The uptake capacities for $PtCl_4$ are considerably higher than those for $Pd(OAc)_2$, consistent with stronger interactions between the framework functional groups and the Cl groups in comparison to the OAc groups of $Pd(OAc)_2$. It should also be noted that $PtCl_4$ is smaller than $Pd(OAc)_2$ and will be more easily accommodated in MOF pores. As with $Pd(OAc)_2$, the larger pore MOFs NOTT-155 and NOTT-125 show much greater capacity for $PtCl_4$ than NOTT-151 in every experiment, especially when larger quantities of MOF are used. For example, NOTT-155, -125 and -151 exhibit 37.1%, 37.6% and 11.0% uptake respectively with 50 mg of MOF added to a 25 ppm solution.

Table 3.3. Uptake of $PtCl_4$ from THF into a series of Cu(II) MOFs. Values highlighted in bold text show the most effective material for each experiment.

MOF (mass / mg)	Pt conc / ppm	% uptake	Uptake / mg g^{-1}	Expected Cu:Pt ratio	Measured Cu:Pt ratio
NOTT-151 (20)	10	2.48	1.5	376 : 1	181 : 1
NOTT-151 (50)	10	26.41	6.6	88 : 1	177 : 1
NOTT-151 (10)	25	0	0	N/A	N/A
NOTT-151 (20)	25	7.86	12.2	47 : 1	54 : 1
NOTT-151 (50)	25	10.97	6.8	85 : 1	88 : 1
NOTT-155 (20)	10	2.60	1.6	359 : 1	121 : 1
NOTT-155 (50)	10	**62.91**	**15.7**	**37 : 1**	75 : 1
NOTT-155 (10)	25	**0.27**	**0.8**	**691 : 1**	N/A
NOTT-155 (20)	25	**46.53**	**72.5**	**8 : 1**	21 : 1
NOTT-155 (50)	25	37.07	23.1	25 : 1	38 : 1
NOTT-125 (20)	10	**12.29**	**7.7**	**77 : 1**	142 : 1
NOTT-125 (50)	10	51.01	12.7	46 : 1	86 : 1
NOTT-125 (10)	25	0	0	N/A	N/A
NOTT-125 (20)	25	5.83	9.1	65 : 1	58 : 1
NOTT-125 (50)	25	**37.58**	**23.4**	**25 : 1**	76 : 1
NOTT-150 (50)	10	2.87	0.7	814 : 1	818 : 1
NOTT-150 (50)	25	2.91	1.8	320 : 1	183 : 1

The highest uptake is demonstrated by amine-functionalised NOTT-155 at 72.5 mg g^{-1} from a 25 ppm solution (equivalent to 4 NH_2 groups per Pt). Interestingly, NOTT-155 is a more effective sorbent for $PtCl_4$ than NOTT-125. As these MOFs are isostructural, this suggests that the interaction between the NH_2 group and the PGM chloride is stronger than that of oxamide groups in NOTT-125. The same is true with the comparison of NOTT-151 and NOTT-150 in which the amine-functionalised NOTT-151 shows much greater sorption capacity than the methyl-functionalised NOTT-150 (26.4% and 11.0% *versus* 2.9% and 2.9% in equivalent experiments). Again this shows the importance of functional group selection on the efficiency of metal encapsulation. The ratios of Cu:Pt calculated from the digested MOF samples show much better agreement with the expected values than the Pd-doped materials. However, the Pt content is still lower than predicted, which suggests that $PtCl_4$ is being removed during the filtration process. This will be discussed in greater detail

later in this Chapter. Powder X-ray diffraction was used to confirm the stability of each MOF in the extraction solution (Figure 3.23).

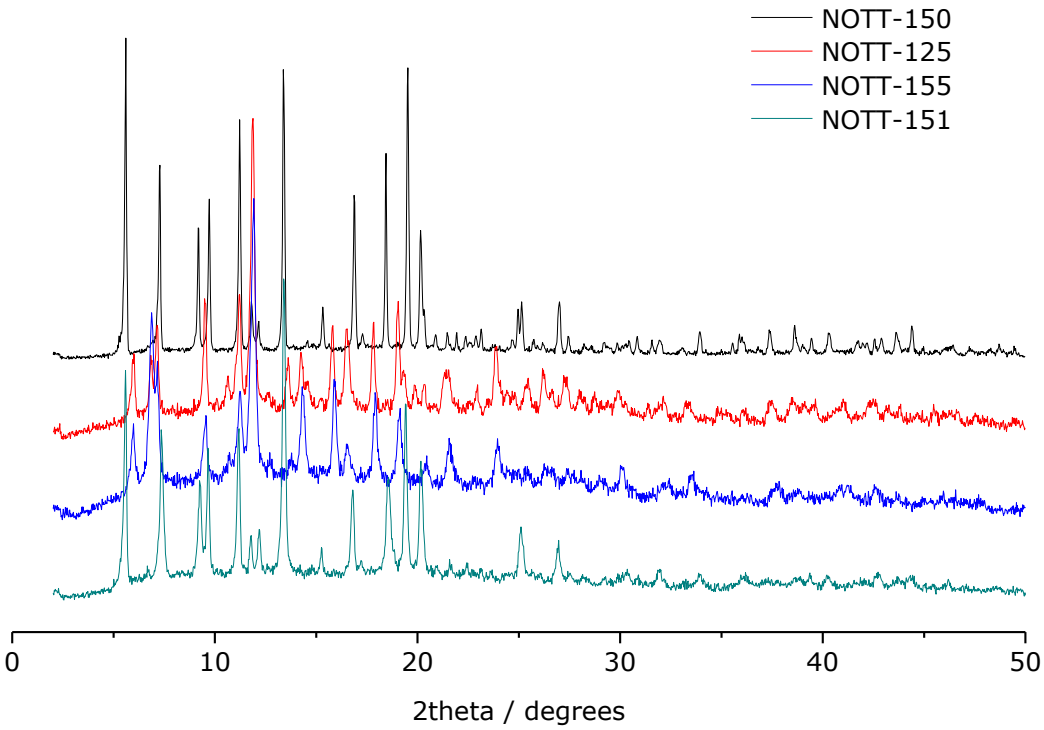


Figure 3.23. Post-extraction PXRD patterns of each Cu(II) MOF from the $PtCl_4$/THF mixture.

The final series of extractions were carried out in a $Rh_2(OAc)_4$/THF mixture, with each MOF showing significantly poorer uptake of Rh in comparison to Pd and Pt (Table 3.4). Comparisons between the different MOFs is difficult as the Rh uptake was very low in the majority of experiments, however NOTT-125 (10 mg) exhibited excellent uptake from a 25 ppm solution of 86.6 mg g^{-1} (3 oxamide groups per Rh). The generally low uptake is attributed to the larger size of the rhodium acetate dimer (6.5 Å x 8.2 Å in diameter) in comparison to $Pd(OAc)_2$ and $PtCl_4$.[37]

Table 3.4. Uptake of $Rh_2(OAc)_4$ from THF into a series of Cu(II) MOFs. Values highlighted in bold text show the most effective material for each experiment.

MOF (mass / mg)	Rh conc / ppm	% uptake	Uptake / mg g^{-1}	Expected Cu:Rh ratio	Measured Cu:Rh ratio
NOTT-151 (20)	10	28.87	15.5	32 : 1	1517 : 1
NOTT-151 (50)	10	0	0	N/A	2498 : 1
NOTT-151 (10)	25	4.05	10.9	46 : 1	574 : 1
NOTT-151 (20)	25	0	0	N/A	624 : 1
NOTT-151 (50)	25	**4.73**	**2.5**	**197 : 1**	963 : 1
NOTT-155 (20)	10	**32.95**	**17.7**	**28 : 1**	888 : 1
NOTT-155 (50)	10	0	0	N/A	N/A
NOTT-155 (10)	25	2.11	5.7	88 : 1	357 : 1
NOTT-155 (20)	25	0	0	N/A	771 : 1
NOTT-155 (50)	25	2.30	1.2	405 : 1	977 : 1
NOTT-125 (20)	10	12.45	6.7	76 : 1	1730 : 1
NOTT-125 (50)	10	0	0	N/A	3033 : 1
NOTT-125 (10)	25	**32.27**	**86.6**	**6 : 1**	642 : 1
NOTT-125 (20)	25	0	0	N/A	1028 : 1
NOTT-125 (50)	25	1.76	0.9	534 : 1	1861 : 1
NOTT-150 (50)	10	0	0	N/A	6570 : 1
NOTT-150 (50)	25	0	0	N/A	N/A

For the cases in which Rh uptake was observed, the Rh content of the digested MOF was much lower than expected (by one or two orders of magnitude). Again, each MOF exhibited good stability in the solution, as shown by PXRD of the post-extraction materials (Figure 3.24).

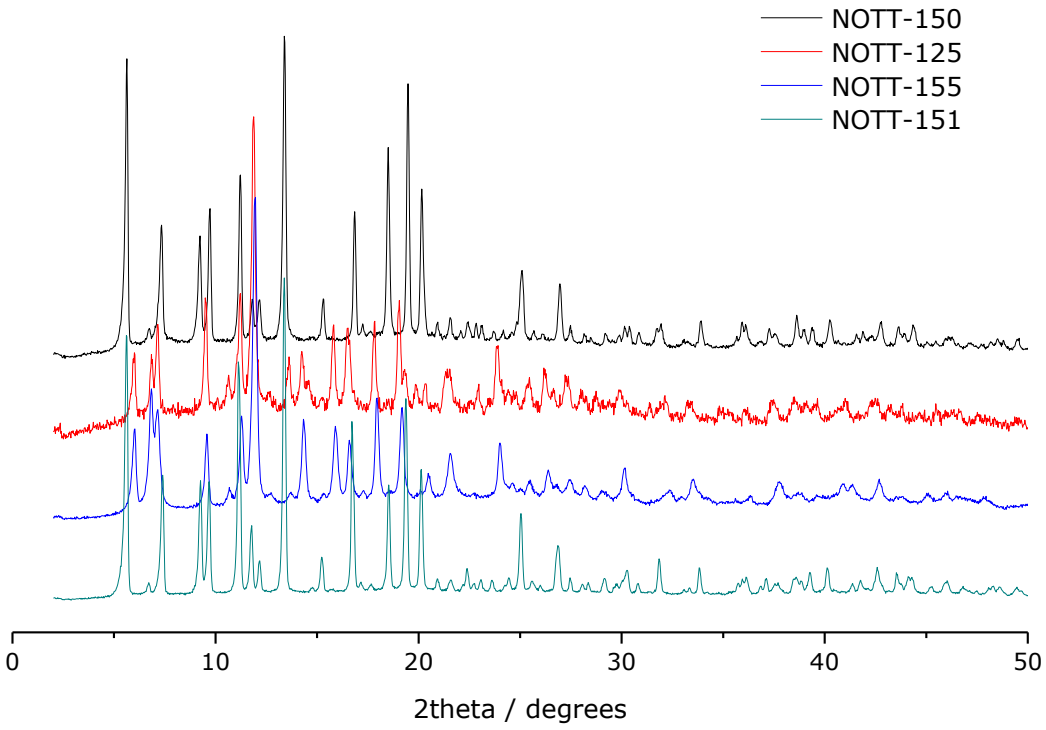


Figure 3.24. Post-extraction PXRD patterns of each Cu(II) MOF from the $Rh_2(OAc)_4$/THF mixture.

3.3.7 X-ray Photoelectron Spectroscopy of PGM-Doped MOFs

To investigate the discrepancies between the expected and predicted ratios of Cu:PGM, the post-extraction samples were analysed by X-ray photoelectron spectroscopy (XPS). XPS is an analytical technique in which spectra are obtained by irradiating a sample with X-rays. These X-rays excite electrons in the sample, which are then emitted from their parent atom if their binding energy is lower than the X-ray energy.[38] The kinetic energy distribution of these emitted electrons can then be measured and a photoelectron spectrum recorded.[39] For every element, there is a characteristic binding energy (directly related to the kinetic energy) associated with each core orbital and consequently, each element will give rise to a characteristic set of peaks in the photoelectron spectrum.[39] From the intensities of these peaks it is

possible to quantitatively analyse the elemental composition of the sample. However, only electrons near the surface (1-10 nm) of the material are emitted before being reabsorbed, thus XPS can only provide information on the elemental composition near the surface.[39]

As instrument time was limited, only the 50 mg/10 ppm extraction samples were analysed for comparison with the ICP-OES data (Table 3.5). The intensity of each element was converted to a molar atomic % in the sample, which was then converted to an atomic mass % to allow direct comparison between the ICP-OES and XPS data. It should be noted that in the case of $PtCl_4$, the binding energy of the Pt 4*f* orbital overlaps with that of the Cu 3*p* orbital, meaning that the direct quantification of Pt is not possible. However, the Cu:Cl ratio may be calculated and converted to a Cu:Pt ratio. As only one Cl environment is evident by XPS, it is assumed that $PtCl_4$ is the only species present in the solution and the Pt:Cl ratio is taken to be 1:4.

Table 3.5. A comparison of the PGM content of the doped Cu MOFs as determined by ICP-OES and XPS.

MOF	PGM	ICP-OES Cu:PGM ratio	XPS Cu:PGM ratio
NOTT-151	$Pd(OAc)_2$	146 : 1	8 : 1
NOTT-155	$Pd(OAc)_2$	188 : 1	6 : 1
NOTT-125	$Pd(OAc)_2$	220 : 1	29 : 1
NOTT-150	$Pd(OAc)_2$	207 : 1	14 : 1
NOTT-151	$PtCl_4$	177 : 1	35 : 1
NOTT-155	$PtCl_4$	75 : 1	19 : 1
NOTT-125	$PtCl_4$	86 : 1	31 : 1
NOTT-150	$PtCl_4$	818 : 1	24 : 1
NOTT-151	$Rh_2(OAc)_4$	2498 : 1	N/A
NOTT-155	$Rh_2(OAc)_4$	N/A	N/A
NOTT-125	$Rh_2(OAc)_4$	3033 : 1	N/A
NOTT-150	$Rh_2(OAc)_4$	6570 : 1	N/A

In the cases of $Pd(OAc)_2$ and $PtCl_4$, the PGM content determined by XPS is significantly higher than that determined by ICP-OES, by one order of magnitude in most cases. As XPS is a surface analysis technique, these results are consistent with PGM encapsulation being limited to the pores at or near the surface of the materials. The increase in PGM content for the Pd-doped samples is markedly higher than the increase observed for the Pt-doped samples, suggesting that a higher proportion of $Pd(OAc)_2$ may be removed from the ICP-OES digestion process by filtration. This also explains the poor agreement between the expected and measured ICP-OES ratios of Cu:Pd for the $Pd(OAc)_2$ extractions. However, the Cu:Rh ratios from both ICP-OES and XPS analysis are in agreement with the ICP-OES showing negligible Rh content in each sample and no trace of Rh observed from XPS.

Whilst the uptake of the three PGM complexes in each MOF appears to be relatively low, we have nonetheless demonstrated the first example of MOFs capable of the removal of neutral PGM species from solution. Further work on these MOFs will include carrying out XPS analysis on every sample to give a full comparison between ICP-OES and XPS data. ^{13}C and ^{15}N solid state NMR of the PGM-doped frameworks will also be used to probe the interactions between the MOFs and the metal complexes.

High resolution PXRD and single crystal XRD studies have been carried out to elucidate the structure of the encapsulated PGM species and the interactions between the PGM and each MOF, however this has been unsuccessful thus far. This is attributed to the poor PGM uptake below the surface layers, as shown by XPS, leading to low crystallographic occupancy of the encapsulated species.

3.3.8 Structure and Properties of MOFs Synthesised from a Novel Amine-Functionalised Ligand

Amongst recent work in the Schröder group, we have had great success using [1,1'-biphenyl]-3,3',5,5'-tetracarboxylic acid (BPTC) as a ligand with a variety of metal ions.[40-45] Most notably this has included selective uptake of CO_2 and SO_2 within an Al(III) framework (NOTT-300)[43] and H_2 uptake in an anionic In(III) framework.[45] With this in mind, a related amine-bridged tetracarboxylate ligand, 5,5'-azanediyldiisophthalic acid, denoted H_4L^{10} (Figure 3.25), was designed and synthesised *via* Buchwald-Hartwig aryl amination.[46-48]

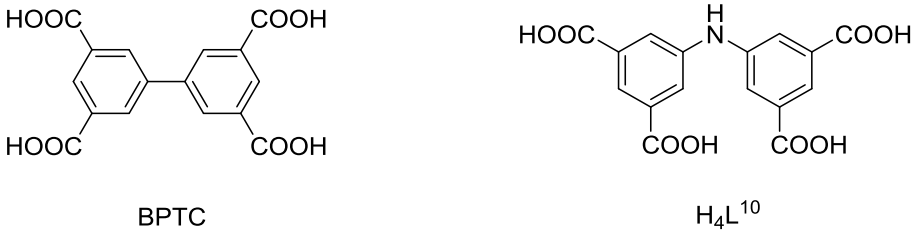
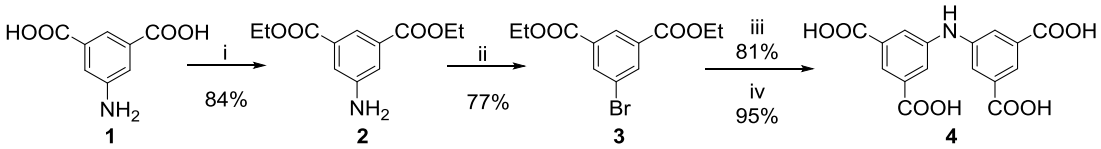


Figure 3.25. The structures of BPTC (left) and H_4L^{10} (right).

3.3.8.1 Synthesis of H_4L^{10}

Ligand synthesis proceeded first *via* the conversion of 5-aminoisophthalic acid to its corresponding ethyl ester by heating in acidified ethanol. The amine group was then converted to a bromide using a Sandmeyer reaction[49] which proceeds *via* the formation of a diazonium salt that reacts rapidly with CuBr in an HBr solution to give the product. The key synthetic step is the reaction between **2** and **3** to give the amine bridged compound **4** using Buchwald-Hartwig cross-coupling (Scheme 3.5).[48]



Scheme 3.5. (i). EtOH, H_2SO_4; (ii). 15% HBr, $NaNO_2$, CuBr; (iii). **2**, Cs_2CO_3, PhMe, $Pd(OAc)_2$, P^tBu_3; (iv). EtOH/THF/NaOH (aq), 37% HCl.

Despite being a very important reaction for C-N bond formation, this method of aryl amination is not commonly used in the preparation of MOF linkers. Our initial attempts at this coupling reaction using strong bases such as KO^tBu, NaO^tBu and NaOMe yielded no product. It was found that a combination of Cs_2CO_3, $Pd(OAc)_2$ and P^tBu_3 in toluene under microwave irradiation gave the product in good yield (81%). A simple hydrolysis of this ester to the corresponding carboxylic acid gave the target ligand, H_4L^{10}.

3.3.8.2 Synthesis and Structural Analysis of $[Co_2(L^{10})(H_2O)_2(DMF)]_n$

A reaction of H_4L^{10} with $Co(NO_3)_2{\cdot}6H_2O$ in a DMF/EtOH/H_2O mixture at 90 °C yielded pink block crystals of $[Co_2(L^{10})(H_2O)_2(DMF)]_n$. Single crystal X-ray diffraction reveals that the material crystallises in the monoclinic space group $P2_1/c$ with unit cell dimensions a = 10.1447(5) Å, b = 18.959(1) Å, c = 15.5864(9) Å, β = 95.398(5)° and V = 2984.4(3) Å^3. The resulting 3D structure is built up of binuclear Co(II) nodes comprising two COO^- units bridging between the Co ions. In addition a further COO^- is bound in bidentate fashion to Co1 with one O atom bridging to Co2 and a fourth ligand is bound in the equatorial positions of Co2. H_2O and DMF molecules occupy the equatorial positions of Co1 and an axial water molecule is bound to Co2. This gives an overall distorted tetrahedral node with underlying 4-connected **sra** toplogy. The structure comprises chains of metal nodes joined by an isophthalate unit with the second isophthalate bridging across to the adjacent chain

(Figure 3.26). This results in pore channels down the *a*- and *c*-axes and a further channel in between crystallographic axes. The square channel between axes measures 5.0 Å in diameter, the channel down the *a*-axis measures 7.7 Å x 13.0 Å and the channel down the *c*-axis is 5.5 Å in diameter. All distances were measured after the removal of coordinated DMF and H_2O molecules.

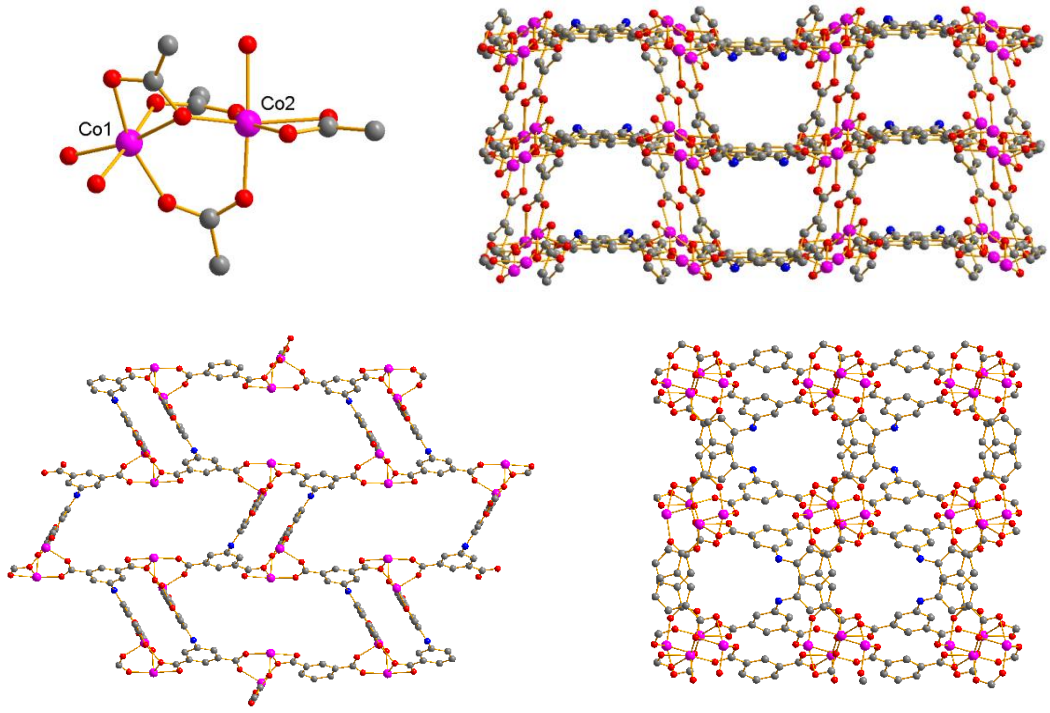


Figure 3.26. View of the metal node (top left), channel between axes (top right) and the channels down the *a*- and *c*-axes (bottom left and bottom right respectively) in desolvated $[Co_2(L^{10})]_n$.

3.3.8.3 Synthesis and Structural Analysis of $[In_4(L^{10})_3]_n[cation_4]_n$

The reaction of H_4L^{10} with $In(NO_3)_3{\cdot}3H_2O$ in a mixture of DMF/EtOH acidified with HBF_4 at 90 °C gave rise to colourless rod crystals of $[In_4(L^{10})_3][cation]{\cdot}xDMF$. This anionic framework crystallises in the monoclinic space group $P2_1/c$ with unit cell dimensions a = 9.8716(9) Å, b = 22.060(1) Å, c = 17.365(2) Å, β = 100.620(9)° and V = 3716.9(6) Å^3. The structure consists of an 8-coordinate In(III) metal node bound

in bidentate fashion by 4 COO^- groups to give a pseudo-tetrahedral cluster. As the metal node is anionic, a counter-cation is required to balance the charge, however this cation cannot be elucidated crystallographically. This indicates that the counterion may be a proton from the HBF_4 used in the synthesis. The framework is built up of chains of these metal nodes bridged by isophthalate groups, with adjacent chains being joined by the linker. The linker exhibits a twist around the central NH of 55.4 ° which leads to the formation of NH-functionalised 1D channels down the *a*-axis of 6.8 Å x 10.4 Å in diameter (Figure 3.27).

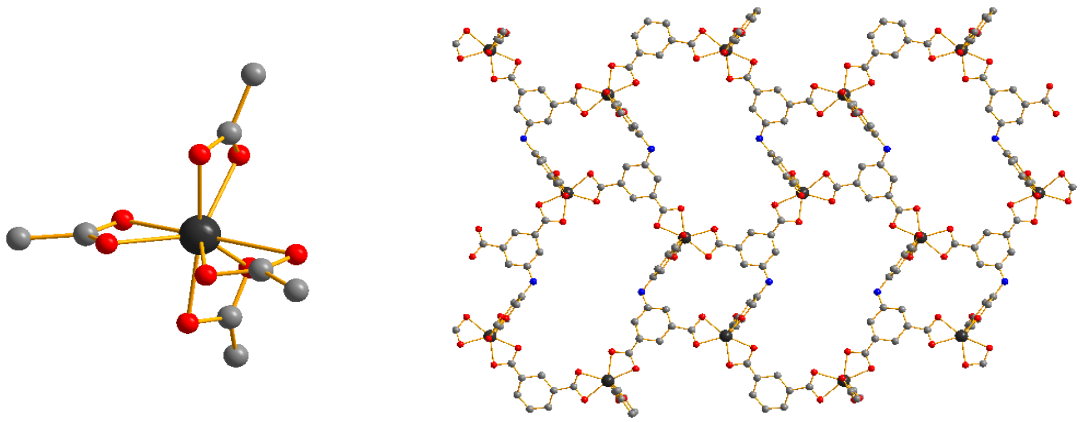


Figure 3.27. View of the metal node (left) and the 1D channel down the *a*-axis (right) in $[In_4(L^{10})_3]$.

3.3.8.4 Thermal Stability and Phase Purity of $[Co_2(L^{10})(H_2O)_2(DMF)]_n$ and $[In_4(L^{10})_3]_n[cation_4]_n$

Powder X-ray diffraction was used to confirm the crystallinity and phase purity of the bulk materials (Figure 3.28), with both being successfully indexed to the correct unit cell from the single crystal structures. During the processing of the PXRD data, the background was subtracted from the $[Co_2(L^{10})(H_2O)_2(DMF)]_n$ pattern as the

fluorescence of Co(II) in Cu Kα radiation resulted in a large background contribution.

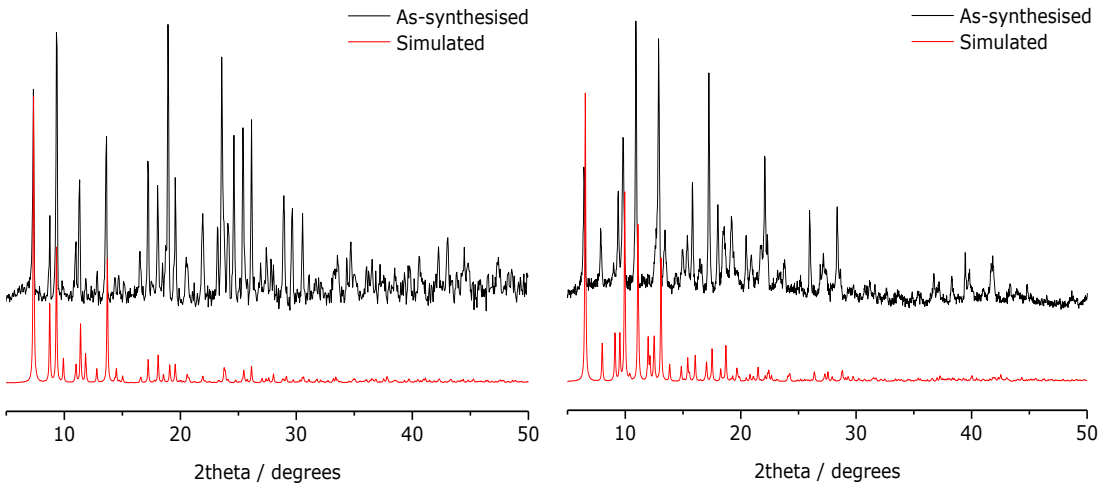


Figure 3.28. PXRD patterns of as-synthesised samples of $[Co_2(L^{10})(H_2O)_2(DMF)]_n$ (left) and $[In_4(L^{10})_3]_n[cation_4]_n$ (right).

Thermogravimetric analysis of an as-synthesised sample of $[Co_2(L^{10})(H_2O)_2(DMF)]_n$ exhibited three distinct mass losses below 240 °C, consistent with the sequential loss of ethanol, water and DMF with increasing temperature. The material is then stable up to ~340 °C, at which point a mass loss corresponding to framework decomposition is observed (Figure 3.29). The TGA trace of the In(III) framework shows a mass loss below 180 °C attributed to solvent loss, with the material decomposition then occurring at ~380 °C, which is consistent with previous reports of anionic In(III) MOFs.[50,51]

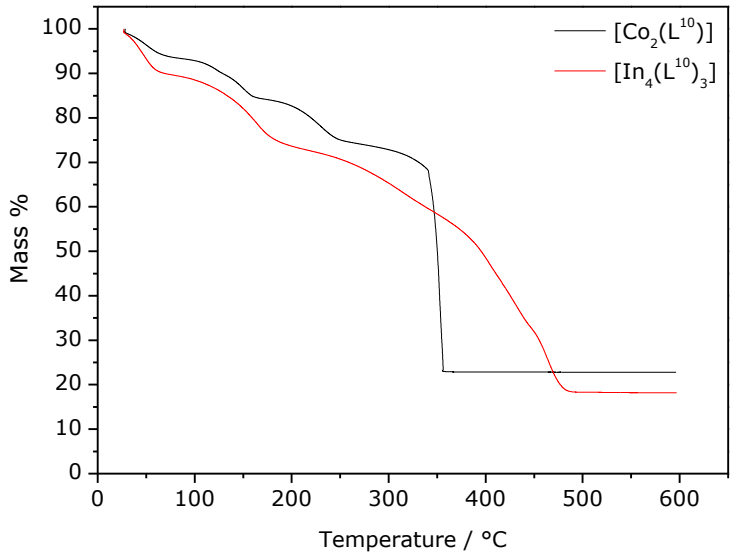


Figure 3.29. TGA traces of as-synthesised samples of $[Co_2(L^{10})(H_2O)_2(DMF)]_n$ and $[In_4(L^{10})_3]_n[cation_4]_n$.

Following characterisation by PXRD and TGA, N_2 isotherms were measured at 77 K for activated samples of each material. However both frameworks were found to be non-porous. PXRD patterns of the activated samples were then recorded, showing clearly that $[In_4(L^{10})_3]_n[cation_4]_n$ had decomposed upon activation (Figure 3.30). Subsequent attempts to exchange this MOF with different solvents (EtOH, $CHCl_3$, MeCN and MeOH) and to activate it using supercritical CO_2 were also unsuccessful. The PXRD pattern of $[Co_2(L^{10})(H_2O)_2(DMF)]_n$ shows only a small degree of amorphous character, thus the lack of N_2 uptake is assigned to DMF remaining on the metal nodes after activation. Efforts to prepare fully activated and stable samples of both frameworks are currently ongoing.

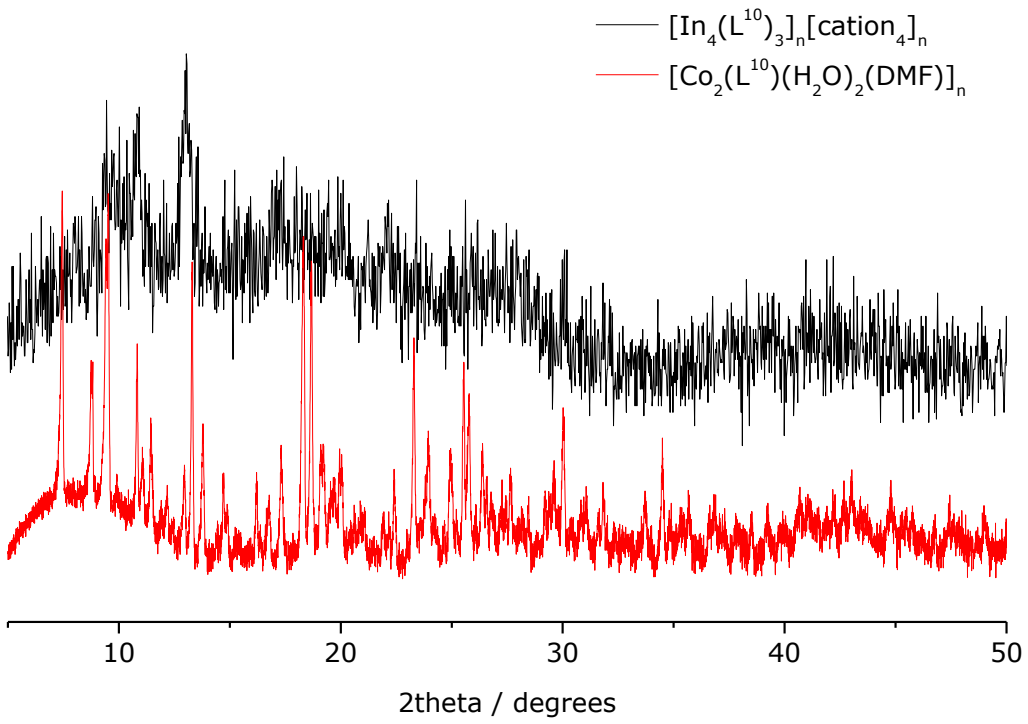


Figure 3.30. PXRD patterns of activated samples of $[Co_2(L^{10})(H_2O)_2(DMF)]_n$ and $[In_4(L^{10})_3]_n[cation_4]_n$.

3.4 Current and Future Work

Our current work is focused on the synthesis of chemically and thermally stable functionalised Fe(III) MOFs prepared from the tetracarboxylate linkers H_4L^6-H_4L^{10} described previously in this Chapter. Fe(III) MOFs that are not based around a terephthalic acid linker have not been commonly reported, although Zhou and co-workers recently published a series of Fe(III)-based structures from a variety of organic linkers.[52] The aim of our work is to prepare a series of stable MOFs for extraction of PGMs from H_2O and HCl in addition to the scavenging of Pd/Pt/Rh species from organic solutions as described above. A wide range of solvothermal reaction conditions were trialled using $FeCl_3{\cdot}6H_2O$ and $Fe_3O(OAc)_6(H_2O)_3$ metal

precursors, DMF, DEF and NMP solvents and PhCOOH/AcOH modulators at 120-150 °C.

Thus far these reactions have yielded a single crystal structure with H_4L^7. The MOF was synthesised from the reaction of H_4L^7 and $Fe_3O(OAc)_6(H_2O)_3$ in a mixture of NMP/AcOH at 120 °C to give large orange block crystals. The structure crystallises in the monoclinic space group $P2_1$ with unit cell dimensions a = 10.0795(4) Å, b = 17.3430(6) Å, c = 15.1751(5) Å, β = 105.938(4) ° and V = 2550.8(2) $Å^3$. The framework consists of a bimetallic node of 6-coordinate Fe centres in which Fe1 is coordinated in bidentate fashion by two COO^- groups with a further two COO^- units bridging between Fe1 and the octahedrally coordinated Fe2 (Figure 3.31). The coordination sphere of Fe2 is completed by another COO^- bridging from Fe1 and three NMP solvent molecules. In combination with the L^7 linker, in which the isophthalate groups are perpendicular to one another, this gives an overall structure of 50% porosity containing amine-functionalised 1D channels (Figure 3.31)

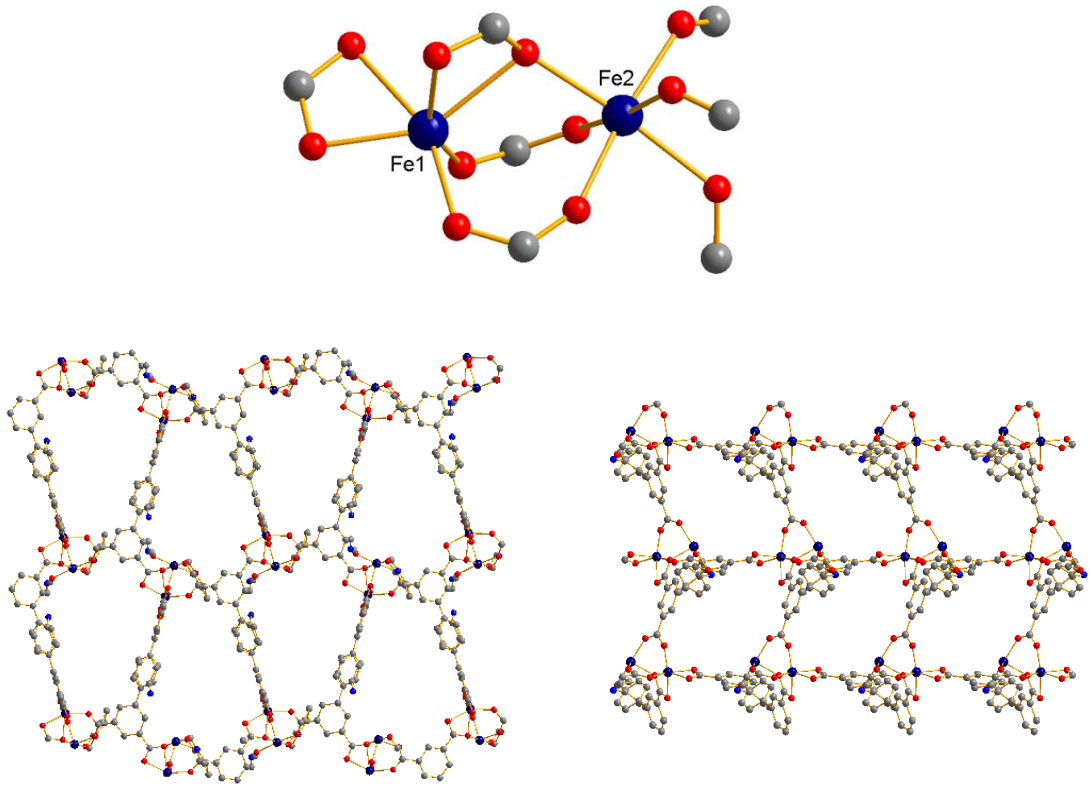


Figure 3.31. The metal node (top), triangular 1D channel (bottom left) and square 1D channel (bottom right) observed in $[Fe_2(L^7)(NMP)_3]_n$.

Two distinct channels are evident within the structure down the *a*- and *c*-axes (Figure 3.30). The channel along the *a*-axis consists of chains of metal nodes linked by isophthalate units, with the linker bridging between adjacent chains to give a triangular cavity lined with amine groups of 6.0 Å x 9.6 Å in diameter. The second channel consists of the metal nodes bridged by isophthalate with the linkers lying along the plane of the *c*-axis joining adjacent clusters of the same chain to give a square cavity measuring 6.2 Å x 7.2 Å in diameter. Attempts to prepare a phase pure sample of $[Fe_2(L^7)(NMP)_3]_n$ for metal extraction and gas storage applications are ongoing. However, preparing new phases of this MOF is also of interest as the three NMP molecules coordinated to the metal node will make $[Fe_2(L^7)(NMP)_3]_n$ very difficult to activate. Furthermore, the stoichiometry of the structure and the Fe-O

bond lengths (2.05 Å – 2.20 Å) suggest that the Fe(III) precursor has been reduced to Fe(II) within the framework, which is likely to be less chemically and thermally stable than an Fe(III) analogue.[52,53]

3.5 Conclusions

In summary, we have demonstrated the uptake of three neutral PGM complexes, $Pd(OAc)_2$, $PtCl_4$ and $Rh_2(OAc)_4$, from THF using four functionalised Cu(II) MOFs. The larger pore MOFs of **fof** topology, NOTT-155 and NOTT-125, show greater uptake of $Pd(OAc)_2$ and $PtCl_4$ than the smaller pore MOF, NOTT-151 (**ssa** topology). The extraction capabilities of NOTT-155 and NOTT-125 are very similar, with the oxamide functionalised NOTT-125 showing a more consistent uptake of $Pd(OAc)_2$ across the experiments. However, the amine functionalised NOTT-155 exhibits slightly higher extraction of $PtCl_4$ than NOTT-125 with a maximum uptake of 73 mg g^{-1}, corresponding to 4 NH_2 groups per $PtCl_4$. We have also demonstrated that the amine functionalised NOTT-151 exhibits much greater uptake than the isostructural methyl functionalised NOTT-150, highlighting the importance of interactions between the framework and the metal complex in this encapsulation process. Finally, the uptake of $Rh_2(OAc)_4$ was poor and inconsistent between experiments, possibly a result of the larger size of the rhodium acetate dimer, although NOTT-125 did exhibit a maximum uptake of 86 mg g^{-1}. Extraction of $Rh_2(OAc)_4$ into a larger pore MOF is described in Chapter 4.

A novel amine-bridged linker, H_4L^{10}, has also been synthesised *via* Buchwald-Hartwig cross-coupling and progress has been made towards stable, functionalised Fe MOFs.

3.6 Experimental

Synthesis of (3,5-bis(ethoxycarbonyl)phenyl)boronic acid

m-Xylene-5-boronic acid (30 g, 0.20 mol) and NaOH (29 g, 0.73 mol) were dissolved in ^{t}BuOH/H_2O (1:3, 1 L). The reaction mixture was heated to 50 °C with stirring and portions of $KMnO_4$ (totalling 198 g, 1.25 mol) were added to the solution once the purple colour of the previous portion had faded. After 150 g of $KMnO_4$ had been added, the reaction temperature was increased to 70 °C and the addition of $KMnO_4$ continued until the purple colour persisted for over 3 h, indicating full oxidation of the methyl groups. Excess $KMnO_4$ was reduced by addition of IPA (200 ml) and the solution was filtered whilst hot. The MnO_2 cake was washed with boiling water (500 ml) and the aqueous filtrate was concentrated to 150 ml by evaporation and acidified with 37% HCl to pH~1. The resulting white precipitate was collected by filtration, washed with cold water and dried to give 5-boronoisophthalic acid (41 g, 98%). ^{1}H NMR (400 MHz, dmso-d_6) δ = 8.27 (t, 1H, *J* = 3.0 Hz), 8.09 (d, 2H, *J* = 3.0 Hz). ^{13}C{^{1}H} NMR (100 MHz, dmso-d_6) δ = 169.3, 143.2, 138.4, 132.0.

Benzene-1,3-dicarboxylic-5-boronic triacid was heated in a solution of EtOH (450 ml) and 95% sulfuric acid (18 ml) at 85 °C for 20 h. Upon completion of the reaction the solution was concentrated to ~ 100 ml, whereupon water (500 ml) was added to give a precipitate which was collected by filtration, washed with water and dried under vacuum, giving the pure product as a white solid (38 g, 73%). ^{1}H NMR (300 MHz, dmso-d_6) δ = 8.64 (t, 2H, *J* = 1.8 Hz), 8.50 (t, 1H, *J* = 1.8 Hz), 4.36 (q, 4H, *J* = 6.0 Hz), 1.35 (t, 6H, *J* = 6.0 Hz); ^{13}C{^{1}H} NMR (75 MHz, dmso-d_6) δ = 165.7, 139.5, 131.5, 130.1, 61.5, 14.6. IR (solid state): ν / cm^{-1} 3361, 1724, 1699, 1602, 1296, 1253, 722, 697. MS(ESI) m/z 267 (M + H). Anal. Calcd (Found) for $C_{12}H_{15}O_6B_1$: C, 54.17 (54.23); H, 5.68 (5.58); N, 0.00 (0.00)%.

Synthesis of H_4L^6

2,6-Dibromoaniline (753 mg, 3 mmol), (3,5-bis(ethoxycarbonyl)phenyl)boronic acid (1.92 g, 7.20 mmol, 2.4 eq.) and K_3PO_4 (7.65 g, 36.0 mmol, 12 eq.) were added to a degassed mixture of 1,4-dioxane/water (5:1, 30 ml). Pd(dppf)Cl_2 (40 mg) was then added under a flow of argon and the reaction was heated in a microwave reactor at 85 °C for 1 hour. Upon completion of the reaction, the solvent was removed under vacuum and the product was extracted into $CHCl_3$. The combined organic phase was subsequently washed with water and brine and dried over $MgSO_4$. After evaporation of $CHCl_3$, the crude product was isolated as a light-brown solid. This solid was then dissolved in CH_2Cl_2 and passed through a plug of silica gel. Removal of CH_2Cl_2 under vacuum gave the pure ester product as an off-white solid (1.43 g, 86%). ^{1}H NMR (270 MHz, dmso-d_6) δ = 8.45 (t, 2H, *J* = 1.6 Hz), 8.23 (d, 4H, *J* = 1.6 Hz), 7.11 (d, 2H, *J* = 7.6 Hz), 6.83 (d, 1H, *J* = 7.6 Hz), 4.59 (s, 2H), 4.38 (q, 8H, *J* = 7.0 Hz), 1.35 (t, 12H, *J* = 7.0 Hz). MS(ESI) m/z 534 (M + H).

This tetraester (1.38 g) was dissolved in a mixture of THF (30 ml) and 2 M NaOH (30 ml) and heated at 75 °C for 16 h. Upon cooling, THF (30 ml) was added, the aqueous layer was separated and 37% HCl was added dropwise to the solution until pH~1. The resulting precipitate was filtered and recrystallised from a mixture of hot DMF/water (5:1) to give the desired product as an off-white solid (1.04 g, 95%). ^{1}H NMR (270 MHz, dmso-d_6) δ = 8.46 (t, 2H, *J* = 1.6 Hz), 8.22 (d, 4H, *J* = 1.6 Hz), 7.13 (d, 2H, *J* = 7.6 Hz), 6.85 (d, 1H, *J* = 7.6 Hz); ^{13}C{^{1}H} NMR (100 MHz, dmso-d_6) δ = 167.0, 140.1, 139.7, 134.5, 132.4, 131.1, 129.4, 128.3, 120.5. MS(ESI) m/z 420 (M - H). Anal. Calcd (Found) for $C_{22}H_{15}N_1O_8$: C, 62.71 (62.00); H, 3.59 (3.88); N, 3.32 (3.56)%.

Synthesis of H_4L^7

2,5-Dibromoaniline (753 mg, 3 mmol), (3,5-bis(ethoxycarbonyl)phenyl)boronic acid (1.92 g, 7.20 mmol, 2.4 eq.) and K_3PO_4 (7.65 g, 36.0 mmol, 12 eq.) were added to a degassed mixture of 1,4-dioxane/water (10:1, 110 ml). Pd(dppf)Cl_2 (40 mg) was then added under a flow of argon and the reaction was heated in a 250 ml Schlenk flask at 85 °C for 3 days. Upon completion of the reaction, the solvent was removed under vacuum and the product was extracted into $CHCl_3$. The combined organic phase was subsequently washed with water and brine and dried over $MgSO_4$. After evaporation of $CHCl_3$, the crude product was isolated as a light-brown solid. This solid was then dissolved in CH_2Cl_2 and passed through a plug of silica gel. Removal of CH_2Cl_2 under vacuum gave the pure ester product as a pale yellow solid (1.51 g, 91%). ^{1}H NMR (300 MHz, dmso-d_6) δ = 8.45 (t, 1H, *J* = 1.6 Hz), 8.43 (t, 1H, *J* = 1.6 Hz), 8.40 (d, 2H, *J* = 1.6 Hz), 8.25 (d, 2H, *J* = 1.6 Hz), 7.21 (d, 1H, *J* = 2.6 Hz), 7.19 (d, 1H, *J* = 3.3 Hz), 7.03 (dd, 1H, *J* = 7.80, 1.8 Hz), 5.23 (s, 2H), 4.40 (q, 8H, *J* = 6.8 Hz), 1.37 (t, 12 H, *J* = 6.0 Hz). MS(ESI) m/z 534 (M + H).

This tetraester (1.51 g) was dissolved in a mixture of THF (30 ml) and 2M NaOH (30 ml) and heated at 75 °C for 16 h. Upon cooling, THF (30 ml) was added, the aqueous layer was separated and 37% HCl was added dropwise to the solution until pH~1. The resulting precipitate was filtered and recrystallised from a mixture of hot DMF/water (5:1) to give the desired product as a pale yellow solid (1.12 g, 98%). ^{1}H NMR (300 MHz, dmso-d_6) δ = 13.35 (s, 4H), 8.46 (t, 1H, *J* = 1.5 Hz), 8.44 (t, 1H, *J* = 1.5 Hz), 8.40 (d, 2H, *J* = 1.50 Hz), 8.23 (d, 2H, *J* = 1.5 Hz), 7.24 (d, 1H, *J* = 1.7 Hz), 7.20 (d, 1H, *J* = 8.0 Hz), 7.05 (dd, 1H, *J* = 8.10, 1.8 Hz), 5.20 (s, 2H); ^{13}C{^{1}H} NMR (100 MHz, dmso-d_6) δ = 167.1, 167.0, 146.7, 141.5, 140.4, 139.2, 134.0,

132.5, 132.3, 131.6, 131.4, 124.3, 115.7, 114.1. MS(ESI) m/z 420 (M - H). Anal. Calcd (Found) for $C_{22}H_{15}N_1O_8$: C, 62.71 (62.21); H, 3.59 (3.64); N, 3.32 (3.11)%.

Synthesis of H_4L^8

A suspension of 5-aminoisophthalic acid (8.4 g, 43.9 mmol) in anhydrous THF (50 ml) was cooled to 0 °C and flushed with argon. A solution of oxalyl chloride (3.24 ml, 37.8 mmol) in anhydrous THF (100 ml) was added dropwise to the reaction mixture over a period of 1 hour, producing a white precipiate. Triethylamine (1.0 ml, 7.3 mmol) was then added dropwise and the mixture was stirred overnight at room temperature. The solvent volume was reduced under vacuum to ~ 30 ml and 2 M HCl was added until pH~1. The solution was stirred for 15 mins and the precipitate was isolated by filtration, washed with water and recrystallised from hot methanol to give the product as a white powder (7.29 g, 80%). ^{1}H NMR (400 MHz, dmso-d_6) δ = 11.25 (s, 2H), 8.73 (d, 4H, J = 1.6 Hz), 8.29 (t, 2H, J = 1.6 Hz); ^{13}C{^{1}H} NMR (100 MHz, dmso-d_6) δ = 166.8, 159.2, 138.8, 132.3, 126.5, 125.7. MS(ESI) m/z 439 (M + Na). Anal. Calcd (Found) for $C_{18}H_{12}N_2O_{10}$: C, 51.93 (51.57); H, 2.91 (2.73); N, 6.73 (6.39)%.

Synthesis of H_4L^9

2,6-Dibromotoluene (1.50 g, 6.0 mmol), (3,5-bis(ethoxycarbonyl)phenyl)boronic acid (3.83 g, 14.4 mmol, 2.4 eq.) and K_3PO_4 (3.05 g, 14.4 mmol, 2.4 eq.) were added to a degassed mixture of 1,4-dioxane/water (5:1, 75 ml). Pd(dppf)Cl_2 (40 mg) was then added under a flow of argon and the reaction was heated in a 250 ml Schlenk flask at 85 °C for 48 h. Upon completion of the reaction, the solvent was removed under vacuum and the product was extracted into $CHCl_3$. The combined organic phase was subsequently washed with water and brine and dried over $MgSO_4$. After

evaporation of $CHCl_3$, the crude product was isolated as a white solid. This solid was then dissolved in CH_2Cl_2 and passed through a plug of silica gel. Removal of CH_2Cl_2 under vacuum gave the pure ester product as a white solid (2.73 g, 85%). ^{1}H NMR (400 MHz, dmso-d_6) δ = 8.50 (s, 2H), 8.21 (s, 4H), 7.44 (t, 1H, *J* = 7.2 Hz), 7.36 (d, 2H, *J* = 7.2 Hz), 4.39 (q, 8H, *J* = 7.0 Hz), 2.01 (s, 3H), 1.37 (t, 12H, *J* = 7.0 Hz); MS(ESI) m/z 555 (M + Na).

This tetraester (2.00 g) was dissolved in a mixture of THF (40 ml) and 2 M NaOH (40 ml) and heated at 75 °C for 16 h. Upon cooling, THF (40 ml) was added, the aqueous layer was separated and 37% HCl was added dropwise to the solution until pH~1. The resulting precipitate was filtered and recrystallised from a mixture of hot DMF/water (5:1) to give the desired product as a white solid (1.52 g, 96%). ^{1}H NMR (400 MHz, dmso-d_6) δ = 13.42 (s, 4H), 8.51 (t, 2H, *J* = 1.4 Hz), 8.18 (d, 4H, *J* = 1.2 Hz), 7.43 (t, 1H, *J* = 7.0 Hz), 7.36 (d, 2H, *J* = 7.2 Hz), 2.07 (s, 3H); ^{13}C{^{1}H} NMR (100 MHz, dmso-d_6) δ = 167.0, 142.7, 141.2, 134.3, 132.8, 132.0, 130.0, 129.1, 126.7, 18.9. Anal. Calcd (Found) for $C_{23}H_{16}O_8$: C, 65.72 (65.44); H, 3.84 (3.76); N, 0.00 (0.00)%.

Synthesis of 3-amino-5-(ethoxycarbonyl)benzoic acid

5-Aminoisophthalic acid (110 g, 0.607 mol) was heated in a solution of ethanol (1.2 L) and 95% sulfuric acid (55 ml) at 80 °C for 24 h. The solution was reduced to ~500 ml under vacuum and deionised water (500 ml) was added, resulting in precipitation of a white solid. This solid was isolated by filtration, washed with water (200 ml) and petroleum ether (200 ml). The crude product was then recrystallised from toluene to give pure 3-amino-5-(ethoxycarbonyl)benzoic acid (121 g, 84%). ^{1}H NMR (300 MHz, dmso-d_6) δ = 8.08 (s, 1H), 7.55 (s, 2H), 4.38 (q, 4H, *J* = 5.6 Hz), 1.41 (t, 6H, *J*

= 7.1 Hz); $^{13}C\{^{1}H\}$ NMR (75 MHz, dmso-d_6) δ = 166.1, 146.4, 131.8, 120.8, 119.8, 61.2, 14.3. MS(ESI) m/z 238 (M + H).

Synthesis of 3-bromo-5-(ethoxycarbonyl)benzoic acid

3-Amino-5-(ethoxycarbonyl)benzoic acid (11.3 g, 47.6 mmol) was dissolved in 15% HBr (200 ml) and cooled to 5 °C. $NaNO_2$ (3.98 g, 57.7 mmol) in H_2O (30 ml) was added slowly to the solution with rapid stirring. The mixture was then added to CuBr (9.80 g, 68.3 mmol) in HBr (45 ml) and left to stir at room temperature for 2 h, at which point a light brown precipitate was observed. This precipitate was removed by filtration and recrystallised from toluene to give pure 3-bromo-5-(ethoxycarbonyl)benzoic acid (11.01 g, 77%). ^{1}H NMR (300 MHz, dmso-d_6) δ = 8.41 (t, 1H, *J* = 1.7 Hz), 8.30 (d, 2H, *J* = 1.5 Hz), 4.37 (q, 4H, *J* = 7.2 Hz), 1.35 (t, 6H, *J* = 7.1 Hz); $^{13}C\{^{1}H\}$ NMR (100 MHz, dmso-d_6) δ = 164.0, 136.2, 132.9, 128.7, 122.6, 62.1, 14.5. MS(ESI) m/z 323 (M + Na).

Synthesis of H_4L^{10}

3-Amino-5-(ethoxycarbonyl)benzoic acid (1.20 g, 4 mmol), 3-bromo-5-(ethoxycarbonyl)benzoic acid (1.13 g, 4.8 mmol, 1.2 eq.) and Cs_2CO_3 (1.82 g, 5.6 mmol, 1.4 eq.) were added to degassed, anhydrous toluene (20 ml) in a 35 ml microwave tube. $Pd(OAc)_2$ (18 mg, 2 mol%) and P^tBu_3 (32.4 mg, 4 mol%) were subsequently added under argon and the microwave tube was heated at 120 °C for 30 mins. The resulting mixture was evaporated to dryness, extracted into $CHCl_3$, filtered through Celite and dried over $MgSO_4$. The $CHCl_3$ solution was removed under vacuum to give the crude product. Recrystallisation from EtOH gave pure tetraethyl-5,5'-azanediyldiisophthalate (1.48 g, 81%). ^{1}H NMR (300 MHz, dmso-d_6) δ = 9.25

(s, 1H), 8.02 (t, 2H, *J* = 1.5 Hz), 7.93 (d, 4H, *J* = 1.4 Hz), 4.36 (q, 8 H, *J* = 7.2 Hz), 1.33 (t, 12 H, *J* = 7.2 Hz). MS(ESI) m/z 480 (M + Na).

Tetraethyl-5,5'-azanediyldiisophthalate (1.48 g, 3.24 mmol) was added to a mixture of THF (20 ml), ethanol (20 ml) and 2M NaOH (20 ml) and heated at 90 °C for 24 h. After separating the layers, 37% HCl was added dropwise to the aqueous layer until a pale yellow precipitate formed. This solid was removed by filtration, dried under vacuum and recrystallised from DMF/H_2O to give pure 5,5'-azanediyldiisophthalic acid as a yellow solid (1.06 g, 95%). ^{1}H NMR (300 MHz, dmso-d_6) δ = 13.22 (s, 4H), 8.01 (t, 2H, *J* = 1.5 Hz), 7.85 (d, 4H, *J* = 1.5 Hz); ^{13}C{^{1}H} NMR (75 MHz, dmso-d_6) δ = 167.0, 143.7, 132.8, 121.5, 117.6. MS(ESI) m/z 344 (M - H). IR (solid state): ν / cm^{-1} 2981 br, 2562 br, 2361, 1698, 1596, 1541, 1410, 1348, 1278, 1262, 1045, 1032, 909, 884, 754, 693, 660. Anal. Calcd (Found) for $C_{16}H_{11}N_1O_8$: C, 55.66 (55.43); H, 3.21 (3.61); N, 4.06 (4.00)%.

Synthesis of $[Cu_2(L^6)(H_2O)_2]\cdot 4DMF\cdot H_2O$ (NOTT-151)

H_4L^6 (100 mg, 0.24 mmol) and $Cu(NO_3)_2\cdot 3H_2O$ (285 mg, 1.18 mmol) were dissolved in DMF (20 ml), to which 2 M HCl (20 drops) was added. This mixture was heated in a sealed 250 ml Schott bottle at 80 °C for 16 h to produce green block crystals which were isolated by filtration and washed with hot DMF (139 mg, 66%). Anal. Calcd (Found) for $C_{34}H_{45}N_5O_{15}Cu_2$: C, 45.84 (46.11); H, 5.09 (4.97); N, 7.86 (7.91)%.

Synthesis of $[Cu_2(L^7)(H_2O)_2]\cdot 7DMF\cdot H_2O$ (NOTT-155)

H_4L^7 (100 mg, 0.24 mmol) and $Cu(NO_3)_2\cdot 3H_2O$ (285 mg, 1.18 mmol) were dissolved in a mixture of DMF/H_2O (20:1; 21 ml), to which 2 M HCl (10 drops) was added. This mixture was heated in a sealed 250 ml Schott bottle at 80 °C for 16 h to produce

green block crystals which were isolated by filtration and washed with hot DMF (182 mg, 69%). Anal. Calcd (Found) for $C_{43}H_{66}N_8O_{18}Cu_2$: C, 46.52 (46.41); H, 5.99 (5.61); N, 10.09 (10.03)%.

Synthesis of $[Cu_2(L^8)(H_2O)_2]\cdot 3DMA\cdot 3H_2O$ (NOTT-125)

H_4L^8 (30 mg, 0.072 mmol) and $Cu(NO_3)_2\cdot 3H_2O$ (60 mg, 0.25 mmol) were dissolved in a mixture of DMA/H_2O (10:1; 5.5 ml), to which 50% HBF_4 (17 drops) was added. This mixture was heated in a sealed 250 ml Schott bottle at 70 °C for 48 h to produce blue block crystals which were isolated by filtration and washed with hot DMA (36 mg, 56%). Anal. Calcd (Found) for $C_{30}H_{45}N_5O_{18}Cu_2$: C, 40.45 (40.29); H, 5.09 (4.98); N, 7.86 (7.57)%.

Synthesis of $[Cu_2(L^9)(H_2O)_2]\cdot 5DMF\cdot 4H_2O$ (NOTT-150)

H_4L^9 (100 mg, 0.24 mmol) and $Cu(NO_3)_2\cdot 3H_2O$ (285 mg, 1.18 mmol) were dissolved in DMF (20 ml), to which 2 M HCl (20 drops) was added. This mixture was heated in a sealed 250 ml Schott bottle at 80 °C for 16 h to produce blue block crystals which were isolated by filtration and washed with hot DMF (190 mg, 78%). Anal. Calcd (Found) for $C_{38}H_{59}N_5O_{19}Cu_2$: C, 44.88 (44.27); H, 5.85 (5.63); N, 6.89 (6.80)%.

Synthesis of $[Co_2(L^{10})(H_2O)(DMF)]_n$

H_4L^{10} (11.5 mg, 0.033 mmol) and $Co(NO_3)_2\cdot 6H_2O$ (24.0 mg, 0.083 mmol) were dissolved in a mixture of DMF/ethanol/water (3:1:1; 2.5 ml) in a 15 ml glass pressure tube. After sonication, this solution was heated at 90 °C for 24 h, yielding pink block crystals (9.6 mg). IR (solid state): ν / cm^{-1} 3246 br, 1652, 1615, 1575, 1547, 1362, 1310, 1103, 1047, 1023, 993, 816, 773, 722, 661.

Synthesis of $[In_4(L^{10})_3][cation]_n$

H_4L^{10} (11.5 mg, 0.033 mmol) and $In(NO_3)_3 \cdot 3H_2O$ (8.7 mg, 0.033 mmol) were dissolved in DMF/ethanol (5:1; 3 ml) in a 15 ml glass pressure tube and 0.1 ml of HBF_4 was added. After sonication, this solution was heated at 90 °C for 72 h, yielding colourless rod crystals (8.3 mg). IR (solid state): ν / cm^{-1} 2967 br, 2359, 1651, 1574, 1367, 1098, 1057, 1033, 1018, 848, 811, 789, 751, 715, 663.

Synthesis of $[Fe_2(L^7)(NMP)_3]_n$

H_4L^7 (10 mg, 0.024 mmol) and $Fe_3O(OAc)_6(H_2O)_3$ (15 mg, 0.025 mmol) were dissolved in a mixture of NMP (2.5 ml) and glacial acetic acid (0.8 ml). This mixture was then heated in an 8 ml glass vial at 120 °C for 48 h to give orange block crystals (12 mg).

3.7 References

1. Phillips, S.; Kauppinen, P., *Platinum Metals Rev.*, **2010**, *54*, 69.
2. Heck, R. F.; Nolley, J. P., *J. Org. Chem.*, **1972**, *37*, 2320.
3. Beletskaya, I. P.; Cheprakov, A. V., *Chem. Rev.*, **2000**, *100*, 3009.
4. Sonogashira, K.; Tohda, Y.; Hagihara, N., *Tetrahedron Lett.*, **1975**, 4467.
5. Chinchilla, R.; Nájera, C., *Chem. Rev.*, **2007**, *107*, 874.
6. Baba, S.; Negishi, E. I., *J. Am. Chem. Soc.*, **1976**, *98*, 6729.
7. Milne, J. E.; Buchwald, S. L., *J. Am. Chem. Soc.*, **2004**, *126*, 13028.
8. Miyaura, N.; Suzuki, A., *J. Am. Chem. Soc., Chem. Commun.*, **1979**, 866.
9. Miyaura, N.; Suzuki, A., *Chem. Rev.*, **1995**, *95*, 2457.
10. Kotha, S.; Lahiri, K.; Kashinath, D., *Tetrahedron*, **2002**, *58*, 9633.
11. Li, H.; Johansson Seechurn, C. C. C.; Colacot, T. J., *ACS Catal.*, **2012**, *2*, 1147.
12. Barnard, C., *Platinum Metals Rev.*, **2008**, *52*, 38.
13. Fagnou, K.; Lautens, M., *Chem. Rev.*, **2003**, *103*, 169.
14. Sidera, M.; Fletcher, S. P., *Nature Chem.*, **2015**, *7*, 935.
15. Zhong, H. A.; Labinger, J. A.; Bercaw, J. E., *J. Am. Chem. Soc.*, **2002**, *124*, 1378.

16. Driver, T. G.; Williams, T. J.; Labinger, J. A.; Bercaw, J. E., *Organometallics*, **2007**, *26*, 294.
17. Lawson, Y. G.; Lesley, M. J. G.; Norman, N. C.; Rice, C. R.; Marder, T. B., *Chem. Commun.*, **1997**, 2051.
18. Shimada, S.; Batsanov, A. S.; Howard, J. A. K.; Marder, T. B., *Angew. Chem., Int. Ed.*, **2001**, *40*, 2168.
19. Pink, C. J.; Wong, H.; Ferreira, F. C.; Livingston, A. G., *Org. Process Res. Dev.*, **2008**, *12*, 589.
20. Galaffu, N.; Man, S. P.; Wilkes, R. D.; Wilson, J. R. H., *Org. Process Res. Dev.*, **2007**, *11*, 406.
21. Rosso, V. W.; Lust, D. A.; Bernot, P. J.; Grosso, J. A.; Modi, S. P.; Rusowicz, A.; Sedergran, T. C.; Simpson, J. H.; Srivastava, S. K.; Humora, M. J.; Anderson, N. G., *Org. Process Res. Dev.*, **1997**, *1*, 311.
22. Ishihara, K.; Nakayama, M.; Kurihara, H.; Itoh, A.; Haraguchi, H., *Chem. Lett.*, **2000**, *29*, 1218.
23. Barbaras, D.; Brozio, J.; Johannsen, I.; Allmendinger, T., *Org. Process Res. Dev.*, **2009**, *13*, 1068.
24. Frankham, J.; Kauppinen, P., *Platinum Metals Rev.*, **2010**, *54*, 200.
25. Májano, G.; Pérez-Ramírez, J., *Helv. Chim. Acta*, **2012**, *95*, 2278.
26. Chen, D-M.; Ma, J. G.; Cheng, P., *Dalton Trans.*, **2015**, *44*, 8926.
27. Tella, A. C.; Ameen, O. A.; Ajibade, P. A.; Alimi, L. O., *J. Porous Mat.*, **2015**, *22*, 1599.
28. Li, Z-X.; Zhao, J-P.; Sañudo, E. C.; Ma, H.; Pan, Z-D.; Zeng, Y-F.; Bu, X-H., *Inorg. Chem.*, **2009**, *48*, 11601.
29. Eubank, J. F.; Wojtas, L.; Hight, M. R.; Bousquet, T.; Kravtsov, V. C.; Eddaoudi, M., *J. Am. Chem. Soc.*, **2011**, *133*, 17532.
30. Dai, F.; Sun, D.; Sun, D., *Cryst. Growth Des.*, **2011**, *11*, 5670.
31. Liu, Y.; Li, J.-R.; Verdegaal, W. M. Liu, T. F.; Zhou, H-C., *Chem. Eur. J.*, **2013**, *19*, 5637.
32. Lin, X.; Telepini, I.; Blake, A. J.; Dailly, A.; Brown, C. M.; Simmons, J. M.; Zoppi, M.; Walker, G. S.; Thomas, K. M.; Mays, T. J.; Hubberstey, P.; Champness, N. R.; Schröder, M., *J. Am. Chem. Soc.*, **2009**, *131*, 2159.
33. Shishilov, O. N.; Stromnova, T. A.; Churakov, A. V.; Kuz'mina, L. G.; Efimenko, I. A., *Russ. J. Inorg. Chem.*, **2006**, *51*, 574.
34. Stanković, M. Z.; Radić, G. P.; Glođović, V. V.; Radojević, I. D.; Stefanović, O. D.; Čomić, L. R.; Klisurić, O. R.; Djinović, V. M.; Trifunović, S. R., *Polyhedron*, **2011**, 30, 2203.

35. Spek, A. L., *Acta Crystallogr., Sect. D: Biol. Crystallogr.*, **2009**, *65*, 148.
36. Alsmail, N. H.; Suyetin, M.; Yan, Y.; Cabot, R.; Krap, C. P.; Lu, J.; Easun, T. L.; Bichoutskaia, E.; Lewis, W.; Blake, A. J.; Schröder, M., *Chem. Eur. J.*, **2014**, *20*, 7317.
37. Pogozhev, D.; Baudron, S. A.; Hosseini, M. W., *Dalton Trans.*, **2011**, *40*, 7403.
38. Hollander, J. M.; Jolly, W. L., *Acc. Chem. Res.*, **1970**, *3*, 193.
39. Watts, J. F., *Vacuum*, **1994**, *45*, 653.
40. Lin, X.; Jia, J.; Zhao, X.; Thomas, K. M.; Blake, A. J.; Walker, G. S.; Champness, N. R.; Hubberstey, P.; Schröder, M., *Angew. Chem., Int. Ed.*, **2006**, *45*, 7358.
41. Ibarra, I. A.; Yang, S.; Lin, X.; Blake, A. J.; Rizkallah, P. J.; Nowell, H.; Allan, D. R.; Champness, N. R.; Hubberstey, P.; Schröder, M., *Chem. Commun.*, **2011**, *47*, 8304.
42. Yang, S.; Callear, S. K.; Ramirez-Cuesta, A. J.; David, W. I. F.; Sun, J.; Blake, A. J.; Champness, N. R.; Schröder, M., *Faraday Discuss.*, **2011**, *151*, 19.
43. Yang, S.; Sun, J.; Ramirez-Cuesta, A. J.; Callear, S. K.; David, W. I. F.; Anderson, D. P.; Newby, R.; Blake, A. J.; Parker, J. E.; Tang, C. C.; Schröder, M., *Nature Chem.*, **2012**, *4*, 887.
44. Yang, S.; Ramirez-Cuesta, A. J.; Newby, R.; Garcia-Sakai, V.; Manuel, P.; Callear, S. K.; Campbell, S. I.; Tang, C. C.; Schröder, M., *Nature Chem.*, **2015**, *7*, 121.
45. Yang, S.; Lin, X.; Blake, A. J.; Thomas, M.; Hubberstey, P.; Champness, N. R.; Schröder, M., *Chem. Commun.*, **2008**, 6108.
46. Hartwig, J. F., *Acc. Chem. Res.*, **1998**, *31*, 852.
47. Wolfe, J. P.; Wagaw, S.; Marcoux, J. F.; Buchwald, S. L., *Acc. Chem. Res.*, **1998**, *31*, 805.
48. Adeniji, A. O.; Twenter, B. M.; Byrns, M. C.; Jin, Y.; Chen, M.; Winkler, J. D.; Penning, T. M., *J. Med. Chem.*, **2012**, *55*, 2311.
49. Herseczki, Z.; Gergely, I.; Hegedues, C.; Szoellosy, A.; Bakos, J., *Tetrahedron:Asymmetry*, **2004**, *15*, 1673.
50. Yang, S.; Lin, X.; Lewis, W.; Suyetin, M.; Bichoutskaia, E.; Parker, J. E.; Tang, C. C.; Allan, D. R.; Rizkallah, P. J.; Hubberstey, P.; Champness, N. R.; Thomas, K. M.; Blake, A. J.; Schröder, M., *Nature Mater.*, **2012**, *11*, 710.
51. Liu, L.; Zhang, X-N.; Han, Z.; Gao, M-L.; Cao, X-M.; Wang, S-M., *J. Mater. Chem., A* **2015**, *3*, 14157.
52. Feng, D.; Wang, K.; Wei, Z.; Chen, Y-P.; Simon, C. M.; Arvapally, R. K.; Martin, R. L.; Bosch, M.; Tiu, T-F.; Fordham, S.; Yuan, D.; Omary, M. A.; Haranczyk, M.; Smit, B.; Zhou, H-C., *Nat. Commun.*, **2014**, *5*, 5723.

53. Goswani, S.; Adhikary, A.; Jena, H. S.; Biswas, S.; Konar, S., *Inorg. Chem.*, **2013**, *52*, 12064.

Chapter 4

Triazine-based MOFs for Metal Scavenging and Gas Adsorption Applications

4.1 Introduction

When considering the design of potentially industrially relevant metal-organic frameworks, a number of key factors must be assessed. The cost of production of the organic linker is one such factor, as is the introduction of chemical functionality which enhances the affinity of the framework for a specific guest molecule. As a method of combining these two features, the work described in this Chapter is concentrated on the use of cyanuric chloride as a building block for a wide range of linkers. In addition to its pyridyl functional groups, cyanuric chloride is exceptionally cheap (1 kg costs 60 GBP from Sigma-Aldrich) and the chloro groups should be readily substituted with amine groups, thus providing a facile route to a central core surrounded by six N atoms (Figure 4.1).

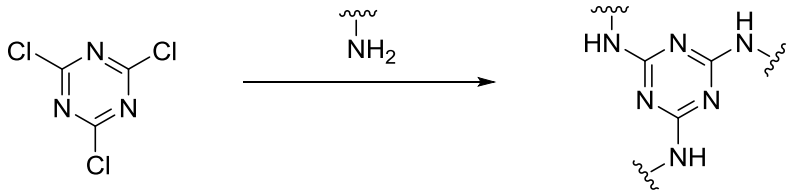


Figure 4.1. The structure of cyanuric chloride and a simplified depiction of chloro group substitution to give a hexa-amine core.

As discussed in Chapters 1-3, these pyridyl and amine functionalities are particularly relevant not only to the extraction of platinum group metals but also for a wide range of gas storage and selectivity applications. A number of literature examples have been reported on the use of this triazine core within MOFs, most notably the groups of Zhou,[1-5] Eddaoudi[6,7] and Li.[8] The first significant report of a triazine-containing framework was published by Zhou *et al.* in 2006 as a Cu(II) MOF prepared from the ligand 4,4',4''-*s*-triazine-1,3,5-triyltri-*p*-aminobenzoate (H_3TATAB), shown in Figure 4.2.[9]

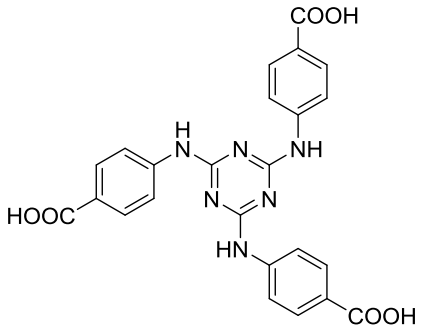


Figure 4.2. The structure of H_3TATAB as used in the synthesis of mesoMOF-1.[9]

This combination of metal cation and linker resulted in a non-interpenetrated, mesoporous framework with exceptional solvent accessible volume (88.3% as calculated from PLATON). The structure, denoted mesoMOF-1, consists of an underlying **tbo** net and contains large octahedral cavities measuring 22.5 x 26.1 Å in diameter (Figure 4.3). Although only N_2 isotherms at 77K were reported, the authors speculated that mesoporous MOFs of this kind could find applications in size-selective catalysis or for separations.[9]

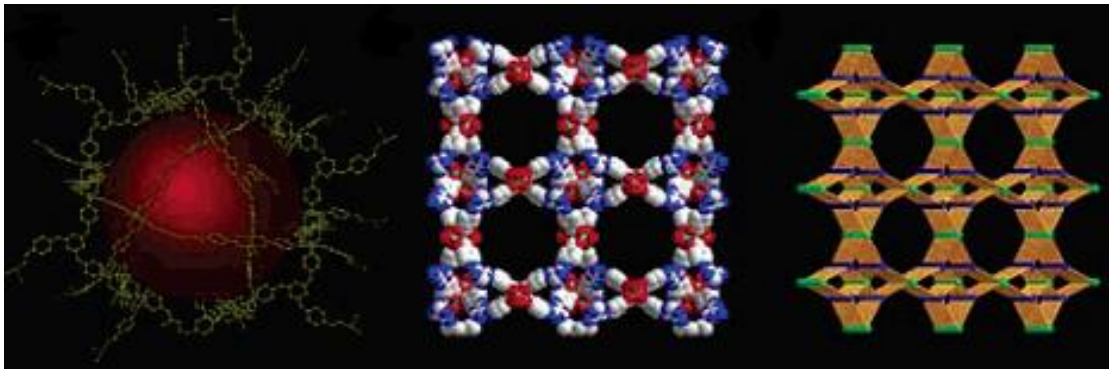


Figure 4.3. The octahedral cavity (left), packing in the [001] direction (centre) and the twisted boracite net (right) exhibited in mesoMOF-1. Reproduced from reference 9.

In 2010, Zhou *et al.* reported the synthesis of the analogous Zn(II) MOF using the $TATAB^{3-}$ ligand, denoted PCN-100 (Figure 4.4).[10] As in mesoMOF-1, PCN-100

exhibits mesopores (27.3 Å in diameter), with accessible pore windows of 13.2 Å x 18.2 Å.

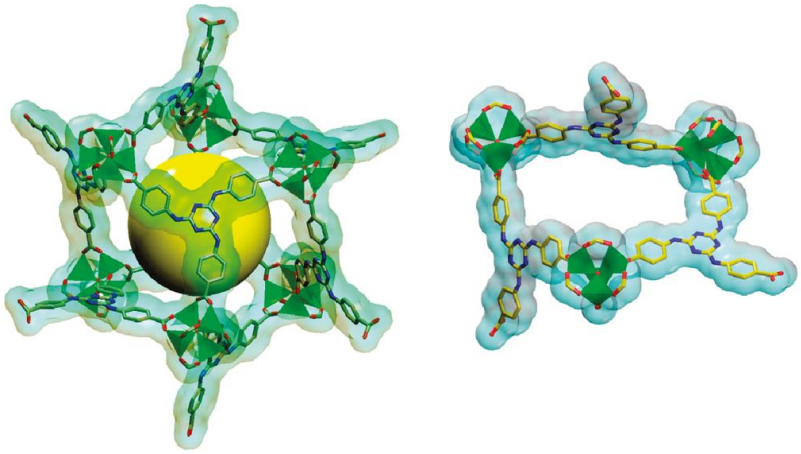


Figure 4.4. The mesoporous cavity (left) and accessible pore window (right) in PCN-100. Reproduced from reference 10.

The structure is of underlying **pyr** topology and has a solvent accessible volume of 80.8%. Whilst this is lower than the porosity exhibited by mesoMOF-1, the chemical and thermal stability of PCN-100 is much greater. As a result of this, the use of PCN-100 for capture of heavy metal ions and as a size selective catalyst was explored. To determine the uptake of heavy metal ions, PCN-100 was soaked in DMF solutions of $Co(NO_3)_2$, $Cd(NO_3)_2$ and $HgCl_2$, with the resulting materials characterised by XRD and ICP-OES. The ICP-OES data showed the adsorption of 1.61 Co(II), 1.63 Cd(II) and 1.38 Hg(II) ions per unit formula in each case, which was attributed to chelation of the metals by the central triazine core. A concomitant reduction in BET surface area, pore volume and N_2 uptake suggested that the metal ions were confined within the cavities rather than simply deposited on the outer surface of the MOF.[10]

In addition to this work on metal capture and catalysis, the groups of Li and Eddaoudi have reported the use of the triazine ligand $TDPAT^{6-}$ (H_6TDPAT = 2,4,6-

tris(3,5-dicarboxylphenylamino)-1,3,5-triazine; Figure 4.5) in the preparation of a Cu(II) MOF that displays exceptional uptake of CO_2 at low pressure.[6,8]

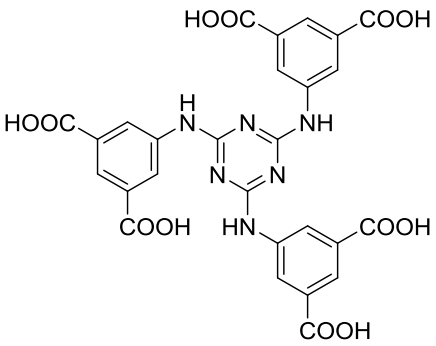


Figure 4.5. The structure of H_6TDPAT as used in the synthesis of Cu_3(TDPAT).[6,8]

This framework forms the expected 3,24-connected **rht** net (Figure 4.6) usually observed from the reaction of a trigonal planar hexacarboxylate linker with Cu(II) paddlewheel centres, which will be described in greater detail later in this Chapter.

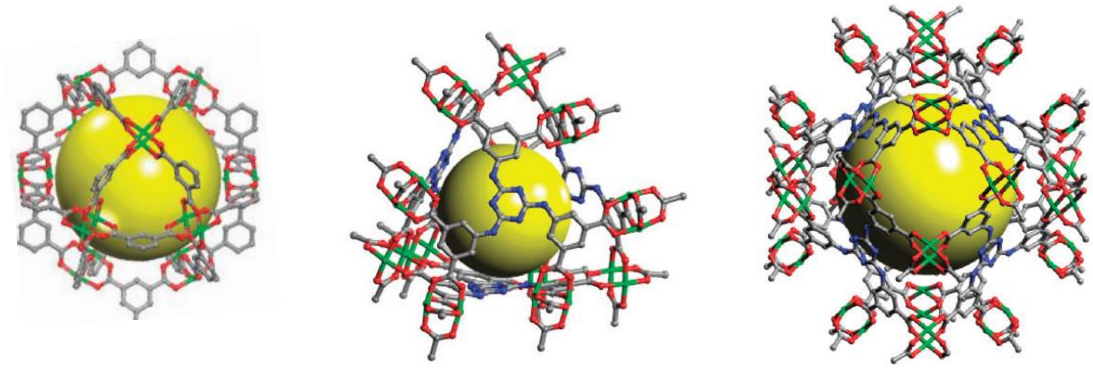


Figure 4.6. The cuboctahedral (left), truncated tetrahedral (centre) and truncated octahedral cages seen in Cu_3(TDPAT). Reproduced from reference 6.

As $TDPAT^{6-}$ is the shortest hexacarboxylate linker known to form an **rht** net, the Cu_3(TDPAT) framework contains a very high density of open Cu(II) metal sites as well as a high proportion of N atoms. Both of these factors are very important for low pressure uptake of CO_2[11] and consequently, Cu_3(TDPAT) is currently the world-

leading MOF for CO_2 uptake at 273 K and 1 bar of pressure (44.5 wt%).[6] It is also worth noting that, unlike the majority of Cu(II) MOFs, Cu_3(TDPAT) is stable in boiling water, as reported by Li *et al.* which is of great interest for our work on PGM extraction.[8]

Triazine linkers have also been shown to be effective in MOFs used for selective adsorption of C_2 hydrocarbons over CH_4. As reported by the groups of Shi[12] and Song,[13] both Cu_3(TDPAT) and Cu_3(TDPAH) are capable of excellent uptake of C_2H_2 and C_2H_4 between 0-1 bar (H_6TDPAH = 2,5,8-tris-(3,5-dicarboxylphenylamino)-s-heptazine; Figure 4.7).

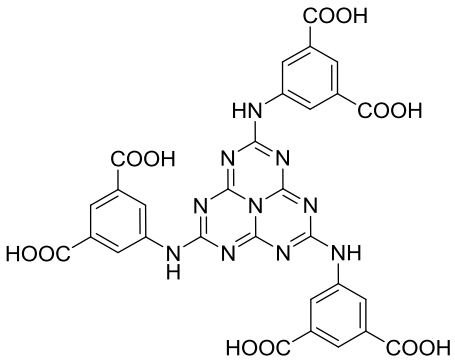


Figure 4.7. Structure of H_6TDPAH as used in the synthesis of Cu_3(TDPAH).[13]

The uptakes of C_2H_2, C_2H_4 and CH_4 in Cu_3(TDPAH) are 155.7, 116.7 and 22.4 cm^3 g^{-1} respectively at 1 bar and 298 K[13] and 177.7, 164.4 and 28.3 cm^3 g^{-1} in Cu_3(TDPAT) under the same conditions (Figure 4.8).[12]

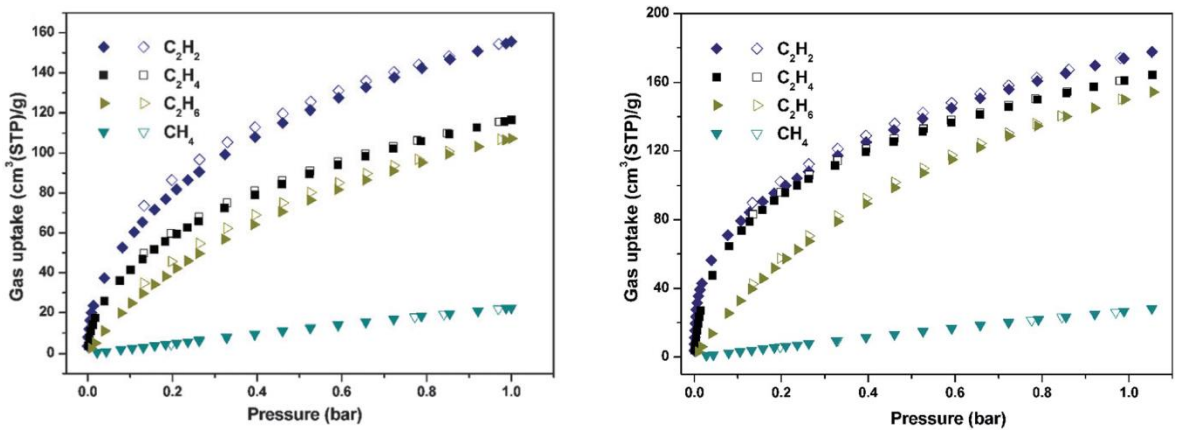


Figure 4.8. C_2 hydrocarbon and CH_4 uptake at 298 K between 0-1 bar in Cu_3(TDPAH), left, and Cu_3(TDPAT), right. Reproduced from references 12 and 13.

As a result of the large differences in uptake between the C_2 hydrocarbons and CH_4, both groups employed Henry's law calculations to estimate the selectivity of one gas over another. These calculations showed that Cu_3(TDPAH) exhibits an 80.9:1 selectivity for C_2H_2 over CH_4 and a 40.6:1 selectivity for C_2H_4 over CH_4 at 298 K. Cu_3(TDPAT) exhibits 127.1:1 and 85.0:1 selectivities for C_2H_2 and C_2H_4 respectively. DFT calculations attributed to the excellent C_2 hydrocarbon uptake on strong interactions between the gas molecules and Lewis basic sites within the linker as well as strong interactions with the open Cu(II) sites.[12]

4.2 Aims of this Work

The aim of this work was to investigate the encapsulation of $Pd(OAc)_2$, $PtCl_4$ and $Rh_2(OAc)_4$ from organic solvents using triazine-based MOFs, as demonstrated in Chapter 3 using functionalised tetracarboxylate-based Cu(II) MOFs. An investigation into the gas adsorption properties of novel triazine MOFs was also of interest, in particular the separation of C_2-hydrocarbons from CH_4 and the high pressure uptake of CO_2, CH_4 and H_2. The separation of hydrocarbons from CH_4 was calculated by

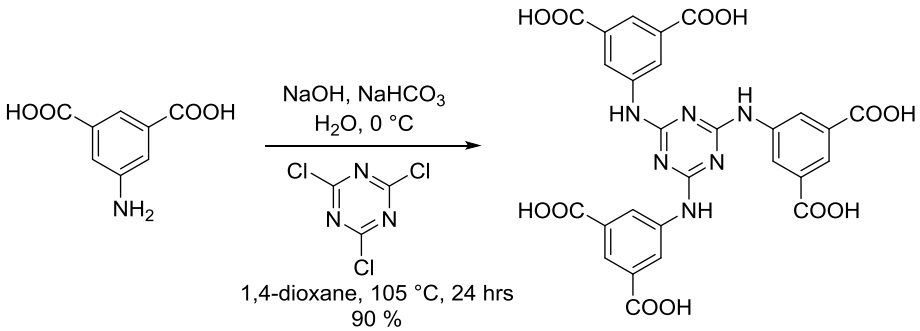
fitting a mathematical model to the isotherm data and using Henry's law and the IAST model to predict the selective adsorption of one gas over the other.

4.3 Results and Discussion

4.3.1 $[Cu_3(L^{11})(H_2O)_3]\cdot 11DMF\cdot 3H_2O$

4.3.1.1 Synthesis of $[Cu_3(L^{11})(H_2O)_3]\cdot 11DMF\cdot 3H_2O$

As discussed above, the framework Cu_3TDPAT (denoted as $[Cu_3(L^{11})]$ in this Chapter) was first synthesised by the groups of Eddaoudi and Li and studied for gas uptake applications with particular focus on CO_2.[6,8] The nitrogen-rich triazine core and facile large-scale synthesis of the organic linker made it an attractive target as a MOF for the extraction of precious metals. Our synthesis of the ligand, 2,4,6-tris(3,5-dicarboxylphenylamino)-1,3,5-triazine (H_6L^{11}), was achieved *via* a nucleophilic substitution reaction between 5-aminoisophthalic acid and cyanuric acid in basic water. Following an acidic work-up and recrystallisation from hot DMF, the pure ligand was obtained in high yield (90%) (Scheme 4.1).



Scheme 4.1. Preparation of H_6L^{11} adapted from reference 6.

The reaction between H_6L^{11} and $Cu(NO_3)_2\cdot 3H_2O$ in acidified DMF at 80 °C yielded blue octahedral crystals of $[Cu_3(L^{11})(H_2O)_3]\cdot 11DMF\cdot 3H_2O$ suitable for single crystal X-ray diffraction. Likewise, the reaction between $Zn(NO_3)_2\cdot 6H_2O$ and H_6L^{11} in

acidified DMF at 80 °C yielded colourless octahedral crystals. However, this Zn(II) analogue, which is isostructural to [$Cu_3(L^{11})$], was not stable to activation and will not be discussed further in this Chapter.

4.3.1.2 Structural Analysis and Characterisation

Single crystal X-ray diffraction reveals that [$Cu_3(L^{11})$] crystallises in the tetragonal space group *I*4/*m* with unit cell dimensions a = 26.6912(3) Å, c = 37.975(1) Å and V = 27054(1) $Å^3$. As expected, the structure is revealed to be a 3,24-connected framework containing 3 distinct cages, **A**, **B** and **C** (Figure 4.9). Cage **A** is a truncated cuboctahedron formed from 12 {$Cu_2(O_2CR)_4$} paddlewheel units and the isophthalate terminus of 24 different linkers. The accessible internal diameter of cage **A**, with the solvent molecules removed from the axial positions of the paddlewheel, is 13.0 Å. The tetrahedral Cage **B** consists of 12 paddlewheels arranged in triangular clusters of three. Four ligands are each connected to three paddlewheels in the same plane such that each ligand forms a face of the tetrahedron. Cage **B** has an internal diameter of 11.0 Å, and with the cage measuring 16.3 Å from end-to-end. The accessible windows to this cage measure 6.4 Å. The largest cage, **C**, is comprised of 24 paddlewheels arranged in six square clusters of four. Eight ligands are connected to three paddlewheels in the same plane such that each ligand spans the face of a truncated cube. Cage **C** has an accessible diameter of 17.8 Å and a cage length measuring 26.7 Å with accessible windows measuring between 6.4 and 8.2 Å. All internal diameters were calculated by fitting a sphere from the centre of the cage to its walls, taking into account Van der Waals radii and window diameters were calculated from the largest sphere able to pass through an aperture. The crystallographic data and cage sizes are in agreement with those previous described in the literature.[6]

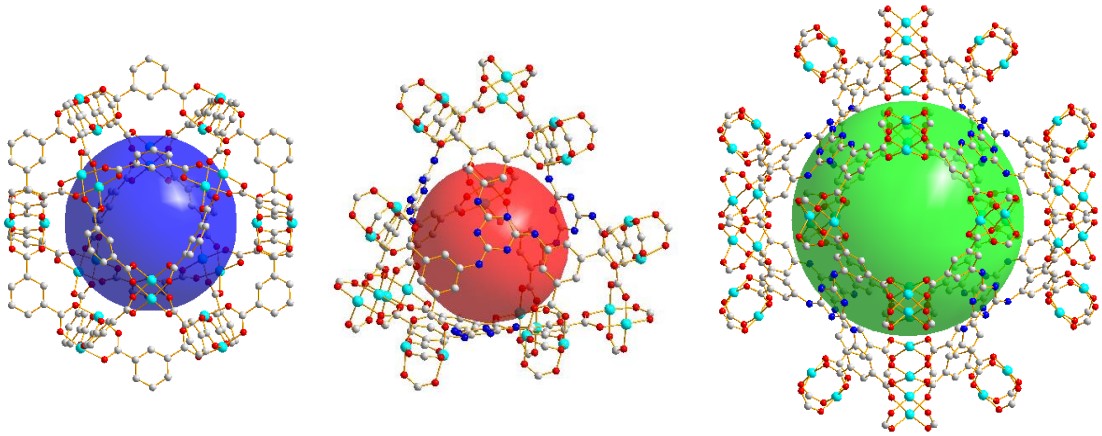


Figure 4.9. View of cages A, B and C present in [$Cu_3(L^{11})$].

4.3.1.3 Phase Purity, Thermal Stability and N_2 Sorption

PXRD patterns of the as-synthesised and acetone exchanged frameworks confirmed that the material was phase pure and were indexed to the same unit cell found for the single crystal structure (Figure 4.10).

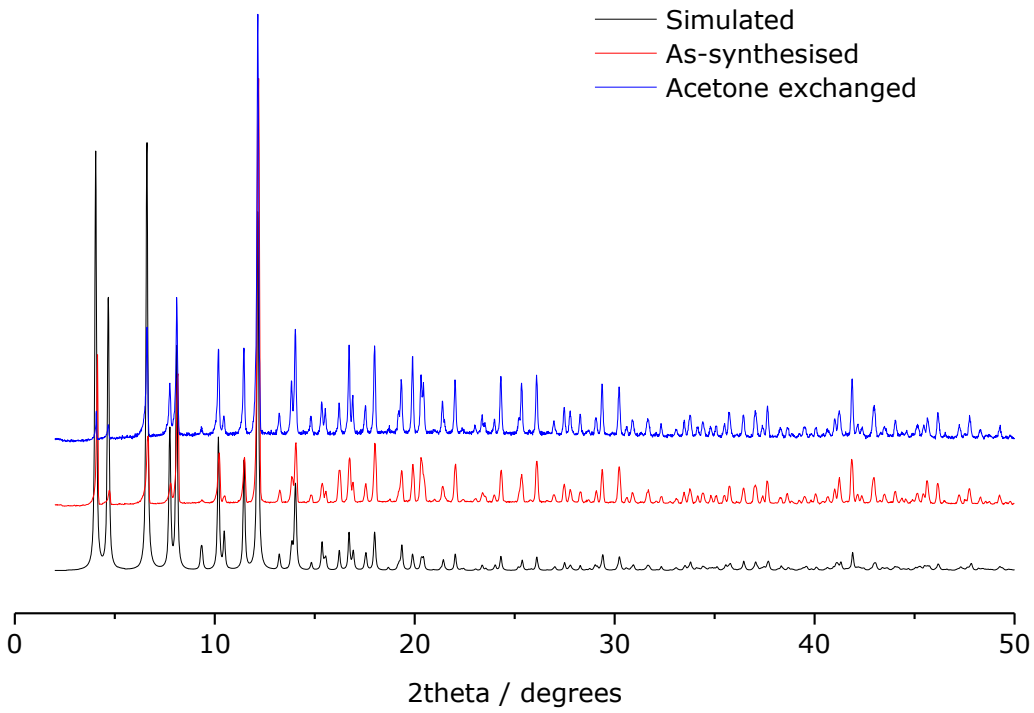


Figure 4.10. Powder X-ray diffraction patterns of simulated, as-synthesised and acetone exchanged [$Cu_3(L^{11})$].

The potential accessible volume of the desolvated material is 70%, as calculated by the PLATON/VOID routine[14] after removal of all guest solvents and coordinated water molecules with a calculated crystal density of 0.789 g cm^{-3}. Thermogravimetric analysis of the as-synthesised sample of $[Cu_3(L^{11})]$ in air showed solvent loss (DMF and H_2O) below 170 °C, with the material then stable up to 270 °C, beyond which point a mass loss corresponding to framework decomposition is observed (Figure 4.11). The acetone exchanged sample exhibits the same stability up to 270 °C, with the majority of solvent loss occurring below 100 °C.

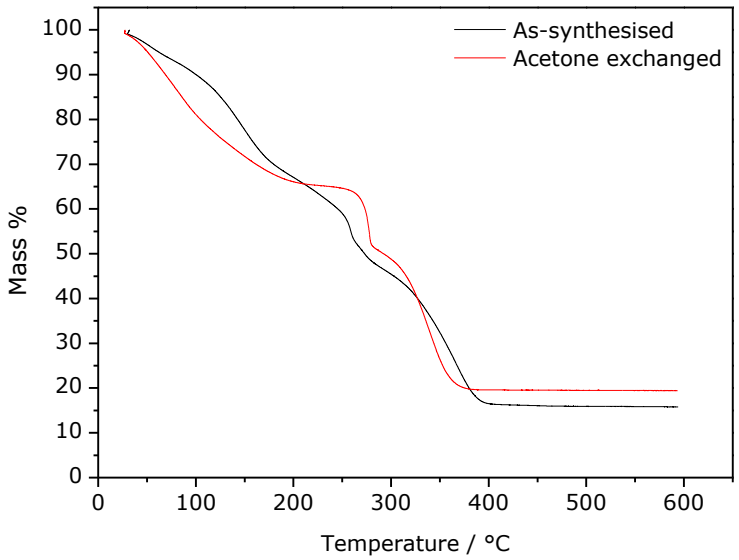


Figure 4.11. TGA trace of as-synthesised and acetone exchanged samples of $[Cu_3(L^{11})]$.

To prepare an activated sample of $[Cu_3(L^{11})]$, the DMF from the as-synthesised sample was exchanged with fresh acetone twice daily for 5 days. The sample was then heated under vacuum at 100 °C for 20 hours. Upon activation, a colour change from dark green to purple was observed, this is a typical indicator of the generation of open Cu(II) metal sites. The permanent porosity of the framework was confirmed

via an N_2 sorption isotherm performed at 77 K indicating reversible type-I behaviour and an uptake of 741 cc g^{-1} at 1 bar (Figure 4.12).

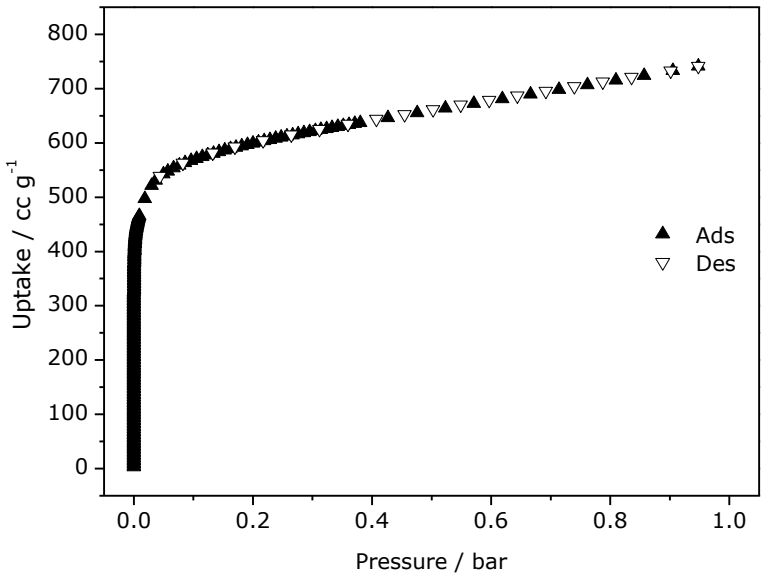


Figure 4.12. N_2 uptake in $[Cu_3(L^{11})]$ from 0-1 bar at 77 K.

The estimated BET surface area of desolvated $[Cu_3(L^{11})]$, as calculated from this isotherm, was 2228 m^2 g^{-1} with a total pore volume of 0.89 cm^3 g^{-1}. For comparison, Li *et al.* reported an N_2 uptake of 600 cc g^{-1} at 1 bar, a BET surface area of 1938 m^2 g^{-1} and a pore volume of 0.93 cm^3 g^{-1}.[8]

4.3.2 Extraction of $Pd(OAc)_2$, $PtCl_4$ and $Rh_2(OAc)_4$ from THF

As with the work described in Chapter 3, $[Cu_3(L^{11})]$ was trialled for the removal of $Pd(OAc)_2$, $PtCl_4$ and $Rh_2(OAc)_4$ from THF. The concentration of the PGMs was varied between 10 and 25 ppm and the mass of the MOF used was altered between 10, 20 and 50 mg. To calculate the concentration of the initial solution, a 10 ml aliquot was left to evaporate and the residue was then re-dissolved in 10 ml of 5 %

HNO_3 and analysed by ICP-OES. The same process was applied to the solution after extraction and the difference in concentration was converted into a % uptake.

Activated samples of $[Cu_3(L^{11})]$ were added to 50 ml solutions of PGM in THF and left at room temperature without stirring for 48 hours. These conditions were chosen after initial test experiments showed that stirring resulted in dissolution of the MOF and that very little extraction was observed after 48 hours. After the extraction experiments were complete, the MOF was removed by filtration, dried and digested by heating in 2 ml of 69% HNO_3 at 70 °C overnight. This was diluted with 10 ml of ultrapure de-ionised H_2O, filtered to remove undissolved linker and analysed by ICP-OES to determine the ratio of PGM to Cu in the sample, denoted as the "measured ratio". This can then be compared to the ratio expected from the solution results (Table 4.1). The "expected ratio" is calculated from the molar quantity of Cu in the MOF and the molar quantity of PGM removed from solution (given by the % uptake) to give a Cu:PGM ratio.

Table 4.1. Extraction of neutral PGM compounds from THF using $[Cu_3L^{11}]$.

PGM (conc / ppm)	Mass of MOF / mg	% uptake	Uptake / mg g^{-1}	Expected Cu:PGM ratio	Measured Cu:PGM ratio
$Pd(OAc)_2$ (10)	20	10.09	5.3	158 : 1	505 : 1
$Pd(OAc)_2$ (10)	50	28.18	5.9	141 : 1	411 : 1
$Pd(OAc)_2$ (25)	10	9.22	24.3	34 : 1	456 : 1
$Pd(OAc)_2$ (25)	20	10.96	14.4	58 : 1	520 : 1
$Pd(OAc)_2$ (25)	50	18.46	9.7	86 : 1	N/A
$PtCl_4$ (10)	20	0	0	N/A	1283 : 1
$PtCl_4$ (10)	50	10.68	2.7	682 : 1	2096 : 1
$PtCl_4$ (25)	10	0	0	N/A	838 : 1
$PtCl_4$ (25)	20	0	0	N/A	1161 : 1
$PtCl_4$ (25)	50	12.80	8.0	228 : 1	700: : 1
$Rh_2(OAc)_4$ (10)	20	17.64	9.5	87 : 1	3145 : 1
$Rh_2(OAc)_4$ (10)	50	0	0	N/A	9248 : 1
$Rh_2(OAc)_4$ (25)	10	19.20	51.5	16 : 1	1314 : 1
$Rh_2(OAc)_4$ (25)	20	13.39	18.0	46 : 1	1507 : 1
$Rh_2(OAc)_4$ (25)	50	0	0	N/A	2752 : 1

As with the tetracarboxylate-based MOFs NOTT-151, NOTT-155 and NOTT-125 described in Chapter 3, [$Cu_3(L^{11})$] exhibits uptake of each PGM, although the extraction is not consistent between experiments. In comparison to the tetracarboxylate MOFs, [$Cu_3(L^{11})$] shows greater uptake of $Pd(OAc)_2$ than the amine functionalised NOTT-151 and NOTT-155 and a similar capacity to that of oxamide functionalised NOTT-125. However, the extraction capacity of [$Cu_3(L^{11})$] for $PtCl_4$ is considerably lower than that exhibited by NOTT-151, -155 and -125. This is assigned to the stronger hydrogen-bonding interactions of these primary amine and oxamide-functionalised frameworks with the chloride groups of metal complex in comparison to the pyridyl and secondary amine functional groups present in [$Cu_3(L^{11})$]. The uptake of $Rh_2(OAc)_4$ is higher and more consistent in [$Cu_3(L^{11})$] than the tetracarboxylate frameworks (maximum uptake of 51.5 mg g^{-1}). As the interactions between the MOF and the metal are unlikely to be stronger than those in NOTT-151, -155 and -125, this is attributed to the larger pores of [$Cu_3(L^{11})$] encapsulating a greater proportion of the PGM.

The Cu:PGM ratios calculated from ICP-OES analysis of the digested MOF samples are all considerably lower than expected from the solution concentrations, in some cases by more than one order of magnitude different. However, XPS analysis of the 50 mg/25 ppm samples shows considerably higher quantities of PGM than is observed by ICP-OES. In the case of $Pd(OAc)_2$, the Cu:Pd ratio was found to be 22.5:1 compared to 273:1 found by ICP-OES and 51:1 as predicted from the solution concentrations. As XPS is a surface analysis technique (maximum depth 10 nm), this strongly suggests that PGM adsorption below the surface layers is limited, hence the ICP-OES analysis of the bulk sample shows a much reduced Pd content. For the $PtCl_4$-doped sample, XPS analysis could not show a direct Cu:Pt comparison as the

Pt 4*f* signal overlaps with the Cu 3*p* signal meaning that quantification of Pt content was not possible. However, analysis of the Cu:Cl ratio was possible and indicated a 5.1:1 ratio with just one chloride environment present, suggesting that the $PtCl_4$ molecules had remained intact upon encapsulation. Thus, this corresponds to a 20.4:1 ratio of Cu:Pt in comparison to the 74:1 ratio predicted from the solution results and the 204:1 ratio observed from the doped MOF sample. Again, this provides strong evidence that encapsulation is only occurring close to the surface of the MOF. For the Rh doped sample, ICP-OES analysis showed no uptake from solution and a very high Cu:Rh ratio of 1810:1 in the material. This was confirmed by XPS analysis, which exhibited no trace of Rh in the doped framework.

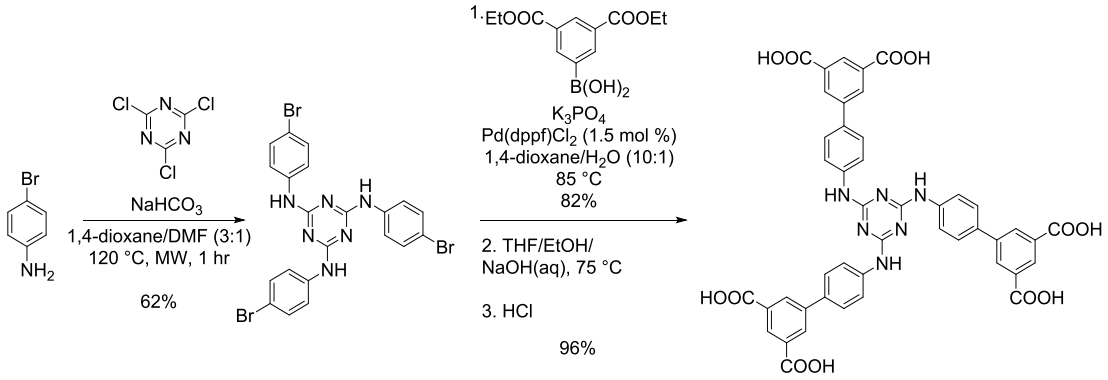
Following these results, extraction of K_2PtCl_6 (25 ppm Pt) from H_2O (100 ml) was attempted using $[Cu_3(L^{11})]$. Unfortunately, despite the stability claims made by Li *et al.*,[8] $[Cu_3(L^{11})]$ was found not to be stable in water and dissolved in this solution over the course of 16 hours. Therefore, the synthesis of novel, more porous and hopefully more stable triazine MOFs for the encapsulation of $Pd(OAc)_2$, $PtCl_4$ and $Rh_2(OAc)_4$ was investigated.

4.3.3 NOTT-160

4.3.3.1 Synthesis of $[Cu_3(L^{12})(H_2O)_3]\cdot 13DMF\cdot 7H_2O$ (NOTT-160)

An analogue of $[Cu_3(L^{11})]$, extended by one phenyl ring on each tripodal arm, (denoted as NOTT-160) was prepared from the hexacarboxylate ligand H_6L^{12}. The initial step in the synthesis of H_6L^{12} was a microwave-assisted nucleophilic substitution reaction to prepare a tribromo intermediate (Scheme 4.2).[15] 4-Bromoaniline and cyanuric chloride were dissolved in a basic solution of 1,4-dioxane/DMF and heated for 1 hour at 120 °C with stirring. The intermediate was

isolated following work-up and recrystallisation from Et_2O. A Pd(II)-catalysed microwave-assisted Suzuki reaction between this intermediate and (3,5-bis(ethoxycarbonyl)phenyl)boronic acid, followed by hydrolysis and acidification, gave H_6L^{12} in good yield (82% and 96% respectively).



Scheme 4.2. Microwave-assisted synthesis of H_6L^{12}.

A solvothermal reaction of H_6L^{12} and $Cu(NO_3)_2{\cdot}3H_2O$ in acidified DMF at 80 °C for 24 hours yielded green octahedral crystals of NOTT-160, ($[Cu_3L^{12}(H_2O)_3]{\cdot}13DMF{\cdot}7H_2O$).

4.3.3.2 Structural Analysis

Single crystal X-ray diffraction reveals that NOTT-160 crystallises in the tetragonal space group *I*4/*m* with unit cell dimensions a = 32.5561(3) Å, c = 47.8548(7) Å and V = 50721(1) Å^3. The structure is revealed to be a 3,24-connected framework of **rht** topology containing the same 3 types of cage, **A**, **B** and **C**, seen in $[Cu_3(L^{11})]$ (Figure 4.13). The cuboctahedral cage **A**, which consists of just Cu paddlewheels and isophthalate groups, is identical to the cage seen in $[Cu_3L^{11}]$ with an accessible internal diameter of 13.0 Å. The tetrahedral cage **B** has an internal diameter of 13.8 Å, with the cage measuring 22.7 Å from end-to-end. The accessible windows to this cage measure between 6.4 Å to 8.4 Å depending on the relative configuration of

neighbouring linkers. The largest cage, **C**, composed of 24 paddlewheels and eight linkers, has an accessible diameter of 19.6 Å and a cage length measuring 35.2 Å with windows measuring between 6.4 and 8.4 Å.

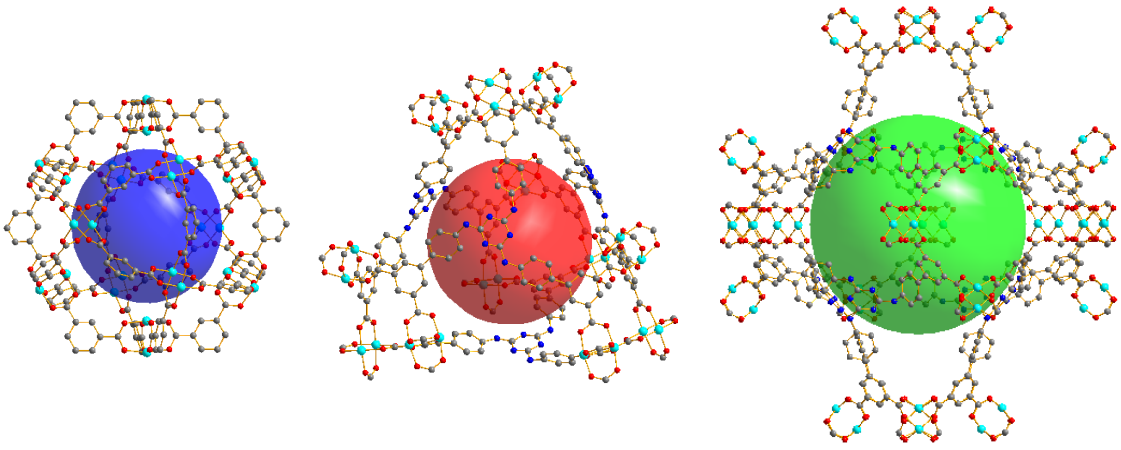


Figure 4.13. Views of Cages A, B and C present in NOTT-160.

The isostructural Zn analogue of NOTT-160 was also synthesised and was found by single crystal XRD to contain a slightly larger unit cell than that of NOTT-160(Cu), in which a = 33.1814(4) Å, c = 48.8650(9) Å and V = 53800.63(163) $Å^3$. The three cages are also larger than those observed in NOTT-160(Cu) with accessible internal diameters of 14.0 Å, 15.0 Å and 22.4 Å for cages A, B and C respectively. However, as NOTT-160(Zn) is not stable to activation, it will not be discussed further in this Chapter.

4.3.3.3 Phase Purity, Thermal Stability and N_2 Sorption

Indexing the PXRD patterns of as-synthesised, acetone exchanged and activated samples of NOTT-160(Cu) to the same unit cell as observed from single crystal diffraction confirmed that the material was phase pure (Figure 4.14).

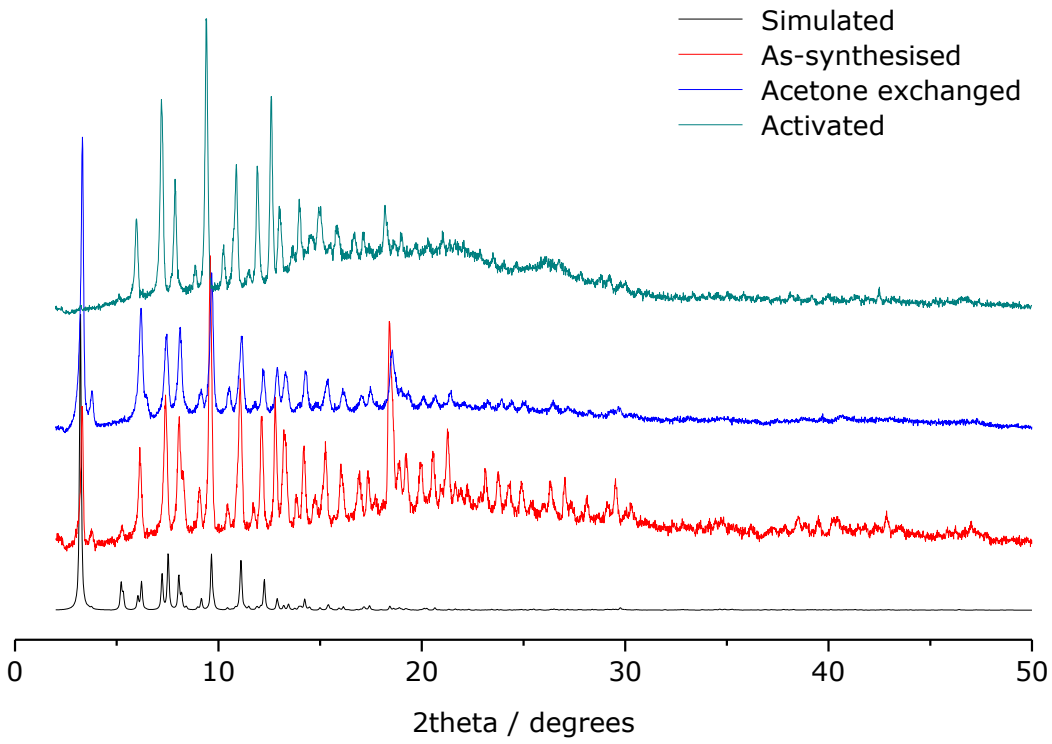


Figure 4.14. Powder X-ray diffraction patterns of simulated, as-synthesised, acetone exchanged and activated NOTT-160.

The potential accessible volume of desolvated NOTT-160 is 77%, as calculated by the PLATON/VOID routine[14] after removal of all guest solvents and coordinated water molecules with a calculated crystal density of 0.540 g cm^{-3}. As expected with the use of a larger linker, this corresponds to higher porosity and lower crystal density than seen for $[Cu_3(L^{11})]$ (70% porosity, ρ = 0.789 g cm^{-3}). Thermogravimetric analysis of the as-synthesised sample of NOTT-160 in air showed solvent loss (DMF and H_2O) below 170 °C, with the material then stable up to 290 °C, beyond which point a mass loss corresponding to framework decomposition is observed (Figure 4.15). The acetone exchanged sample exhibits the same stability up to 290 °C, with the majority of solvent loss occurring below 100 °C.

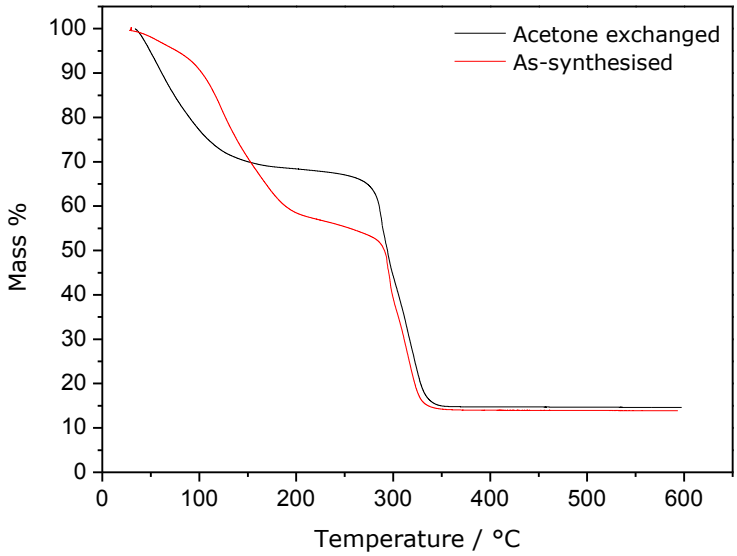


Figure 4.15. TGA trace of as-synthesised and acetone exchanged samples of NOTT-160.

To prepare activated NOTT-160a for gas sorption experiments, the solvent of the as-synthesised sample was exchanged with fresh acetone twice daily for 5 days. The sample was then activated under vacuum at 100 °C for 20 hours, after which time the material had undergone the anticipated colour change from green to purple. The permanent porosity of the framework was confirmed *via* an N_2 sorption isotherm performed at 77 K indicating reversible type-I behaviour and an uptake of 983 cc g^{-1} at 1 bar (Figure 4.16), an increase of 242 cc g^{-1} over [$Cu_3(L^{11})$].

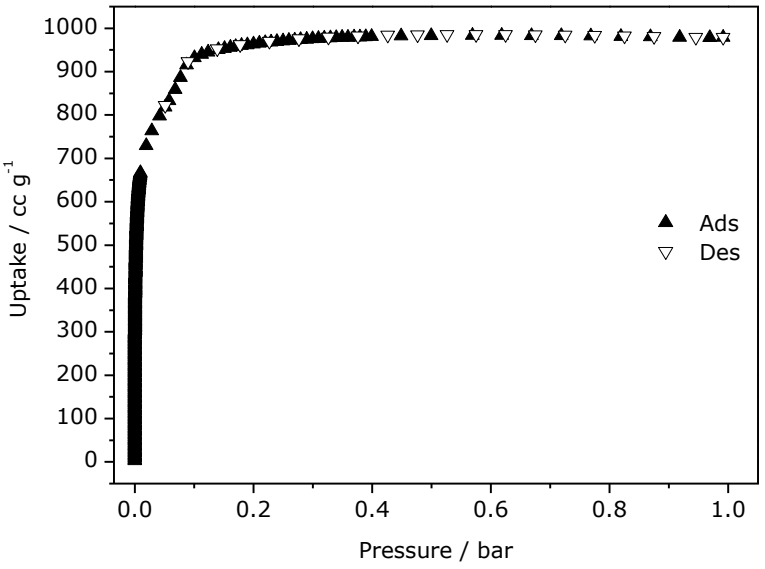


Figure 4.16. N_2 isotherm for NOTT-160a from 0-1 bar at 77 K.

The slight changes in gradient between 30 – 120 mbar are assigned to the sequential filling of the micro- and mesoporous cages. The estimated BET surface area of NOTT-160a, as calculated from this isotherm, is 3847 m^2 g^{-1} with a total pore volume of 1.52 cm^3 g^{-1}. Again, this represents a significant increase in porosity in comparison to [$Cu_3(L^{11})$] (BET surface area = 2228 m^2 g^{-1}; pore volume = 0.89 cm^3 g^{-1}).

Unfortunately it was found that NOTT-160 was not stable to the PGM scavenging conditions in THF as described for [$Cu_3(L^{11})$] and could therefore not be used for this application. However, as stated in the introduction, triazine-containing MOFs have shown excellent capacity for gas storage at low pressure and several **rht** MOFs have exhibited exceptional gas sorption at higher pressures.[16-25] Two areas of significant interest in recent years are the capture of CO_2[26-33] and the separation of C_2 hydrocarbons from methane.[34-40] CO_2 is well-established as the leading contributor to global warming and over 85% of the world's energy demand involves the burning of

fossil fuels.[41,42] As such, materials capable of storing CO_2 from flue gas and automobiles are in high demand.[42] Likewise, natural gas is in incredibly high demand as a fuel for both industrial and residential applications in addition to providing a feedstock for a variety of chemicals.[43] Consisting mainly of CH_4, it is also increasingly being utilised in vehicles as its high H to C ratio results in lowered emissions of CO and CO_2.[43] The main sources of impurity in natural gas are the C_2 hydrocarbons (C_2H_2, C_2H_4 and C_2H_6).[12] Removing these hydrocarbons increases the purity of natural gas and provides a source of C_2 hydrocarbons for further chemical manipulation.[13] The removal is traditionally achieved by cryogenic distillation, a very energy intensive process.[13] A much more efficient alternative could be to separate the different components at room temperature using a selective adsorbate.

4.3.3.4 CO_2, CH_4 and H_2 Sorption from 0-20 Bar

High pressure (0-20 bar) isotherms for NOTT-160a were performed using CO_2 and CH_4 at 298 K and 273 K (Figure 4.17) and at 77 K and 87 K for H_2 (Figure 4.18). The material shows exceptional capacity for CO_2 storage at 20 bar with 558 cc g^{-1} (110 wt%) and 719 cc g^{-1} (141 wt%) uptake at 298 K and 273 K respectively. This unsaturation uptake of CO_2 at 298 K is one of the highest reported for a metal-organic framework. To our knowledge the current record uptake under these conditions is 627 cc g^{-1} (123 wt%) in MOF-177 (a Zn(II)-based benzenetribenzoate MOF).[44] At 195 K and 1 bar NOTT-160 nears saturation at 881 cc g^{-1} (173 wt%). CH_4 uptake at 20 bar is 199 cc g^{-1} (14.2 wt%) at 298 K and 274 cc g^{-1} (19.6 wt%) at 273 K. H_2 uptake at 20 bar is 6.4 wt% at 77 K and 5.3 wt% at 87 K, whilst uptake at 1 bar is 2.14 wt% at 77 K and 1.40 wt% at 87 K. The H_2 and CH_4 uptake values are similar to those observed for other highly porous 3,24-connected **rht** MOFs reported previously by the Schröder group[16-21] and other groups.[22-25]

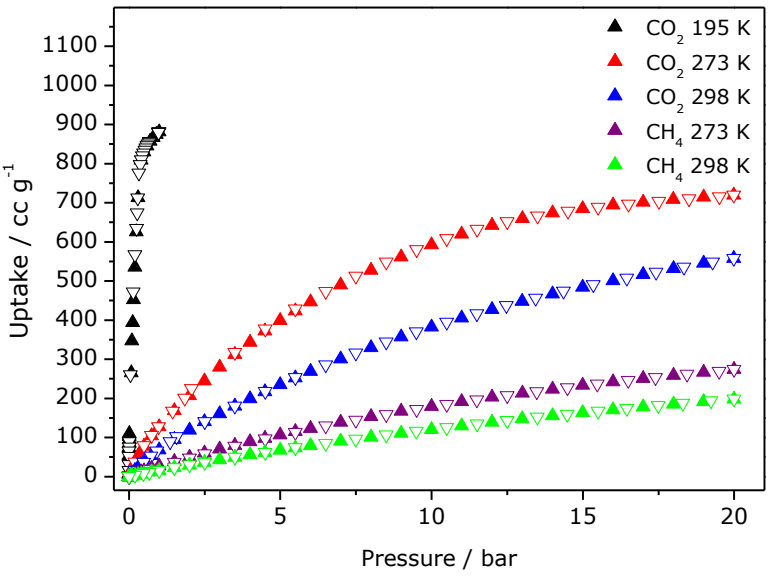


Figure 4.17. CO_2 and CH_4 isotherms for NOTT-160a from 0-20 bar (filled triangles: adsorption; open triangles: desorption).

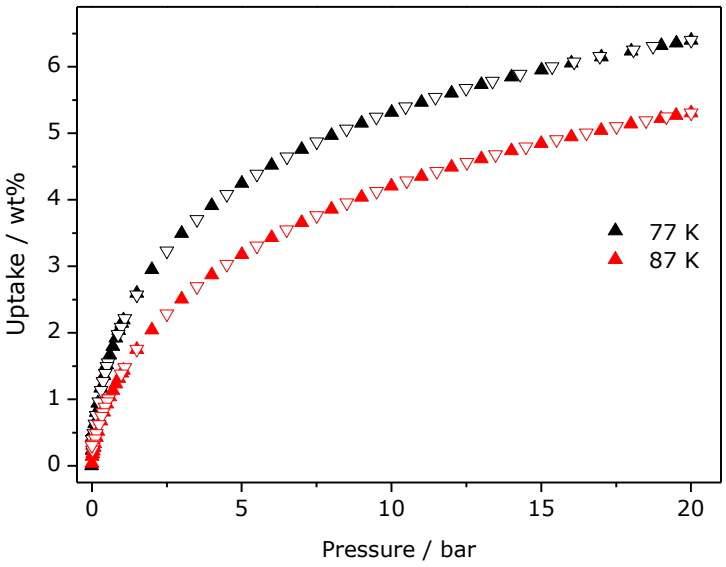


Figure 4.18. H_2 isotherms for NOTT-160a from 0-20 bar (filled triangles: adsorption; open triangles: desorption).

4.3.3.5 Low Pressure Sorption of C_2 Hydrocarbons and CH_4

Low pressure (0-1 bar) isotherms of C_2 hydrocarbons were measured at 298 K and 273 K for comparison to the data obtained for CH_4. The uptakes of C_2H_2, C_2H_4 and C_2H_6 are 212.3 cc g^{-1}, 175.2 cc g^{-1} and 201.3 cc g^{-1} respectively at 273 K (Figure 4.19). At 298 K this becomes 127.8 cc g^{-1}, 115.0 cc g^{-1} and 110.0 cc g^{-1} (Figure 4.20). Whilst these values are slightly lower than those reported with Cu_3TDPAT and Cu_3TDPAH,[12,13] the extremely low uptake of CH_4 at 1 bar (15.3 cc g^{-1} at 298K, 27.1 cc g^{-1} at 273 K) in NOTT-160 makes the material of great interest for selective separation of C_2 hydrocarbons over CH_4.

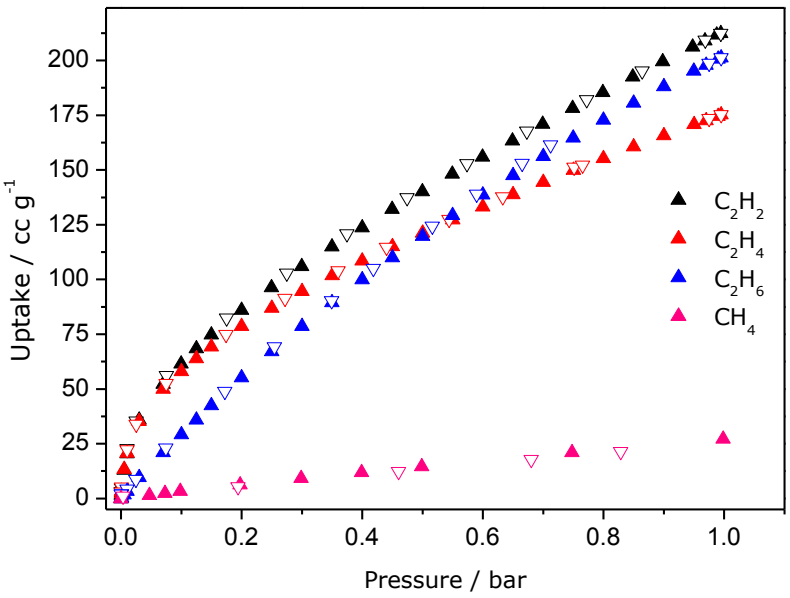


Figure 4.19. Hydrocarbon isotherms for NOTT-160a from 0-1 bar at 273 K.

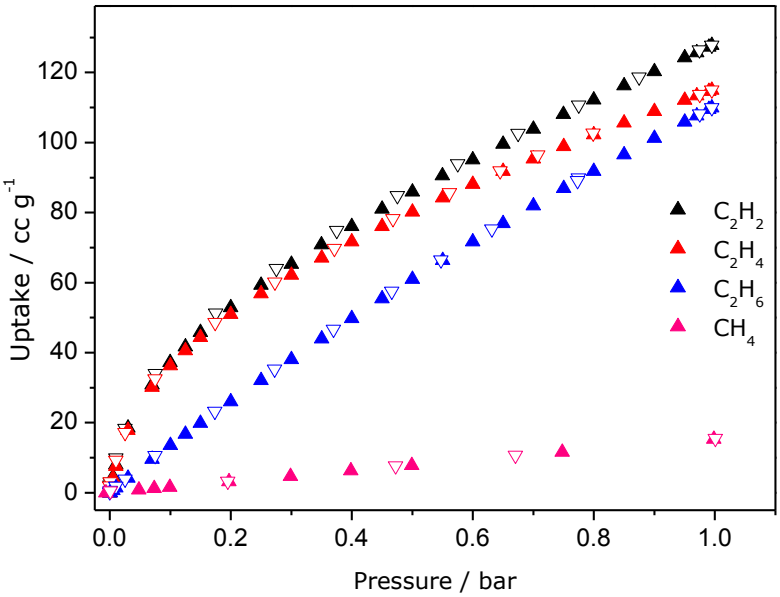


Figure **4.20.** Hydrocarbon isotherms for NOTT-160a from 0-1 bar at 298 K.

4.3.3.6 Virial Fitting and Henry's Law Selectivity of 0-1 Bar Isotherms

To calculate the Henry's law selectivity of one gas over another, the adsorption isotherms from 0-1 bar were fitted to the virial equation shown below (eqn (1)).

$$ln(n/P) = A_0 + A_1n + A_2n^2 + A_3n^3 \qquad \textbf{eqn (1)}$$

In this case P is the pressure in Pa, n is the quantity adsorbed in mol g^{-1} and A_0-A_3 are virial coefficients. Each regression coefficient was greater than 0.99, showing that the models used were accurate fits to the data. Having fitted the data, the Henry's law constant was calculated as $K_H = \exp(A_0)$. The virial fitting of the C_2H_2 isotherm at 298 K is shown below in Figure 4.21. Virial fittings of all other isotherms are shown in the Appendices (Figures A2.1 to A2.10).

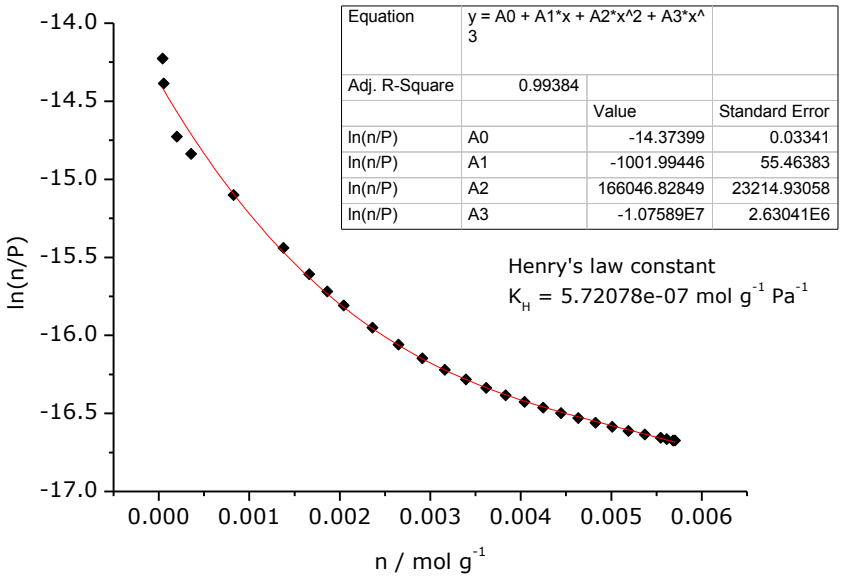


Figure 4.21. Virial fitting of the C_2H_2 isotherm for NOTT-160a at 298 K.

The selectivity, S_{ij} of one gas, *i*, over a second gas, *j*, was then determined from the equation shown below(eqn (2)).

$$S_{ij} = K_{Hi}/K_{Hj} \qquad \textbf{Eqn(2)}$$

The calculated C_2H_2:CH_4, C_2H_4:CH_4 and C_2H_6:CH_4 selectivities are 103.7:1, 130.4:1 and 9.9:1 respectively at 273 K. At 298 K this becomes 78.8:1, 69.6:1 and 8.7:1 respectively. To the best of our knowledge the C_2H_2:CH_4 separation of 78.8:1 at 298 K is the third highest reported for a MOF (Cu_3TDPAT[12] 127.1:1; Cu_3TDPAH[13] 80.9:1). Notably this is significantly higher than the selectivites reported for smaller pore Cu MOFs such as UTSA-50a[45] and UTSA-15a (Table 4.2).[46] The C_2H_4:CH_4 separation in NOTT-160 at 298 K (69.6:1) is the second highest reported value behind Cu_3TDPAT (85.0:1).[12] Isosteric heats of adsorption (Q_{st}) for each gas were calculated using a virial method to fit the sorption isotherms at 273 K and 298 K. The

heats of adsorption at zero-loading for CO_2, C_2H_2, C_2H_4 and C_2H_6 are 30.04, 36.65, 35.69 and 23.76 kJ mol^{-1} respectively. Each has a higher zero-loading Q_{st} than CH_4 (23.11 kJ mol^{-1}) which, in common with the work by Shi *et al.*[13] on Cu_3TDPAH, we assign to increased van der Waals and electrostatic interactions between the larger gas molecules and the framework. This goes some way to explain the selectivity for the C_2 hydrocarbons over CH_4. The Q_{st} values follow the same pattern as the selectivities over CH_4 at 298 K – C_2H_2 > C_2H_4 >> C_2H_6, although at 273 K C_2H_4:CH_4 selectivity is greater than the C_2H_2:CH_4 selectivity (130.4:1 *versus* 103.7:1).

Table 4.2. Comparison of C_2H_2:CH_4 selectivity in several MOFs at 298 K. [a] Gas uptake is measured in cc g^{-1} at 1 bar, [b] Q_{st} (kJ mol^{-1}) refers to heat of adsorption at zero coverage.

MOF	C_2H_2 uptake[a]	CH_4 uptake[a]	Q_{st} C_2H_2[b]	Q_{st} CH_4[b]	$S_{i/j}$	Reference
Cu_3TDPAT	178	28.3	42.5	20.7	127.1	12
Cu_3TDPAH	155	22.1	23.5	13.8	80.9	13
NOTT-160a	**127.8**	**15.3**	**36.7**	**23.1**	**78.8**	**This work**
UTSA-50a	90.6	18.8	39.4	18.6	68	45
UTSA-15a	34	2.5	39.5	13.6	55.6	46
UTSA-36a	57	13	29.0	24.4	13.8	47
$Zn_5(BTA)_6(TDA)_2$	44	10	37.3	26.1	15.5	48
$[Zn_4(OH)_2(BTC)_2]$	53	10	28.2	14.8	14.7	49
Cu(BDC–OH)	43	13	25.7	18.5	21	50

The selectivity for C_2H_2 over CO_2 (15.3:1 at 298 K; 16.2:1 at 273 K) demonstrates the potential of NOTT-160a for the purification of acetylene, in which CO_2 is a common impurity. It has been previously demonstrated by Kitagawa *et al.* that N-containing ligands do not improve selectivity for C_2H_2 over CO_2 using a tetrazolate-based Zn(II) MOF.[51] Their study suggested that the functional groups of the MOF may result in H-bonding interactions with C_2H_2, giving an increased uptake of C_2H_2

over CO_2. However, the uptake of each gas was almost identical at ~90 cc g^{-1} at 1 bar (195 K), leading the authors to conclude that the functional groups were not hydrogen bonding to the guest C_2H_2 molecules.[51] Thus, for NOTT-160a, we attribute this selectivity not to the triazine core but to the greater van der Waals interactions between the framework and the larger C_2H_2 molecules. This is in common with work reported by Kim and co-workers for selective uptake of C_2H_2 over CO_2 in porous formates.[52] The separation of CO_2 from C_2H_2 is notoriously difficult as a result of their similar size and sublimation points.[53] Thus, the high selectivity for C_2H_2 over CO_2 in NOTT-160 is a very promising finding. Our work represents the second greatest selectivity for a MOF for this separation, behind only $Cu_2(pzdc)_2(pyz)$ ($pzdc^{2-}$ = pyrazine-2,3-dicarboxylate; pyz = pyrazine), reported by Mita *et al.* in 2005 (C_2H_2:CO_2 = 26:1 at 1.1kPa and 270 K).[54] However, the saturation uptake of C_2H_2 in $Cu_2(pzdc)_2(pyz)$ is just 42 cc g^{-1} (273 K, 1 bar) in comparison to 212.3 cc g^{-1} for NOTT-160a under the same conditions.

It should be noted that repetition of these isotherms gives identical results, showing the stability of NOTT-160 to repeated activation and re-use.

4.3.3.7 Langmuir-Freundlich Fitting of Isotherm Data and Predicted IAST Selectivities

In addition to using Henry's law to define selectivities, the gas selectivities for C_2H_2:CH_4, C_2H_4:CH_4, C_2H_6:CH_4 and C_2H_2:CO_2 in a binary mixture were predicted and analysed using ideal adsorbed solution theory (IAST). The isotherms of C_2H_2, C_2H_4, C_2H_6, CH_4 and CO_2 from 0-1 bar were fitted using a Langmuir-Freundlich model (eqn (3)).

$$n = (q_1 b_1 P^{v1}/1 + b_1 P^{v1}) + (q_2 b_2 P^{V2}/1 + b_2 P^{V2}) \qquad \textbf{eqn (3)}$$

In eqn (3), n is the adsorbed quantity in mmol g^{-1}, b is the Langmuir parameter in bar^{-1}, P is the pressure in bar, v^i is the Freundlich parameter for sites 1 and 2 and q is the saturation capacity in mmol g^{-1}. Each of the fittings was modelled as either single-site or dual-site in which the parameters q_1, b_1, ν_1, q_2, b_2, ν_2 are denoted as P1-P6 respectively. The choice of a single or dual-site fitting was based on the model which showed the best fit. In each case the regression coefficient is greater than 0.9999, showing the excellent fitting of the models to the data. The Langmuir-Freundlich fitting of the C_2H_2 isotherm at 298 K is shown below in Figure 4.22. Langmuir-Freundlich fittings of all other isotherms are shown in the Appendices (Figures A3.1 to A3.10).

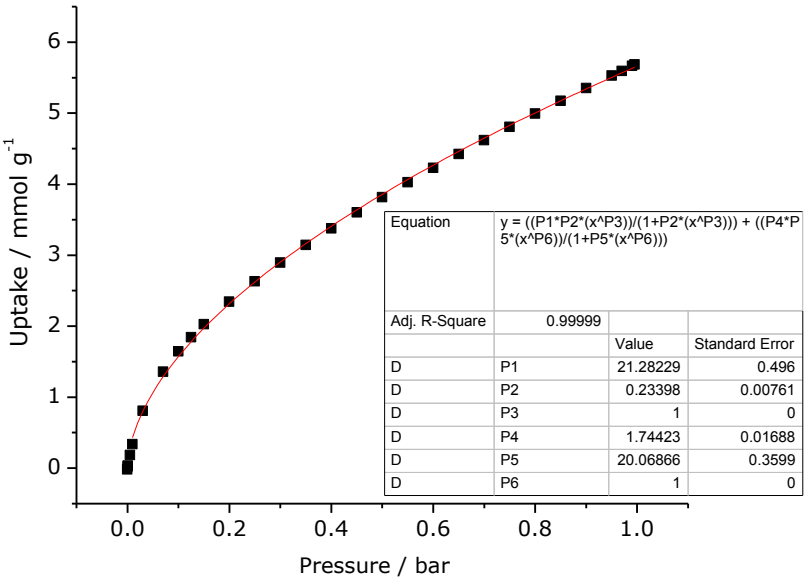


Figure 4.22. Langmuir-Freundlich fitting of the C_2H_2 isotherm for NOTT-160a at 298 K.

The individual selectivities are then determined by $S_{i/j} = (x_i/y_i)/(x_j/y_j)$, in which x is the amount of each component adsorbed as predicted by IAST and y is the mole fraction of each component in the gas phase at equilibrium. The selectivities were then calculated as a function of pressure for each mixture at a composition of 50:50.

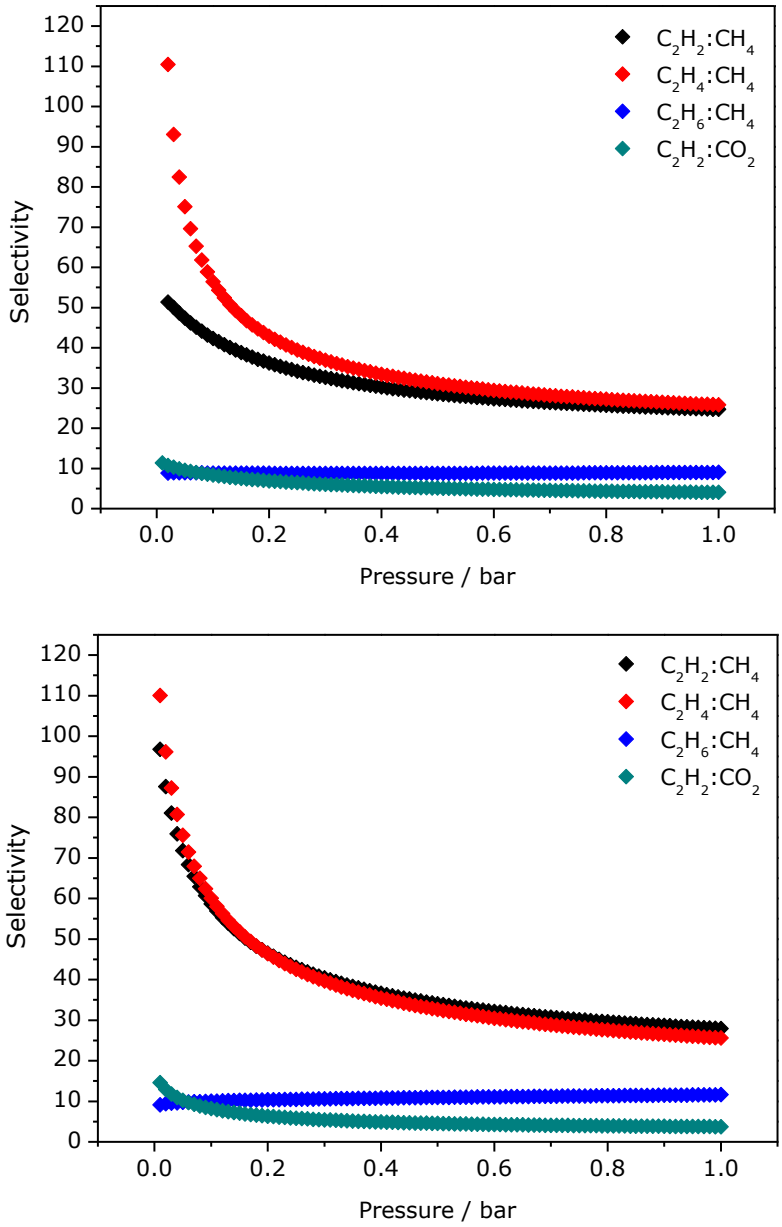


Figure 4.23. Predicted IAST selectivities for NOTT-160a at 298 K (top) and 273 K (bottom).

The selectivity for each mixture (Figure 4.23) is in agreement with the Henry's law calculations at 273 K, as the order of selectivity over CH_4 is shown to be C_2H_4 > C_2H_2 >> C_2H_6. At very low pressures (~20 mbar) the C_2H_4:CH_4 selectivity is predicted to be 110:1, which decreases rapidly with increasing pressure before reaching 26:1 at 1 bar. The C_2H_2:CH_4 selectivity is 97:1 at very low pressures and decreases to 28:1 at 1 bar. At 298 K the IAST predictions show that the selectivity for C_2H_4 over CH_4 is much greater than that of C_2H_2 at low pressures (111:1 *vs* 51:1), although the selectivities are approximately equal at 1 bar.

4.3.3.8 High Pressure CH_4 Adsorption

While the removal of C_2 hydrocarbons from CH_4 at low pressure is essential to increase the purity of natural gas, the storage of large quantities of CH_4 at high pressure is also of great importance for potential use in automobiles. The U.S. Department of Energy (DoE) in particular has great interest in materials capable of storing large quantities of CH_4 at 35 and 80 bar.[55] As the automobile industry require 5 bar of unused CH_4 to remain in a fuel tank, a more important figure is that of the "working capacity" of a storage material.[55,56] The working capacity is defined as the quantity of methane calculated by subtracting the uptake at the operational desorption capacity (5 bar) from the maximum adsorption capacity at the operational pressure (35 bar or 80 bar).[55,56] NOTT-160a demonstrates very low CH_4 uptake at low pressures and the large cavities in the material suggest that high pressure capacity for CH_4 should be very high. Thus, the working capacity of NOTT-160a for CH_4 at 80 bar was of significant interest. A sample of NOTT-160a (~500 mg) was sent to collaborators at General Motors for a high pressure (0-80 bar) CH_4 sorption experiment (Figure 4.24).

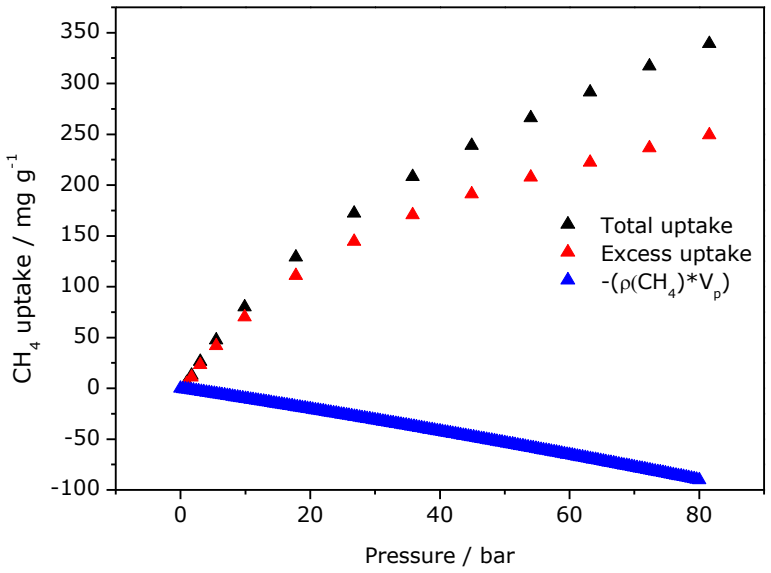


Figure 4.24. Excess and total uptake of CH_4 for NOTT-160a from 0-80 bar at 298 K.

This showed that NOTT-160a exhibited a good excess uptake capacity for CH_4 of 249 mg g^{-1} at 80 bar. The total uptake of CH_4, which cannot be determined experimentally, was estimated according to the equation shown below (eqn (4)).

*Total uptake = Excess uptake + (bulk density of CH_4 * pore volume (V_P))* **Eqn(4)**

The total CH_4 uptake at 80 bar in NOTT-160a was calculated to be 339 mg g^{-1}. As the volumetric working capacity is the most important criterion when considering uptake of CH_4, a comparison between NOTT-160a and other highly porous materials is shown below in Table 4.3. This shows clearly that the working capacity of NOTT-160a at 80 bar (221 cm^3 cm^{-3}) is exceptionally high and to our knowledge is the second highest reported for a metal-organic framework behind MOF-519 (230 cm^3 cm^{-3}).[56]

Table 4.3. A comparison of MOFs used for high pressure CH_4 uptake. [a] Uptake of CH_4 in $cm^3\ cm^{-3}$.

Material	Pore Volume / $cm^3\ g^{-1}$	Density / g cm^{-3}	Total uptake at 35 bar[a]	Total uptake at 80 bar[a]	Working capacity at 35 bar[a]	Working capacity at 80 bar[a]	Reference
MOF-519	0.94	0.953	200	279	151	230	56
NOTT-160a	**1.52**	**0.540**	**155**	**253**	**122**	**221**	**This work**
MOF-520	1.28	0.586	162	231	125	194	56
MOF-5	1.38	0.605	126	198	104	176	55
MOF-177	1.89	0.427	122	205	102	185	55
MOF-205	2.16	0.380	120	205	101	186	55
MOF-210	3.60	0.250	82	166	70	154	55
Ni-MOF-74	0.51	1.195	230	267	115	152	57
HKUST-1	0.69	0.881	225	272	153	200	57
PCN-14	0.83	0.819	200	250	128	178	58
AX-21	1.64	0.487	153	222	103	172	57
Bulk CH_4	N/A	N/A	33	83	29	79	

This capacity is attributed partly to the crystal density of NOTT-160a, which at 0.540 g cm^{-3} is higher than other mesoporous materials such as MOF-177, MOF-205 and MOF-210 (0.427, 0.380 and 0.250 g cm^{-3} respectively). As a result, the volumetric capacity for a given quantity of NOTT-160a is higher than these less dense materials. However, the main cause of the exceptional working capacity is the poor uptake at lower pressures and the high uptake above 35 bar. As a comparative example, PCN-14 (an anthracene-containing Cu(II) MOF) exhibits a very high capacity for CH_4 at 35 bar (200 $cm^3\ cm^{-3}$) but the sorption soon plateaus and does not increase significantly beyond this point (Figure 4.25).[58]

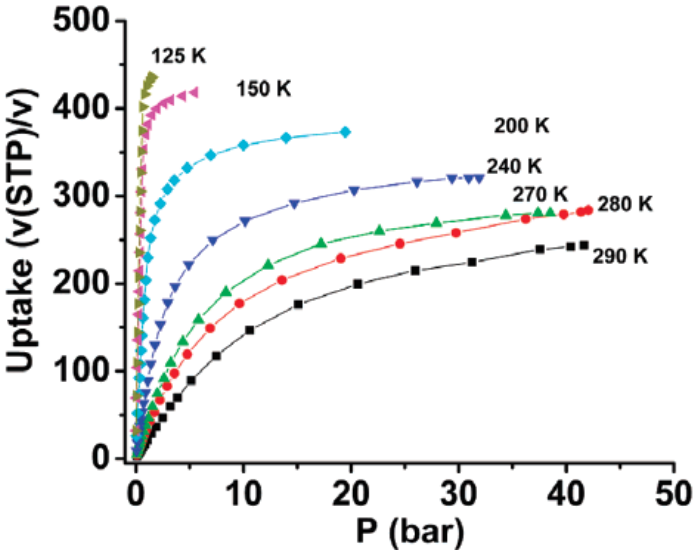


Figure 4.25. CH_4 isotherms from 0-50 bar for PCN-14 at a range of temperatures between 125 K and 290 K. Reproduced from reference 58.

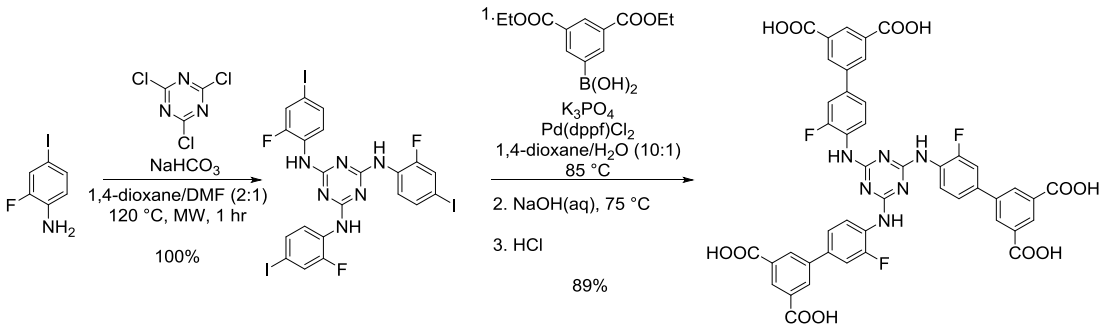
For NOTT-160a the uptake of CH_4 at 5 bar is very poor (32.5 cm^3 cm^{-3}) and is moderate at 35 bar (155 cm^3 cm^{-3}). However, the increase in uptake between 35 bar and 80 bar of 98 cm^3 cm^{-3} is far larger than that exhibited by any of the materials in Table 4.3 (MOF-205 is the second highest at 85 cm^3 cm^{-3}) and contributes hugely to the excellent working capacity of NOTT-160a. In comparison, more porous MOFs such as MOF-205 and MOF-210 are not close to reaching saturation at 80 bar and therefore the working capacity of these MOFs is considerably lower than that of NOTT-160a.[55] This shows that NOTT-160a exhibits an ideal level of porosity and crystal density to facilitate high volumetric uptake of CH_4 between 5 and 80 bar.

4.3.4 NOTT-161

4.3.4.1 Synthesis of $[Cu_3L^{13}(H_2O)_3]\cdot 6DMF\cdot 5H_2O$ (NOTT-161)

In order to investigate the effect of adding further polar functional groups on the low pressure adsorption of CO_2 and C_2 hydrocarbons, a fluoride functionalised ligand, H_6L^{13}, was prepared. The initial step in the synthesis of H_6L^{13} was a nucleophilic

substitution reaction to prepare a triiodo intermediate.[15] 2-Fluoro-4-iodoaniline and cyanuric chloride were dissolved in a basic solution of 1,4-dioxane/DMF and heated in a microwave reactor for 1 hour at 120 °C with stirring (Scheme 4.3). The intermediate was isolated following work-up and recrystallization from Et_2O. A Pd(II) catalysed microwave-assisted Suzuki reaction between this intermediate and (3,5-bis(ethoxycarbonyl)phenyl)boronic acid gave a solid that was insoluble in common organic solvents. The solid was hydrolysed and acidified without purification to give H_6L^{13} as a pale purple powder.



Scheme **4.3.** Synthesis of H_6L^{13}.

Despite extensive screening of solvothermal conditions, the corresponding Cu(II) MOF could not be isolated as a pure powder. However, reaction of H_6L^{13} with $Zn(NO_3)_2{\cdot}6H_2O$ in acidified DMF at 90 °C yielded a phase pure sample of NOTT-161(Zn) as colourless octahedral crystals. This material was transmetallated over a period of four weeks with a solution of $Cu(NO_3)_2{\cdot}3H_2O$ in DMF, exchanged with a fresh solution every 24 hours, to give NOTT-161(Cu). The progress of this exchange was monitored by ICP-OES to ensure that full transmetallation of the cluster from $\{Zn_2(O_2CR)_4\}$ to $\{Cu_2(O_2CR)_4\}$ had occurred. Powder X–ray diffraction was used to confirm that NOTT-161(Zn) and NOTT-161(Cu) are isostructural (Appendices Figure A4.1).

4.3.4.2 Structural Analysis of NOTT-161

Single crystal X-ray diffraction reveals that NOTT-161(Zn) crystallises in the tetragonal space group *I*4/*m* with unit cell dimensions *a* = 33.1819(2) Å, *c* = 48.3988(7) Å and *V* = 53160(1) Å^3. The structure is revealed to be isoreticular to that of NOTT-160, being a 3,24-connected framework containing 3 distinct cages, **A**, **B** and **C** (Figure 4.26). Cage **A** is a truncated cuboctahedron formed from 12 $\{Zn_2(O_2CR)_4\}$ paddlewheel units and the isophthalate terminus of 24 different linkers. The accessible internal diameter of cage **A**, with the solvent molecules removed from the axial positions of the paddlewheel, is 14.0 Å. Cage **B** consists of 12 Zn(II) paddlewheels arranged in triangular clusters of three. Four ligands are each connected to three paddlewheels in the same plane such that each ligand forms a face of the tetrahedron. Cage **B** has an internal diameter of 13.7 Å, 1.3 Å smaller than in NOTT-160(Zn), a result of the twist of the phenyl ring connected to the triazine core. This is assigned to a steric repulsion caused by the introduction of the fluoride group on this ring. This results in both the amine groups of the triazine core and the fluoride groups surrounding the windows to the cavity. The F-F distances in cage **B** are 8.6 Å and 6.0 Å depending on the relative orientations of adjacent ligands. Cage **C** is comprised of 24 paddlewheels arranged in six square clusters of four. Eight ligands are connected to three paddlewheels in the same plane such that each ligand spans the face of a truncated cube. Cage **C** has an accessible diameter of 20.8 Å (1.6 Å smaller than NOTT-160(Zn)) and a cage length measuring 36.5 Å. As in cage **B**, the fluoride and amine groups surround the windows to the cavity. The F-F distances were measured to be 7.7 Å and 5.4 Å. The positioning of the fluoride groups also leads to a fluorinated channel seen down the *a*-axis (Figure 4.26). This narrow

channel with F-F distances of 8.6 Å between adjacent fluorides and 5.4 Å between opposing fluorides should be ideally sized for interactions with guest molecules.

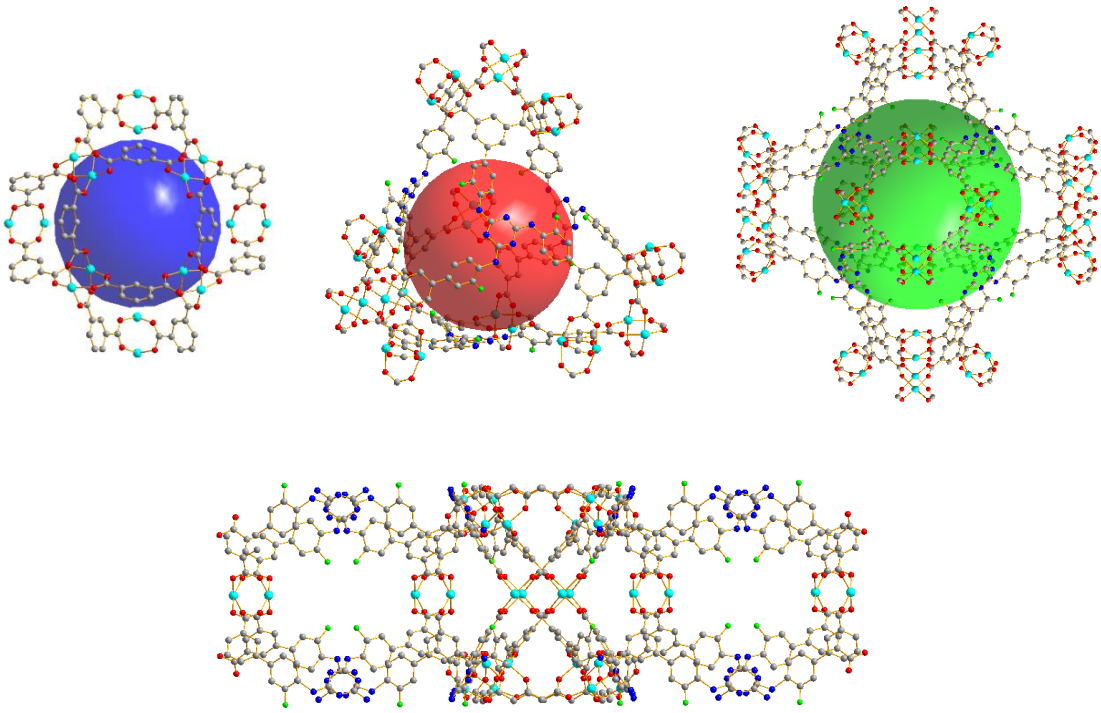


Figure 4.26. View of cages A, B and C observed in NOTT-161 (top) and the fluorinated channel down the *a*-axis (bottom).

Gas adsorption measurements on NOTT-161 analogous to those performed with NOTT-160 are yet to be completed.

4.4 Current and Future Work

In addition to the gas storage and metal scavenging applications described above, this work has also been focused on the organic synthesis of novel triazine based linkers (Figure 4.27).

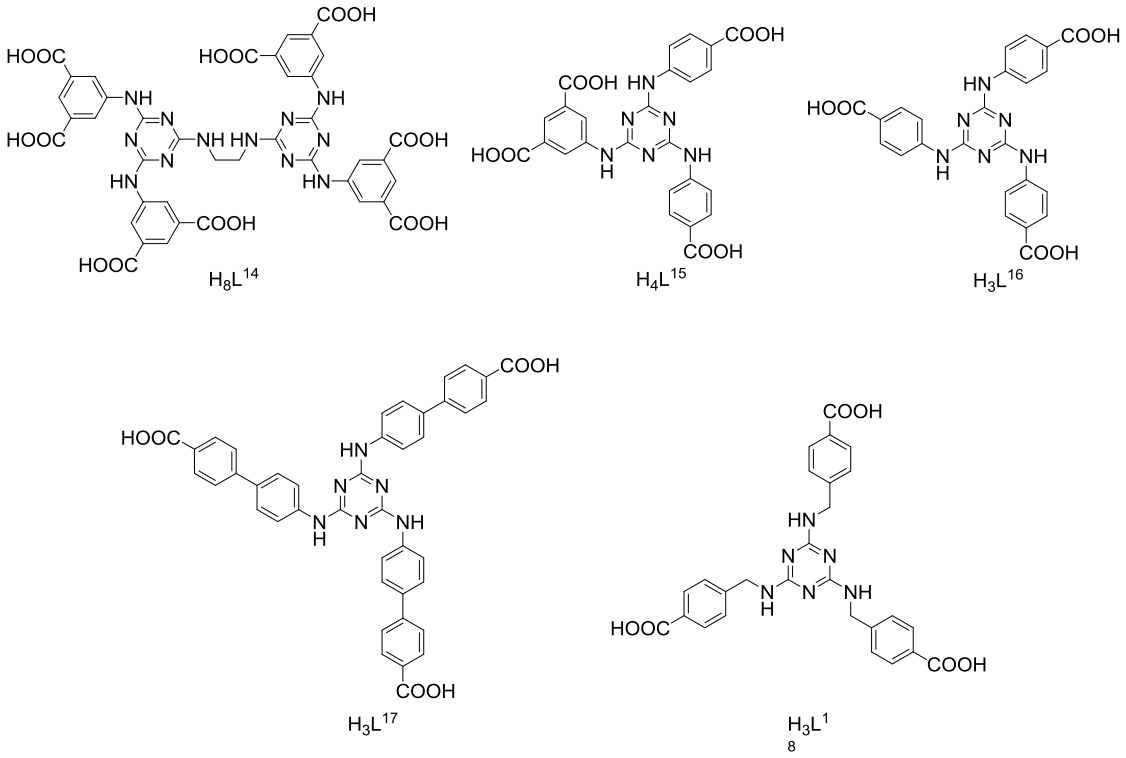


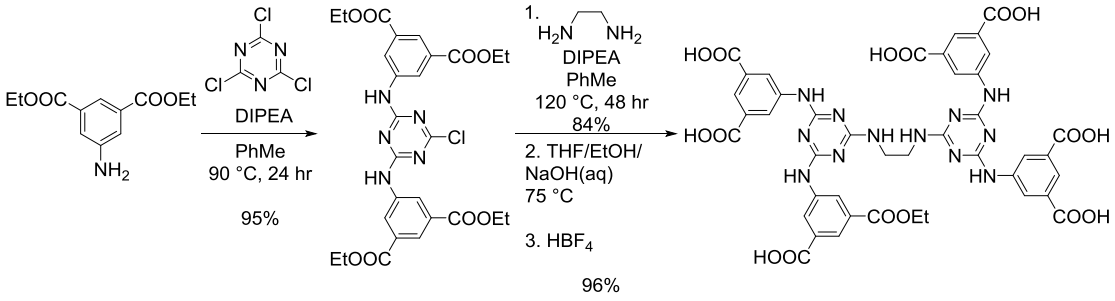
Figure 4.27. Triazine-based linkers for the synthesis of novel metal-organic frameworks.

4.4.1 $[Zn_3(L^{14})(H_2O)_2]_n$

4.4.1.1 Synthesis of H_8L^{14} and $[Zn_3(L^{14})(H_2O)_2]_n$

The first such linker prepared for the synthesis of new metal-organic frameworks was the octacarboxylate ligand H_8L^{14} shown above. The synthesis of H_8L^{14} involved the addition of an ethylenediamine bridge between two triazine moieties as an effective method to increase the number of N atoms within the linker to enhance interactions between the MOF and guest molecules. The first step in the preparation of H_8L^{14} was a 2:1 stoichiometric reaction of 3-amino-5-(ethoxycarbonyl)benzoic acid and cyanuric chloride in a solution of toluene and DIPEA (diisopropylethylamine) at 90 °C to give a monochloride species.[59] This intermediate was then added to a solution of toluene, DIPEA and 0.5 eq. of ethylenediamine and

heated under reflux for 48 hours to give a diamine bridged octacarboxylate ester.[59] After this ester was isolated and purified by recrystallization from toluene, it was hydrolysed in NaOH(aq), acidified with HBF_4 and washed to give pure H_8L^{14} (Scheme 4.4).



Scheme 4.4. Synthesis of H_8L^{14}.

Reaction conditions for MOF synthesis using H_8L^{14} and metal ions (Cu^{2+}, Zn^{2+}, Co^{2+}, Zr^{4+}) were trialled, with the solvent system, temperature, pH and the acid used all being varied systematically. From these trials, a successful solvothermal reaction of H_8L^{14} and $Zn(NO_3)_2{\cdot}6H_2O$ in acidified DMF at 80 °C for 120 hours yielded $[Zn_3(L^{14})(H_2O)_2]$ as colourless block crystals.

4.4.1.2 Structural Analysis

Single crystal X-ray diffraction reveals that $[Zn_3(L^{14})(H_2O)_2]$ crystallises in the monoclinic space group $P2_1/n$ with unit cell dimensions a = 19.323(3) Å, b = 23.585(3) Å, c = 23.964(2) Å, β = 98.878(9)° and V = 10790(2) Å^3. $[Zn_3(L^{14})(H_2O)_2]$ is revealed to be a 3D framework of a topology not previously reported for a solid material, containing three channels within the structure. The geometry of the ligand within the material is determined by the bridging ethylenediamine unit which is almost perpendicular to the plane of the adjacent triazine moieties which are almost coplanar, offset by the C_2 of the bridge (Figure 4.28). This results in a less "open"

framework than would be expected if the bridge remained in the plane of the ligand. Three distinct zinc environments are observed within the structure; one tetrahedral and two 5-coordinate nodes. One 5-coordinate node, **A**, consists of a carboxylate unit bound monodentate, a pyridyl nitrogen from the same ligand bound in the axial position and a further two carboxylate units from two different ligands, with one binding in monodentate fashion, the other in bidentate fashion. This results in two "free" carboxylate O groups around the node, a potentially important feature for gas uptake or metal ion scavenging. The additional two zinc environments **B** and **C** form a second node, separated from node **A** by an isophthalate unit. The tetrahedral Zn, **B**, is bound in a monodentate fashion by one COOH, a second COOH from the same ligand bridges to **C**, as do a further two carboxylates from two separate ligands. Two water molecules complete the coordination sphere of **C**. In total, three "free" carboxylate O groups per ligand are available for interaction with guest molecules. Three distinct channels can be identified within the framework, an elliptical channel directed down the *c*-axis which is lined with open metal sites (upon removal of coordinated H_2O) and free COOH groups, and two channels (one triangular, one square) between crystallographic axes lined with free COOH groups.

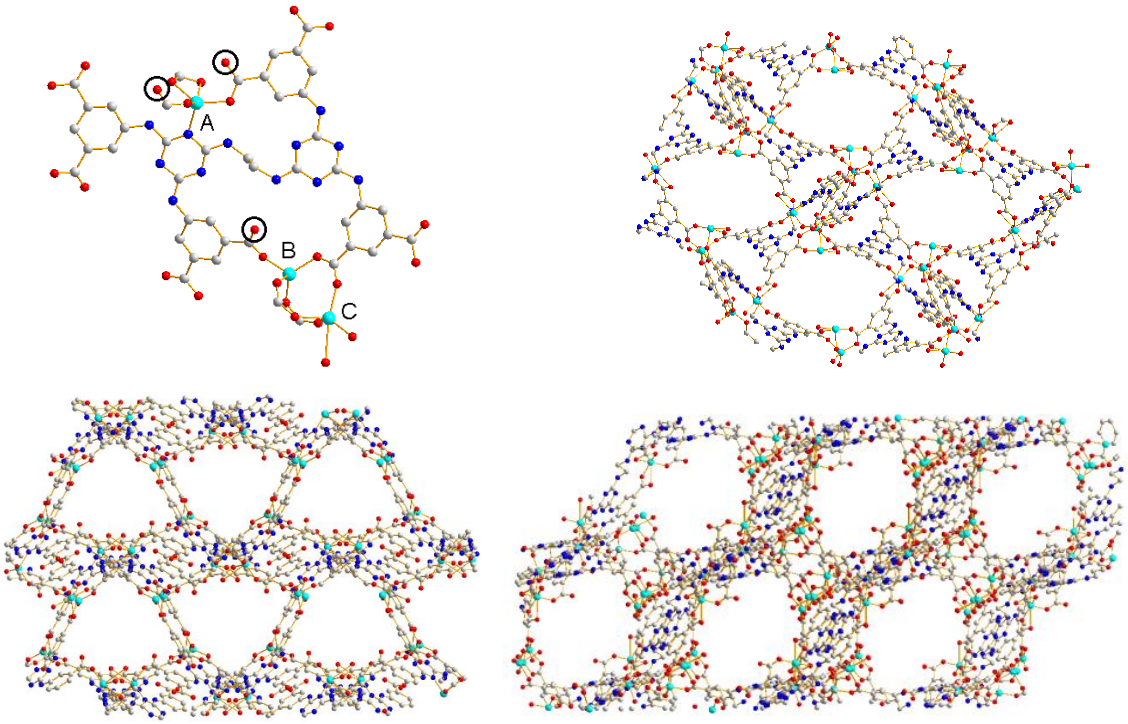


Figure 4.28. View of the linker geometry and metal nodes (top left) and the three distinct pore channels observed in $[Zn_3(L^{14})(H_2O)_2]$. For clarity, the free carboxylate O groups are circled.

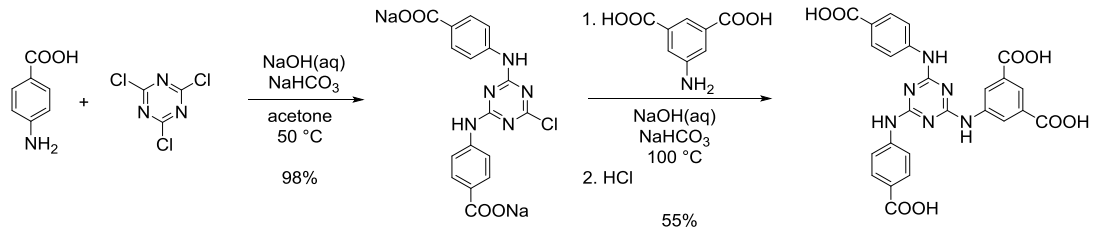
Whilst single crystals were obtained from this synthesis, the majority of the product consisted of an amorphous powder. Work is ongoing to prepare a phase pure sample of $[Zn_3(L^{14})(H_2O)_2]$ for gas storage measurements, with particular focus on the low pressure uptake of CO_2 and the C_2 hydrocarbons.

4.4.2 $[Cu_3(L^{15})(OH)_2]$

4.4.2.1 Synthesis of H_4L^{15} and $[Cu_3(L^{15})(OH)_2]$

To investigate the effect of an asymmetrical ligand geometry, the chloride groups of a cyanuric chloride core were substituted by two different carboxylic acids to give H_4L^{15} (Scheme 4.5). The initial synthetic step was the addition of two equivalents of 4-aminobenzoic acid to cyanuric chloride in a basic solution at 50 °C to give a di-substituted intermediate.[60] This intermediate was then reacted with 5-

aminoisophthalic acid in sodium hydroxide at 100 °C and H_4L^{15} was isolated following acidification and recrystallisation.



Scheme 4.5. Synthesis of H_4L^{15}.

As with H_8L^{14}, a series of reaction conditions between H_4L^{15} and various metal ions (Cu^{2+}, Zn^{2+}, Zr^{4+}, Fe^{3+}) were trialled. From these reactions, a successful solvothermal reaction of H_4L^{15} and $Cu(NO_3)_2{\cdot}3H_2O$ in a mixture of NMP/H_2O at 80 °C for 20 hours yielded $[Cu_2(L^{15})(OH)_2]$ as green plate crystals.

4.4.2.2 Structural Analysis

Single crystal X-ray diffraction reveals that $[Cu_2(L^{15})(OH)_2]$ crystallises in the triclinic space group *P*-1 with unit cell dimensions a = 13.0524(8) Å, b = 14.692(1) Å, c = 17.210(1) Å, α = 104.778(6)°, β = 98.878(9)°, γ = 93.658(5)° and V = 3157.4(4) Å^3. The resulting structure is a 4,4-connected net consisting of linkers with all COOH groups in the same plane connected to four Cu clusters. This unusual cluster comprises two Cu(II) ions and two Cu(I) ions with two interstitial OH groups each bridging between three Cu ions (Figure 4.29), with each cluster connected to four linkers.

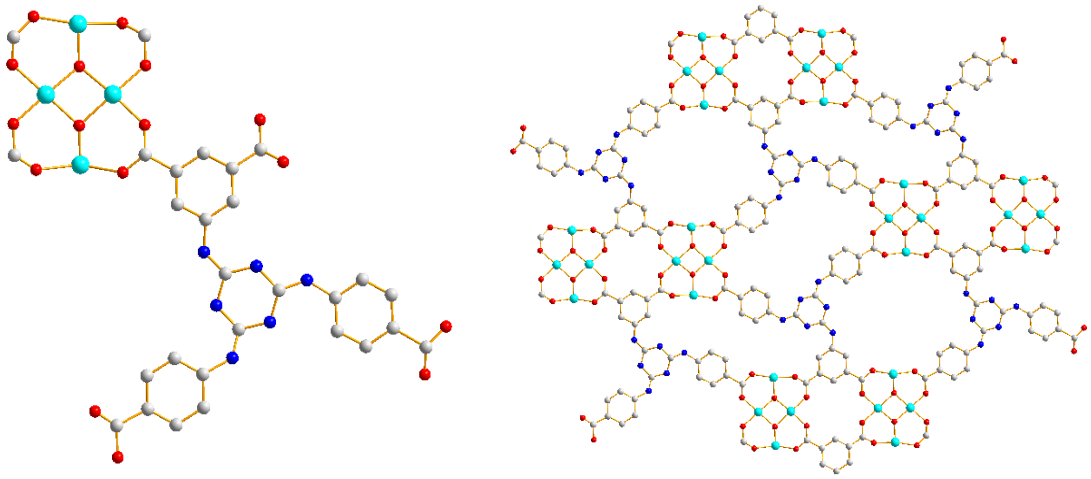
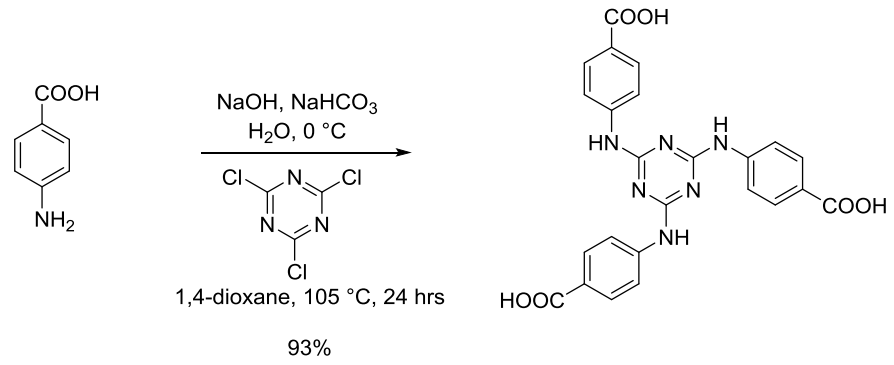


Figure 4.29. View of the linker and metal cluster geometry in $[Cu_2(L^{15})(OH)_2]$ (left) and the extended 2D framework (right) of $[Cu_2(L^{15})(OH)_2]$.

This linker and metal node combination give an overall 2D structure which exhibited no porosity when an N_2 isotherm was measured from 0-1 bar at 77 K. Work to prepare a stable 3D Fe(III) or Zr(IV) framework incorporating L^{15} is ongoing.

4.4.3 Synthesis of H_3L^{16}, H_3L^{17} and H_3L^{18}

A number of recent literature reports have shown that highly porous, stable M(III) and M(IV) frameworks can be prepared with a variety of tripodal ligands.[56,61,62] As such, we have prepared two tripodal triazine ligands, H_3L^{16} and H_3L^{17}, for the synthesis of Fe(III) and Zr(IV) MOFs. These frameworks would be suitable for a variety of applications, for example the storage of corrosive gases such as SO_2 and NH_3, metal scavenging, catalysis and drug delivery. H_3L^{16} was synthesised from a nucleophilic substitution reaction between cyanuric chloride and 4-aminobenzoic acid in a basic solution, followed by acidification and recrystallisation from hot DMF to give the pure product (Scheme 4.6).



Scheme 4.6. Synthesis of H_3L^{16}.

Reactions between H_3L^{16} and $ZrCl_4$, $Fe_3O(OAc)_6(H_2O)_3$ and $FeCl_3{\cdot}6H_2O$ metal precursors were trialled using a variety of solvents (DMF, DEF, DMA, NMP) and modulators (AcOH, HCOOH, TFA, PhCOOH) at 120 °C for Zr(IV) and 150 °C for Fe(III). The most promising results for Zr(IV), as identified by PXRD, were from the reaction of H_4L^{15} (10 mg), $ZrCl_4$ (10 mg) and PhCOOH in DMF (4 ml) heated at 120 °C for 72 hours. The initial product, prepared using 25 eq. of PhCOOH modulator, exhibited a broad peak in the powder X-ray diffractogram at ~5° 2θ. In an attempt to improve the crystallinity of the product, subsequent reactions using increased quantities of PhCOOH were carried out. These showed a slight increase in the crystallinity of the powder (Figure 4.30), however with 80 equivalents the crystallinity was reduced and with 100 and 120 equivalents no product was formed. While these represent promising initial results, efforts are ongoing to find the ideal conditions to prepare and solve the structure of a crystalline product.

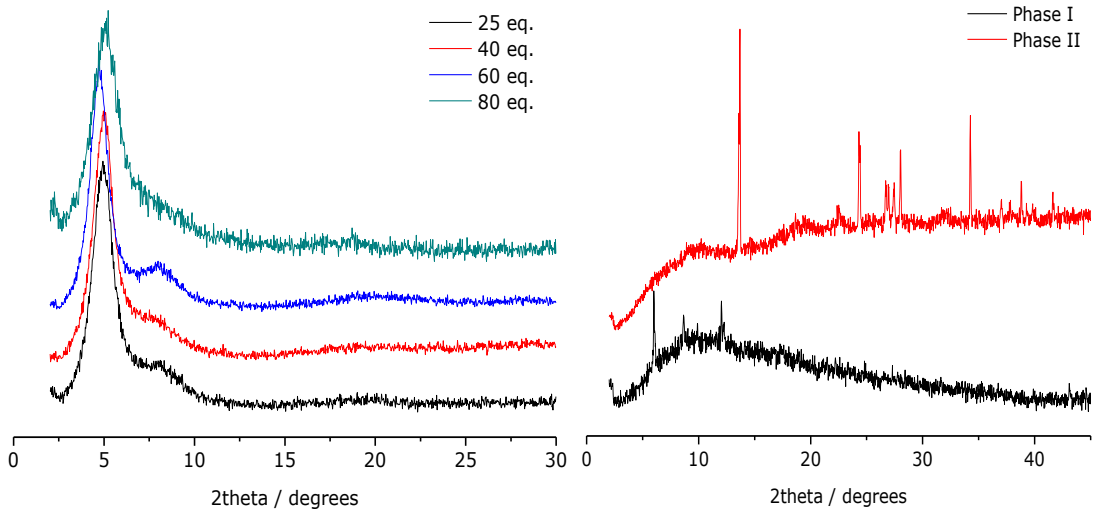
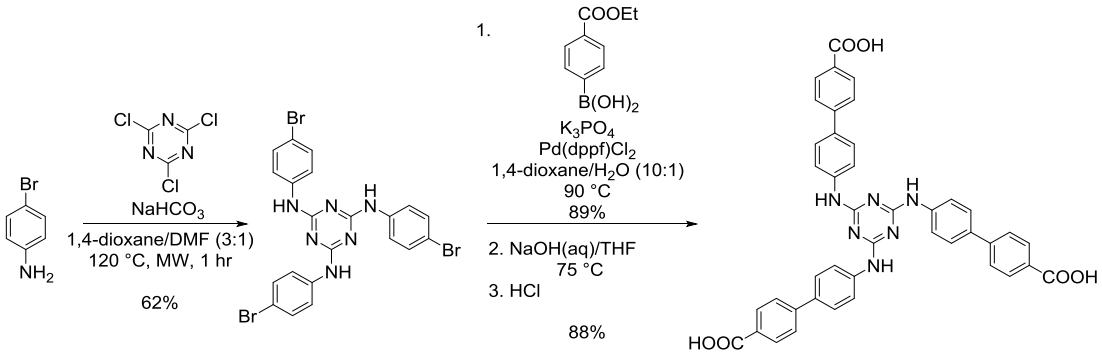


Figure 4.30. PXRD patterns of Zr (left) and Fe (right) products formed with H_3L^{16}.

With Fe(III), two distinct phases have been prepared under different conditions (Figure 4.30). Phase I was prepared using H_3L^{16}, $Fe_3O(OAc)_6(H_2O)_3$ and AcOH in DEF at 120 °C and exhibits three low angle peaks below 12° 2θ. Whilst the powder pattern shown in Figure 4.30 exhibits very few peaks, it should be noted that Fe fluorescence in the Cu Kα radiation produces a large background signal which may obscure higher angle peaks. Phase II was formed *via* the reaction of H_3L^{16} and $FeCl_3{\cdot}6H_2O$ in a DEF/TFA solution at 150 °C. The PXRD pattern clearly shows 8 sharp peaks, indicating a good degree of crystallinity, however the initial peak at ~13.5° 2θ (d-spacing ~6.4 Å) suggests that the material is not a highly porous framework. As with the Zr(IV) reactions, efforts to find the ideal conditions to prepare single crystals or highly crystalline powders from which a structure may be elucidated are ongoing.

An analogue of H_3L^{16}, extended by one phenyl ring in each of the tripodal arms, was also prepared and denoted as H_3L^{17} (Scheme 4.7). The first step in the synthesis of H_3L^{17} was a microwave-assisted nucleophilic substitution reaction between cyanuric

chloride and 4-bromoaniline to give a tribromo intermediate.[15] The intermediate was then reacted with (4-(ethoxycarbonyl)phenyl)boronic acid in a microwave using Pd(dppf)Cl_2 as a catalyst to give the triester product in excellent yield (89%). This ester was then hydrolysed in NaOH and acidified with 37% HCl to give H_3L^{17}.



Scheme 4.7. Synthesis of H_3L^{17}.

As with $H_3L^{16,}$ attempts to prepare Zr(IV) and Fe(III) MOFs with H_3L^{17} were carried out. Whilst no successful conditions for a Zr(IV) MOF were found, a reaction between H_3L^{17} and $FeCl_3{\cdot}6H_2O$ in a mixture of DEF/TFA at 150 °C produced a microcrystalline powder.

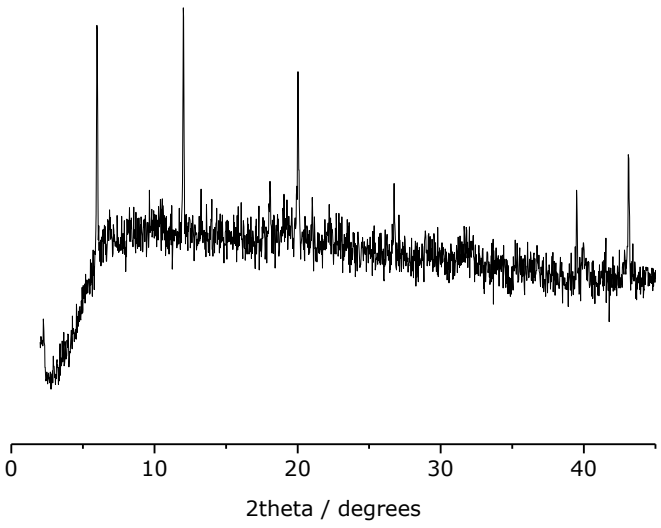
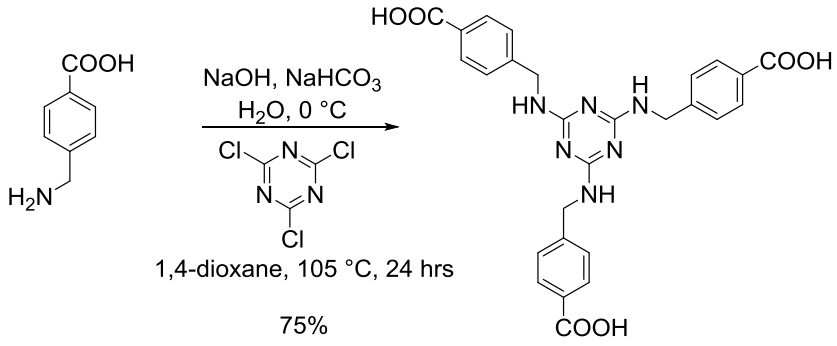


Figure 4.31. PXRD pattern of an Fe(III) material formed from H_3L^{17}.

The PXRD pattern (Figure 4.31) shows clearly that the material is crystalline, with sharp low angle peaks (and therefore large d-spacings) suggesting that the product is not a simple metal salt or a metal oxide. There were not enough peaks present to index to a unit cell but a sample of the material will be taken to beamline I11 at Diamond Light Source for high-resolution PXRD scans for structure determination.

The final tripodal triazine ligand synthesised was a flexible methylamino functionalised linker, H_3L^{18}, designed to reduce the delocalisation of electron density from the NH group into the benzene rings for enhanced interaction with guest molecules (Scheme 4.8).



Scheme 4.8. Synthesis of H_3L^{18}.

H_3L^{18} was synthesised via a reaction between 4-(aminomethyl)benzoic acid and cyanuric chloride in a basic solution followed by acidification and recrystallisation from DMF to give the pure ligand. Despite extensive screening of over 250 conditions with Zn(II), Cu(II) and Zr(IV) metal salts, no crystalline products have been synthesised.

4.5 Conclusions

In this Chapter, the adsorption of $Pd(OAc)_2$, $PtCl_4$ and $Rh_2(OAc)_4$ from THF solutions using a triazine based Cu(II) MOF, $[Cu_3L^{11}]$ has been demonstrated. In

particular, [Cu_3L^{11}] shows an enhanced capacity for $Rh_2(OAc)_4$ in comparison to the tetracarboxylate MOFs investigated in Chapter 3. A highly porous, novel MOF of **rht** topology, denoted NOTT-160, which exhibits excellent selectivity for C_2 hydrocarbons over CH_4 has also been synthesised. The selectivities calculated by Henry's law of 78.8:1 for C_2H_2:CH_4 and 69.6:1 for C_2H_4 at 298 K, represent the third highest and second highest reported values respectively for a MOF under these conditions. NOTT-160 also shows an excellent total uptake of CH_4 at high pressure (339 mg g^{-1} at 80 bar), with a volumetric working capacity of 221 cm^3 cm^{-3} at 80 bar. To the best of our knowledge this represents the second highest working capacity for CH_4 in a MOF behind MOF-519 (230 cm^3 cm^{-3}).[55] Current work is focused on the preparation of new highly stable Fe(III) and Zr(IV) MOFs with a range of triazine functionalised linkers for use as aqueous metal sorbents and for the capture of harmful and corrosive gases such as SO_2 and NH_3.

4.6 Experimental

Synthesis of H_6L^{11}

5-Aminoisophthalic acid (3.94 g, 21.7 mmol, 3.5 eq) was added to a solution of H_2O (50 ml) and 5 M NaOH (10 ml). $NaHCO_3$ (1.84 g, 21.7 mmol) was then added, the solution cooled to 0 °C and left to stir for 90 mins. Cyanuric chloride (1.14 g, 6.25 mmol, 1 eq) in 1,4-dioxane (10 ml) was added dropwise and the mixture was left to heat at 105 °C for 24 h. After cooling to room temperature, 37% HCl was added dropwise until pH ~ 1, giving a white precipitate. This precipitate was redissolved in NaOH and acidified with HCl to remove impurities. The resulting solid was isolated by filtration, washed with copious water and dried under vacuum to give H_6L^{11} (3.48 g, 90%). ^{1}H NMR (400 MHz, dmso-d_6) δ = 9.53 (s, 3H), 8.40 (d, 6H, J = 1.4 Hz),

8.17 (t, 3H, J = 1.4 Hz); $^{13}C\{^{1}H\}$ NMR (100 MHz, dmso-d_6) δ = 168.0, 164.8, 140.1, 133.7, 125.3, 124.6. MS(ESI) m/z 617 (M – H). Anal. Calcd (Found) for $C_{27}H_{18}N_6O_{12}$: C, 52.44 (52.21); H, 2.93 (3.38); N, 13.59 (13.32)%.

Synthesis of H_6L^{12}

Cyanuric chloride (736 mg, 3.99 mmol) was added to a mixture of 4-bromoaniline (2.20 g, 12.8 mmol, 3.2 eq.) and $NaHCO_3$ (1.08 g, 12.8 mmol, 3.2 eq.) in 1,4-dioxane/DMF (3:1, 30 ml) and heated at 120 °C in a microwave reactor for 1 h. Upon completion of the reaction, the solvent was removed under vacuum and the remaining solid was washed with water (2 x 20 ml) and extracted into Et_2O. The organic layer was separated and the solvent removed under vacuum. The resulting white solid was recrystallized from Et_2O/hexane (1:1), filtered and dried to give the pure product, N^2,N^4,N^6-tris(4-bromophenyl)-1,3,5-triazine-2,4,6-triamine (1.46 g, 62%). ^{1}H NMR (400 MHz, dmso-d_6) δ = 9.54 (s, 3H), 7.80 (d, 6H, J = 6.8 Hz), 7.46 (d, 6H, J = 8.8 Hz); $^{13}C\{^{1}H\}$ NMR (100 MHz, dmso-d_6) δ = 164.3, 139.7, 131.6, 122.7, 114.2. MS(ESI) m/z 591 (M + H).

N^2,N^4,N^6-tris(4-bromophenyl)-1,3,5-triazine-2,4,6-triamine (1.32 g, 2.23 mmol), (3,5-bis(ethoxycarbonyl)phenyl)boronic acid (2.14 g, 8.05 mmol, 3.6 eq.) and K_3PO_4 (8.50 g, 40.1 mmol, 18 eq.) were added to a degassed mixture of 1,4-dioxane/water (10:1, 110 ml). Pd(dppf)Cl_2 (40 mg) was then added and the reaction was heated in a microwave reactor at 85 °C for 1 h. Upon completion of the reaction, the solvent was removed under vacuum and the product was extracted into $CHCl_3$. The organic phase was subsequently washed with water and brine and dried over $MgSO_4$. After evaporation of $CHCl_3$, the crude product was purified by silica column chromatography with EtOAc/hexane (2:1) to give the pure ester product as a white

solid (1.86 g, 82%). ^{1}H NMR (300 MHz, dmso-d_6) δ = 9.58 (s, 3H), 8.42 (t, 3H, *J* = 1.5 Hz), 8.39 (d, 6H, *J* = 1.5 Hz), 8.04 (d, 6H, *J* = 6.0 Hz), 7.71 (d, 6H, *J* = 8.7 Hz), 4.37 (q, 12H, *J* = 7.1 Hz), 1.35 (t, 18H, *J* = 7.1 Hz); ^{13}C{^{1}H} NMR (100 MHz, dmso-d_6) δ = 165.8, 165.1, 139.6, 138.6, 131.9, 131.5, 130.1, 129.8, 127.5, 121.4, 61.6, 14.6.

This hexaester (1.70 g, 1.67 mmol) was dissolved in a mixture of THF (30 ml), EtOH (30 ml) and 2 M NaOH (30 ml) and heated at 75 °C for 16 h. Upon cooling, fresh THF (30 ml) was added, the aqueous layer was separated and concentrated HCl was added dropwise to the solution until pH~1. The resulting precipitate was filtered and recrystallised from a mixture of hot DMF/water (5:1) to give H_6L^{12} as a white solid (1.36 g, 96%). ^{1}H NMR (400 MHz, dmso-d_6) δ = 9.59 (s, 3H), 8.44 (t, 3H, *J* = 1.6 Hz), 8.39 (d, 6H, *J* = 1.6 Hz), 8.04 (d, 6H, *J* = 8.0 Hz), 7.73 (d, 6H, *J* = 8.8 Hz); ^{13}C{^{1}H} NMR (100 MHz, dmso-d_6) δ = 167.1, 164.5, 141.4, 140.8, 132.6, 132.4, 131.3, 128.7, 127.5, 121.2. Anal. Calcd (Found) for $C_{45}H_{30}N_6O_{12}$: C, 63.83 (63.39); H, 3.57 (3.45); N, 9.93 (9.80)%.

Synthesis of H_6L^{13}

Cyanuric chloride (368 mg, 2.00 mmol) was added to a mixture of 2-fluoro-4-iodoaniline (1.89 g, 7.97 mmol, 4 eq.) and $NaHCO_3$ (672 mg, 8.00 mmol, 6 eq.) in 1,4-dioxane/DMF (2:1, 15 ml) and heated at 120 °C in a microwave reactor for 1 h. Upon completion of the reaction, the solvent was removed under vacuum and the remaining solid was washed with water (2 x 20 ml) and extracted into Et_2O. The organic layer was separated and the solvent removed under vacuum. The resulting white solid was recrystallized from warm Et_2O, filtered and dried to give the pure

product (1.57 g, 100%). ^{1}H NMR (300 MHz, dmso-d_6) δ = 8.92 (s, 3H), 7.66 (d, 3H, *J* = 1.5 Hz), 7.63 (t, 3H, *J* = 0.9 Hz), 7.45 (s, 3H).

This intermediate (1.57 g, 2.00 mmol), (3,5-bis(ethoxycarbonyl)phenyl)boronic acid (1.91 g, 7.18 mmol, 3.6 eq.) and K_3PO_4 (7.63 g, 36 mmol, 18 eq.) were added to a degassed mixture of 1,4-dioxane/water (10:1, 110 ml). Pd(dppf)Cl_2 (40 mg) was then added and the solution was heated under argon at 85 °C for 3 days. Upon completion of the reaction, the solvent was removed under vacuum and the product was washed with $CHCl_3$ (3 x 30 ml) to give an insoluble grey-brown solid. This solid was added to a 2 M aqueous solution of NaOH (30 ml) and heated at 75 °C for 2 h. 37% HCl was added dropwise until pH~1, giving a grey-purple precipitate. This precipitate was isolated by filtration, dried, recrystallised from a mixture of hot DMF/MeCN (1:1) and dried under vacuum to give H_6L^{13} as an off-white solid (1.60 g, 89%). ^{1}H NMR (400 MHz, dmso-d_6) δ = 8.78 (s, 3H), 8.46 (t, 3H, *J* = 1.6 Hz), 8.40 (d, 6H, *J* = 1.6 Hz), 8.10 (t, 3H, *J* = 8.0 Hz), 7.70 (dd, 3H, *J* = 12.0, 2.0 Hz), 7.57 (dd, 3H, *J* = 8.4, 1.6 Hz); ^{13}C{^{1}H} NMR (100 MHz, dmso-d_6) δ = 166.9, 164.7, 162.8, 140.1, 135.0, 132.6, 131.5, 129.3, 127.9, 127.8, 126.2, 122.9.

Synthesis of H_8L^{14}

Diethyl-5-aminoisophthalate (2.76 g, 11.6 mmol, 2 eq.) in toluene (40 ml) was added dropwise to a solution of cyanuric chloride (1.08 mg, 5.8 mmol, 1 eq.) and DIPEA (1.96 ml, 11.6 mmol, 2 eq.) stirring in toluene (40 ml). This solution was left to heat at 90 °C for 48 h. Upon completion of the reaction the toluene was removed under vacuum to give a white solid which was stirred in H_2O for 2 h, filtered and dried to give tetraethyl 5,5'-((6-chloro-1,3,5-triazine-2,4-diyl)bis(azanediyl))diisophthalate (TCBDI) as a white powder (3.26 g, 95%). ^{1}H NMR (300 MHz, dmso-d_6) δ = 10.79

(s, 2H) 8.48 (d, 4H, *J* = 1.5 Hz), 8.15 (d, 2H, *J* = 1.5 Hz), 4.35 (q, 8H, *J* = 7.5 Hz), 1.29 (t, 12H, *J* = 6.8 Hz). MS(ESI) m/z 586 (M + H).

TCBDI (1.40 g, 2.4 mmol, 2 eq.) was dissolved in a solution of toluene (50 ml) and DIPEA (0.42 ml, 2.4 mmol, 2 eq.). Ethylenediamine (83 µl, 1.20 mmol, 1 eq.) was then added and the solution was heated at 120 °C for 48 h, by which point a white precipitate had formed. This solid was isolated by filtration, washed with hexane (40 ml) and hot EtOH (3 x 30 ml) and dried under vacuum to give the product (1.16 g, 84%). ^{1}H NMR (400 MHz, dmso-d_6) δ = 9.67 (s, 4H), 8.56 (d, 8H, *J* = 1.5 Hz), 8.09 (d, 4H, *J* = 1.5 Hz), 7.49 (s, 2H), 4.27 (q, 16H, *J* = 7.2 Hz), 3.58 (m, 4H), 1.25 (t, 24H, *J* = 5.3 Hz). MS(MALDI): m/z 1159.

This solid (1.05 g) was added to a solution of THF (30 ml), EtOH (30 ml) and 2 M NaOH (30 ml) and heated at 75 °C overnight. Upon cooling, an additional 20 ml of NaOH was added and the layers were separated. 50% HBF_4 was added dropwise to the aqueous layer until pH~1, producing a white precipitate. This solid was isolated by filtration, washed with cold DMF (30 ml) and MeOH (30 ml) and dried under vacuum to give H_8L[14] as a white solid (815 mg, 96%). ^{1}H NMR (400 MHz, dmso-d_6) δ = 9.67 (s, 4H), 8.61 (d, 8H, *J* = 1.5 Hz), 8.11 (t, 4H, *J* = 1.5 Hz), 7.49 (s, 2H) 3.51 (m, 4H). MS(ESI) m/z 935 (M + H); ^{13}C{^{1}H} NMR (125 MHz, dmso-d_6) δ = 167.2, 165.8, 164.3, 140.4, 132.0, 125.3, 125.0, 39.3. Anal. Calcd (Found) for $C_{40}H_{30}N_{12}O_{16}$: C, 51.40 (51.28); H, 3.24 (3.08); N, 17.98 (17.94)%.

Synthesis of H_4L[15]

A solution of cyanuric chloride (1.25 g, 6.9 mmol) in acetone (7.5 ml) was added dropwise to a solution of 4-aminobenzoic acid (1.89 g, 13.8 mmol) and $NaHCO_3$ (1.15 g, 13.8 mmol) in H_2O (25 ml) and 5 M NaOH (5.5 ml). The mixture was then

stirred at 50 °C for 20 h and cooled to room temperature. EtOH (100 ml) was then added, forming a white precipitate which was isolated by filtration. This solid was washed with warm DMF (2 x 25 ml) and dried to give the product (2.91 g, 98%).

This intermediate (2.75 g, 6.4 mmol) was added to a solution of 5-aminoisophthalic acid (1.16 g, 6.4 mmol), $NaHCO_3$ (537 mg, 6.4 mmol) and NaOH (285 mg, 6.4 mmol) in H_2O (50 ml). This mixture was then refluxed at 100 °C for 24 h. Upon cooling to room temperature, 37% HCl was added dropwise until pH~1, producing a white precipitate. This precipitate was removed by filtration, dried, recrystallised from hot DMF and dried under vacuum to give H_4L^{15} (1.88 g, 55%). ^{1}H NMR (300 MHz, dmso-d_6) δ = 9.87 (s, 1H), 9.81 (s, 2H), 8.43 (d, 2H, *J* = 1.5 Hz), 8.20 (t, 1H, *J* = 1.5 Hz), 7.95 (d, 4H, *J* = 9.0 Hz), 7.85 (d, 4H, *J* = 9.0 Hz); ^{13}C{^{1}H} NMR (75 MHz, dmso-d_6) δ = 167.6, 167.1, 164.5, 164.2, 132.1, 130.7, 130.6, 126.6, 124.3, 119.7. Anal. Calcd (Found) for $C_{25}H_{18}N_6O_8$: C, 56.61 (55.84); H, 3.42 (3.63); N, 15.84 (15.37)%.

Synthesis of H_3L^{16}

4-Aminobenzoic acid (5.44 g, 39.7 mmol, 3.2 eq.) was added to a solution of H_2O (100 ml) and 5 M NaOH (20 ml). $NaHCO_3$ (3.36 g, 39.7 mmol, 3.2 eq.) was added and the solution cooled to 0 °C and left to stir for 90 mins. Cyanuric chloride (2.28 g, 12.5 mmol, 1 eq.) in 1,4-dioxane (15 ml) was added dropwise and the mixture was left to heat at 105 °C for 24 h. After cooling to room temperature, 37% HCl was added dropwise until pH~1, giving a white precipitate. This solid was isolated by filtration and recrystallised from hot DMF to give H_3L^{16} (5.64 g, 93%). ^{1}H NMR (300 MHz, dmso-d_6) δ = 12.58 (s, 3H), 9.83 (s, 3H), 7.99 (d, 6H, *J* = 1.5 Hz), 7.89 (d, 6H, *J* = 1.5 Hz); ^{13}C{^{1}H} NMR (75 MHz, dmso-d_6) δ = 167.7, 164.4, 144.4,

130.5, 124.7, 119.7. MS(ESI) m/z = 485 (M – H). Anal. Calcd (Found) for $C_{24}H_{18}N_6O_6$: C, 59.26 (59.09); H, 3.73 (3.82); N, 17.28 (17.45)%.

Synthesis of H_3L^{17}

Cyanuric chloride (736 mg, 3.99 mmol) was added to a mixture of 4-bromoaniline (2.20 g, 12.8 mmol, 3.2 eq.) and $NaHCO_3$ (1.08 g, 12.8 mmol, 3.2 eq.) in 1,4-dioxane/DMF (3:1, 30 ml) and heated at 120 °C in a microwave reactor for 1 h. Upon completion of the reaction, the solvent was removed under vacuum and the remaining solid was washed with water (2 x 20 ml) and extracted into Et_2O. The organic layer was separated and the solvent removed under vacuum. The resulting white solid was recrystallized from Et_2O/hexane (1:1), filtered and dried to give H_3L^{17} (1.46 g, 62%). ^{1}H NMR (400 MHz, dmso-d_6) δ = 9.54 (s, 3H), 7.80 (d, 6H, *J* = 6.8 Hz), 7.46 (d, 6H, *J* = 8.8 Hz). ; $^{13}C\{^1H\}$ NMR (100 MHz, dmso-d_6) δ = 164.3, 139.7, 131.6, 122.7, 114.2.

This intermediate (700 mg, 1.18 mmol), (4-(ethoxycarbonyl)phenyl)boronic acid (827 mg, 4.26 mmol, 3.6 eq.) and K_3PO_4 (904 mg, 4.26 mmol, 3.6 eq.) were added to a degassed mixture of 1,4-dioxane/water (10:1, 22 ml). Pd(dppf)Cl_2 (40 mg) was then added and the solution was heated in a microwave reactor at 90 °C for 1 h. Upon completion of the reaction, the solvent was removed under vacuum and the product was extracted into $CHCl_3$. The combined organic phase was subsequently washed with water and brine and dried over $MgSO_4$. After evaporation of $CHCl_3$, the crude product was passed through a plug of silica gel in DCM to give the pure ester product as a white solid (840 mg, 89%). ^{1}H NMR (300 MHz, dmso-d_6) δ =9.57 (s, 3H), 8.03 (d, 6H, *J* = 8.4 Hz), 8.00 (d, 6H, *J* = 8.0 Hz), 7.84 (d, 6H, *J* = 8.4 Hz), 7.73 (d, 6H, *J* = 8.6 Hz), 4.34 (q, 6H, *J* = 7.5 Hz), 1.35 (t, 9H, *J* = 6.8 Hz); $^{13}C\{^1H\}$ NMR

(100 MHz, dmso-d_6) 166.1, 144.9, 140.4, 130.3, 130.2, 128.5, 127.5, 126.8, 121.1, 61.2, 14.7.

This triester (820 mg, 1.03 mmol) was dissolved in a mixture of THF (30 ml) and 2 M NaOH (30 ml) and heated at 75 °C for 16 h. Upon cooling, THF (30 ml) was added, the aqueous layer was separated and concentrated HCl was added dropwise to the solution until pH~1. The resulting precipitate was filtered and recrystallised from a mixture of hot DMF/water (5:1) to give H_3L^{17} as an off-white solid (626 g, 88%). ^{1}H NMR (400 MHz, dmso-d_6) δ = 9.58 (s, 3H), 8.03 (d, 6H, *J* = 8.0 Hz), 7.99 (d, 6H, *J* = 16.0 Hz), 7.83 (d, 6H, *J* = 8.0 Hz), 7.75 (d, 6H, *J* = 8.0 Hz); ^{13}C{^{1}H} NMR (100 MHz, dmso-d_6) δ = 167.6, 144.4, 140.3, 133.3, 130.5, 129.5, 127.5, 126.7, 121.4.

Synthesis of H_3L^{18}

4-(aminomethyl)benzoic acid (7.50 g, 49.6 mmol, 4 eq.) was added to a solution of H_2O (100 ml) and 5 M NaOH (20 ml). $NaHCO_3$ (4.20 g, 49.6 mmol, 4 eq.) was added and the solution cooled to 0 °C and left to stir for 90 mins. Cyanuric chloride (2.28 g, 12.5 mmol, 1 eq.) in 1,4-dioxane (15 ml) was added dropwise and the mixture was left to heat at 105 °C for 24 h. After cooling to room temperature, 37% HCl was added dropwise until pH~1, giving a white precipitate. This solid was isolated by filtration and recrystallised from hot DMF to give the pure product (4.93, 75%). ^{1}H NMR (300 MHz, dmso-d_6) δ = 12.86 (s, 3H), 7.92 (dd, 6H, *J* = 8.1, 1.5 Hz) 7.46 (d, 6H, *J* = 8.1, 1.5 Hz), 4.62 (d, 6H, *J* = 6.4 Hz); ^{13}C{^{1}H} NMR (75 MHz, dmso-d_6) δ = 167.5, 167.4, 143.5, 129.9, 127.9, 44.0. MS(ESI) m/z 529 (M + H).

Synthesis of $[Cu_3(L^{11})(H_2O)_3]\cdot 11DMF\cdot 3H_2O$

H_6L^{11} (30.9 mg, 0.05 mmol) and $Cu(NO_3)_2\cdot 3H_2O$ (36.2 mg, 0.15 mmol) were added to a 15 ml glass pressure tube containing DMF (2.5 ml) and 3 M HNO_3 (1.2 ml in

DMF). After sonication, the solution was left to heat for 24 h at 80 °C, yielding green octahedral crystals which were isolated by filtration and washed with hot DMF (42 mg, 49%). Anal. Calcd (Found) for $C_{60}H_{101}N_{17}O_{29}Cu_3$: C, 42.02 (41.79); H, 5.94 (5.68); N, 13.88 (14.06)%.

Synthesis of $[Cu_3(L^{12})(H_2O)_3]\cdot 13DMF\cdot 7H_2O$ (NOTT-160)

A sample of NOTT-160 for structure determination was prepared on a small scale by dissolution of H_6L^{12} (20 mg, 0.024 mmol) and $Cu(NO_3)_2\cdot 3H_2O$ (22.8 mg, 0.094 mmol) in DMF (1.5 ml). Addition of 3 M HNO_3 in DMF (0.6 ml) followed by heating in a sealed vial at 80 °C for 20 h produced green octahedral crystals which were isolated by filtration and washed with hot DMF. A microcrystalline sample of NOTT-160 for gas sorption experiments was prepared on a larger scale. H_6L (100 mg, 0.118 mmol) and $Cu(NO_3)_2\cdot 3H_2O$ (114 mg, 0.472 mmol, 4 eq.) were added to DMF/H_2O (8 ml; 15:1, v/v) and sonicated until dissolution. 3M HNO_3 in DMF (3 ml) was added and the solution was heated in a 50 ml Schott bottle at 80 °C for 20 h. The crystalline product was removed by filtration, washed with copious hot DMF and dried to yield a green powder of $[Cu_3(L^{12})(H_2O)_3]\cdot 13DMF\cdot 7H_2O$ (210 mg, 82%) Anal. Calcd (Found) for $C_{84}H_{135}N_{19}O_{35}Cu_3$: C, 46.67 (46.28); H, 6.29 (6.23); N, 12.31 (12.42)%.

Synthesis of $[Cu_3(L^{13})(H_2O)_3]\cdot 6DMF\cdot 5H_2O$ (NOTT-161)

H_6L^{13} (100 mg, 0.11 mmol) and $Zn(NO_3)_2\cdot 6H_2O$ (132 mg, 0.45 mmol) were dissolved in DMF (10 ml), to which 37% HCl (10 drops) was added. This mixture was heated in a sealed vial at 90 °C for 48 h to produce colourless octahedral crystals which were isolated by filtration and washed with hot DMF. These crystals were soaked in a solution of $Cu(NO_3)_2\cdot 3H_2O$/DMF for 2 months, washed with copious

DMF and dried to give green octahedral crystals of $[Cu_3(L^{13})(H_2O)_3]\cdot 6DMF\cdot 5H_2O$ (135 mg, 77%). Anal. Calcd (Found) for $C_{60}H_{70}N_{11}O_{24}F_3Cu_3$: C, 45.70 (45.81); H, 4.47 (4.31); N, 9.77 (9.95)%.

Synthesis of $[Zn_3(L^{14})(H_2O)_2]$

H_8L^{14} (10 mg, 0.011 mmol) and $Zn(NO_3)_2\cdot 6H_2O$ (16.5 mg, 0.055 mmol) were dissolved in DMF (2 ml), to which 69% HNO_3 (1 drop) was added. This mixture was heated in a sealed vial at 90 °C for 120 h to produce colourless block crystals which were isolated by filtration and washed with hot DMF.

Synthesis of $[Cu_2(L^{15})(OH)_2]$

H_4L^{15} (10 mg, 0.019 mmol) and $Cu(NO_3)_2\cdot 6H_2O$ (18.2 mg, 0.075 mmol) were dissolved in a mixture of NMP/H_2O (5:1, 2.5 ml) and heated at 80 °C to produce green plate crystals. After washing with hot DMF, the product was isolated by filtration (14 mg).

4.7 References

1. Ke, Y.; Collins, D. J; Sun, D.; Zhou, H-C., *Inorg. Chem.*, **2006**, *45*, 1897.
2. Ma, S.; Yuan, D.; Wang, X-S.; Zhou, H-C., *Inorg. Chem.*, **2009**, *48*, 2072.
3. Sun, D.; Ma, S.; Ke, Y.; Petersen, T. M.; Zhou, H-C., *Chem. Commun.*, **2005**, 2663.
4. Ma, S.; Eckert, J.; Forster, P. M.; Yoon, J. W.; Hwang, Y. K.; Chang, J-S.; Collier, C. D.; Parise, J. B.; Zhou, H-C., *J. Am. Chem. Soc.*, **2008**, *130*, 15896.
5. Sun, D.; Ke, Y.; Collins, D. J.; Lorigan, G. A.; Zhou, H-C., *Inorg. Chem.*, **2007**, *46*, 2725.
6. Luebke, R.; Eubank, J. F.; Cairns, A. J.; Belmabkhout, Y.; Wojtas, L.; Eddaoudi, M., *Chem. Commun.*, **2012**, *48*, 1455.
7. Luebke, R.; Weseliński, L. J.; Belmabkhout, Y.; Chen, Z.; Wojtas, L.; Eddaoudi, M., *Cryst. Growth Des.*, **2014**, *14*, 414.

8. Li, B.; Zhang, Z.; Li, Y.; Yao, K.; Zhu, Y.; Deng, Z.; Yang, F.; Zhou, X.; Li, G.; Wu, H.; Nijem, N.; Chabal, Y. J.; Lai, Z.; Han, Y.; Shi, Z.; Feng, S.; Li, J., *Angew. Chem., Int. Ed.,* **2012**, *51*, 1412.
9. Wang, X-S.; Ma, S.; Sun, D.; Parkin, S.; Zhou H-C., *J. Am. Chem. Soc.,* **2006**, *128*, 16474.
10. Fang, Q-R.; Yuan, D-Q.; Sculley, J.; Li, J-R.; Han, Z-B.; Zhou, H-C., *Inorg. Chem.*, **2010**, *49*, 11637.
11. Pham, T.; Forrest, K. A.; Eckert, J.; Georgiev, P. A.; Mullen, A.; Luebke, R.; Cairns, A. J.; Belmabkhout, Y.; Eubank, J. F.; McLaughlin, K.; Lohstroh, W.; Eddaoudi, M.; Space, B., *J. Phys. Chem. C*, **2014**, *118*, 439.
12. Liu, K.; Ma, D.; Li, B.; Li, Y.; Yao, K.; Zhang, Z.; Han, Y.; Shi, Z., *J. Mater. Chem. A,* **2014**, *2*, 15823.
13. Liu, K.; Li, B.; Li, Y.; Li, X.; Yang, F.; Zeng, G.; Peng, Y.; Zhang, Z.; Li, G.; Shi, Z.; Feng, S.; Song, D., *Chem. Commun.*, **2014**, *50*, 5031.
14. Spek, A. L., *Acta Crystallogr., Sect. D: Biol. Crystallogr.,* **2009**, *65*, 148.
15. Sha, Y.; Dong, Y., *Synth. Commun.,* **2003**, *33*, 2599.
16. Yan, Y.; Lin, X.; Yang, S.; Blake, A. J.; Dailly, A.; Champness, N. R.; Hubberstey, P.; Schröder, M., *Chem. Commun.,* **2009**, 1025.
17. Yan, Y.; Telepeni, I.; Yang, S.; Lin, X.; Kockelmann, W.; Dailly, A.; Blake, A. J.; Lewis, W.; Walker, G. S.; Allan, D. R.; Barnett, S. A.; Champness, N. R.; Schröder, M., *J. Am. Chem. Soc.*, **2010**, *132*, 4092.
18. Yan, Y.; Blake, A. J.; Lewis, W.; Barnett, S. A.; Dailly, A.; Champness, N. R.; Schröder, M., *Chem. Eur. J.,* **2011**, *17*, 11162.
19. Yan, Y.; Yang, S.; Blake, A. J.; Lewis, W.; Poirier, E.; Barnett, S. A.; Champness, N. R.; Schröder, M., *Chem. Commun.*, **2011**, *47*, 9995.
20. Yan Y.; Suyetin, M.; Bichoutskaia, E.; Blake, A. J.; Allan, D. R.; Barnett, S. A.; Schröder, M., *Chem. Sci.,* **2013**, *4*, 1731.
21. Yan, Y.; Yang, S.; Blake, A. J.; Schröder, M., *Acc. Chem. Res.,* **2013**, *47*, 296.
22. Farha, O. K.; Yazaydin, A. Ö.; Eryazici, I.; Malliakas, C. D.; Hauser, B. G.; Kanatzidis, M. G.; Nguyen, S. T.; Snurr, R. Q.; Hupp, J. T., *Nature Chem.,* **2010**, *2*, 944.
23. Yuan, D.; Zhao, D.; Sun, D.; Zhou, H.-C., *Angew. Chem., Int. Ed.,* **2010**, *49*, 5357.
24. Farha, O. K.; Wilmer, C. E.; Eryazici, I.; Hauser, B. G.; Parilla, P. A.; O'Neill, K.; Sarjeant, A. A.; Nguyen, S. B. T.; Snurr, R. Q.; Hupp, J. T., *J. Am. Chem. Soc.*, **2012**, *134*, 9860.

25. Farha, O. K.; Eryazici, I.; Jeong, N. C.; Hauser, B. G.; Wilmer, C. E.; Sarjeant, A. A.; Snurr, R. Q.; Nguyen, S. B. T.; Yazaydin, A. Ö.; Hupp, J. T., *J. Am. Chem. Soc.*, **2012**, *134*, 15016.
26. Yang, S.; Sun, J. L.; Ramirez-Cuesta, A. J.; Callear, S. K.; David, W. I. F.; Anderson, D. P.; Newby, R.; Blake, A. J.; Parker, J. E.; Tang, C. C.; Schröder, M., *Nature Chem.*, **2012**, *4*, 887.
27. An, J.; Geib, S. J.; Rosi, N. L., *J. Am. Chem. Soc.*, **2010**, *132*, 38.
28. Millward, A. R.; Yaghi, O. M., *J. Am. Chem. Soc.*, **2005**, *127*, 17998.
29. McDonald, T. M.; Lee, W. R.; Mason, J. A.; Wiers, B. M.; Hong, C. S.; Long, J. R., *J. Am. Chem. Soc.*, **2012**, *134*, 7056.
30. Arstad, B.; Fjellvåg, H.; Kongshaug, K. O.; Swang, O.; Blom, R., *Adsorption*, **2008**, *14*, 755.
31. Alsmail, N. H.; Suyetin, M.; Yan, Y.; Cabot, R.; Krap, C. P.; Lü, J.; Easun, T. L.; Bichoutskaia, E.; Lewis, W.; Blake, A. J.; Schröder, M., *Chem. Eur. J.*, **2014**, *20*, 7317.
32. Mulfort, K. L.; Farha, O. K.; Malliakas, C. D.; Kanatzidis, M. G.; Hupp, J. T., *Chem. Eur. J.*, **2010**, *10*, 276.
33. Bae, Y-S.; Snurr, R. Q., *Angew. Chem., Int. E*d., **2011**, *50*, 11586.
34. He, Y.; Song, C.; Ling, Y.; Wu, C.; Krishna, R.; Chen, B., *APL Mater.*, **2014**, *2*, 124102.
35. Herm, Z. R.; Bloch, E. D.; Long, J. R., *Chem. Mater.*, **2014**, *26*, 323.
36. Trung, T. K.; Trens, P.; Tanchoux, N.; Bourrelly, S.; Llewellyn, P. L.; Loera-Serna, S.; Serre, C.; Loiseau, T.; Fajula, F.; Férey, G., *J. Am. Chem. Soc.*, **2008**, *130*, 16926.
37. Xu, H.; He, Y.; Zhang, Z.; Xiang, S.; Cai, J.; Cui, Y.; Yang, Y.; Qian, G.; Chen, B., *J. Mater. Chem. A*, **2013**, *1*, 77.
38. Verma, P.; Xu, X.; Truhlar,D. G., *J. Phys. Chem. C*, **2013**, *117*, 12648.
39. Chen, Z.; Xiang, S.; Arman, H. D.; Mondal, J. U.; Li, P.; Zhao, D.; Chen, B., *Inorg. Chem.*, **2011**, *50*, 3442.
40. Cai, J.; Yu, J.; Xu, H.; He, Y.; Duan, X.; Cui, Y.; Wu, C.; Chen, B.; Qian, G., *Cryst. Growth Des.*, **2013**, *13*, 2094.
41. S.A. Rackley, *Carbon Capture and Storage*, Elsevier, **2010**.
42. Li, J-R.; Ma, Y.; McCarthy, M. C.; Sculley, J.; Yu, J.; Jeong, H-K.; Balbuena, P. B.; Zhou, H-C., *Coord. Chem. Rev.*, **2011**, *255*, 1791.
43. Czaja, A. U.; Trukhan, N.; Müller, U., *Chem. Soc. Rev.*, **2009**, 38, 1284.
44. Furukawa, H.; Ko, N.; Go, Y. B.; Aratani, N.; Choi, S. B.; Choi, E.; Yazaydin, A. Ö.; Snurr, R. Q.; O'Keeffe, M.; Kim, J.; Yaghi, O. M., *Science*, **2010**, *329*, 424.

45. Xu, H.; He, Y.; Zhang, Z.; Xiang, S.; Cai, J.; Cui, Y.; Yang, Y.; Qian, G.; Chen, B., *J. Mater. Chem. A*, **2013**, *1*, 77.
46. Chen, Z.; Xiang, S.; Arman, H. D.; Mondal, J. U.; Li, P.; Zhao, D.; Chen, B., *Inorg. Chem.*, **2011**, *50*, 3442.
47. Das, M. C.; Xu, H.; Xiang, S.; Zhang, Z.; Arman, H. D.; Qian, G.; Chen, B., *Chem. Eur. J.*, **2011**, *17*, 7817.
48. Zhang, Z.; Xiang, S.; Chen, Y.; Ma, S.; Lee, Y.; Phely-Bobin, T.; Chen, B., *Inorg. Chem.*, **2010**, *49*, 8444.
49. Zhang, Z.; Xiang, S.; Rao, X.; Zheng, Q.; Fronczek, F. R.; Qian, G.; Chen, B., *Chem. Commun.*, **2010**, *46*, 7205.
50. Chen, Z.; Xiang, S.; Arman, H. D.; Li, P.; Tidrow, S.; Zhao, D.; Chen, B., *Eur. J. Inorg. Chem.*, **2010**, 3745.
51. Li, J-R.; Tao, Y.; Yu, Q.; Bu, X-H.; Sakamoto, H.; Kitagawa, S., *Chem. Eur. J.*, **2008**, *14*, 2771.
52. Samsonenko, D. G.; Kim, H.; Sun, Y.; Kim, G-H.; Lee, H-S.; Kim, K., *Chem. Asian J.*, **2007**, *2*, 484.
53. Zhang, Z.; Xiang, S.; Chen, B., *CrystEngComm.*, **2011**, *13*, 5983.
54. Matsuda, R.; Kitaura, R.; Kitagawa, S.; Kubota, Y.; Belosludov, R. V.; Kobayashi, T. C.; Sakamoto, H.; Chiba, T.; Takata, M.; Kawazoe, Y.; Mita, Y., *Nature*, **2005**, *436*, 238.
55. Furukawa, H.; Ko, N.; Go, Y. B.; Aratani, N.; Choi, S. B.; Choi, E.; Yazaydin, A. Ö.; Snurr, R. Q.; O'Keeffe, M.; Kim, J.; Yaghi, O. M., *Science*, **2010**, *329*, 424.
56. Gàndara, F.; Furukawa, H.; Lee, S.; Yaghi, O. M., *J. Am. Chem. Soc.*, **2014**, *136*, 5271.
57. Mason, J. A.; Veenstra, M.; Long, J. R., *Chem. Sci.*, **2014**, *5*, 32.
58. Ma, S.; Sun, D.; Simmons, J. M.; Collier, C. D.; Yuan, D.; Zhou, H-C., *J. Am. Chem. Soc.*, **2008**, *130*, 1012.
59. Zacharie, B.; Abbott, S. D.; Bienvenu, J-F.; Cameron, A. D.; Cloutier, J.; Duceppe, J-S.; Ezzitouni, A.; Fortin, D.; Houde, K.; Lauzon, C.; Moreau, N.; Perron, V.; Wilb, N.; Asselin, M.; Doucet, A.; Fafard, M-E.; Gaudreau, D.; Grouix, B.; Sarra-Bournet, F.; St-Amant, N.; Gagnon, L.; Penney, C. L., *J. Med. Chem.*, **2010**, *53*, 1138.
60. Wang, Y-X.; Li, Z-Y.; Zhu, J.; Wang, X-Q.; Xu, L. L.; Lachgar, A.; Zhang, J-J., *CrystEngComm.*, **2013**, *15*, 6395.
61. Park, J.; Feng, D.; Zhou, H-C., *J. Am. Chem. Soc.*, **2015**, *137*, 1663.
62. Feng, D.; Wang, K.; Su, J,; Liu, T. F.; Park, J.; Wei, Z.; Bosch, M.; Yakovenko, A.; Zou, X.; Zhou, H-C., *Angew. Chem., Int. Ed.*, **2015**, *54*, 149.

Chapter 5

Conclusions

The work presented in this Thesis has successfully achieved the initial aims of demonstrating PGM extraction from aqueous and organic solutions using a range of stable, functionalised MOFs.

In Chapter 2, water-stable Zr(IV) MOFs were synthesised and proved to be effective for the extraction of $PtCl_6^{2-}$ from aqueous and acidic solutions using ICP-OES and UV-Vis techniques. This represents the first report of a MOF used for extraction of the hexachloroplatinate anion and the first use of a MOF for PGM extraction performed in acidic conditions. UiO-66-NH_2 was shown to be more effective than four industrially used materials for the removal of $PtCl_6^{2-}$ from water over a range of different concentrations. This MOF also exhibited good uptake of $PtCl_6^{2-}$ and $PdCl_6^{2-}$ from HCl solutions and showed excellent selectivity for Pd over Pt (20:1). ^{13}C SS-NMR spectroscopy clearly showed the interaction between the NH_2 groups of UiO-66-NH_2 and the PGM species and an XPS study of the PGM-doped materials showed a low Cl content, suggesting that the encapsulated species may be $PtCl_3(NH_2)_3$ or $PtCl_4(NH_2)_2$. Finally, it was demonstrated that UiO-66-NH_2 was capable of 100% selective uptake of $PtCl_6^{2-}$ and $PdCl_6^{2-}$ over common base metal impurities $CuCl_2$ and $CuSO_4$ from HCl solutions, including cases in which the Cu species was in 100-fold excess.

To further this work, the extraction of $PdCl_2$ from acidic HCl solutions will be investigated using UiO-66-NH_2, as will the separation of $PdCl_2$ from Pt and Cu salts. Likewise, the separation of PGM anions from Ni salts (common impurities in PGM-containing ores) will also be studied. To further probe the exact nature of the interactions between the framework and PGM anions, ^{15}N DNP SS-NMR spectroscopy of the activated and PGM-doped MOFs could be carried out. Finally, results from the work carried out on NOTT-300(Al) suggested that the design and

synthesis of a MOF containing 1D channels and amine functionality could show high uptake of PGM anions from HCl solutions – this would be a natural extension of the work presented in Chapter 2.

In Chapter 3, four functionalised tetracarboxylate linkers were synthesised for the preparation of a series of related Cu(II) MOFs (Figure 5.1) for extraction of neutral PGM complexes from organic solutions. The linker design allowed for a comparison between MOFs of **ssa** and **fof** topology as well as a comparison between amide, oxamide and methyl groups for the encapsulation of $Pd(OAc)_2$, $PtCl_4$ and $Rh(OAc)_4$.

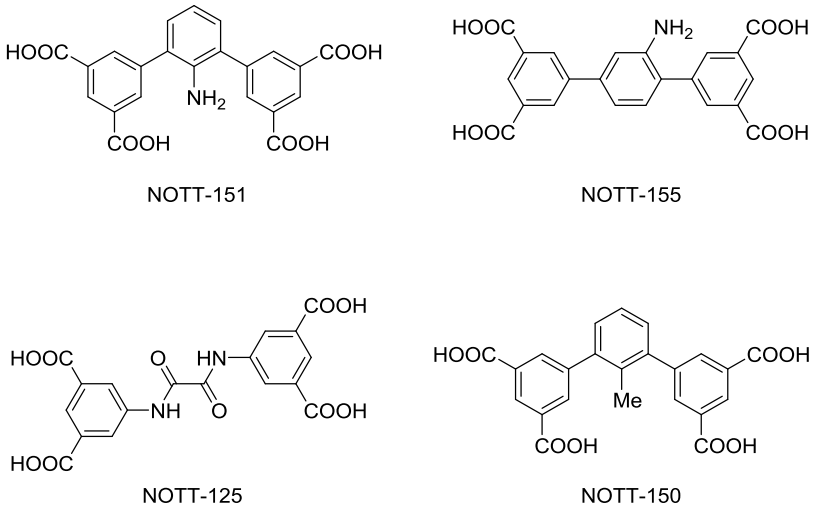


Figure 5.1. The linkers and corresponding MOF nomenclature for the frameworks described in Chapter 3.

Importantly, each MOF exhibited uptake of the PGM complexes by ICP-OES and XPS techniques. The MOFs of **fof** topology, NOTT-155 and NOTT-125, clearly showed greater uptake of $Pd(OAc)_2$ and $PtCl_4$ from THF than the **ssa** MOFs, NOTT-151 and NOTT-150. In particular, the comparison between amine-functionalised NOTT-155 and NOTT-151 suggested that the larger pores in NOTT-155 were responsible for the higher uptake. Of the **fof** MOFs, NOTT-125 showed higher and

more consistent uptake of $Pd(OAc)_2$ than NOTT-155, while NOTT-155 exhibited a higher capacity for $PtCl_4$. As predicted, the methyl-functionalised NOTT-150 showed considerably lower uptake of $Pd(OAc)_2$ and $PtCl_4$ than the amine and oxamide-functionalised MOFs, showing the importance of a including a functional group able to coordinate with the guest metal complex. XPS analysis of the doped samples showed significantly greater PGM content than the ICP-OES data. This strongly suggested that the extraction was only occurring near the surface of the MOFs, as XPS analysis has a maximum depth of 10 nm, whereas ICP-OES gives information on the bulk sample. Finally, uptake of $Rh_2(OAc)_4$ was shown to be very low for each framework by both ICP-OES and XPS, this was attributed to the large size of the rhodium acetate dimer. Further work to be carried out on these materials includes ^{13}C and ^{15}N SS-NMR spectroscopy of the PGM-doped frameworks to probe the interactions between the MOFs and the guest metal complexes. Future experiments could include the synthesis of water-stable Fe/Zr/Al analogues of the MOFs reported in Chapter 3. Such materials could be used for the extraction of neutral PGM complexes from organic solvents and extraction of PGM anions from aqueous and acidic solutions. Crystallographic refinement of PGM positions in these MOFs would also be of great interest and may be attained by slow heating/cooling of a MOF in the desired PGM solution to maximise ordering of the metal complex within the pores.

In Chapter 4, a triazine containing MOF of **rht** topology, denoted $[Cu_3L^{11}]$, was prepared for the extraction of $Pd(OAc)_2$, $PtCl_4$ and $Rh_2(OAc)_4$ from THF. ICP-OES analysis revealed that $[Cu_3L^{11}]$ exhibited a similar capacity for $Pd(OAc)_2$ as NOTT-125 and a greater capacity than the other Cu(II) MOFs described in Chapter 3. However, uptake of $PtCl_4$ in $[Cu_3L^{11}]$ was significantly lower than that observed for

NOTT-151, NOTT-155 and NOTT-125. This was attributed to the weaker interactions of the pyridyl and secondary amine groups of [Cu_3L^{11}] with the metal complex in comparison to the oxamide and primary amine groups of the tetracarboxylate MOFs. In contrast, [Cu_3L^{11}] showed a more consistent and higher uptake of $Rh_2(OAc)_4$ than NOTT-151, NOTT-155 and NOTT-125, which was assigned to the larger cages in [Cu_3L^{11}] (17.8 Å in diameter) allowing the encapsulation of a greater proportion of the PGM. A more porous analogue of [Cu_3L^{11}], denoted as NOTT-160, was also synthesised for the separation of C_2 hydrocarbons from CH_4 and CO_2. The calculated Henry's law selectivity for C_2H_2:CH_4 of 78.8:1 at 298 K for NOTT-160 is the third highest reported in a MOF to date, with the C_2H_4:CH_4 selectivity of 69.6:1 representing the second highest reported value. NOTT-160 also exhibits an unexpectedly high selectivity for C_2H_2 over CO_2 of 16.2:1 at 273 K. Finally, the high pressure uptake of CH_4 was investigated, with NOTT-160 showing an exceptional capacity of 339 mg g^{-1} at 80 bar and a volumetric working capacity of 221 cm^3 cm^{-3}. Future work to be carried out on NOTT-160 includes DFT calculations and inelastic neutron scattering (INS) studies to explain the observed selectivity for C_2H_2 over CO_2 and the selectivity for C_2 hydrocarbons over CH_4. A natural extension of the work reported in Chapter 4 would be the synthesis of highly stable Fe/Al/Zr MOFs prepared from triazine-containing linkers. These frameworks would have a number of applications, particularly for the extraction of PGM anions from aqueous and acidic solutions and for the storage of harmful and corrosive gases such as SO_2 and NH_3.

Appendices

Appendix 1

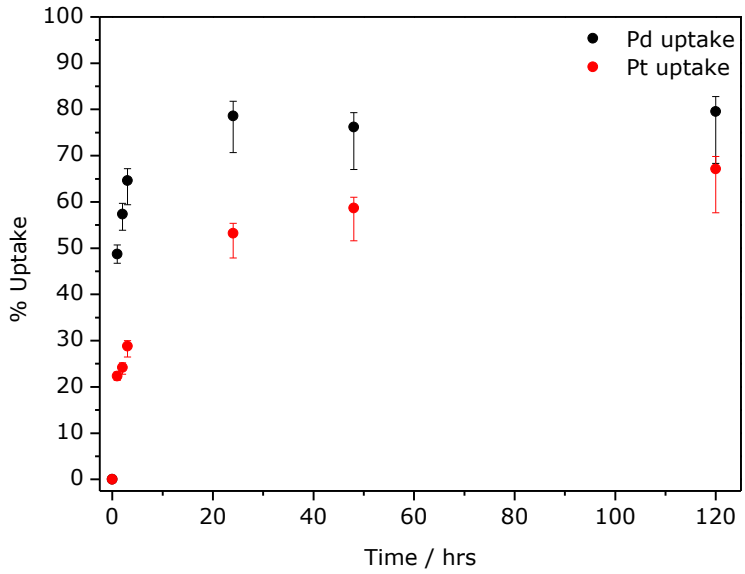


Figure A1.1. Sorption of a mixed 25 ppm Pt/Pd solution of 0.1 M HCl using 50 mg of UiO-66-NH_2.

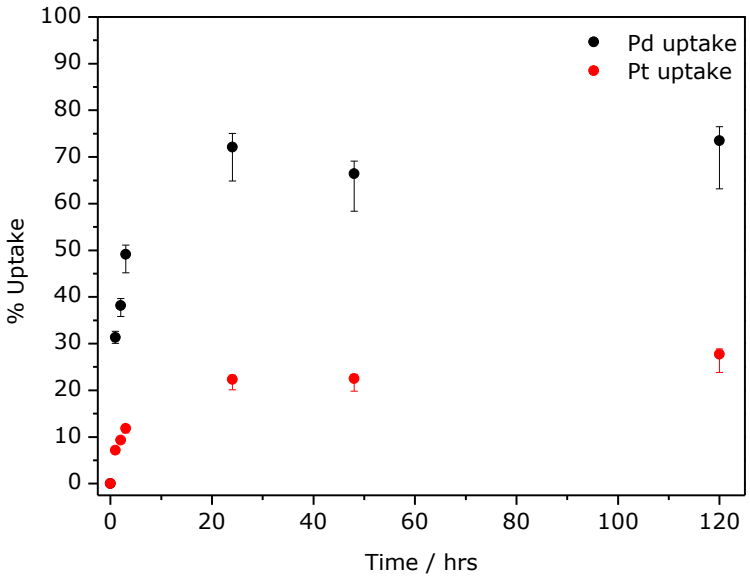


Figure A1.2. Sorption of a mixed 25 ppm Pt/Pd solution of 0.5 M HCl using 50 mg of UiO-66-NH_2.

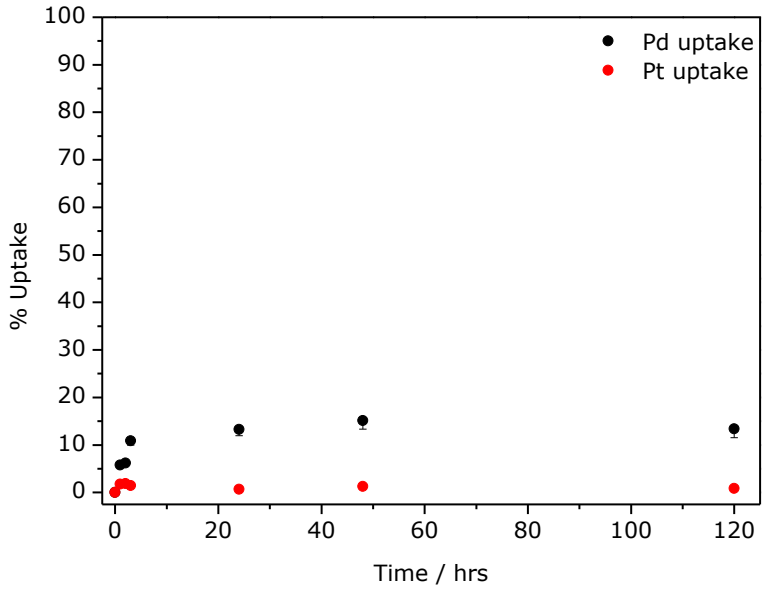


Figure A1.3. Sorption of a mixed 25 ppm Pt/Pd solution of 2 M HCl using 50 mg of UiO-66-NH_2.

Appendix 2

Virial Fitting of 0-1 Bar Isotherms for NOTT-160a

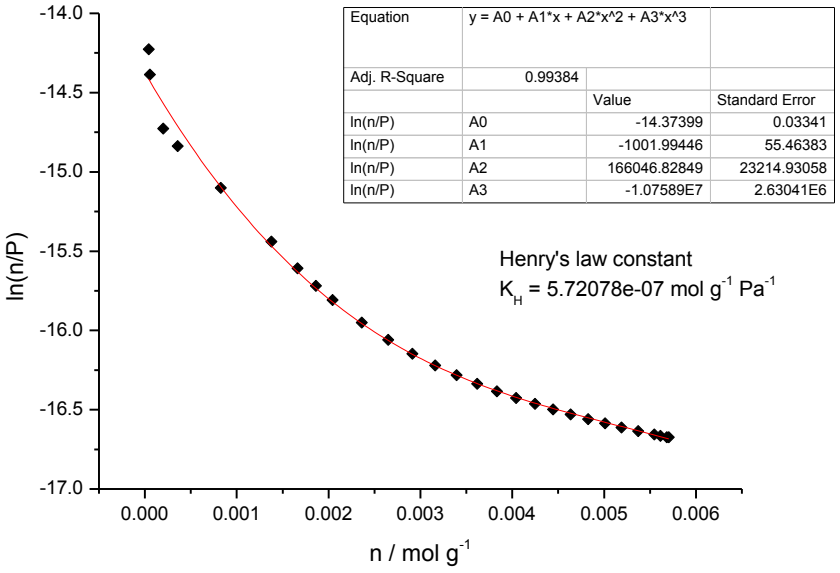


Figure A2.1. Virial analysis of the C_2H_2 isotherm at 298 K.

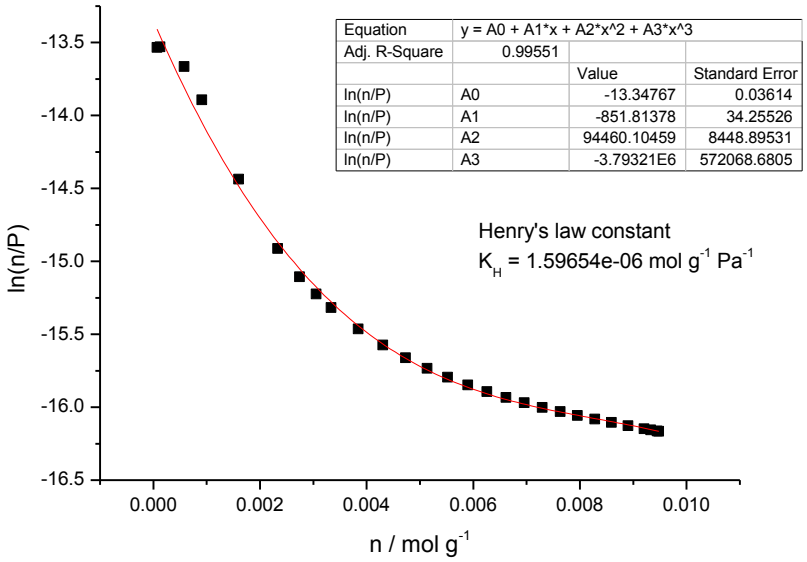


Figure A2.2. Virial analysis of the C_2H_2 isotherm at 273 K.

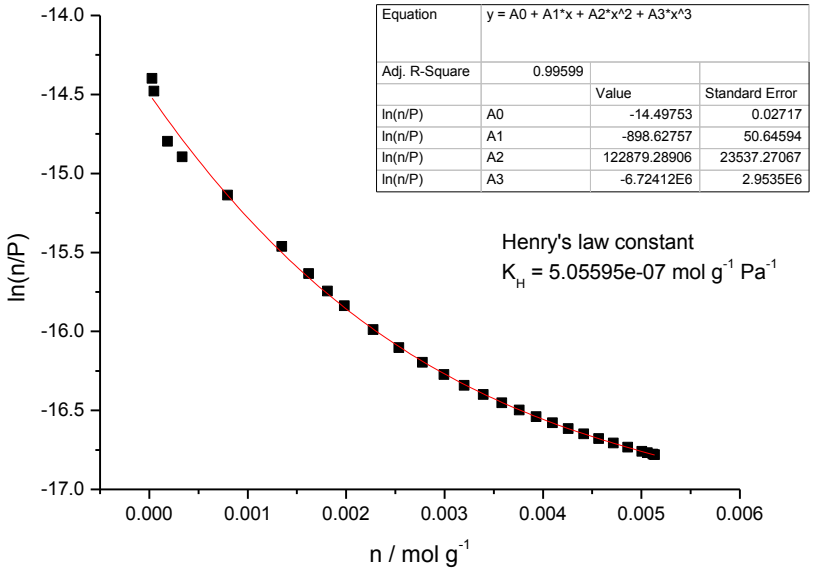


Figure A2.3. Virial analysis of the C_2H_4 isotherm at 298 K.

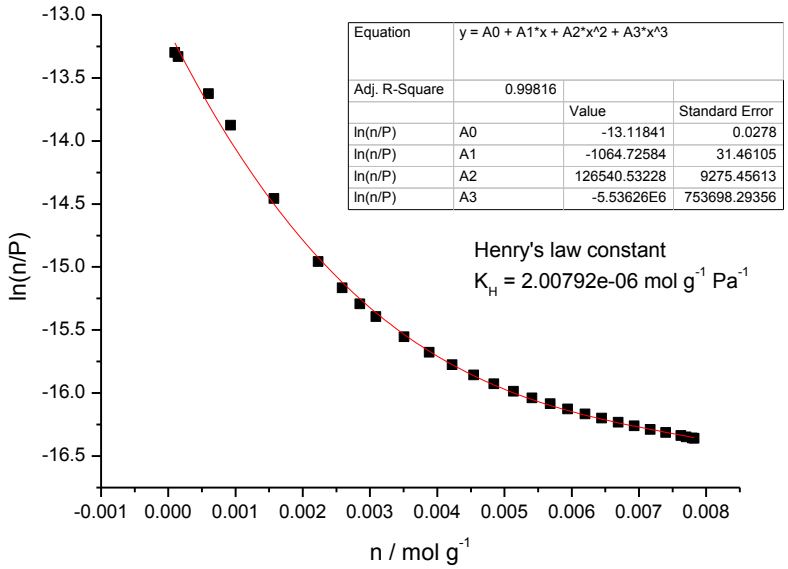


Figure A2.4. Virial analysis of the C_2H_4 isotherm at 273 K.

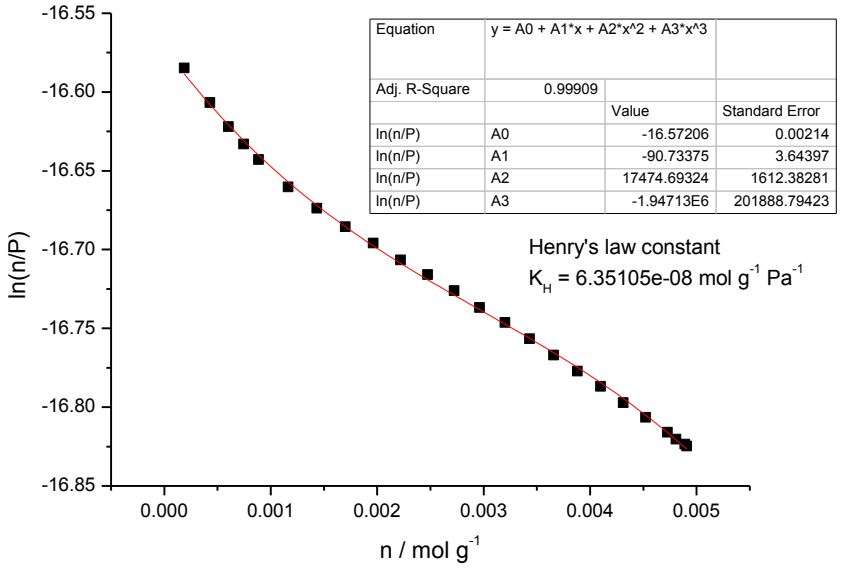


Figure A2.5. Virial analysis of the C_2H_6 isotherm at 298 K.

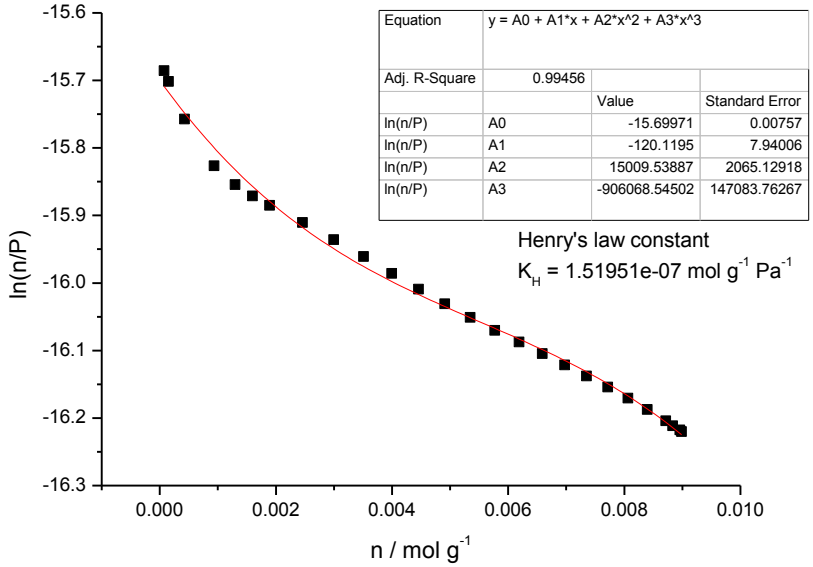


Figure A2.6. Virial analysis of the C_2H_6 isotherm at 273 K.

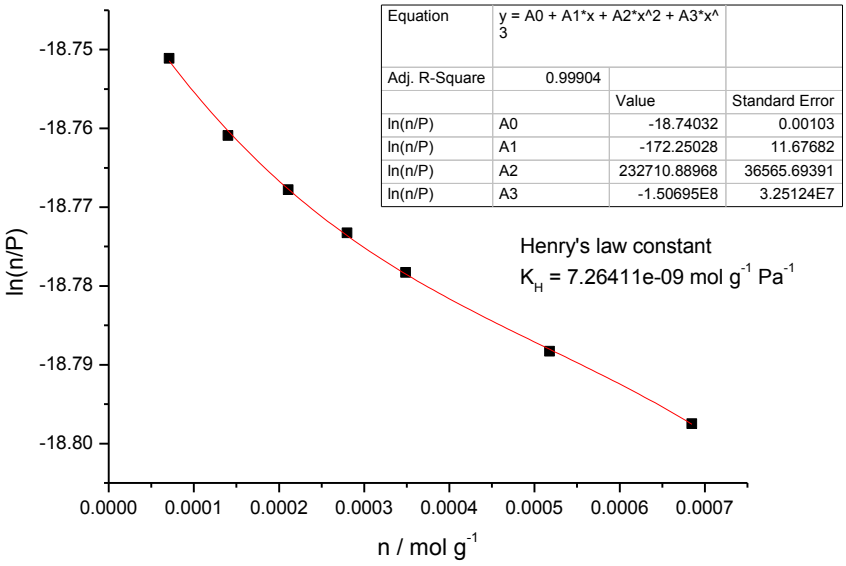


Figure A2.7. Virial analysis of the CH_4 isotherm at 298 K.

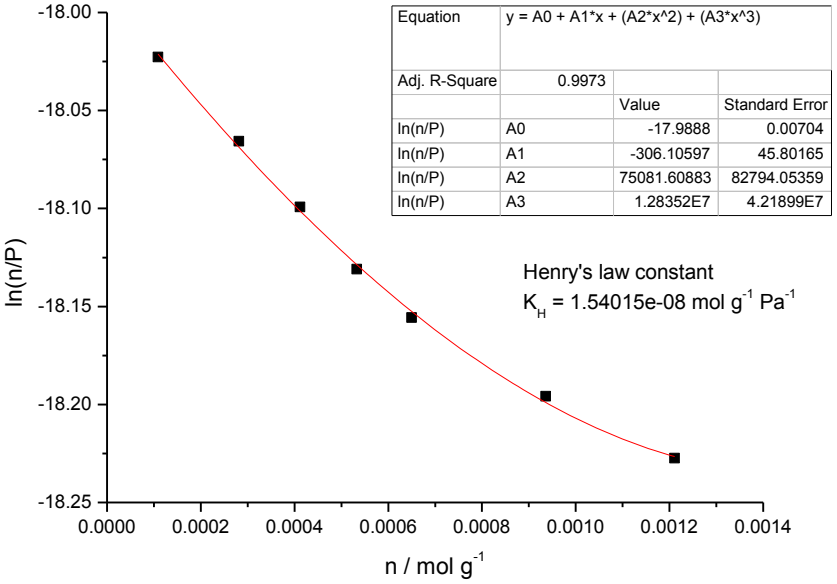


Figure A2.8. Virial analysis of the CH_4 isotherm at 273 K.

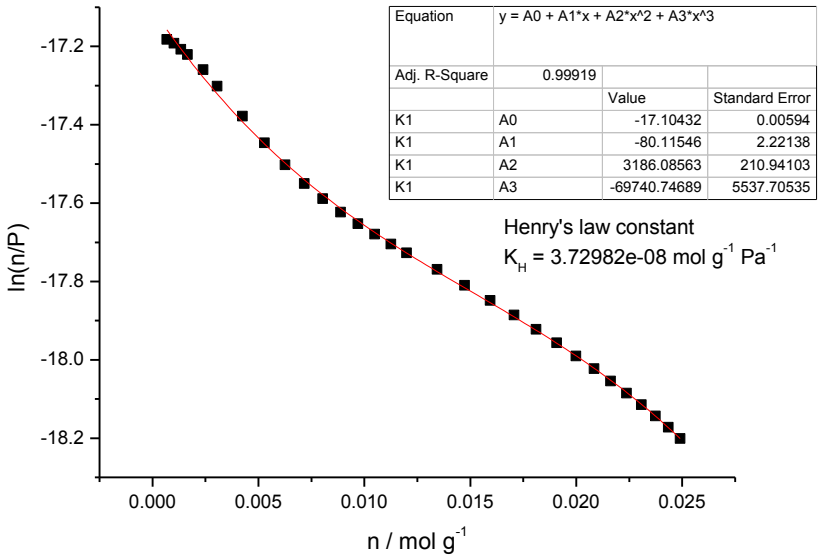


Figure A2.9. Virial analysis of the CO_2 isotherm at 298 K.

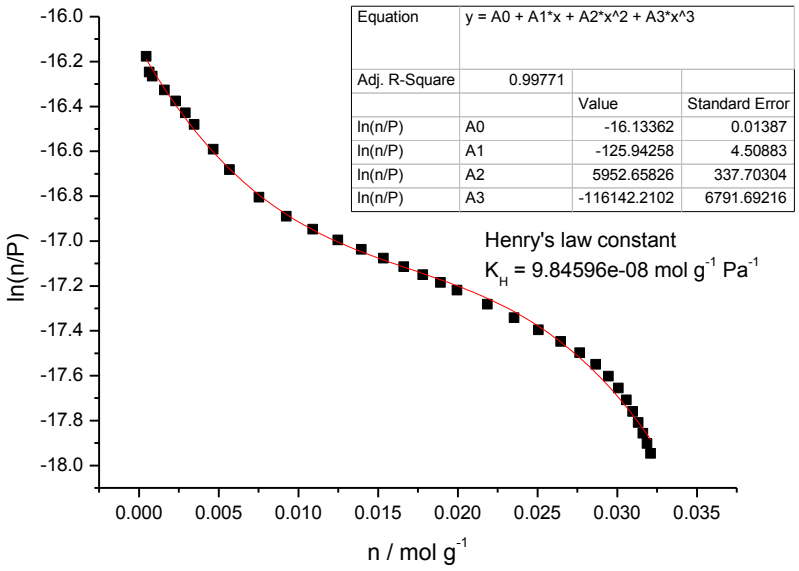


Figure A2.10. Virial analysis of the CO_2 isotherm at 273 K.

Appendix 3

Langmuir-Freundlich Fitting of Isotherm Data for NOTT-160a

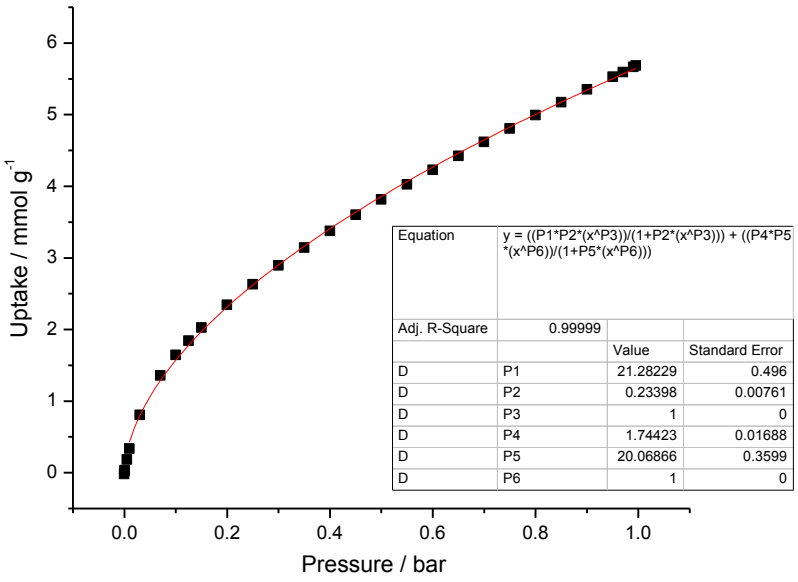


Figure A3.1. Dual-site Langmuir fitting of the C_2H_2 isotherm at 298 K.

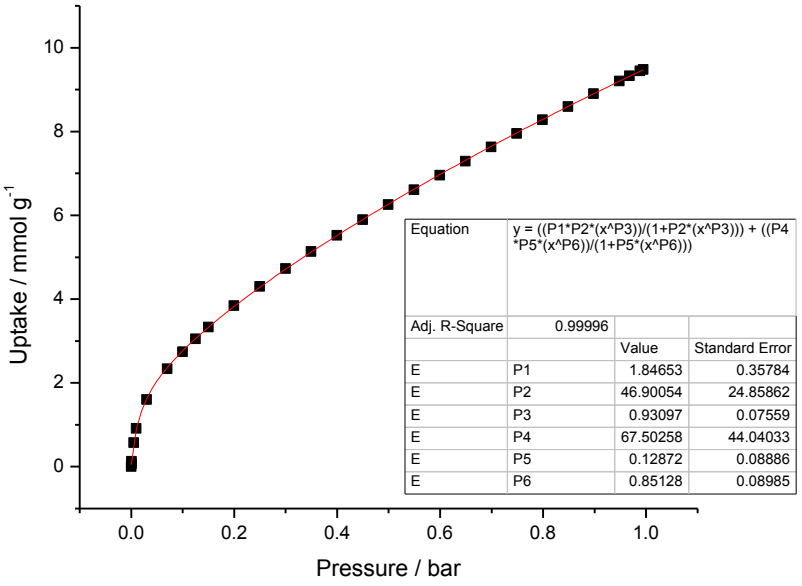


Figure A3. 2. Dual-site Langmuir fitting of the C_2H_2 isotherm at 273 K.

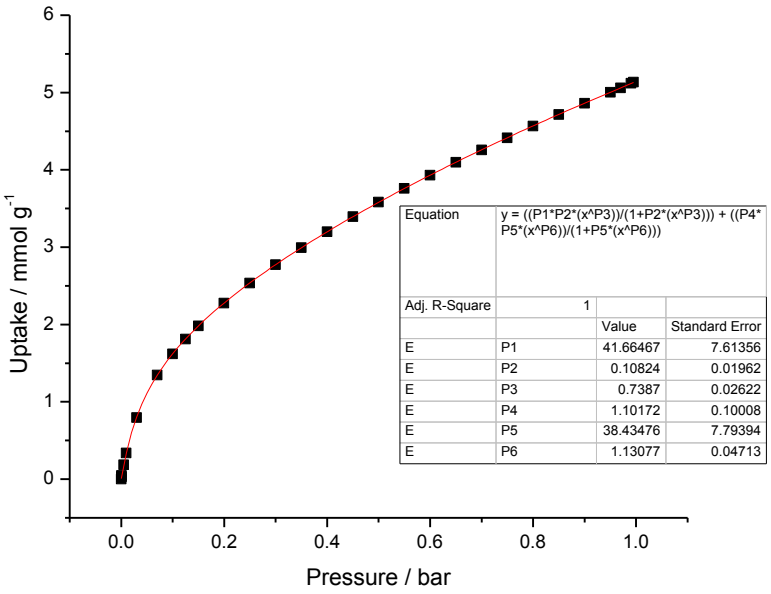


Figure A3.3. Dual-site Langmuir fitting of the C_2H_4 isotherm at 298 K.

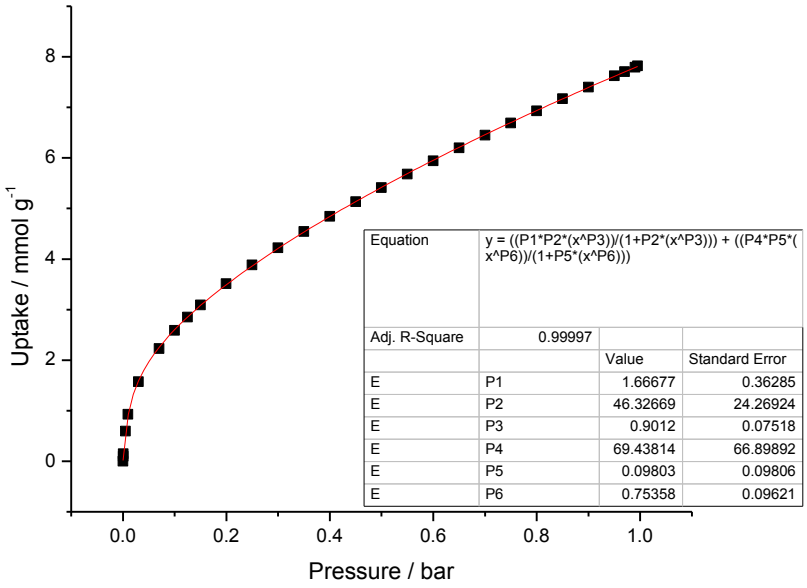


Figure A3.4. Dual-site Langmuir fitting of the C_2H_4 isotherm at 273 K.

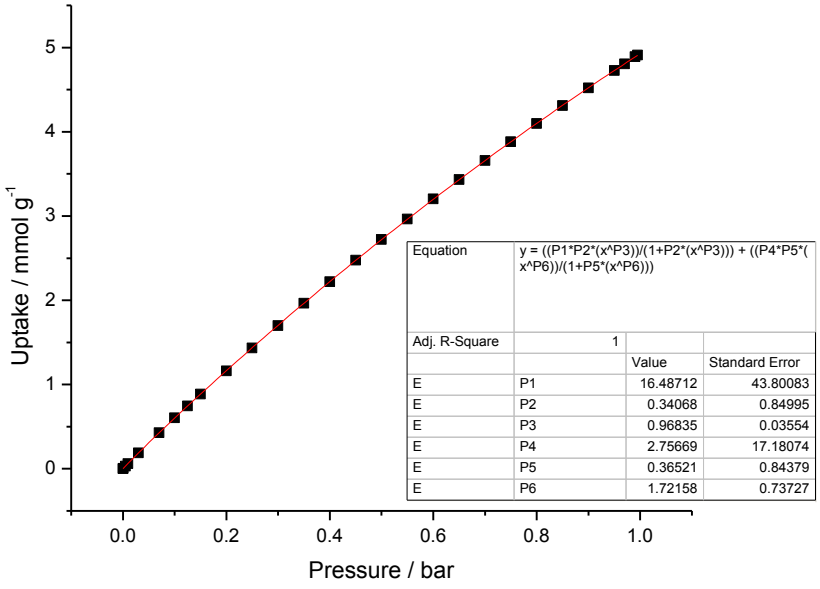


Figure A3.5. Dual-site Langmuir fitting of the C_2H_6 isotherm at 298 K.

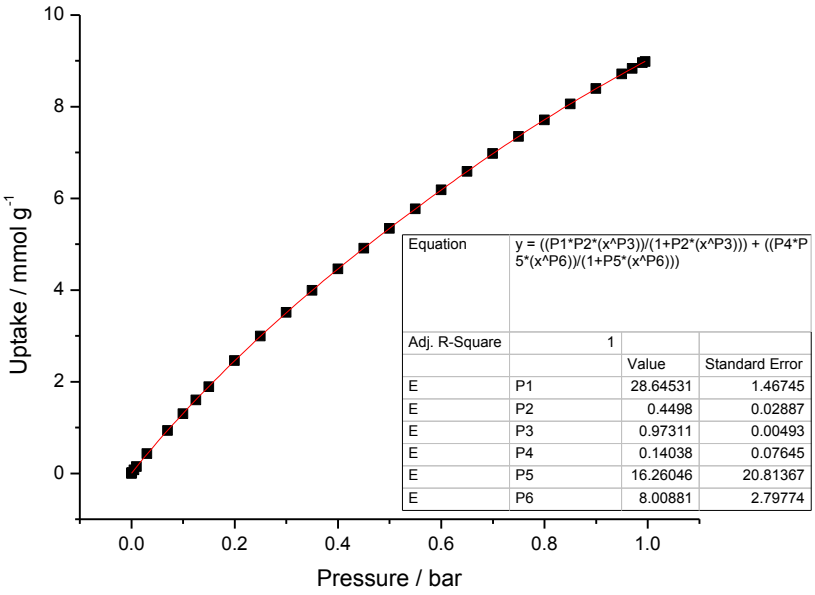


Figure A3.6. Dual-site Langmuir fitting of the C_2H_6 isotherm at 273 K.

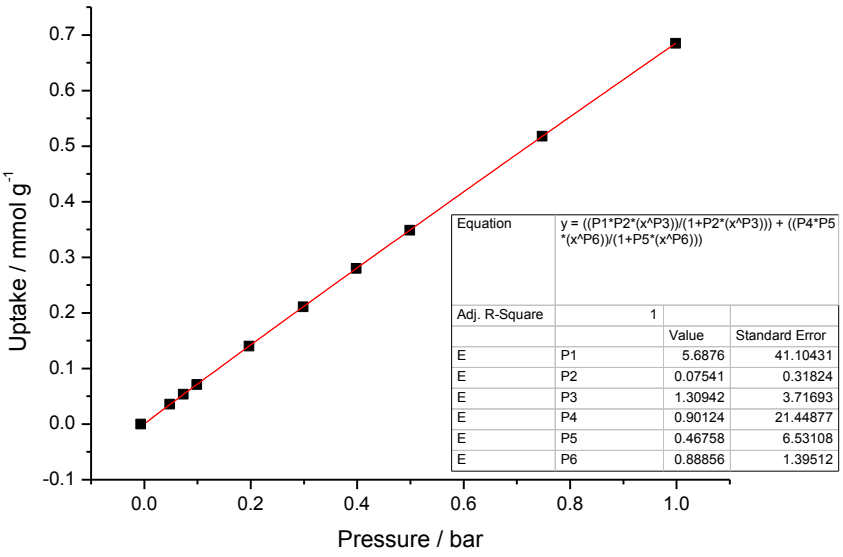


Figure A3.7. Dual-site Langmuir fitting of the CH_4 isotherm at 298 K.

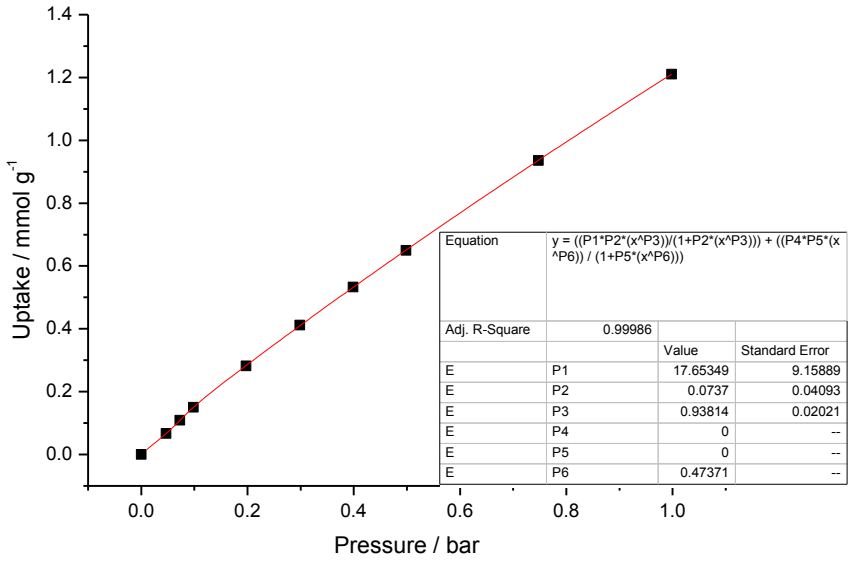


Figure A3.8. Single-site Langmuir fitting of the CH_4 isotherm at 273 K.

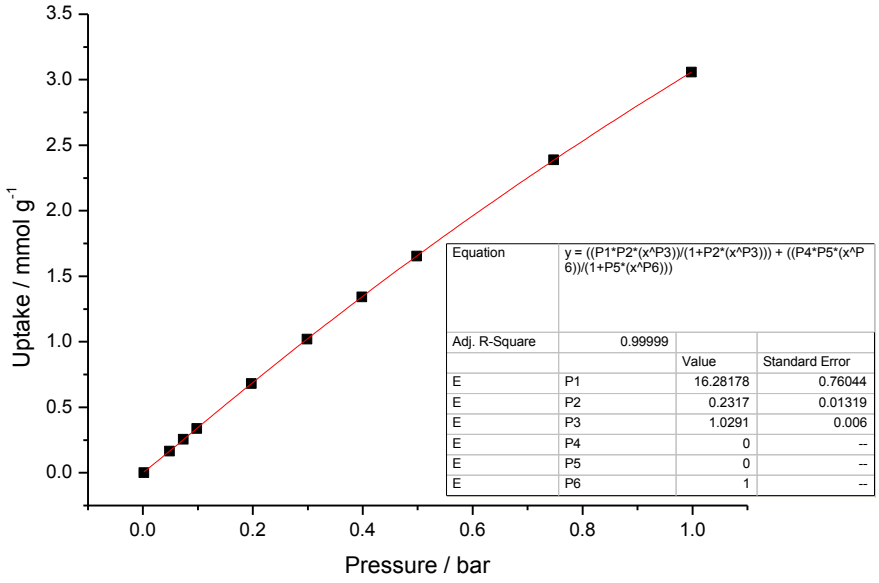


Figure A3.9. Single-site Langmuir fitting of the CO_2 isotherm at 298 K.

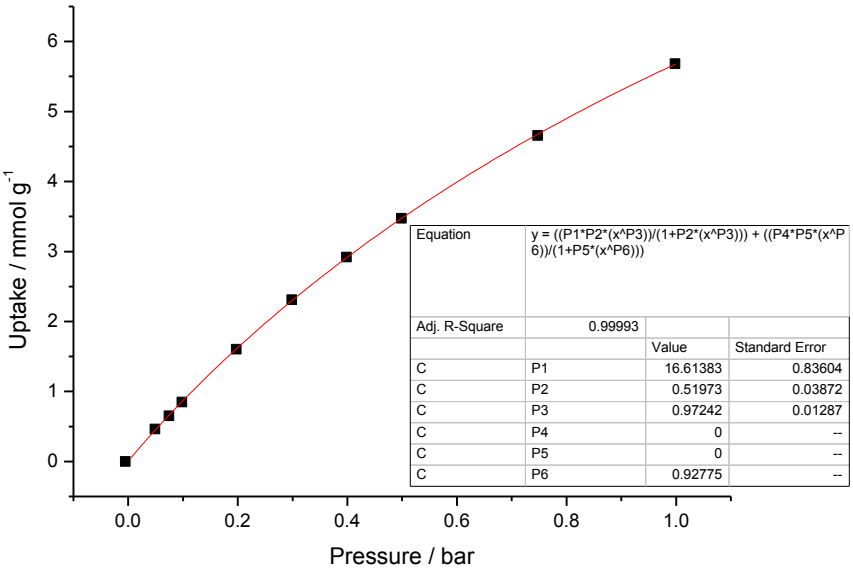


Figure A3.10. Single-site Langmuir fitting of the CO_2 isotherm at 273 K.

Appendix 4

Structural analysis of NOTT-161

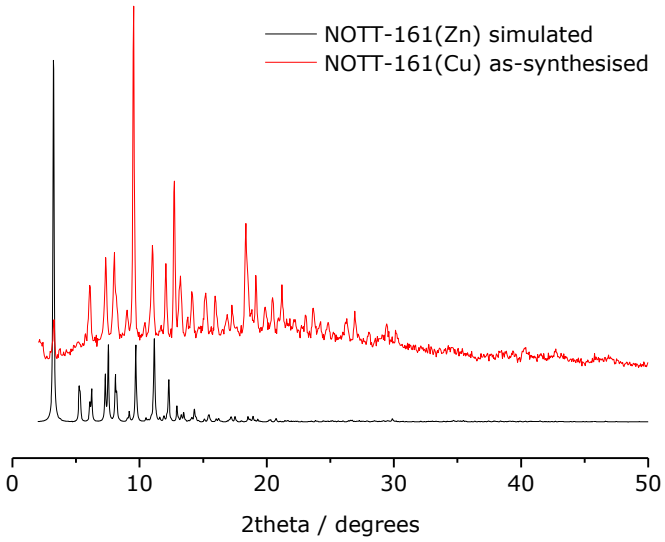


Figure A4.1. PXRD pattern of NOTT-161(Cu) compared to the pattern simulated from the single crystal structure of NOTT-161(Zn).

Appendix 5

Crystallographic data

Table A5.1 NOTT-151

Formula	$Cu_{12}\ C_{132}\ H_{90}\ N_6\ O_{60}$
Formula weight	3482.7 g mol^{-1}
Temperature	120(2) K
Radiation type	Cu Kα
λ / Å	1.54
Crystal system	Hexagonal
Space group	$P6_3/mmc$
a	18.326(8) Å
b	18.326(8) Å
c	23.99(2) Å
α	90 °
β	90 °
γ	120 °
Volume	6977(8) $Å^3$
Z	6
Density	0.829 g cm^{-3}
F(000)	1662
Reflections collected	2665
Completeness	100%
GooF	0.798
Final R indices [Fo > 4 σ(Fo)]	0.0724
Final R indices (all data)	R1 = 0.1134, wR2 = 0.2296
Difference Fourier map: maximum peak, minimum trough (e $Å^{-3}$)	0.50, -0.37

Table A5.2 NOTT-155

Formula	$Cu_{18}\ C_{234}H_{90}\ N_9\ O_{40}$
Formula weight	5611.3 g mol^{-1}
Temperature	120(2) K
Radiation type	Cu Kα
λ / Å	1.54
Crystal system	Trigonal
Space group	*R*_3*m*
a	18.6224(5) Å
b	18.6224(5) Å
c	38.284(1) Å
α	90 °
β	90 °
γ	120 °
Volume	114971.9(7) $Å^3$
Z	36
Density	0.865 g cm^{-3}
F(000)	9792
Reflections collected	2871
Completeness	99%
GooF	1.14
Final R indices [Fo > 4 σ(Fo)]	0.0844
Final R indices (all data)	R1 = 0.0930, wR2 = 0.2695
Difference Fourier map: maximum peak, minimum trough (e $Å^{-3}$)	0.78, -0.96

Table A5.3 NOTT-150

Formula	$Cu_{12}\ C_{132}\ H_{90}\ N_6\ O_{60}$
Formula weight	3458.7 g mol^{-1}
Temperature	120(2) K
Radiation type	Cu Kα
λ / Å	1.54
Crystal system	Hexagonal
Space group	$P6_3/mmc$
a	18.3804(4) Å
b	18.3804(4) Å
c	23.8606(4) Å
α	90 °
β	90 °
γ	120 °
Volume	6981.1(4) $Å^3$
Z	6
Density	0.823 g cm^{-3}
F(000)	1752
Reflections collected	2655
Completeness	100%
GooF	1.061
Final R indices [Fo > 4 σ(Fo)]	0.0669
Final R indices (all data)	R1 = 0.0717, wR2 =0.2487
Difference Fourier map: maximum peak, minimum trough (e $Å^{-3}$)	0.56, -0.45

Table A5.4 $[Co_2(L^{10})(H_2O)(DMF)]_n$

Formula	$Co_8\ C_{76}\ H_{72}\ N_8\ O_{44}$
Formula weight	2772.9 g mol^{-1}
Temperature	120(2) K
Radiation type	Cu Kα
λ / Å	1.54
Crystal system	Monoclinic
Space group	$P2_1/c$
a	10.1447(5) Å
b	18.959(1) Å
c	15.5864(9) Å
α	90 °
β	95.398(5) °
γ	90 °
Volume	2984.4(3) $Å^3$
Z	4
Density	1.265 g cm^{-3}
F(000)	1472
Reflections collected	5823
Completeness	95%
GooF	1.043
Final R indices [Fo > 4 σ(Fo)]	0.0539
Final R indices (all data)	R1 = 0.0672, wR2 = 0.1693
Difference Fourier map: maximum peak, minimum trough (e $Å^{-3}$)	0.56, -0.63

Table A5.5 $[In_4(L^{10})_3][cation]_n$

Formula	$In_3\ C_{64}\ H_{28}\ N_4\ O_{32}$
Formula weight	1708.8 g mol^{-1}
Temperature	120(2) K
Radiation type	Cu Kα
λ / Å	1.54
Crystal system	Monoclinic
Space group	$P2_1/c$
a	9.8716(9) Å
b	22.060(1) Å
c	17.365(2) Å
α	90 °
β	100.620(9) °
γ	90 °
Volume	3716.9(6) $Å^3$
Z	2
Density	0.913 g cm^{-3}
F(000)	1686
Reflections collected	7362
Completeness	97%
GooF	0.817
Final R indices [Fo > 4 σ(Fo)]	0.0948
Final R indices (all data)	R1 = 0.1381, wR2 = 0.2881
Difference Fourier map: maximum peak, minimum trough (e $Å^{-3}$)	1.76, -1.27

Table A5.6 $[Fe_2(L^7)(NMP)_3]_n$

Formula	$Fe_4\,C_{82}\,H_{60}\,N_8\,O_{22}$
Formula weight	1732.8 g mol^{-1}
Temperature	120(2) K
Radiation type	Synchrotron
λ / Å	0.6889
Crystal system	Monoclinic
Space group	$P2_1$
a	10.0795(4) Å
b	17.3430(6) Å
c	15.1751(5) Å
α	90 °
β	105.938(4) °
γ	90 °
Volume	2550.77(16) $Å^3$
Z	1
Density	1.128 g cm^{-3}
F(000)	814
Reflections collected	10138
Completeness	97%
GooF	0.921
Final R indices [Fo > 4 σ(Fo)]	0.0624
Final R indices (all data)	R1 = 0.0651, wR2 = 0.1933
Difference Fourier map: maximum peak, minimum trough (e $Å^{-3}$)	0.54, -0.51

Table A5.7 Cu_3L^{11}

Formula	$Cu_{48}\ C_{432}\ H_{192}\ N_{96}\ O_{240}$
Formula weight	13617.0 g mol^{-1}
Temperature	120(2) K
Radiation type	Cu Kα
λ / Å	1.54
Crystal system	Tetragonal
Space group	*I*4/*m*
a	26.6912(3) Å
b	26.6912(3) Å
c	37.975(1) Å
α	90 °
β	90 °
γ	90 °
Volume	27054(1) $Å^3$
Z	16
Density	0.836 g cm^{-3}
F(000)	7168
Reflections collected	12587
Completeness	90%
GooF	1.075
Final R indices [Fo > 4 σ(Fo)]	0.057
Final R indices (all data)	R1 = 0.0642, wR2 = 0.1811
Difference Fourier map: maximum peak, minimum trough (e $Å^{-3}$)	1.73, -0.53

Table A5.8 NOTT-160(Cu)

Formula	$Cu_{48}C_{720}H_{384}N_{96}O_{192}$
Formula weight	16502.0 g mol^{-1}
Temperature	120(2) K
Radiation type	Synchrotron
λ / Å	0.6889
Crystal system	Tetragonal
Space group	*I*4/*m*
a	32.5561(3) Å
b	32.5561(3) Å
c	47.8548(7) Å
α	90 °
β	90 °
γ	90 °
Volume	50721(1) $Å^3$
Z	16
Density	0.540 g cm^{-3}
F(000)	21798
Reflections collected	45787
Completeness	100%
GooF	0.765
Final R indices [Fo > 4 σ(Fo)]	0.0775
Final R indices (all data)	R1 = 0.1597, wR2 = 0.2234
Difference Fourier map: maximum peak, minimum trough (e $Å^{-3}$)	0.78, -0.4

Table A5.9 NOTT-160(Zn)

Formula	$Zn_{48}C_{720}H_{384}N_{96}O_{192}$
Formula weight	16589.6 g mol^{-1}
Temperature	120(2) K
Radiation type	Cu Kα
λ / Å	1.54
Crystal system	Tetragonal
Space group	*I*4/*m*
a	33.1814(4) Å
b	33.1814(4) Å
c	48.8650(9) Å
α	90 °
β	90 °
γ	90 °
Volume	53800(2) $Å^3$
Z	16
Density	0.510 g cm^{-3}
F(000)	8352
Reflections collected	26913
Completeness	96%
GooF	0.759
Final R indices [Fo > 4 σ(Fo)]	0.0764
Final R indices (all data)	R1 = 0.1179, wR2 =0.2247
Difference Fourier map: maximum peak, minimum trough (e $Å^{-3}$)	0.46, -0.44

Table A5.10 NOTT-161(Zn)

Formula	$Zn_{48}\ C_{720}\ H_{336}\ N_{96}\ F_{48}\ O_{192}$
Formula weight	17452.8 g mol^{-1}
Temperature	120(2) K
Radiation type	Cu Kα
λ / Å	1.54
Crystal system	Tetragonal
Space group	*I*4/*m*
a	33.1419(2) Å
b	33.1419(2) Å
c	48.3988(7) Å
α	90 °
β	90 °
γ	90 °
Volume	53160(1) $Å^3$
Z	16
Density	0.551 g cm^{-3}
F(000)	8736
Reflections collected	25251
Completeness	90%
GooF	1.035
Final R indices [Fo > 4 σ(Fo)]	0.0854
Final R indices (all data)	R1 = 0.1363, wR2 = 0.2974
Difference Fourier map: maximum peak, minimum trough (e $Å^{-3}$)	0.72, -0.79

Table A5.11 $[Zn_3(L^{14})(H_2O)_2]$

Formula	$Zn_{12}\ C_{160}\ H_{116}\ N_{48}\ O_{72}$
Formula weight	4647.6 g mol^{-1}
Temperature	120(2) K
Radiation type	Cu Kα
λ / Å	1.54
Crystal system	Monoclinic
Space group	$P2_1/n$
a	19.323(3) Å
b	23.585(3) Å
c	23.964(2) Å
α	90 °
β	98.878(9) °
γ	90 °
Volume	10790(2) $Å^3$
Z	8
Density	0.715 g cm^{-3}
F(000)	4752
Reflections collected	21335
Completeness	96%
GooF	0.712
Final R indices [Fo > 4 σ(Fo)]	0.0944
Final R indices (all data)	R1 = 0.2037, wR2 = 0.2368
Difference Fourier map: maximum peak, minimum trough (e $Å^{-3}$)	0.57, -0.64